APPLIED COMPUTATIONAL ELECTROMAGNETICS SOCIETY JOURNAL

August 2020
Vol. 35 No. 8
ISSN 1054-4887

The ACES Journal is abstracted in INSPEC, in Engineering Index, DTIC, Science Citation Index Expanded, the Research Alert, and to Current Contents/Engineering, Computing & Technology.

The illustrations on the front cover have been obtained from the research groups at the Department of Electrical Engineering, The University of Mississippi.

AUGUST 2020 REVIEWERS: REGULAR PAPERS

Iftikhar Ahmed
Marco Arjona
Sami Barmada
John Borchardt
Vedula Chakravarthy
Massimo Donelli
Ping Du
Alistair Duffy
Pavel Hazdra
Tianqi Jiao
William Kefauver
Aymen Khaleel
Nikolai Kolev
Neelam Sanjeev Kumar
Sathis Kumar
K. Kumarasamy
Sergio Ledesma
Alberto Leggieri
German Leon
Zahéra Mekkioui
Antonio Orlandi
Panagiotis Papakanellos
Milos Pavlovic
Mirjana Peric
Sobhan Roshani
Babajide Salau
Stefano Selleri
Farzin Shama
Junwu Tao
Anilkumar Tirunagari
Bojan Trkulja
Qian Xu
Ravindra Yadav
Guohui Yang
Min Zhang

AUGUST 2020 REVIEWERS: EXPRESS PAPERS

Tuan Li
Naobumi Michishita
Christopher Trueman

THE APPLIED COMPUTATIONAL ELECTROMAGNETICS SOCIETY JOURNAL

Vol. 35 No. 8 August 2020

TABLE OF CONTENTS – REGULAR PAPERS

TABLE OF CONTENTS – EXPRESS PAPERS

A Straight-Forward Method of Moments Procedure to Solve the Time Domain Integral Equation Applicable to PEC Bodies via Triangular Patch Modeling

Sadasiva M. Rao

Naval Research Laboratory
Washington DC 20375, USA

Abstract – In this work, a simple and straightforward method of moments solution (MOM) procedure is presented to obtain the induced current distribution on an arbitrarily-shaped conducting body illuminated by a Gaussian plane wave directly in the time domain using a patch modeling approach. The method presented in this work, besides being stable, is also capable of handling multiple excitation pulses of varying frequency content incident from different directions in a trivial manner. The method utilizes standard Rao-Wilton-Glisson (RWG) functions and simple triangular functions for the space and time variables, respectively, for both expansion and testing. The method adopts conventional MOM and requires no further manipulation invariably needed in standard time-marching methods. The moment matrix generated via this scheme is a block-wise Toeplitz matrix and, hence, the solution is extremely efficient. The method is validated by comparing the results with the data obtained from the frequency domain solution. Several simple and complex numerical results are presented to validate the procedure.

Index Terms – Electromagnetic fields, Integral equations, Method of moments, Numerical methods, Time Domain.

I. INTRODUCTION

In recent times, the transient analysis of electromagnetic scattering has received a great deal of attention. With the advent of faster computers and an increase of memory space, many scattering problems of complex objects are being performed directly in the time domain because of the generation of a broad-band data in a single simulation. Further, the direct time domain (TD) techniques provide an opportunity to observe and interpret electromagnetic scattering behavior.

Some of the early analytical work in transient electromagnetic problems were based on physical optics to obtain the approximate impulse response from conducting flat plates, spheres, and prolate spheroids [1]. A time domain solution for an infinite cylindrical antenna was performed by Wu in 1961 [2]. Next, Bennett derived an integro-differential equation applicable to a perfectly conducting square plate by enforcing the boundary condition on the electric field and then solved directly in the time domain [3]. Bennett labeled this technique as the space-time integral-equation (STIE) technique. The STIE method discretizes the scatterer into square patches, the time axis divided into equal increments, and the currents at each instant are determined by the knowledge of the incident field and currents at previous instants.

Next, we note that the STIE solution methodology has been applied to many different geometrical shapes, simple as well as complex, and now is known as the Marching-on-in-Time (MOT) method [4]. Although MOT algorithm is popular, it is prone to late-time instabilities with growing oscillations as time progresses which makes the technique unreliable. Unfortunately, most of the proposed remedies to either arrest these oscillations or eliminate them completely, work only for simple problems, and invariably fail for complex objects. In the last 20 years, there has been an explosion of proposed remedies with limited success and only a few selected publications are cited here for completeness [5-19].

Recently, a new type of algorithm was applied to wire-grid models of arbitrary bodies to solve the time domain integral equation (TDIE) using the method of moments (MOM) [20] and [21]. The numerical procedure presented in [21] and [22] is not a MOT scheme and there is no time marching involved. We solve the integral equation over a space-time grid, and hence no error accumulation as happens in MOT schemes. This procedure eliminates marching-on-in-time altogether, remains stable and

Submitted On: February 5, 2016
Accepted On: March 14, 2016
https://doi.org/10.47037/2020.ACES.J.350801

also ideally suited to handle a large number of excitations in a trivial manner. In the present work, we apply this procedure to perfectly electric conducting (PEC) bodies via planar triangular patch modeling.

Next, we further note that the present method is not either explicit or implicit methods commonly available to solve the time-domain integral equation [4]. In our view, both the explicit and the implicit methods are related to Marching-on-in-Time (MOT) method. The only difference being the length of the time step. If the time step is smaller than the smallest spatial distance between the spatial basis functions, R_{min}, then we have explicit scheme. Otherwise we have implicit scheme. In both cases, the solution is achieved by time marching method. In such a scheme, currents are evaluated at the first time instant, $t_1 = \Delta t$ by solving the governing equation and, using this knowledge, move to obtain currents at the second time instant $t_2 = 2\Delta t$. Next, proceed to obtain currents at 3rd, 4th, and later time instants in a similar way. Obviously, these methods are prone to error accumulation which is avoided in the present work.

In the following section, we present the detailed mathematical steps describing the algorithm. In Section III, we present numerical solution scheme and several important guidelines to apply the procedure successfully. In Section IV, we present several numerical results to test the validity of the technique. Finally, Section V discusses important conclusions along with possible improvements and future work to be undertaken in this area.

II. INTEGRAL EQUATION FORMULATION

Let S denote an open or closed perfectly conducting arbitrarily-shaped body as shown in Fig. 1, illuminated by a time-domain pulse. An electric field $\boldsymbol{E}^i(\boldsymbol{r},t)$, defined in the absence of the scatterer, is incident on and induces a surface current $\boldsymbol{J}(\boldsymbol{r},t)$ on S. Using basic mathematical steps outlined in [4], the scattered electric field $\boldsymbol{E}^s(\boldsymbol{r},t)$ computed from the surface current is given by:

$$\boldsymbol{E}^s(\boldsymbol{r},t) = -\frac{\partial \boldsymbol{A}(\boldsymbol{r},t)}{\partial t} - \nabla\Phi(\boldsymbol{r},t), \qquad (1)$$

where the magnetic vector potential and the electric scalar potentials are given by:

$$\boldsymbol{A}(\boldsymbol{r},t) = \mu \int_S \frac{\boldsymbol{J}(\boldsymbol{r}', t-\frac{R}{c})}{4\pi R}\, dS', \qquad (2)$$

and

$$\Phi(\boldsymbol{r},t) = \frac{1}{\epsilon}\int_S \frac{q_s(\boldsymbol{r}', t-\frac{R}{c})}{4\pi R}\, dS'. \qquad (3)$$

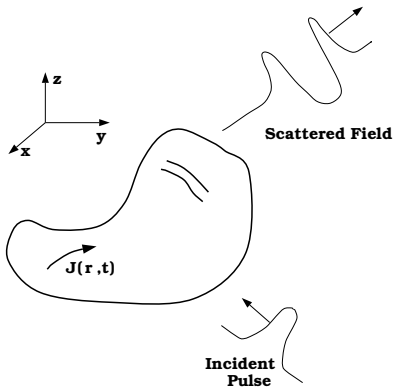

Fig. 1. An arbitrary body illuminated by a Gaussian plane wave.

In Eqs. (2) and (3), $R = |\boldsymbol{r} - \boldsymbol{r}'|$, μ and ϵ denote the permeability and permittivity of the surrounding medium, respectively, $\boldsymbol{r}$ and $\boldsymbol{r}'$ are the locations of the observation and source points on S and c is the velocity of the electromagnetic wave. The surface charge density q_s is related to the induced current $\boldsymbol{J}$ by the continuity equation given by,

$$\nabla_s \cdot \boldsymbol{J} = -\frac{\partial q_s}{\partial t}. \qquad (4)$$

Differentiating Eq. (3) with respect to time and using Eq. (4), we obtain the following expression for the time derivative of the scalar potential as:

$$\Psi \triangleq \frac{\partial \Phi}{\partial t} = \frac{-1}{\epsilon}\int_\ell \frac{\nabla_s \cdot \boldsymbol{J}(\boldsymbol{r}', t-R/c)}{4\pi R}\, dS'. \qquad (5)$$

Next, an integro-differential equation for $\boldsymbol{J}$ can be derived using the boundary condition $(\boldsymbol{E}^i + \boldsymbol{E}^s)_{tan} = 0$ on S as:

$$\left[\frac{\partial \boldsymbol{A}}{\partial t} + \nabla\Phi\right]_{tan} = \boldsymbol{E}^i_{tan}. \qquad (6)$$

The charge density appearing in the scalar potential of Eq. (6) may be eliminated by differentiating Eq. (6) with respect to time and using Eq. (5). Thus, the popular electric field integral equation (EFIE) for an arbitrarily-shaped conducting body in time domain is given by:

$$\left[\frac{\partial^2 \boldsymbol{A}}{\partial t^2} + \nabla\Psi\right]_{tan} = \left[\frac{\partial \boldsymbol{E}^i}{\partial t}\right]_{tan}, \qquad (7)$$

which needs to be solved for the unknown current $\boldsymbol{J}(\boldsymbol{r},t)$.

III. NUMERICAL SOLUTION SCHEME

The first step in the numerical scheme is to describe adequately the given geometry to the digital

computer. This task is most easily accomplished by covering the body surface with planar triangular patches to generate a "patch model" of the given body. We choose the planar triangular patches to model the body because they have the ability to conform to any geometrical surface or boundary. In fact, simple as well as complex bodies, can be easily modeled by planar triangular patches and can be described to the computer using automated schemes. Further, for numerical purposes, it is very easy to increase the patch density in areas where more resolution is required.

Next, we note that the triangular mesh consists of several electrically short patches, mutually attached to each other to approximate the given body. The common edge where several patches are attached is known as an *interior edge*. If only one patch is attached to an edge, then that edge is referred to as a *boundary edge* and removed from the solution scheme. When only two triangular patches are attached to a given edge, that interior edge is referred to as an *ordinary edge* and one unknown is associated with this edge. Further, if more than two triangular patches are attached to a given edge, then we have a *junction edge* and the number of unknowns associated with this junction edge is one less than the total number of patches connected to this edge.

The next task in the numerical solution procedure is to develop an algorithm to solve the integral equation (7). We accomplish this task by selecting the well-known method of moments [22].

A. Definition of space and time basis functions

Assuming that the body is modeled with triangular patches, we use the well-known Rao-Wilton-Glisson (RWG) functions [23] for expansion and testing of space variables. Referring to Fig. 2, the RWG function for any edge m common to the two triangles $T_m^{\pm}$ is given by,

$$\boldsymbol{f}_m(\boldsymbol{r}) = \begin{cases} \frac{l_m}{2A_m^+}\boldsymbol{\rho}_m^+ & \text{for } \boldsymbol{r} \in T_m^+ \\ \frac{l_m}{2A_m^-}\boldsymbol{\rho}_m^- & \text{for } \boldsymbol{r} \in T_m^- \\ 0 & \text{otherwise.} \end{cases} \tag{8}$$

In Eq. (8), l_m denotes the length of the m^{th} edge and $A_m^{\pm}$ is the area of triangle $T_m^{\pm}$. Further, an arbitrary point in T_m^+ may be located by the position vector $\boldsymbol{r}$, relative to the origin, O, or by $\boldsymbol{\rho}_m^+$, referenced at the free vertex of T_m^+. For an arbitrary point in T_m^-, the position vector $\boldsymbol{\rho}_m^-$ is similarly defined except that it is directed toward the free vertex of T_m^-. The "+" or "−" convention is determined by

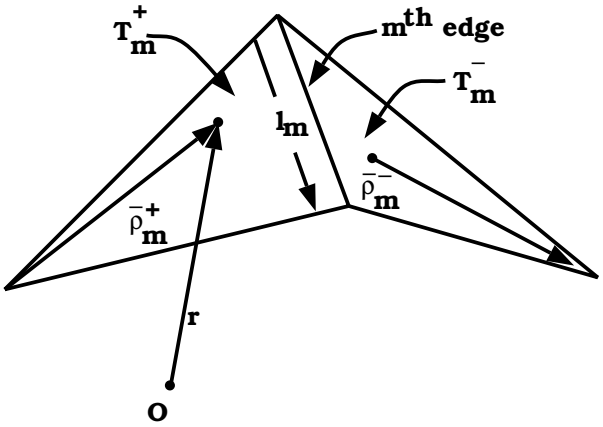

Fig. 2. Triangle pair and geometrical parameters associated with the m^{th} interior edge.

choosing a reference direction for positive current flow for the m^{th} edge. This current is assumed to flow from T_m^+ to T_m^-. Also, we follow the convention where superscripts refer to the faces and subscripts refer to the edges. For example, T_m^+ is the positive triangle associated with edge m.

Now, let us define the triangle functions for the time variable. In order to do so, let us first define an upper limit on the time variable $t = T$, where T represents the time when the incident pulse becomes negligible. Then, we divide the time axis $0 \to T$ into N_t uniform time intervals given by Δt and denote $t_n = n\Delta t$ for $n = 1, 2, ...N_t$. We note that, initially, the MOM scheme is applied to a finite interval $0 \to T$. We also note that extending the time interval to later times is trivial and discussed later. The mathematical description of the triangle function for the time variable is given as,

$$g_n(t) \equiv \begin{cases} 1 - \frac{|t-t_n|}{\Delta t} & t \in (t_{n-1}, t_{n+1}) \\ 0 & \text{otherwise.} \end{cases} \tag{9}$$

Next, we approximate the induced current $\boldsymbol{J}(\boldsymbol{r}, t)$ as:

$$\boldsymbol{J}(\boldsymbol{r}, t) \approx \sum_{m=1}^{N_S} \sum_{n=1}^{N_t} I_{m,n}\, \boldsymbol{f}_m(\boldsymbol{r})\, g_n(t), \tag{10}$$

where N_S and N_t represent the number of basis (expansion) functions in space and time, respectively. Thus, for a complex body approximated by a triangular mesh, we have N_S space basis functions including basis functions associated with junction edges, N_t time functions. Thus, a straight forward MOM application results in $P = N_S \times N_t$ unknowns to be evaluated. The MOM procedure to obtain each unknown by solving Eq. (7) is described in the following:

B. Testing procedure

Considering the Galerkin testing procedure, we use the same functions defined in Eqs. (8) and (9) for testing of space and time variables, respectively. Defining

$$< \boldsymbol{f}_m(\boldsymbol{r}) g_n(t), \boldsymbol{F}(\boldsymbol{r},t) > = \int_S \int_T \boldsymbol{f}_m(\boldsymbol{r}) g_n(t) \bullet \boldsymbol{F}(\boldsymbol{r},t)\, dS\, dt, \tag{11}$$

we can write Eq. (7) as:

$$< \boldsymbol{f}_m(\boldsymbol{r}) g_n(t), \left[\frac{\partial^2 \boldsymbol{A}}{\partial t^2} + \nabla\Psi\right] > \;=\; < \boldsymbol{f}_m(\boldsymbol{r}) g_n(t), \left[\frac{\partial \boldsymbol{E}^i}{\partial t}\right] > \tag{12}$$

for $m = 1, 2, \cdots N_S$ and $n = 1, 2, \cdots N_t$. Further, we can rewrite Eq. (12) as,

$$\begin{aligned} &\int_t g_n(t)\, \frac{\partial^2}{\partial t^2} \int_S \left[\boldsymbol{f}_m(\boldsymbol{r}) \bullet \boldsymbol{A}(\boldsymbol{r},t)\, dS\right] dt \\ &+ \int_t g_n(t) \int_S [\boldsymbol{f}_m(\boldsymbol{r}) \bullet \nabla\Psi(\boldsymbol{r},t)\, dS]\, dt \\ &= \int_t g_n(t) \int_S \left[\boldsymbol{f}_m(\boldsymbol{r}) \bullet \frac{\partial \boldsymbol{E}^i(\boldsymbol{r},t)}{\partial t}\, dS\right] dt. \end{aligned} \tag{13}$$

Now, using the well-known integration by parts scheme on the first integral of Eq. (13) and using Eq. (9), we can re-write Eq. (13) as:

$$\begin{aligned} &\int_S \boldsymbol{f}_m(\boldsymbol{r}) \bullet \left[\frac{\boldsymbol{A}(\boldsymbol{r},t_{n+1}) - 2\boldsymbol{A}(\boldsymbol{r},t_n) + \boldsymbol{A}(\boldsymbol{r},t_{n-1})}{\Delta t^2}\right] dS \\ &\quad + \int_S \boldsymbol{f}_m(\boldsymbol{r}) \bullet [\nabla\Psi(\boldsymbol{r},t_n)]\, dS \\ &\quad = \int_S \boldsymbol{f}_m(\boldsymbol{r}) \bullet \left[\frac{\partial \boldsymbol{E}^i(\boldsymbol{r},t_n)}{\partial t}\right] dS. \end{aligned} \tag{14}$$

Now let us look at each term in Eq. (14), as follows:

Using Eq. (8), we can write vector potential term at any time instant as,

$$\begin{aligned} &\int_S \boldsymbol{f}_m(\boldsymbol{r}) \bullet \boldsymbol{A}(\boldsymbol{r},t_n)\, dS \\ &= \int_{T_m^+} \frac{l_m}{2A_m^+} \boldsymbol{\rho}_m^+ \bullet \boldsymbol{A}(\boldsymbol{r},t_n)\, dS \\ &+ \int_{T_m^-} \frac{l_m}{2A_m^-} \boldsymbol{\rho}_m^- \bullet \boldsymbol{A}(\boldsymbol{r},t_n)\, dS. \end{aligned} \tag{15}$$

The integrals will be approximated by evaluating $\boldsymbol{A}(\boldsymbol{r},t_n)$ at the centroid of the $T_m^{\pm}$ triangle. Therefore,

$$\begin{aligned} &\int_S \boldsymbol{f}_m(\boldsymbol{r}) \bullet \boldsymbol{A}(\boldsymbol{r},t_n)\, dS \\ &\approx \left[\boldsymbol{A}(\boldsymbol{\rho}_m^{c+},t_n) \bullet \frac{l_m}{2A_m^+} \int_{T_m^+} \boldsymbol{\rho}_m^+\, dS \right. \\ &\left. + \boldsymbol{A}(\boldsymbol{\rho}_m^{c-},t_n) \bullet \frac{l_m}{2A_m^-} \int_{T_m^-} \boldsymbol{\rho}_m^-\, dS\right]. \end{aligned} \tag{16}$$

The integrations in Eq. (16) are trivial and the result is given by:

$$\begin{aligned} &\int_S \boldsymbol{f}_m(\boldsymbol{r}) \bullet \boldsymbol{A}(\boldsymbol{r},t_n)\, dS \\ &\approx \frac{l_m}{2}\left[\boldsymbol{A}(\boldsymbol{\rho}_m^{c+},t_n) \bullet \boldsymbol{\rho}_m^{c+} + \boldsymbol{A}(\boldsymbol{\rho}_m^{c-},t_n) \bullet \boldsymbol{\rho}_m^{c-}\right], \end{aligned} \tag{17}$$

where $\boldsymbol{\rho}_m^{c+}$ is the vector from the free vertex to the centroid of T_m^+ and $\boldsymbol{\rho}_m^{c-}$ is the vector from the centroid to the free vertex of T_m^-.

Next, let's consider the scalar potential term in Eq. (14). Using the vector identity $\nabla \bullet (\Psi \boldsymbol{A}) = \boldsymbol{A} \bullet \nabla\Psi + \Psi\nabla \bullet \boldsymbol{A}$ and using the properties of the RWG function $\boldsymbol{f}_m$, we have:

$$\begin{aligned} &\int_S \boldsymbol{f}_m \bullet \nabla\Psi(\boldsymbol{r},t_n)\, dS = \\ &\quad -\int_S \Psi(\boldsymbol{r},t_n) \nabla \bullet \boldsymbol{f}_m(\boldsymbol{r}) dS. \end{aligned} \tag{18}$$

By approximating the integrand at the centroids of the triangles, Eq. (18) becomes.

$$\begin{aligned} &\int_S \boldsymbol{f}_m \bullet \nabla\Psi(\boldsymbol{r},t_n)\, dS = \\ &-\left[\frac{l_m}{A_m^+} \int_{T_m^+} \Phi(\boldsymbol{r},t_n)\, dS - \frac{l_m}{A_m^-} \int_{T_m^-} \Phi(\boldsymbol{r},t_n)\, dS\right] \\ &\quad \approx -l_m[\Phi(\boldsymbol{\rho}_m^{c+},t_n) - \Phi(\boldsymbol{\rho}_m^{c-},t_n)]. \end{aligned} \tag{19}$$

Finally, consider incident field term in Eq. (14). The evaluation of this term is identical to the vector potential term and the result is given by,

$$\begin{aligned} &\int_S \boldsymbol{f}_m \bullet \frac{\partial \boldsymbol{E}^i(\boldsymbol{r},t_n)}{\partial t}\, dS = \\ &\frac{l_m}{2}\left[\frac{\partial \boldsymbol{E}^i(\boldsymbol{\rho}_m^{c+},t_n)}{\partial t} \bullet \boldsymbol{\rho}_m^{c+} + \frac{\partial \boldsymbol{E}^i(\boldsymbol{\rho}_m^{c-},t_n)}{\partial t} \bullet \boldsymbol{\rho}_m^{c-}\right]. \end{aligned} \tag{20}$$

C. Expansion procedure

Let us first look at the determination of the vector potential at some observation point $\boldsymbol{r} = \boldsymbol{r}_m$ at time $t = t_n$. Substituting Eq. (10) into Eq. (2) gives:

$$\begin{aligned}
&\boldsymbol{A}(\boldsymbol{r}_m, t_n) \\
&= \mu \sum_{p=1}^{N_S} \sum_{q=1}^{N_t} I_{p,q} \int_S \frac{\boldsymbol{f}_p(\boldsymbol{r}') g_q(t_n - \frac{|\boldsymbol{r}_m - \boldsymbol{r}'|}{c})}{4\pi |\boldsymbol{r}_m - \boldsymbol{r}'|} \, dS' \\
&\approx \sum_{p=1}^{N_S} \sum_{q=1}^{N_t} I_{p,q} \\
&\quad \left[g_q(t_n - \frac{R^+_{mp}}{c}) \boldsymbol{\kappa}^+_{mp} + g_q(t_n - \frac{R^-_{mp}}{c}) \boldsymbol{\kappa}^-_{mp} \right], \quad (21)
\end{aligned}$$

with

$$\begin{aligned}
\boldsymbol{\kappa}^{\pm}_{mp} &= \int_{T^{\pm}_p} \frac{\mu \boldsymbol{f}^{\pm}_p}{4\pi R_m} \, dS', & (22) \\
R^{\pm}_{mp} &= |\boldsymbol{r}_m - \boldsymbol{r}^{c\pm}_p|, & (23) \\
R_m &= |\boldsymbol{r}_m - \boldsymbol{r}'|, & (24)
\end{aligned}$$

where $T^{\pm}_p$ represent the triangles connected to p^{th}-basis function.

Now, we consider the evaluation of the derivative of the scalar potential at some observation point $\boldsymbol{r} = \boldsymbol{r}_m$ and time $t = t_n$. Following steps similar to the evaluation of the vector potential, we combine Eqs. (5) and (10) to get:

$$\begin{aligned}
&\Psi(\boldsymbol{r}_m, t_n) \\
&\quad \approx \sum_{p=1}^{N_S} \sum_{q=1}^{N_t} I_{p,q} \left[g_q(t_n - \frac{R^+_{mp}}{c}) \psi^+_{mp} \right. \\
&\qquad \left. + g_q(t_n - \frac{R^-_{mp}}{c}) \psi^-_{mp} \right], \quad (25)
\end{aligned}$$

where

$$\psi^{\pm}_{mp} = \frac{-l_p}{A^{\pm}_p} \int_{T^{\pm}_k} \frac{dS'}{4\pi\epsilon R_m}. \quad (26)$$

Using the expansion and testing procedures described so far, let us generate a matrix equation $\boldsymbol{Z}\boldsymbol{X} = \boldsymbol{Y}$ of dimension $P = N_S \times N_t$. The elements of the $\boldsymbol{Z}$-matrix are formed by using Eqs. (17), (19), (21) and (25). Note that $Z_{j,i}$ represents a matrix element of the $\boldsymbol{Z}$-matrix, where

$$\begin{aligned}
&j = (n-1)N_S + m, \qquad i = (q-1)N_S + p, \\
&n, q = 1, 2, \cdots, N_S, \quad \text{and} \quad m, p = 1, 2, \cdots, N_t.
\end{aligned}$$

Here, we note that the $\boldsymbol{Z}$-matrix in this case is not a full matrix, unlike in the frequency domain MOM procedure. In fact, it is a lower triangular, blockwise Toeplitz matrix and given by,

$$\boldsymbol{Z} = \begin{bmatrix} \boldsymbol{Z}_{1,1} & \boldsymbol{O} & \cdots & \boldsymbol{O} \\ \boldsymbol{Z}_{2,1} & \boldsymbol{Z}_{2,2} & \cdots & \boldsymbol{O} \\ \vdots & \vdots & \vdots & \vdots \\ \boldsymbol{Z}_{N_S,1} & \boldsymbol{Z}_{N_S,2} & \cdots & \boldsymbol{Z}_{N_S,N_S} \end{bmatrix}, \quad (27)$$

where each $\boldsymbol{Z}_{m,p}$, $m = 1, 2, \cdots N_S$ and $p = 1, 2, \cdots, N_S$ is a matrix of dimension N_S representing the mutual interaction between the spatial basis functions for a given pair of testing time function and source time function. The solution of such a matrix equation is very efficient, involves inverting only once a matrix of size $N_S \times N_S$, and solving the matrix equation.

The right hand side of the matrix equation $\boldsymbol{Y}$ is obtained by using the Eq. (20) and consists of N_t blocks of matrices of dimension N_S. At this stage, we note that multiple incident pulses with varying frequency content can be easily accommodated by adding more column blocks to the $\boldsymbol{Y}$-matrix. Also, we note that obtaining currents for T to $2T$ and later instants is similar to solving the equation for 0 to T and presented in [20, 21].

Lastly, note that the numerical procedure presented so far allows to obtain the current distribution on the scattering structure as a function of time. Once an accurate current distribution is obtained, it is a simple process to obtain near-fields, far-fields, and any other required parameters. The mathematical details to obtain such parameters are well-known and available in [4] and hence not repeated here.

Before we present several numerical results obtained using the procedure presented so far, a few salient points must be noted as discussed in the following:

1. The first point to be noted is that the present procedure is *not* the same as the conventional MOT scheme although it might appear so for a casual reader. It is because, in the conventional MOT scheme, further mathematical manipulations are carried out wherein a MOT equation is developed to obtain the current at a present instant as a function of incident field plus currents at previous instants [4]. Hence, the numerical solution involves obtaining all the currents at a given instant before moving to the next instant. One cannot proceed to the next instant before completing the current calculations at the given instant because these currents are required for calculating the currents at next instant. This may be the primary cause for error accumulation and late-time instabilities. However, in the procedure presented in this work, we are actually solving the complete problem in a way wherein all the currents at all instants (*i.e.*, from 0 to T) are obtained at once. There is no time marching involved and, hence, no error propagation or accumulation.

2. In this work, we have used triangular functions to represent the time variable which is simple and efficient. However, it is also possible to use other functions such as Gaussian functions, as done in [21], Lagurre Polynomials or spline functions where the time-derivatives can be easily handled. The important points to be noted for this procedure is: application of the MOM procedure in space and time dimensions, solving for unknowns at all locations and all time instants simultaneously, and efficient numerical solution.

3. It may be noted that for time-domain calculations, it is customary to use a Gaussian pulse as the incident pulse since a true impulse cannot be generated numerically. Hence, it is always a good idea to estimate the frequency content in the selected time pulse for spatial discretization. The normal guideline in the solution of a time domain scattering problem is to obtain λ_{min} corresponding to the maximum frequency component in the incident pulse. Obviously, for a band-limited pulse λ_{min} is easy to obtain. For a Gaussian pulse, one needs to estimate the maximum frequency limit in a judicious manner. Then, it is necessary to make sure that all the edge lengths are sufficiently smaller (*i.e.*, less than one tenth of λ_{min}).

4. It should be further noted that a sloppy discretization would appear as growing instability even for the time period 0 to T. Fortunately, such discretization in the frequency domain problem simply generates an inaccurate result. However, in the time domain, one may see a completely unacceptable, an even misleading, solution. Hence, the spatial discretization must confirm to the prescribed limit.

5. It appears that the time domain solution is very sensitive to numerical processing and requires accurate evaluation of required quantities such as vector and scalar potentials. The numerical integrations must be carried out to a high degree of precision in each and every case.

6. The number of time functions to be used in the solution is not very critical, at least, for the excitation pulse used in this work. Here we emphasize that the time functions are used to represent the time variation in the interval 0 to T, where T represents the time instant at which time the incident field goes to zero. Note that the parameter T depends upon the pulse width of the excitation pulse as discussed in the following:

IV. NUMERICAL RESULTS

In this section, we present numerical results for several conducting objects modeled by triangular patches. For all the examples presented in this section, the incident field given by,

$$\boldsymbol{E}^i(t,\boldsymbol{r}) = \boldsymbol{E}_o \frac{4}{T_P\sqrt{\pi}} \mathrm{e}^{-\gamma^2}, \tag{28}$$

where

$$\gamma = \frac{4}{T_P}(ct - ct_o - \boldsymbol{r}\cdot\boldsymbol{a}_k). \tag{29}$$

In Eqs. (28) and (29), $\boldsymbol{a}_k$ is the unit vector in the direction of propagation of the incident wave, T_P is the pulse width of the Gaussian impulse, $\boldsymbol{E}_o \cdot \boldsymbol{a}_k = 0$, $\boldsymbol{r}$ is a position vector relative to the origin, c is the velocity of propagation in the external medium, and t_o is a time delay which represents the time at which the pulse peaks at the origin.

Initially, we present several examples showing the current density at a given location on the scatterer as a function of time and compare with the frequency domain MOM using the same spatial patch scheme and an inverse discrete Fourier transform (FD-IDFT). For these examples we have, referring to Eqs. (28) and (29), $\boldsymbol{E}_o = 120\pi\boldsymbol{a}_x$, $T_P = 4.0$ LM, $\boldsymbol{k} = -\boldsymbol{a}_z$, $ct_0 = 1.5T_p$ LM, and $T = 2 * ct_0$. Note that 1 LM = 3.333 nSecs. The FD-IDFT solution is obtained by using 512 frequency samples in the 0 to 512 MHz range. We also note that sharper pulse can be used by adjusting the pulse width T_p.

As a first example, consider a square plate of 2.0×2.0 m, located in the XY-plane. There are 153

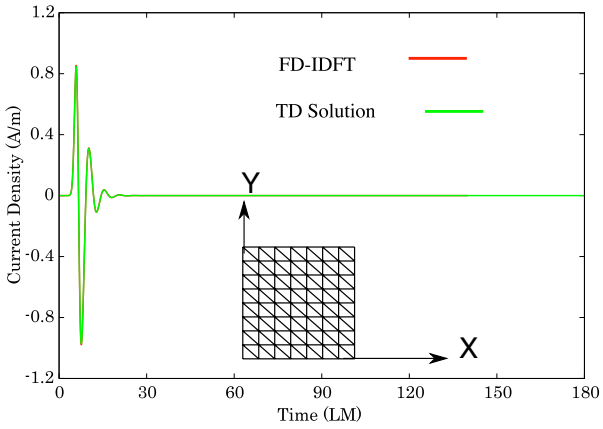

Fig. 3. Current induced at the center of a square plate (L=2.0 m) illuminated by a Gaussian plane wave.

and 108 basis functions for space and time variables,

respectively, for the time-domain solution. Note that, although 30 to 60 basis functions are sufficient for the time variable, we have deliberately used a higher number to show that the actual number of functions is not critical. For illustration purposes, the induced current density at the center of the plate is shown in Fig. 3. We note that the TD and FD-IDFT solutions compare very well for this case.

Next, we consider a sphere of radius 1.0 m, located with the center coinciding with the coordinate origin. The sphere is modeled with 722 triangular patches with 1083 spatial basis functions and 60 basis functions for time variable. For illustration purposes, the induced current density at the equator is shown in Fig. 4 and note that TD and FD-IDFT solutions compare very well.

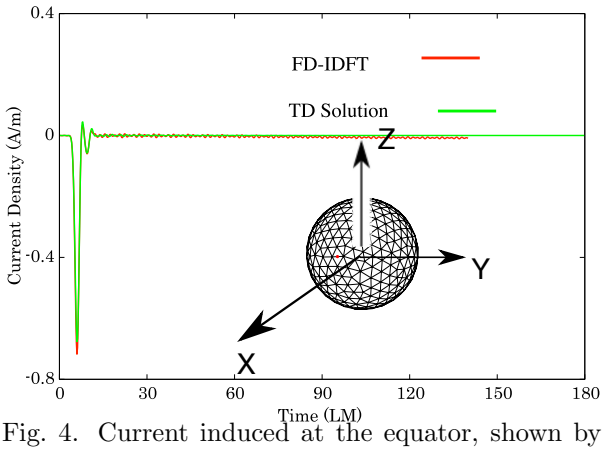

Fig. 4. Current induced at the equator, shown by a red dot, of a conducting sphere (a=1.0 m) illuminated by a Gaussian plane wave.

Next, we consider a conducting cube of side length 1.0 m, located with the center coinciding with the coordinate origin. The cube is modeled with 224 triangular patches with 336 spatial basis functions and 60 basis functions in time. For illustration purposes, the induced current density at the center of the top face is shown in Fig. 5 and both solutions compare very well.

Next, we consider a combination of two square plates, each of side length $a = 1.0$ m and separated by a distance $d = 0.1$ m, located with the center of the bottom plate coinciding with the coordinate origin. Each plate is modeled with 112 triangular patches resulting in 366 spatial basis functions. The time-domain solution is obtained by employing 60 basis functions for the time variable. For illustration purposes, the induced current density at the center of the top plate is shown in Fig. 6 and note that the solutions compare very well. We note that the induced current oscillates for a long time because of the close proximity of the plates and the TD solution captures this phenomenon very well.

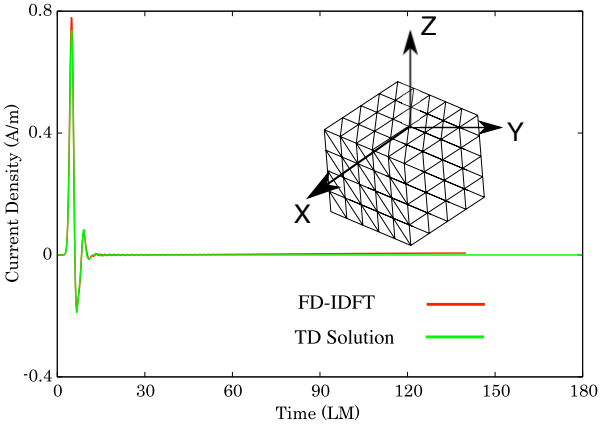

Fig. 5. Current induced at the center of the top face of a conducting cube (a=1.0 m) illuminated by a Gaussian plane wave.

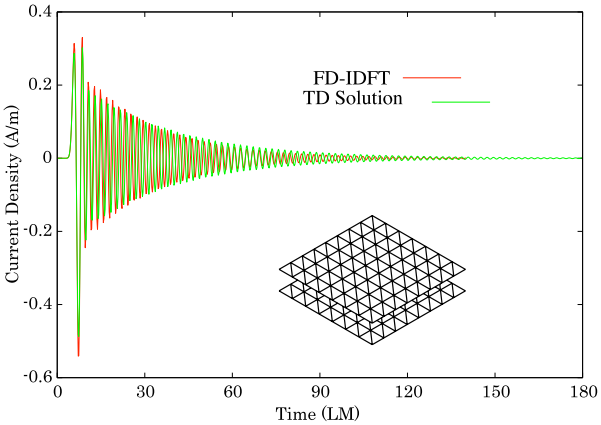

Fig. 6. Current induced at the center of the top plate of a parallel plate configuration (a=1.0 m, d=0.1 m) illuminated by a Gaussian plane wave.

Now, we consider a combination of three square plates, each of side length $a = 1.0$ m and separated by a distance $d = 0.2$ m, located with the center of the center plate coinciding with the coordinate origin. Each plate is modeled with 180 triangular patches resulting in 753 spatial basis functions. The time variable is approximated with 60 functions. For illustration purposes, the induced current density at the center of the middle plate is shown in Fig. 7 and note that the solutions compare very well. It is obvious that this configuration represents a complex scattering structure from the scattering point of view. The electromagnetic wave bounces back and forth between the plates and takes a very long time to decay to a negligible value.

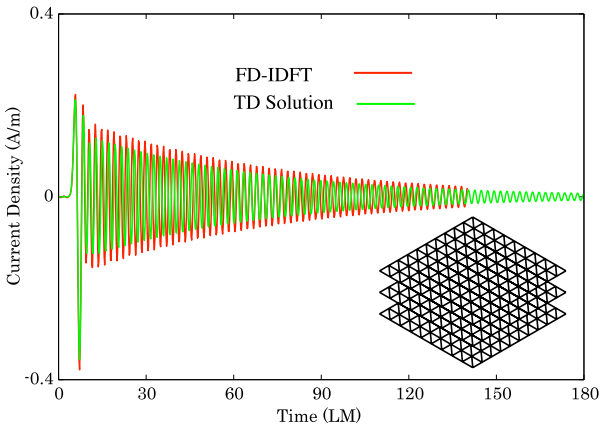

Fig. 7. Current induced at the center of the center plate of a 3-parallel plate configuration (a=1.0 m, d=0.2 m) illuminated by a Gaussian plane wave.

Next, we consider an almond-shaped structure described in the inset of Fig. 8. The almond is modeled with 432 triangular patches resulting in 648 spatial basis functions. The time variable is approximated with 60 functions. For illustration purposes, the induced current density at the center of the equator is shown in Fig. 8 and note that the solutions compare very well. It is well-known that the almond-shaped body represents a body with low radar cross section and the time domain solution performs very well for this case.

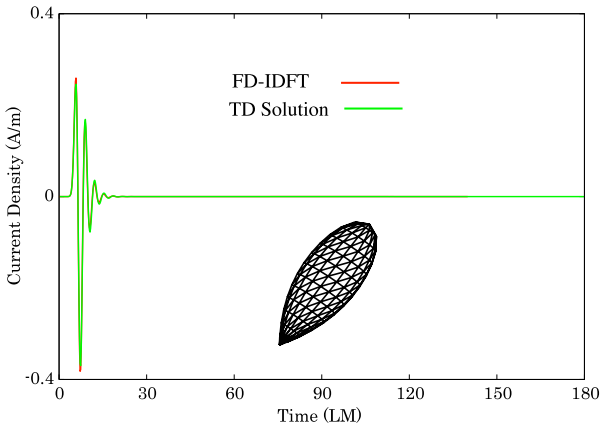

Fig. 8. Current induced at the center of the equator of an almond-shaped structure illuminated by a Gaussian plane wave.

Next, we consider an aircraft-like object, as shown in Fig. 9. The object is symmetrically placed in the XY-plane such that the center of the lower-side (belly) approximately coincides with the coordinate origin. The object dimensions are: 0.97 m, 0.86 m, and 0.25 m along the X, Y, and Z axes, respectively. We have used 1000 and 48 basis functions for space and time variables, respectively. The current is sampled at the middle of an edge shown by a dot in the Fig. 9. The results obtained by FD-IDFT, and the present method are shown in Fig. 10. Again, we note good comparison between the two solutions.

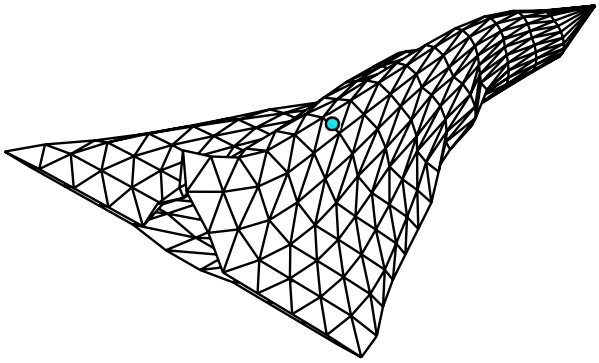

Fig. 9. An aircraft-like body modeled by triangular patches.

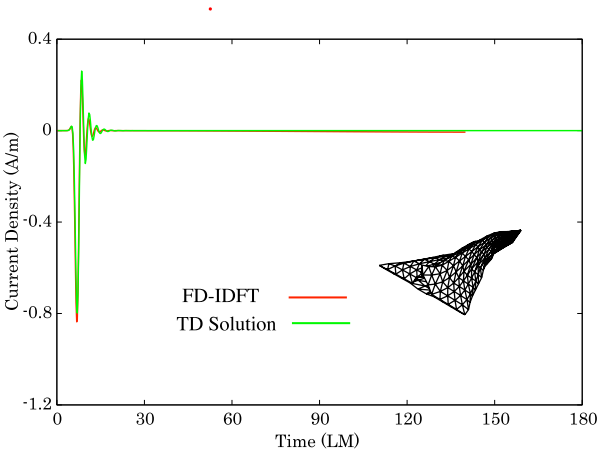

Fig. 10. Current induced on an aircraft-like structure illuminated by a Gaussian plane wave.

Next, we consider a more complex aircraft-like object, as shown in Fig. 11. The object dimensions are: 5.85 m, 3.5 m, and 1.46 m along the X, Y, and Z axes, respectively. We have used 2673 and 40 basis functions for space and time variables, respectively. The current is sampled on a wing, shown by a red dot, in the Fig. 11. The IDFT solution is obtained in a similar manner as in the previous example. The results obtained by FD-IDFT, and the present method are shown in Fig. 12. Again, we note good comparison between the two solutions. The negligible discrepancies in both solutions may be attributed insufficient number of unknowns at the higher end of the frequency.

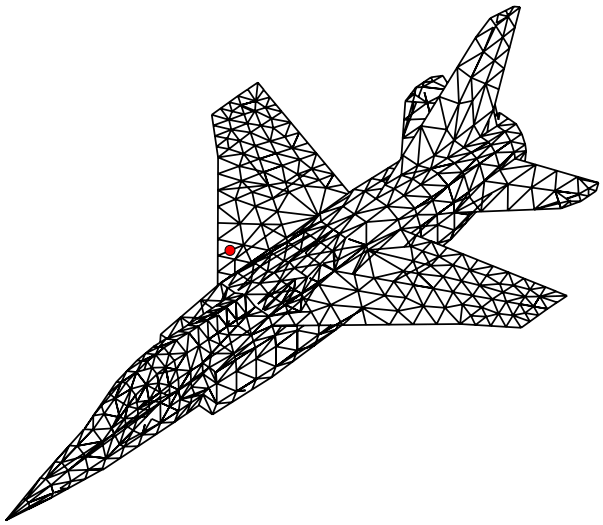

Fig. 11. Triangulated model of an aircraft-like body.

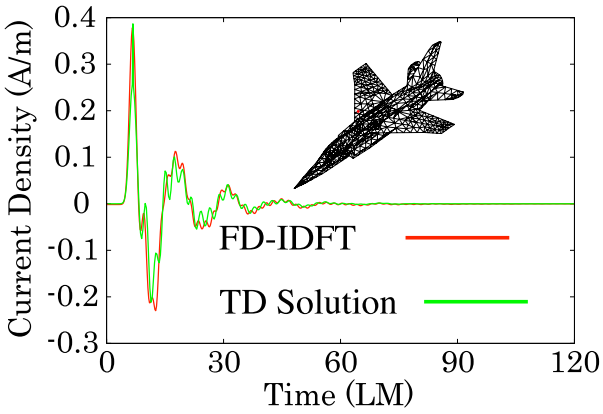

Fig. 12. Current induced on the wing of a model aircraft illuminated by a Gaussian plane wave.

Next, we consider a deep cavity as shown in the inset of Fig. 13. The depth of the cavity is 2.0 m. The inner and outer radii of cavity are 0.267 m and 0.4 m, respectively. The object is symmetrically placed in the XY-plane such that the center of the bottom surface coincides with the coordinate origin. We have used 552 and 40 basis functions for space and time variables, respectively. The current is sampled at an edge located in the inner surface at the bottom of the cavity. The results obtained by FD-IDFT, and the present method are shown in Fig. 13. Although we see a reasonable comparison, considering the complexity of the problem, it is speculated that neither solution is converged to the correct solution because of the coarse spatial sampling. The currents inside the deep zone are difficult to obtain and may require much higher number of unknowns.

Next, we consider a ship-like object, shown in

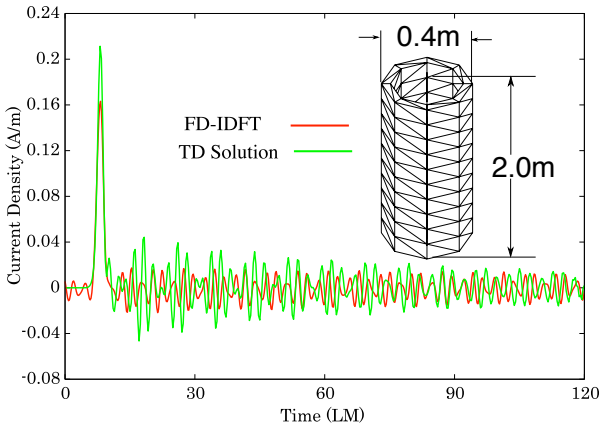

Fig. 13. Current induced on the bottom surface of a deep cavity illuminated by a Gaussian plane wave.

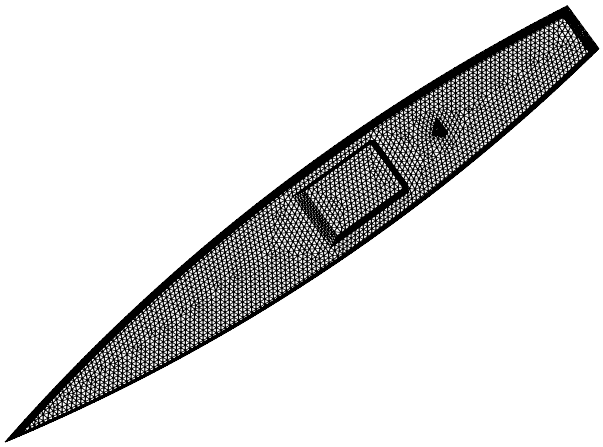

Fig. 14. Triangular patch model of a ship-like object.

Fig. 14. The ship is 5.56 m long, 0.716 m wide, and 0.387 m height and placed such that the origin is approximately coinciding with center of the top deck. There are 13,395 and 40 basis functions for space and time variables, respectively, for the time domain solution. The current is sampled at the middle of the upper-deck approximately coinciding with $x = y = 0$. The numerical results obtained by the method presented in this work is shown in Fig. 15. Also, note that IDFT solution for this example is prohibitively expensive and hence not attempted.

Now, we present radar cross section (RCS) of a few selected objects at a selected frequency using the time domain solution. Although, we can calculate RCS at any frequency within the pass band of the incident pulse, we choose a single frequency for illustration purposes. We note that once the induced current at all locations on a given object is obtained as a function of time, it is easy to use the straight-forward Fourier Transform method to ob-

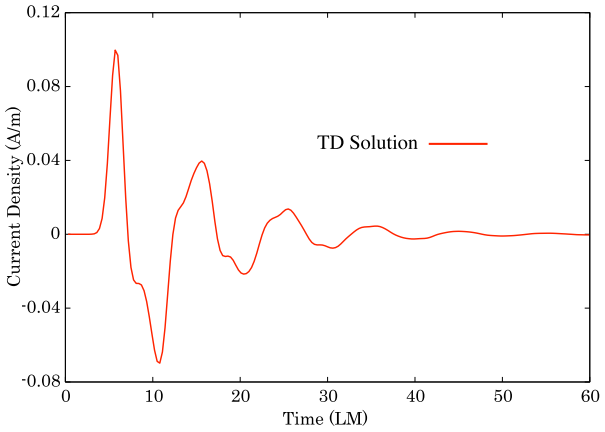

Fig. 15. Current at the selected point on the ship-like object modeled by triangular patches.

tain the currents at a given frequency. The Fourier transform for a time domain data may be defined as:

$$I_k(f) = \int_{t=0}^{\infty} i_k(t) e^{-j2\pi\, f\, t}\, dt, \tag{30}$$

where $i_k(t)$ is the current induced at k^{th}-basis function and f is the given frequency. Here, we note that the induced current is zero for $t < 0$.

Since the current data is obtained at equal time intervals, the integral in Eq. (30) may be easily approximated by:

$$I_k(f) = \sum_j i_k(j\Delta t) e^{-j2\pi\, f\, j\Delta t}\, \Delta t, \tag{31}$$

where Δt is the time interval. Next, the far-scattered electric field is obtained by the expression, given by:

$$\boldsymbol{E}^s(\boldsymbol{r}) = -j\omega\mu\, \frac{e^{-jkr}}{4\pi r} \int_S \boldsymbol{f}_k(\boldsymbol{r}')\, e^{j\boldsymbol{a}_k\cdot\boldsymbol{r}'}\, dS', \tag{32}$$

where $\boldsymbol{f}_k$ represents the k^{th}-basis function, $\omega = 2\pi f$, $k = \frac{\omega}{c}$ is the wave number, $\boldsymbol{a}_k$ represents the unit vector from the origin to the observation point, and c is the velocity of the electromagnetic wave.

Lastly, the radar cross section (σ) is given by,

$$\sigma(\theta,\phi) = \lim_{\boldsymbol{r}\to\infty} 4\pi \boldsymbol{r}^2 \frac{|\boldsymbol{E}^s|^2}{|\boldsymbol{E}^{inc}|^2} \tag{33}$$

which can be easily computed from Eq. (32) and the incident field given in Eq. (28).

In the following, we present normalized RCS (σ) at 900 MHz for four objects, *i.e.*, a) square plate, b) conducting sphere, c) a deep cavity and d) an aircraft=like body shown Fig. 9. We present two cases *viz.* a) Elevation cut (E-cut) where σ is obtained as a function of θ at $\phi = 0^0$ and b) Horizontal cut (H-cut) where σ is obtained as a function of ϕ at $\theta = 90^0$. The time domain solution is obtained with a much sharper pulse with pulse width $T_p = 0.5$ LM providing a bandwidth from 0 to 1000 MHz. We also note that, the square plate, conducting sphere, deep cavity, and aircraft-like body have been approximated by 2628, 2160, 2208 and 4025 basis functions, respectively. The RCS plots are shown in Figs. 16, 17, 18 and 19. Although both solution compare well, the minor deviations may be attributed to the selected incident pulse in the time domain because at the selected frequency the amplitude of the incident pulse is quite low and hence, the normalization amplified the deviation even more.

V. CONCLUSIONS

In this work, a simple and efficient method of moments (MOM) solution procedure is developed to determine the transient scattering from arbitrarily shaped, conducting scatterers by a Gaussian incident pulse directly in the time domain. The scatterer may either be an opened or closed, finite three-dimensional object and described to the computer via planar triangular patch modeling scheme. The numerical solution scheme involves a straightforward method of moments application and requires no further mathematical manipulation. The MOM matrix thus generated is a lower triangular matrix which can be very efficiently filled because the matrix elements are also block-wise Toeplitz. As a result, the matrix equation can be very efficiently solved. Presently, work is in progress to apply the new method to material bodies.

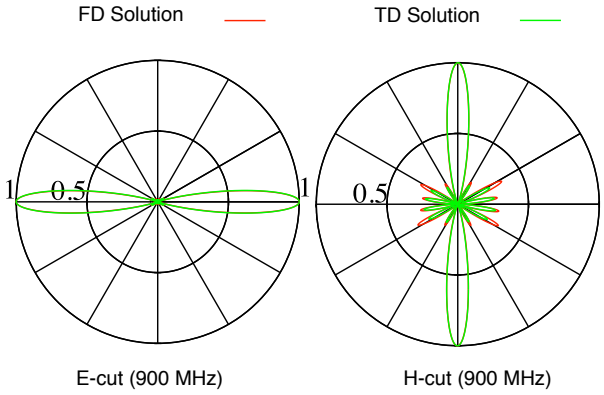

Fig. 16. Normalized bistatic RCS of a square plate (0.5×0.5 m) located in the XY-plane with center coinciding with the origin at 900 MHz. $N_S = 2628$.

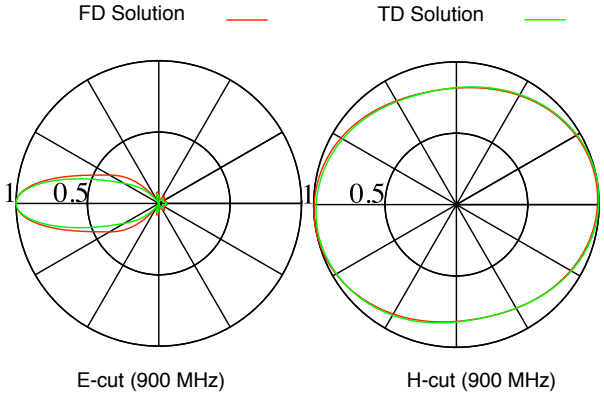

Fig. 17. Normalized bistatic RCS of a conducting sphere, radius=0.5 m, located with center coinciding with the origin at 900 MHz. $N_S = 2160$.

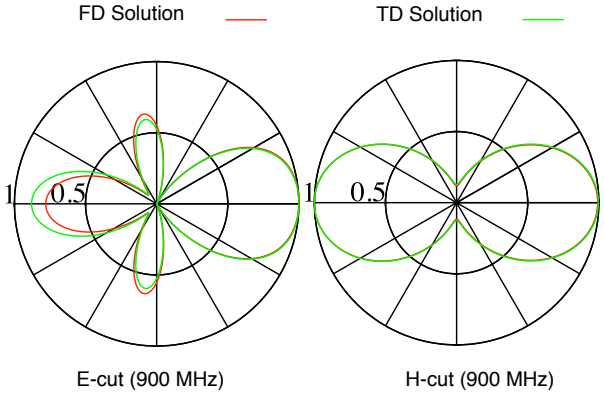

Fig. 18. Normalized bistatic RCS of a conducting cavity, length=0.25 m, inner and outer radii of cavity 0.08 m and 0.1 m, respectively, located with center coinciding with the origin, at 900 MHz. $N_S = 2208$.

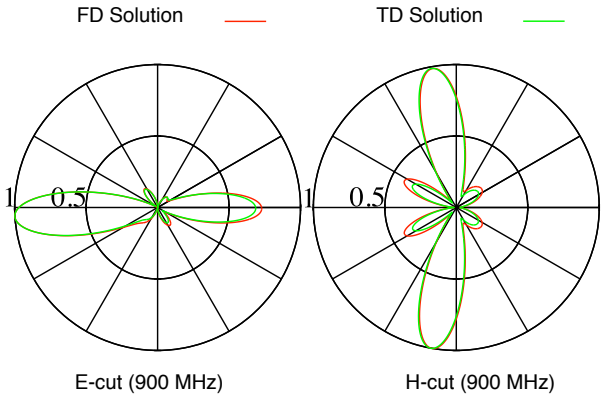

Fig. 19. Normalized bistatic RCS of an aircraft-like body, $N_S = 4025$.

ACKNOWLEDGEMENTS

This research was conducted under the Naval Research Laboratory Base Program sponsored by the Office of Naval Research.

REFERENCES

[1] E. M. Kennaugh and R. L. Cosgriff, "The use of impulse response in electromagnetic scattering Problems," *IRE National Convention Record*, pp. 72- 77, 1958.

[2] T. T. Wu, "A transient response of a dipole antenna," *Journal of Mathematical Physics*, vol. 2, Iss. 6, pp. 892- 894, 1961.

[3] C. L. Bennett, *A technique for computing approximate electromagnetic impulse response of conducting bodies*," Ph.D. Thesis, Purdue University, August 1968.

[4] S. M. Rao, *Time Domain Electromagnetics*, Academic Press, New York, 1999.

[5] G. H. Zhang, M. Xia, and X. M. Jiang, "Transient analysis of wire structures using time domain integral equation method with exact matrix elements," *Progress In Electromagnetics Research*, vol. 45, pp. 281-298, 2009.

[6] Y. Shi, M. Xia, R. Chen, E. Michielssen, and M. Lu, "Stable electric field TDIE solvers via quasi-exact evaluation of MOT matrix elements," *IEEE Transactions on Antennas and Propagation*, vol. 59, no. 2, pp. 574-585, February 2011.

[7] H. A. Ulku and A. A. Ergin, "Application of analytical retarded-time potential expressions to the solution of time domain integral equations," *IEEE Transactions on Antennas and Propagation*, vol. 59, no. 11, pp. 4123-4131, November 2011.

[8] B. H. Jung, Y. S. Chung, and T. K. Sarkar, "Time-domain EFIE, MFIE, and CFIE formulations using Laguerre polynomials as temporal basis functions for the analysis of transient scattering from arbitrarily shaped conducting structures," *Progress in Electromagnetics Research*, vol. 39, pp. 1-45, 2003.

[9] B. H. Jung, T. K. Sarkar, Y. S. Chung, M. Salazar-Palma, and Z. Ji, "Time-domain combined field integral equation using Laguerre polynomials as temporal basis functions," *International Journal of Numerical Modeling: Electronic Networks, Devices and Fields*, vol. 17, pp. 251-268, 2004.

[10] Y. S. Chung, T. K. Sarkar, B. H. Jung, M. Salazar-Palma, Z. Ji, S. M. Jang, and K. J. Kim, "Solution of time domain electric field integral equation using the Laguerre polynomials," *IEEE Transactions on Antennas and Propagation*, vol. 52, no. 9, pp. 2319-2328, September 2004.

[11] Z. Ji, T. K. Sarkar, B. H. Jung, M. Yuan, and M. Salzar-Palma, "Solving time domain electric field integral equation without the time variable," *IEEE Transactions on Antennas and Propagation*, vol. 54, no. 1, pp. 258-262, January 2006.

[12] N. J. Sekljic, M. M. Ilic, and B. M. Notaros, "Spatially large and temporally entire-domain electric field integral equation method of moments for 3-D scattering analysis in time domain," *IEEE Transactions on Antennas and Propagation*, vol. 63, no. 6, pp. 2614-2626, June 2015.

[13] A. J. Pray, N. V. Nair, and B. Shanker, "Stability properties of the time domain electric field integral equation using a separable approximation for the convolution with the retarded potential," *IEEE Transactions on Antennas and Propagation*, vol. 60, no. 8, pp. 3772 - 3781, 2012.

[14] Y. Beghein, K. Cools, H. Bagci, and D. De Zutter, "A space-time mixed Galerkin marching-on-in-time scheme for the time-domain combined field integral equation," *IEEE Transactions on Antennas and Propagation*, vol. 61, no. 3, pp. 1228-1238, March 2013.

[15] Y. Beghein, K. Cools, and F. P. Andriulli, "A DC-stable, well-balanced, Calderon preconditioned time domain electric field integral equation," *IEEE Transactions on Antennas and Propagation*, vol. 63, no. 12, pp. 5650-5660, Dec. 2015.

[16] Y. Beghein, K. Cools, and F. P. Andriulli, "A DC stable and large-time step well-balanced TD-EFIE based on quasi-Helmholtz projectors," *IEEE Transactions on Antennas and Propagation* vol. 63, no. 7, pp. 3087-3097, July 2015.

[17] Z. He, H. H. Zhang, and R. S. Chen, "Parallel marching-on-in-degree solver of time-domain combined field integral equation for bodies of revolution accelerated by MLACA," *IEEE Transactions on Antennas and Propagation*, vol. 63, no. 8, pp. 3705-3710, August 2015.

[18] Z. He, R. S. Chen, and W. E. I. Sha, "An efficient marching-on-in-degree solution of transient multi-scale EM scattering problems," *IEEE Transactions on Antennas and Propagation*, vol. 64, no. 7, pp. 3039-3046, July 2016.

[19] M. D. Zhu, T. K. Sarkar, and H. Chen, "A stabilized marching-on-in-degree scheme for the transient solution of the electric field integral equation," *IEEE Transactions on Antennas and Propagation*, vol. 67, no. 5, pp. 3232-3240, May 2019.

[20] S. M. Rao, "A stable marching-on-in-time algorithm capable of handling multiple excitations - application to wire junction problems," *IET Journal of Microwaves, Antennas and Propagation*, vol. 12, iss. 4, pp. 472- 478, 2018.

[21] S. M. Rao, "A simple and efficient method of moments solution procedure for solving time domain integral equation - application to wire-grid model of perfect conducting objects," *IEEE Journal on Multiscale and Multiphysics Computational Techniques*, vol. 4, pp. 57- 63, 2019.

[22] R. Harrington, *Field Computation by Moment Methods*, Macmillan, New York, 1968.

[23] S. M. Rao, D. R. Wilton, and A. W. Glisson, "Electromagnetic scattering by surfaces of arbitrary shape," *IEEE Transactions on Antennas and Propagation*, vol. 30, pp. 409-418, 1982.

A Novel Method for Output Characteristics Calculation of Electromagnetic Devices using Multi-kernel RBF Neural Network

Feng Ding, Yunyun Gao, and Jianhui Tian

Department of Mechanical and Electronic Engineering
Xi'an Technological University, Xi'an, 710021, China
dd_feng@sina.com, 1032660865@qq.com, carl8@qq.com

Abstract ─ The action performance and reliability of electromagnetic devices is critical to the entire working system. In this paper, a new method for calculating the output characteristics of electromagnetic devices is proposed. This method uses the multi-kernel radial basis function neural network (MK-RBFNN) approximation modeling by the finite element calculation results at the key nodes. It obtains the output response of the electromagnetic device under different coil voltages and air gaps. The key of establishing a MK-RBFNN is to obtain the weight coefficients of each single-kernel radial basis function (RBF) model by using a heuristic weighting strategy. When the electromagnetic output characteristics is calculated in the optimization design of the electromagnetic device, this method solves the problem that the traditional method is difficult to balance the calculation accuracy and speed. The effectiveness of the method is verified by the calculation results of the electromagnetic torque of a typical electromagnetic relay.

Index Terms ─ Electromagnetic device, finite element, multi-kernel radial basis function, neural network, optimal design.

I. INTRODUCTION

The key to the optimal design or robust design of the electromagnetic device is to analyze the influence of the input parameters on the output characteristics, and it is necessary to repeatedly calculate the static characteristics [1]. The existing methods for solving output characteristics of electromagnetic devices mainly include magnetic equivalent circuit method (MEC), finite element method (FEM) and approximation model, but they all need to be further improved. In this paper, the multi-kernel RBF neural network is used to solve the output characteristics of the electromagnetic device, which can further improve the calculation speed while ensuring the calculation accuracy.

The traditional MEC has high computational efficiency but its calculation accuracy is not good because of neglecting magnetic flux leakage and magnetic saturation. Therefore, many researchers have conducted research in recent years to improve the calculation accuracy of MEC. Amrhein and Krein [2] used the magnetic resistance network method to establish a three-dimensional magnetic circuit model of the electromagnetic device based on the distribution of the spatial magnetic field. However, this method complicates the analysis of the magnetic circuit and increases the amount of calculation for non-linear solutions. It still has not improved the calculation efficiency.

The high accuracy and time-consuming characteristics of FEM make it difficult to adapt to a robust design or optimization process. The researchers tried to combine the advantages of FEM and MEC to establish an approximate model of the electromagnetic output response. Encica et al. [3] used the idea of spatial mapping to construct a geometric model whose matching result matched the finite element. However, it is difficult to establish a mapping relationship in a complex magnetic circuit with multiple design parameters.

The wide application of intelligent algorithms has led researchers to try to establish an approximate model through mathematical methods to achieve rapid calculation of electromagnetic characteristics. Xia et al. [4] constructed the Kriging approximation model of the electromagnetic device and optimized the parameters of the superconducting coil. The accuracy of the Kriging method depends on the choice of the basis function type. However, there is currently no uniform method to select this basis function. An approximate model of the electromagnetic device obtained using the custom interpolation function is presented in [5]. This method uses a custom interpolation function, but it is difficult to construct a suitable interpolation function according to different electromagnetic devices.

In 1989, Jackson demonstrated the approximation performance of Radial basis function (RBF) neural networks for nonlinear continuous functions. Papers [6,7] showed the advantages of RBF neural networks in predicting compared to other neural networks through experiments in different fields. Benbouza [8] explored the effects of radial basis functions in the field of

Submitted On: September 19, 2019
Accepted On: April 10, 2020
https://doi.org/10.47037/2020.ACES.J.350802

electromagnetic computing. Papers [9] improved the existing RBF neural network to meet the needs of different occasions. A number of studies have shown that the RBF approximation model has higher predicting accuracy than other approximation models in the case of linearity, weak nonlinearity and strong nonlinearity. These findings provide support for the application of RBF neural networks in the field of electromagnetic device computing.

This paper aims to propose a new method for calculating the output characteristics of electromagnetic devices quickly and accurately. The method adopts the idea of approximate modeling. By selecting the finite element calculation results at key nodes as sample points, a MK-RBFNN is constructed to determine the output characteristics (electromagnetic torque) of electromagnetic devices under different coil voltages and air gaps. As a case study of the clapper-type electromagnetic mechanism of a typical electromagnetic relay, the accuracy and rapidity of the method are verified significantly and effectively.

II. METHOD DESCRIPTION

The implementation steps of the novel method proposed in this paper are shown in Fig. 1. It makes great use of the advantages of each single-kernel RBF neural network, which can quickly and accurately calculate the output characteristics of the electromagnetic device.

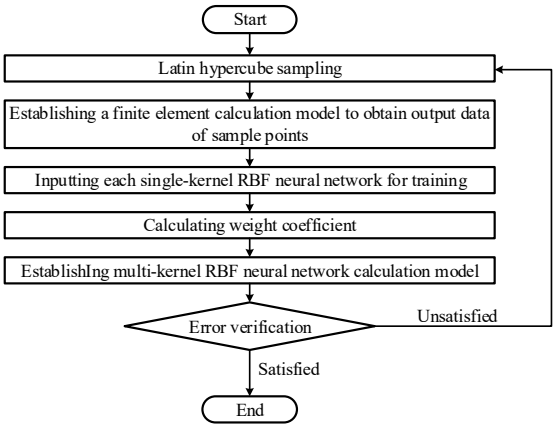

Fig. 1. Flow chart of method for output characteristics calculation of electromagnetic device.

A. Latin hypercube sampling

(a) Determining input variables and output variables

The appropriate input variables and output variables must be selected before the test design, which is the premise of the approximate numerical calculation. Taking a rotating electromagnetic device as an example, the differential equation of electromagnetic output characteristics can be established by the voltage balance equation and the D'Alembert [10] equation of motion, the expression is:

$$\begin{cases} u_0 = i(\psi,\theta)R + \dfrac{d\psi}{dt} \\ J\dfrac{d\omega}{dt} = T(U,\theta) - T_f(\theta) \cdot \\ \omega = \dfrac{d\theta}{dt} \end{cases} \tag{1}$$

In (1), u_0 is the power supply voltage of the coil circuit; i is the current of the coil; R is the resistance of the coil; ψ is the flux linkage; J is the torque of inertia; ω is the angular velocity; U is the voltage of the coil; θ is the rotation angle of armature; T is the electromagnetic torque; T_f is mechanical torque.

The coil voltage U and the rotation angle θ of armature of the electromagnetic device will vary over time during operation. In the dynamic characteristic calculation process, it is necessary to analyze the electromagnetic characteristics corresponding to different voltages U and different rotation angles θ. U and θ in (1) have two conditions: static (U and θ are fixed), dynamic (U and θ follow Change of time).

Therefore, the voltage U and the rotation angle θ are input variables, and the electromagnetic torque T of the armature is the output variable when calculating the output characteristics of the rotating electromagnetic device.

(b) Generating sample data

The basis of constructing the approximate model is sample data. The appropriate number of experimental data with uniform distribution can better reflect the information of the whole space. Conversely, improper sample data will result in a model with poor fitting accuracy, and even get the wrong model, so it is especially important to choose the appropriate experimental design method.

The Latin hypercube sampling (LHS) [11] method was proposed by M. D. McKay and R. J. Beckman in 1979. The LHS is a method of approximately random sampling from a multivariate parameter distribution. The basic principle is: if N sample points need to be collected, then the interval with m variables is divided into N intervals with equal probability, take a random value for each variable in each interval, so each variable has N values. Finally, the N values of m groups are randomly combined into a whole sample.

The LHS steps can be summarized as the following three steps:

i) Selecting the parameters to be sampled. Such as the rotation angle θ of armature and the voltage U of coil.

ii) Generating random number. Each variable x_i is divided into K non-overlapping intervals with equal

probability, the probability of each interval is $1/k$, then a representative parameter x_i^k is generated from each subinterval with equal probability. This parameter is usually the midpoint of the interval.

iii) Generating samples. The representative samples of each parameter x_i^k are arranged by random number. Thus, *N* random combinations are formed, each of which contains a representative sample x_i^k of all variables.

The LHS ensures that the sample points taken represent the entire design space, and each level of each design variable is considered only once. Therefore, the sample points obtained by this method are less repetitive, and the number of samples can be set flexibly, which has good sampling efficiency and balance performance. This paper uses the LHS method for initial sampling based on the above advantages when establishing an approximate calculation model for electromagnetic devices.

B. Establishing finite element calculation model

The solution of electromagnetic field is generally based on Maxwell's equations, and the FEM is one of the most advanced and powerful methods for solving Maxwell's equations [12]. FLUX is the leading simulation software for electromagnetic and thermal calculations based on finite element theory developed by Altair [13].

The simulation calculation process includes geometry, meshing and physical description, these preparations make the established model as close as possible to the real model. The basic steps of establishing the finite element model of electromagnetic equipment with the FLUX are shown in Fig. 2.

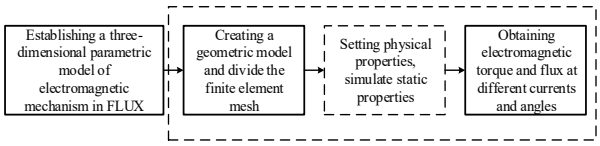

Fig. 2. Basic steps of constructing a finite element calculation model.

According to the finite element model established by FLUX software, the output response value of each input variable sample is calculated to form the sample set of corresponding output variables.

C. Inputting each single-kernel RBF neural network for training

In recent years, RBF have been widely studied in the field of neural networks. Their excellent interpolation quality has led to their application in computational electromagnetics [14]. The expression of the RBF is:

$$\hat{y}(x) = \beta_0 + \sum_{i=1}^{N} \beta_i \varphi(||x - x_i||). \quad (2)$$

In (2), β_0 is a polynomial function (determined form), N is the size of the hidden layer, and its value generally does not exceed the number of sample points, β_i is the weight value between the *i-th* input layer neuron and the *p-th* hidden layer neuron, φ is the kernel function, also known as the transfer function of the hidden layer, x_i is the center of hidden layer node of neural network, $\|\|$ is Euclidean distance.

It is worth noting that the determination method of center x_i. After testing, the commonly used k-means clustering algorithm is not ideal, and its global accuracy is poor. In this paper, the center x_i is determined based on the orthogonal least square (OLS) method. Because OLS finds the best function of matching data by minimizing the sum of squares of errors, it is possible to control the fitting accuracy by setting errors during the training process, and adaptively determine the number of hidden nodes according to the error requirements. On the contrary, in the process of using the k-means clustering algorithm, the number of hidden nodes needs to be determined first. Different values have a great influence on the results of the fitting calculation, which is inconvenient for the application of the method in this paper.

The kernel functions commonly used in the RBF model are shown in Table 1 [15]. r represents the Euclidean distance between x and center x_i. The shape parameter c can be specified by experience.

Table 1: Commonly used kernel functions in the RBF model

Name	Expression	Abbreviation
Linear Function	$\varphi(r) = r$	LN
Cubic Function	$\varphi(r) = (r + c)^3$	CB
Thin Plate Spline	$\varphi(r) = (r^2 + c^2) ln(r + c)$	TPS
Multi-quadric Function	$\varphi(r) = \sqrt{r^2 + c^2}$	MQ
Inverse Multi-quadric Function	$\varphi(r) = \frac{1}{\sqrt{r^2 + c^2}}$	IMQ
Gaussian Function	$\varphi(r) = e^{-\frac{r^2}{2c^2}}$	GA

According to the test, the application effect of the last four kernel functions in Table 1 is better. The single-kernel RBF neural network with them as kernel functions has a good fitting effect on the output characteristics of electromagnetic equipment.

D. Establishing MK-RBFNN calculation model

(a) Introduction of MK-RBFNN model

The RBF model has strong nonlinear mapping ability and optimal function approximation performance, and has fast calculation speed. However, further research shows

that its robustness is poor, so it is necessary to choose different kernel functions to build RBF model according to different problem types. In view of the above shortcomings, this paper proposes a MK-RBF model constructed by multiple kernel functions based on the merits of each kernel function. This model has higher fitting precision and stronger robustness than the general RBF model constructed by a single kernel function.

According to the four kernel functions mentioned in Section IIC, the MK-RBFNN model is established. The expression are:

$$\begin{cases} \hat{y}_{MK-RBF}(x) = \sum_{i=1}^{M} \lambda_i \hat{y}_i(x) \\ \sum_{i=1}^{M} \lambda_i = 1 \end{cases}. \tag{3}$$

In (3), M is the number of single-kernel RBF models needed to construct the final MK-RBF neural network model, $\hat{y}_{MK-RBF}$ is the predicted value of the MK-RBF neural network model, $\hat{y}_i(x)$ is the predicted value of the i single-kernel RBF neural network model, and λ_i is the weight coefficient corresponding to the i single-kernel RBF neural network model.

The establishing structure of the multi-kernel RBF neural network model are shown in Fig. 3.

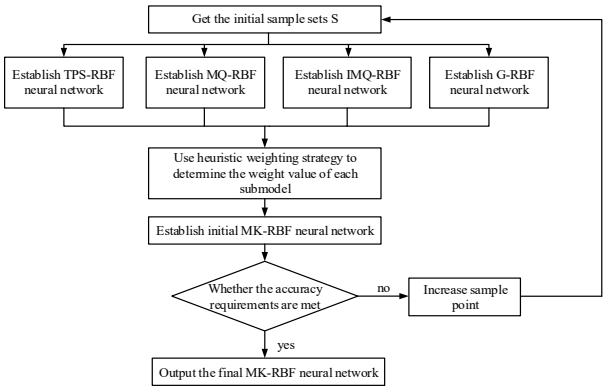

Fig. 3. Establishing structure of MK-RBFNN model.

(b) Calculating weight coefficient

The weight coefficient is very important in constructing the final approximation model. The heuristic weighting strategy can better balance the weight values of each single-kernel RBF model, and can make the final MK-RBF model get better fitting effect. The basic expressions are:

$$\begin{cases} \lambda_i = \lambda_i^* \Big/ \sum_{i=1}^{M} \lambda_i^* \\ \lambda_i^* = \left(E_i + \alpha E_{avg}\right)^{\beta} \\ E_{avg} = \dfrac{1}{M} \sum_{i=1}^{M} E_i \end{cases}. \tag{4}$$

In (4), $\alpha < 1, \beta < 0$, α and β respectively represent parameters that have a large influence on the degree of emphasis on the constituent model. A smaller α values and a larger $|\beta|$ values indicate higher weights for single-kernel RBF models with higher prediction accuracy. A larger α value and a smaller $|\beta|$ value indicate a higher average confidence for each single-kernel RBF model. According to experience, this paper takes $\alpha = 0.05, \beta = -1$, so that each single-kernel RBF model has the optimal weight coefficient. In this paper, E_i is generally obtained by Generalized Mean Square Cross-validation Error (*GMSE*). The expression is:

$$E_i = \sqrt{GMSE_i} = \sqrt{\frac{1}{k} \sum_{j=1}^{k} \left(f_j - \hat{f}_j^{(-j)}\right)^2}. \tag{5}$$

In (5), k represents the total number of sample points taken by the i-th single-kernel RBF model, and $\hat{f}_j^{(-j)}$ represents the predicted value of the i-th single-kernel RBF model at point $x^{(j)}$, which is constructed by the remaining $k-1$ points (excluding point $\left(x^{(j)}, f_j\right)$).

E. Error verification

In the case of a fixed number of sample points, the researchers usually use some error indicators to evaluate the fitting accuracy of the approximate model. The error is further divided into relative error and absolute error. When the value of a certain type of data is originally small, the relative error can well characterize the fitting accuracy. Therefore, this paper chooses the relative error with strong applicability.

In this paper, two global error indicators and one local error indicator are used to evaluate the performance of the model, as follows:

a) Coefficient of multiple correlation (R^2):

$$R^2 = 1 - \frac{\sum_{i=1}^{m} \left(y_i - \hat{y}_i\right)^2}{\sum_{i=1}^{m} \left(y_i - \bar{y}\right)^2} = 1 - \frac{MSE}{Var}. \tag{6}$$

b) Relative root mean square error (*RRMSE*):

$$RRMSE = \frac{1}{STD} \sqrt{\frac{\sum_{i=1}^{m} \left(y_i - \hat{y}_i\right)^2}{m}}. \tag{7}$$

c) Relative maximum absolute error (*RMAE*):

$$RMAE = \frac{\max\limits_{i=1,2,\ldots,m} |y_i - \hat{y}_i|}{STD}. \tag{8}$$

Where m represents the number of points sampled when validating the model, y_i represents the true value, $\hat{y}_i$ represents the predicted value obtained by the established model, and $\bar{y}$ represents the average of all true values. *MSE*, *Var*, and *STD* represent the mean square error, the variance of the true value, and the

standard deviation, the calculation expressions are:

$$MSE = \frac{\sum_{i=1}^{m}(y_i - \hat{y}_i)^2}{m}, \quad (9)$$

$$Var = \frac{\sum_{i=1}^{m}(y_i - \bar{y})^2}{m}, \quad (10)$$

$$STD = \sqrt{Var}. \quad (11)$$

The global error indicators R^2 and *RRMSE* are all related to the *MSE*. As can be seen from the above formulas, a larger R^2 and a smaller *RRMSE* indicate a smaller *MSE*. The approximate model established at this time has a small global error and a high prediction accuracy. The local error indicator *RMAE* characterizes the local fitting accuracy of the approximate model. The smaller *RMAE* indicates that the approximate model has higher fitting accuracy. Otherwise, it indicates that the approximation model has poor fitting accuracy in a certain region.

III. APPLICATION EXAMPLE: OUTPUT CHARACTERISTIC CALCULATION OF ELECTROMAGNETIC RELAY

A. Introduction to application example

Aiming at the above mentioned calculation method of multi-core radial basis function neural network applied in the field of electromagnetic calculation, this paper takes ARM2F relay as the research object, establishes a fast calculation model of armature electromagnetic torque of its electromagnetic system, in order to verify the effectiveness of this method. As shown in Fig. 4, the electromagnetic system of ARM2F relay belongs to a typical clapper-type electromagnetic structure, which is composed of yoke iron, armature, iron core and coil.

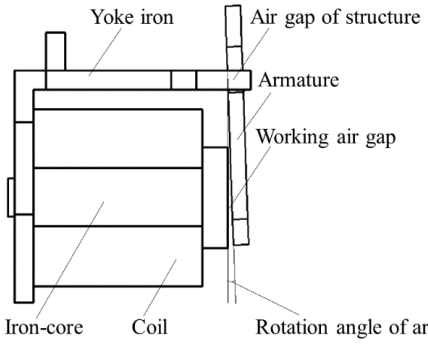

Fig. 4. Structure of the ARM2F electromagnetic system.

B. Method application

The geometry of the coil is established in flux, and the input parameters of the coil are automatically generated by the software. Then, through generating grid, applying voltage (current), adding material B-H characteristics and other parameters, the software gets the flux density based on the finite element method, and gets the electromagnetic torque of the armature in the post-processing module.

Taking the magnetic flux density of the electromagnetic mechanism with the 6V voltage and the rotation angle of armature at 2.1° as an example, the calculated flux density is shown in Fig. 5.

In the range $(0 \le U \le 24\text{V}, 0 \le \theta \le 2.1°)$ of input parameters of electromagnetic system, 44 groups of sample points of input parameters are obtained by Latin hypercube sampling, and the output response of input samples is calculated by FLUX software to form the initial sample set S.

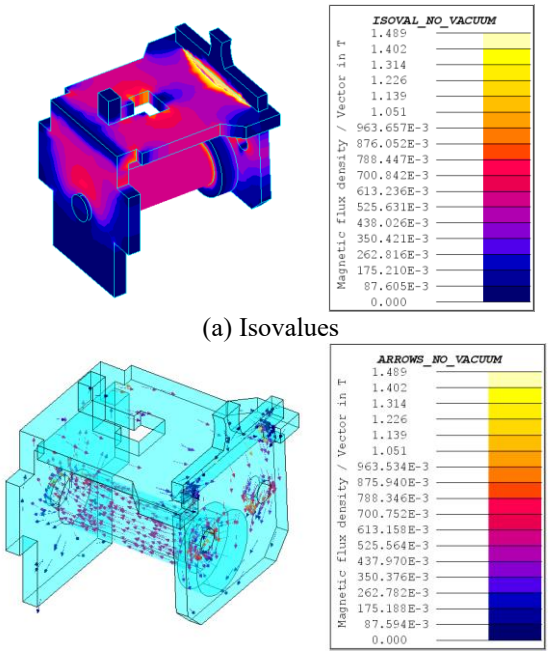

(a) Isovalues

(b) Arrows

Fig. 5. Magnetic flux density (Isovalues and Arrows).

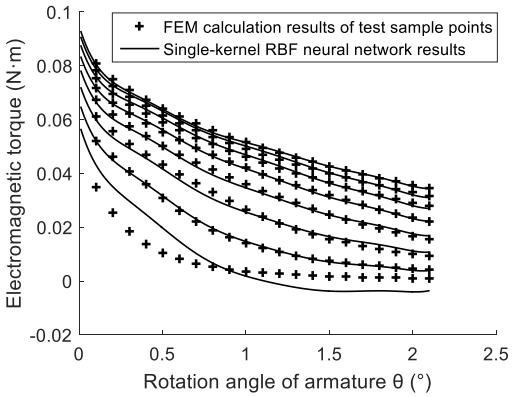

(a) Kernel function – IMQ

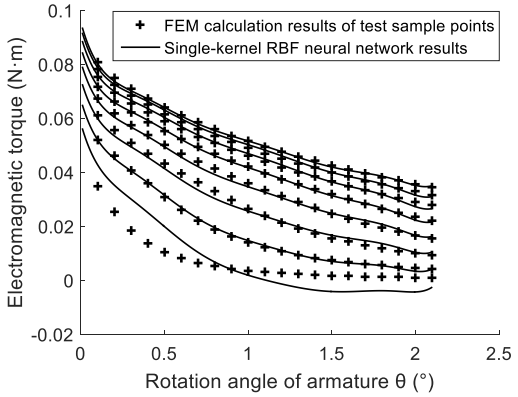

(b) Kernel function – MQ

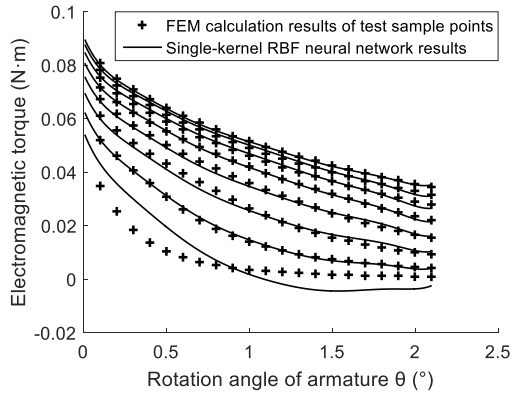

(c) Kernel function – TPS

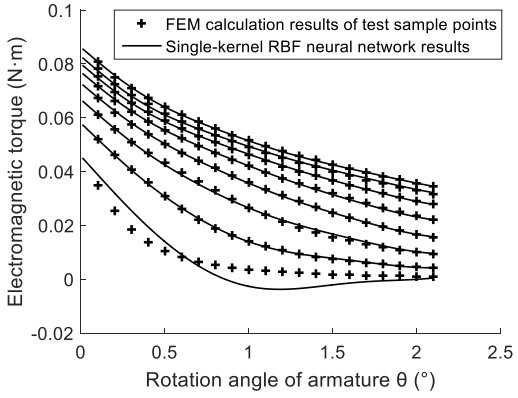

(d) Kernel function – GA

Fig. 6. Comparison of four single-kernel RBF neural network results and the FEM calculation results of test sample points.

The sample set S is input into the single-kernel RBF neural networks with four different kernel functions for training, and four kinds of single-kernel RBF neural networks are obtained. 168 test sample points are taken at equal intervals within the range of input parameters of electromagnetic system, and the output response of test sample points is calculated by using the software of FLUX. The comparison between the calculation results of different single-kernel RBF neural network and the test sample results calculated based on the FEM is shown in Fig. 6. The total 8 curves in Fig. 6 represent the relationship between the rotation angle of armature and the output electromagnetic torque when the voltage is 24V, 21V, 18V, 15V, 12V, 9V, 6V and 3V respectively. The RBF neural network models established with different kernel functions are shown in (a), (b), (c), and (d) of Fig. 6. The kernel functions are IMQ, MQ, TPS, and GA.

It can be seen from Fig. 6 that the calculated results of the RBF neural network trained by four different kernel functions are roughly the same as those of the finite element calculation of the test point in the range of 6V-24V. But in the case of voltage below 6V, there is a large deviation. Low voltage will lead to a sharp decrease in the main flux of the coil, and the nonlinearity of electromagnetic torque with the change of rotation angle of armature is much higher than that of high voltage. Therefore, a small number of sample points make the prediction accuracy of RBF neural network sharply reduced in this range.

In order to solve the problem of excessive local deviation, this paper constructs different neural networks in different intervals. For the part below 6V, increasing the sample points for neural network training. Specifically, in the voltage range of 0V-6V, 11 sampling points are obtained through LHS again. In this interval, an RBF neural network is additionally constructed with a similar kernel function to reflect the response of the electromagnetic torque to the armature rotation angle in this range. Ultimately, two RBF neural networks are constructed by using 55 samples in two intervals to calculate the output response in the whole range of input parameters. The final calculation results of this scheme are shown in Fig. 7.

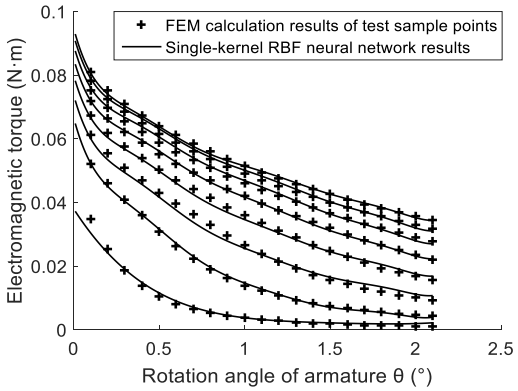

(a) Kernel function – IMQ (two parts of RBFNN)

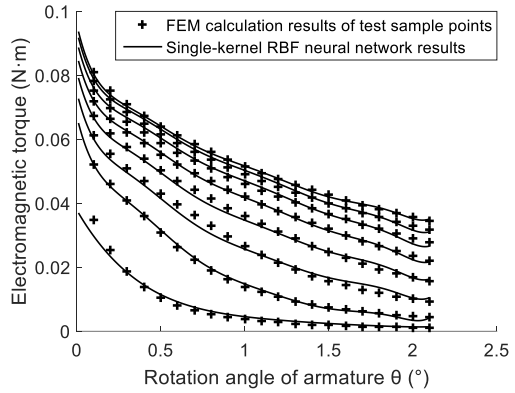

(b) Kernel function – MQ (two parts of RBFNN)

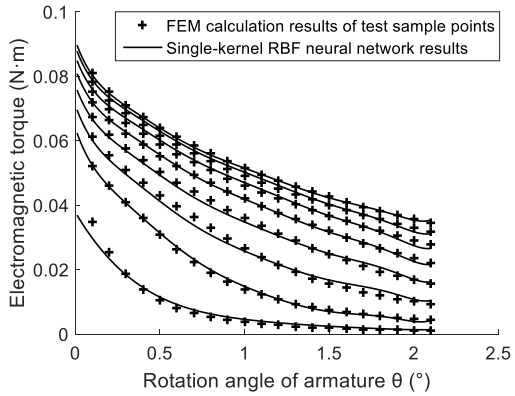

(c) Kernel function – TPS (two parts of RBFNN)

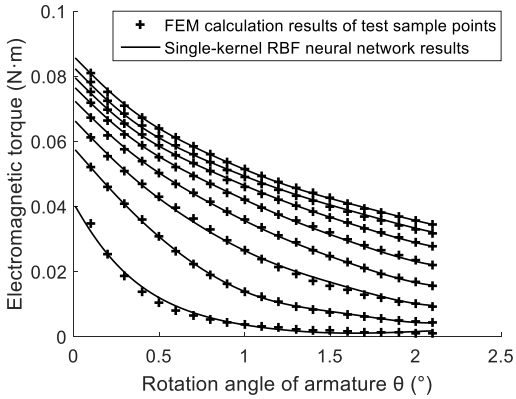

(d) Kernel function – GA (two parts of RBFNN)

Fig. 7. Comparison of two parts of four single-kernel RBF neural network results and the FEM calculation results of test sample points.

It can be seen from Fig. 8 that the accuracy of the results calculated by the two-part neural network constructed by using the separated interval is significantly improved within the voltage of 6V. In order to balance the calculation accuracy in the global range of parameters, the MK-RBF neural network model constructed by multiple kernel functions is established by the method described in Section II. The weight coefficients of each single-kernel RBF neural network are calculated as shown in Table 2. The final calculation results of MK-RBF neural network and the FEM calculation results of test sample points are shown in Fig. 8.

Table 2: The weight coefficient of each single-kernel RBF neural network

Type of Single-kernel RBF Neural Network	Weight Coefficient λ
IMQ-RBF	0.21608
MQ-RBF	0.24299
TPS-RBF	0.24292
GA-RBF	0.29801

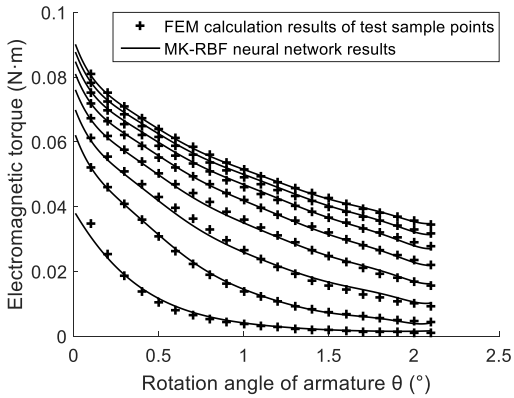

Fig. 8. Comparison of MK-RBF neural network results and the FEM calculation results of test sample points.

C. Analysis of calculation results of application example

The calculation accuracy of MK-RBF neural network can be reflected by the error evaluation indicator. If the model has a large R^2 and a smaller *RRMSE* and *RMAE*, which means that the model has higher prediction accuracy and fitting accuracy. 224 error test sample points are randomly selected in the range of input parameters, and the output response (electromagnetic torque) of test sample points is calculated by finite element method. Finally, the error results of RBF neural network with different kernel functions are shown in Table 3.

Whether it is to observe the comparison with the finite element results, or to compare the error evaluation indicators, it is found that the accuracy of each single-kernel RBF neural network within the different variation range of the input variables is different. For example, the IMQ-RBF and MQ-RBF neural networks have higher calculation accuracy than the TPS-RBF and GA-RBF neural networks under the conditions of an armature rotation angle of 0.1° or below it. In the working condition about the rotation angle of armature of 0.1° or over it, it is obvious that the GA-RBF neural network has

higher calculation accuracy than the other three single-kernel neural networks.

Table 3: Error results of RBF neural network with different kernel functions

Evaluation Indicator	IMQ-RBF	MQ-RBF	TPS-RBF	GA-RBF	MK-RBF
R^2	0.99629	0.99567	0.99574	0.99529	0.99704
RRMSE	0.06086	0.06582	0.06525	0.06857	0.05442
RMAE	0.34876	0.36196	0.36784	0.29412	0.32147

After the coil of the electromagnetic relay is excited by the rated voltage, with the increase of time, the rotation angle of the armature gradually approaches to 0°, the voltage gradually rises to its rated voltage, and the electromagnetic torque of the armature gradually tends to the maximum value. So it is very important to accurately calculate the electromagnetic torque at high voltage and small angle. In this case, the calculation accuracy of MK-RBF neural network model is better than GA-RBF when the rotation angle of armature is within 0.1°. In 0.1°-2.1°, the calculation accuracy of MK-RBF neural network model is better than that of the other three RBF neural networks because of the addition of GA kernel function, which has reached a satisfactory level as a whole.

It can be seen from Table 3 that the global error performance of the MK-RBF neural network is much better than any single-kernel neural network, and the local error can be controlled within a certain range. It combines the advantages of each single-kernel neural network and enhances the robustness of the calculation.

IV. CONCLUSIONS

Aiming at the need of rapidity and accuracy of the calculation process, this paper proposes a new method for calculating the output characteristics of electromagnetic devices. The following conclusions are obtained:

a) In terms of computational efficiency, in the case of a coil voltage and an rotation angle of armature of the above mentioned clapper-type electromagnetic relay, it takes about 3.2 minutes to calculate the electromagnetic torque by the finite element method. The calculation takes only 0.412 seconds to use the multi-kernel radial basis neural network proposed in this paper. (Note: The computer performance used in this example calculation process is dual-kernel CPU frequency 2.6GHz, memory 8GB). The superiority of the proposed method is reflected in the extremely high computational efficiency of such calculations.

b) In terms of computational accuracy, it is greatly improved by the multi-kernel RBF neural network. This is because the method uses the result of finite element calculation as the sample input, and the global accuracy of electromagnetic torque calculation based on multi-kernel radial basis neural network is obviously better than any single-kernel radial basis neural network. This is mainly due to the advantages of each single-kernel RBF neural network being synthesized by the MK-RBF neural network through different weight coefficients.

c) In terms of the scope of application of the model, the calculation method proposed in this paper can also be used in other fields of nonlinear engineering calculation. The method of multi-kernel RBF neural networks is obviously more applicable than single-kernel RBF neural networks. The method solves the weight value of each single-kernel RBF model by heuristic weighting strategy, which reduces the requirements of the modeler's own level in the modeling process.

ACKNOWLEDGMENT

This research was financially supported by the National Science Foundation of China (Grant No. 51275374) and the Basic Research Plan of Natural Science in Shannxi Province (No. 2018JM5099).

REFERENCES

[1] A. Saha and, T. Ray, "Practical robust design optimization using evolutionary algorithms," *Journal of Mechanical Design*, vol. 133, no. 10, pp. 101012.1-101012.19, Oct. 2011.

[2] M. Amrhein and T. Krein, "Induction machine modeling approach based on 3-D magnetic equivalent circuit framework," *IEEE Trans. Magn.*, vol. 25, no. 2, pp. 339-347, May 2010.

[3] L. Encica, J. Makarovic, E. A. Lomonova, and A. J. A. Vandenput, "Space mapping optimization of a cylindrical voice coil actuator," *IEEE Transactions on Industry Application*, vol. 42, no. 6, pp. 1437-1444, Nov. 2006.

[4] B. Xia, Z. Ren, and C.-S. Koh, "Utilizing kriging surrogate models for multi-objective robust optimization of electromagnetic devices," *IEEE Trans. Magn.*, vol. 50, no. 2, pp. 835-838, Feb. 2014.

[5] Y. Xuerong, D. Jie, W. Yingqi, and Z. Guofu, "An approximate calculation model for electromagnetic device based on user-defined interpolating function," *Journal of Magnetics*, vol. 19, no. 4, pp. 378-384, Dec. 2014.

[6] H. A. Tayebi, M. Ghanei, K. Aghajani, and M. Zohrevandi, "Modeling of reactive orange 16 dye removal from aqueous media by mesoporous silica/crosslinked polymer hybrid using RBF, MLP and GMDH neural network models," *Journal of Molecular Structure*, vol. 1178, pp. 514-523, Feb. 2019.

[7] H. K. Ghritlahre and R. K. Prasad, "Exergetic performance prediction of solar air heater using MLP, GRNN and RBF models of artificial neural network technique," *Journal of Environmental*

Management, vol. 223, pp. 566-575, Oct. 2018.
[8] N. Benbouza, F. Z. Louai, and N. Nait-Said, "Application of meshless Petrov Galerkin (MLPG) method in electromagnetic using radial basis functions," *4th IET Conference on Power Electronics, Machines and Drives*, May 2008.
[9] Q. Junfei, M. Xi, and L. Wenjing, "An incremental neuronal-activity-based RBF neural network for nonlinear system modeling," *Neurocomputing*, vol. 302, pp. 1-11, Aug. 2018.
[10] J. W. Perram, "Criterion for the validity of D'Alembert's equations of motion," *Advances in Quantum Chemistry*, vol. 75, pp. 103-116, 2017.
[11] M. Stein, "Large sample properties of simulations using Latin hypercube sampling," *Technometrics*, vol. 29, no. 2, pp. 143-151, 1987.
[12] A. Capozzoli, O. Kilic, C. Curcio, and A. Liseno, "The success of GPU computing in applied electromagnetics," *ACES Journal*, vol. 33, no. 2, pp. 148-151, Feb. 2018.
[13] Z. Guofu, W. Qiya, and R. Wanbin, "An output space-mapping algorithm to optimize the dimensional parameter of electromagnetic relay," *IEEE Trans. Magn.*, vol. 47, no. 9, pp. 2194-2199, Sep. 2011.
[14] R. K. Gordon and W. E. Hutchcraft, "The use of multiquadric radial basis functions in open region problems," *ACES Journal*, vol. 21, no. 2, pp. 127-134, July 2006.
[15] R. K. Gordon and W. E. Hutchcraft, "Comparison of solution accuracy using different sets of radial basis functions," *25th Annual Review of Progress in ACES*, pp. 413-418, Mar. 2009.

Feng Ding received his M.E. degree and the Ph.D. degree in Mechanical Engineering from Xi'an Jiaotong University, China. He is a Professor of the Department of Mechanical and Electronic Engineering, Xi'an Technological University, China. His research interests include condition monitoring, intelligent diagnosis and prognostics, reliability engineering.

Yunyun Gao is a M.E. candidate in the Department of Mechanical and Electronic Engineering, Xi'an Technological University, Xi'an, China. His research interests include structural design, simulation and optimization of mechanical equipment, and numerical algorithm theory.

Jianhui Tian received his Ph.D. degree in Mechanical Design and Theory from Hunan University, China. He is an Associate Professor of the Department of Mechanical and Electronic Engineering, Xi'an Technological University, China. His research interests include engineering optimization design and simulation technology.

A Modified Adaptive Integral Method for Analysis of Large-scale Finite Periodic Array

Mingxuan Zheng, Huiling Zhao, and Zhonghui Zhao

School of Electronics and Information
Northwestern Polytechnic University, Xi'an, Shaanxi, 710129, China
x408859786@mail.nwpu.edu.cn

Abstract ─ A fast algorithm based on AIM is proposed to analyze the scattering problem of the large-scale finite array. In this method, by filling zeros into the local transformation matrix, the near and far fields are isolated thoroughly to eliminate the near correction process. In the far part, a 5-level block-toeplitz matrix is employed to avoid saving the idle grids without adding artificial interfaces. In the near part, only one local cube is required to compute the local translation matrix and near impedance matrix, which can be shared by all elements. Furthermore, the block Jacobi preconditioning technique is applied to improve the convergence, and the principle of pattern multiplication is used to accelerate the calculation of the scattering pattern. Numerical results show that the proposed method can reduce not only the CPU time in filling and solving matrix but also the whole memory requirement dramatically for the large-scale finite array with large spacings.

Index Terms ─ Adaptive integral method, diagonal block preconditioning, large-scale finite periodic array, multilevel block-toeplitz, scattering problem.

I. INTRODUCTION

Periodic arrays [1] have been widely used in microwave engineering, antennas and metamaterials design. It is well known that the method of moment (MoM) [2] possess high accuracy, but inefficient in solving large-scale problems. In the past three decades, a lot of fast algorithms based on MoM have been proposed, such as multilevel fast multipole algorithm (MLFMA) [3], integral-equation fast Fourier transform (IE-FFT) algorithm [4,5], the adaptive integral method (AIM) [6], etc. For large-scale quasi-plane problems, these methods could reduce computational complexity from $O(N^2)$ to $O(N\log N)$, and memory requirements from $O(N^2)$ to $O(N)$. Among these methods, IE-FFT and AIM are FFT-based methods, and less dependent on the integral kernels. This feature enables them to be implemented with the standard and efficient FFT libraries available online.

The IE-FFT algorithm employs Cartesian grids for interpolating Green's functions, which has been successfully used in analyzing the large planar microstrip antenna arrays [7] and integrated circuits [8]. Different from IE-FFT, AIM is based on an "equivalent" source approximation, where the unstructured basis functions are mapped to the uniform grids by multipole expansion [6] without interpolating. This suggests that AIM is more accurate in analysis of arbitrary three-dimensional (3D) electromagnetic problems. Many hybrid methods have been proposed to solve the problems of periodic structures. For example, AIM is combined with the model-based parameter estimation [9] for the infinite periodic structures, with multisolution sparse matrix (MR SM/AIM) [10] for large finite 2.5D antenna arrays, with the MultiLayer method [11] for the multilayer printed arrays, with Synthetic Function eXpansion (SFX) domain-decomposition approach [12] and with characteristic basis function method for aperiodic tiling-based antenna arrays [13].

Nevertheless, there are two drawbacks in AIM based hybrid methods when the finite periodic array is rather large with large spacings. For the first drawback, referring Fig. 1, there are a lot of idle grids which do not contribute to far field interactions, but still waste a lot of computational source. Consequently, the speed of matrix-vector product (MVP) is slow down. To address this problem, the circulant AIM (CAIM) [14] and subdomain AIM (SAIM) [15] are developed. However, CAIM is only efficient for quasi-cylindrical structures and SAIM requires to build complicated artificial interfaces among different subdomains, which is less efficient for large-scale arrays. The second drawback is that it will cost a lot of time to correct the nonzeros in near field correction process. Moreover, it is hard to find a suitable preconditioner [16] for the corrected matrix.

In this paper, a novel array AIM is proposed for the large-scale finite periodic array with large spacings. Different from SAIM, the proposed method avoids saving the idle grids through adopting a 5-level block-toeplitz matrix without adding artificial interfaces. In

Submitted On: December 27, 2019
Accepted On: May 17, 2020
https://doi.org/10.47037/2020.ACES.J.350803

addition, the near correction is eliminated, thus the near and far matrix can be isolated thoroughly. To the best of author's knowledge, it is seldom reported on the AIM-based technique without near correction. To further improve the convergence of iteration, the block diagonal preconditioner is applied to reduce the cost of computation and memory. The rest of paper is organized as follows. In Section II, the details of the proposed method are illustrated, including the process of filling matrix, preconditioning, solving and post computation. Section III gives some numerical simulation results to validate the accuracy and efficiency of the proposed method. Finally, the summary and conclusions are presented in Section IV.

II. FORMULATION

A. The conventional AIM

For an arbitrary 3D perfect electric conductor (PEC), the conventional MoM under Galerkin's testing procedure is applied to form a matrix equation as:

$$\mathbf{ZI} = \mathbf{V}, \tag{1}$$

where $\mathbf{I}$ is the current coefficients of basis functions and $\mathbf{V}$ denotes the excitation. To reduce the memory requirements, the impedance matrix $\mathbf{Z}$ is divided into near and far parts as $\mathbf{Z} = \mathbf{Z}^{near} + \mathbf{Z}^{far}$ in AIM [6], where $\mathbf{Z}^{near}$ is a sparse matrix and $\mathbf{Z}^{far}$ is compressed as the multiplications of several sparse matrices:

$$\mathbf{Z}^{near} = \mathbf{Z}^{MoM} - \mathbf{Z}^{AIM}, \tag{2}$$

$$\mathbf{Z}^{far} = \sum_{q=x,y,z,D} \mathbf{\Lambda}_q \mathbf{G} \mathbf{\Lambda}_q^T, \tag{3}$$

where $\mathbf{Z}^{MoM}$ is the near interaction calculated by MoM, $\mathbf{Z}^{AIM}$ is the inaccurate contribution from grids, $\mathbf{G}$ is the block-toeplitz transformation matrix of Green's function on the auxiliary grids, and $\mathbf{\Lambda}_q$ are the sparse translation matrices. To solve equation (1) efficiently, preconditioning techniques, such as threshold-based incomplete LU (ILUT) [17], shifted symmetric successive over-relaxation (SSOR) [18] or parallel sparse approximate inverse (PSAI) [19], are generally applied to improve the convergence of iteration.

However, for large-scale finite periodic array, the conventional AIM will become less efficient. Firstly, filling $\mathbf{Z}^{near}$ costs a lot of time especially for the calculation of $\mathbf{Z}^{AIM}$. It is worth noting that computing $\mathbf{Z}^{AIM}$ with FFT is less efficient when the number of grids is quite large. Instead, $\mathbf{Z}^{AIM}$ should be calculated according to (3) in order to improve the filling speed. Secondly, the construction of the preconditioning matrix will cost more time if $\mathbf{Z}^{near}$ or $\mathbf{Z}^{MoM}$ has more nonzeros. The reasons of the long time filling and preconditioning are the unseparated near and far fields. In other word, the MVP for $\mathbf{Z}^{far}$ and $\mathbf{I}$ brings the inaccurate values to the near part, which forces $\mathbf{Z}^{MoM}$ need to be corrected. Finally, although each element is identical, the multipole expansion remains to be repeated many times because the distance between the basis functions and the surrounding grids may be different for each element. Moreover, the huge number of idle grids will also influence the peak memory requirements and speed of FFT.

To overcome these problems, a modified AIM called array AIM is proposed for the finite periodic array with large spacings in the next part.

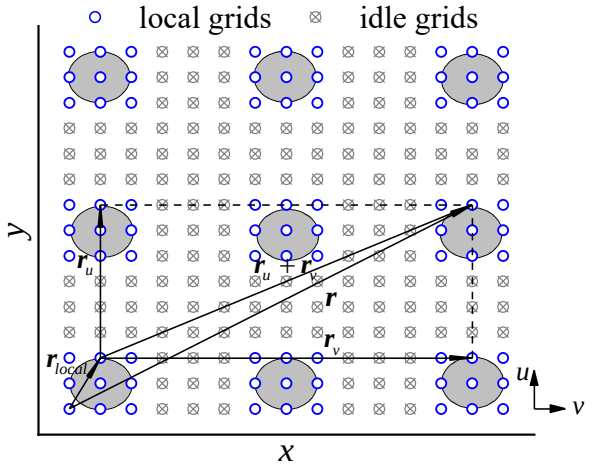

Fig. 1. Geometry of local and idle grids for an array in *xoy* plane. The array elements are depicted in gray.

B. Array AIM for the finite periodic array

In this part, the Green's function matrix is reconstructed at first in order to avoid saving the idle grids. Then the near correction is eliminated by isolating the near and far fields. The modified MVP is given at the end of the part.

For a common 3D electromagnetic problem, $\mathbf{G}$ is constructed as the form of three-level block-toeplitz matrix in the traditional AIM. However, for the array with large spacings as depicted in Fig. 1, $\mathbf{G}$ has to keep many idle or unoccupied auxiliary point sources to maintain the Toeplitz property [20].

To avoid saving these idle grids, firstly each element is enclosed in a small local cube instead of a huge global cube for the whole array. Then the translation matrices $\mathbf{\Lambda}_l$ are computed just in the small local cube by the multipole expansion. Since each element is identical, $\mathbf{\Lambda}_l$ are calculated only once and shared by all elements.

Secondly, the three-level block-toeplitz $\mathbf{G}$ used in SAIM is replaced by five-level block-toeplitz $\mathbf{G}_{Array}$ without adding artificial surfaces. The interactions between any two elements are computed directly by (3) because they are well separated to meet the far-field condition. Based on the denotation for multilevel block-toeplitz matrix in [20], $\mathbf{G}_{Array}$ can be expressed as $\mathbf{T}^5(N_u, N_v, N_z, N_y, N_x)$, where N_u, N_v are the number of elements at two orthogonal directions u,v in array plane

respectively, and N_x, N_y, N_z are the number of grids on x, y, z directions in the local cube. In the final level, the Green's function between two different grids is calculated as:

$$g(\boldsymbol{r}) = \exp(-jk|\boldsymbol{r}|)/4\pi|\boldsymbol{r}|, \boldsymbol{r} = \boldsymbol{r}_{local} + \boldsymbol{r}_u + \boldsymbol{r}_v, \quad (4)$$

where k is the wave number, $\boldsymbol{r}$ denotes the distance vector measured from source point to field point, $\boldsymbol{r}_{local}$ is the position vector if the two points are translated into one cube, $\boldsymbol{r}_u$ and $\boldsymbol{r}_v$ are the position vectors between two elements at u and v directions respectively, as illustrated in Fig. 1. It should be noted that $\boldsymbol{r}_{u,v}$ and $\boldsymbol{r}_{local}$ may not be orthogonal.

Finally, if the far part of impedance matrix calculated by using $\mathbf{G}_{Array}$ is expressed as $\mathbf{Z}_{Array}$, then its expression is:

$$\begin{aligned}\mathbf{Z}_{Array} &= \sum_{q=x,y,z,D} \boldsymbol{\Lambda}'_q \mathbf{G}_{Array} \boldsymbol{\Lambda}'^{T}_q \\ &= \sum_{q=x,y,z,D} \left[diag(\boldsymbol{\Lambda}_{l,q})\right] \mathbf{G}_{Array} \left[diag(\boldsymbol{\Lambda}_{l,q})\right]^T,\end{aligned} \quad (5)$$

where $\boldsymbol{\Lambda}'_q$ is a block diagonal matrix, in which there are $N_u N_v$ local sparse matrices $\boldsymbol{\Lambda}_l$. $\mathbf{G}_{Array}$ is saved as the form of $\tilde{\mathbf{G}}_{Array} = \mathrm{FFT}(\mathbf{G}_{Array})$, whose length is $N_A = \prod_{p=u,v,x,y,z} (2N_p - 1)$ to meet the circular Toeplitz property. And the submatrices of $\mathbf{G}_{Array}$ for the different elements are asymmetric three-level block-toeplitz matrices although scalar Green's function is applied.

Next, we focus on calculation of self-impedance matrix $\mathbf{Z}_l$ for each element. To eliminate the near correction, the global and local fields should be isolated.

It is well known that the diagonal values of $\mathbf{G}$ are set to zeros to avoid the singularity when the source and field grids are the same. From another point of view, the self-interactions from the same grids are blocked by zeros. Inspired by this point, the blocked region could be enlarged to cover the whole local cube so that the global and local fields are separated thoroughly. This could be implemented by adding a constraint condition to (4) as:

$$s.t. \quad g(\boldsymbol{r}) = 0 \text{ when } \boldsymbol{r}_u = \boldsymbol{r}_v = \mathbf{0}. \quad (6)$$

For example, consider a linear array with only three elements. The array impedance matrix in (5) is rewritten as:

$$\mathbf{Z}_{Array} = \sum_{q=x,y,z,D} \left[diag\left(\boldsymbol{\Lambda}_{l,q}\right)\right] \begin{bmatrix} \mathbf{0} & \mathbf{G}_{12} & \mathbf{G}_{13} \\ \mathbf{G}_{21} & \mathbf{0} & \mathbf{G}_{23} \\ \mathbf{G}_{31} & \mathbf{G}_{32} & \mathbf{0} \end{bmatrix} \left[diag\left(\boldsymbol{\Lambda}_{l,q}\right)\right]^T, \quad (7)$$

where $\mathbf{G}_{mn}$ denotes the transformation matrix between m and n elements. The diagonal submatrices of $\mathbf{G}_{Array}$ are all zeros to isolate global and local regions. In this way, $\mathbf{Z}^{AIM}$ in (2) is not needed and $\mathbf{Z}^{near}$ is filled by MoM for the local region since usually the array element is relatively small. At last, the whole impedance matrix $\mathbf{Z}$ is written as:

$$\mathbf{Z} = \mathbf{Z}_{self} + \mathbf{Z}_{Array} = \left[diag\left(\mathbf{Z}_l\right)\right] + \mathbf{Z}_{Array}, \quad (8)$$

where $\mathbf{Z}_{self}$ is a diagonal matrix and $\mathbf{Z}_l$ is a dense matrix shared by all the elements. As a result, the MVP can be computed by:

$$\begin{aligned}\mathbf{V}' &= \mathbf{Z}_{self}\mathbf{I} + \mathbf{Z}_{Array}\mathbf{I} \\ &= \begin{bmatrix} \mathbf{Z}_l\mathbf{I}_1 \\ \mathbf{Z}_l\mathbf{I}_2 \\ \vdots \\ \mathbf{Z}_l\mathbf{I}_M \end{bmatrix} + \sum_{q=x,y,z,d} \left[diag(\boldsymbol{\Lambda}_{l,q})\right] \mathrm{IFFT}\left(\tilde{\mathbf{G}}_{Array} \circ \mathrm{FFT} \begin{bmatrix} \boldsymbol{\Lambda}^T_{l,q}\mathbf{I}_1 \\ \boldsymbol{\Lambda}^T_{l,q}\mathbf{I}_2 \\ \vdots \\ \boldsymbol{\Lambda}^T_{l,q}\mathbf{I}_M \end{bmatrix} \right),\end{aligned} \quad (9)$$

where $\circ$ denotes Hadamard product operator, $\mathbf{I}_m$ is the current coefficients of the mth element, M is the number of total elements and $\mathbf{V}'$ is the output vector of the MVP. The MVP is speeded up by 5D FFT and IFFT in this paper. From (9) it is obvious that both $\mathbf{Z}_l$ and $\boldsymbol{\Lambda}_l$ are reused by each element. Hence, only one copy of $\mathbf{Z}_l$ and $\boldsymbol{\Lambda}_l$ are required, which could reduce a lot of memory if the number of the array elements is quite huge.

C. Block Jacobi preconditioning

In order to improve the convergence of iteration, block Jacobi (BJ) preconditioner is applied to alleviate the ill-condition of the impedance matrix. This preconditioner is generally more robust because of the diagonal dominance of $\mathbf{Z}_{self}$. Thus, with the help of BJ, the MVP in (9) could be multiplied by $\mathbf{Z}^{-1}_{self}$ as:

$$\begin{aligned}\mathbf{Z}^{-1}_{self}\mathbf{V}' &= \mathbf{Z}^{-1}_{self}\left(\mathbf{Z}_{self}\mathbf{I} + \mathbf{Z}_{Array}\mathbf{I}\right) \\ &= \mathbf{I} + \mathbf{Z}^{-1}_{self}\mathbf{V}_{Array} \\ &= \mathbf{I} + \begin{bmatrix} \mathbf{Z}^{-1}_l\mathbf{V}_{Array,1} \\ \mathbf{Z}^{-1}_l\mathbf{V}_{Array,2} \\ \vdots \\ \mathbf{Z}^{-1}_l\mathbf{V}_{Array,M} \end{bmatrix},\end{aligned} \quad (10)$$

where $\mathbf{V}_{Array} = \mathbf{Z}_{Array}\mathbf{I}$ could be divided into M parts for each element. Since $\mathbf{Z}_l$ in (9) is replaced by $\mathbf{Z}^{-1}_l$ in (10) and $\mathbf{Z}^{-1}_l$ is shared by all elements, the preconditioner doesn't consume extra memory. Moreover, all the multiplications of matrix-vector are moved to the global part without adding extra computations, which is hard to be implemented by other preconditioning technique. Furthermore, $\mathbf{Z}^{-1}_l$ could be precomputed by inversing $\mathbf{Z}_l$ directly if $\mathbf{Z}_l$ is very small. Otherwise, one can also use LU decomposition on $\mathbf{Z}_l$ and solve $\mathbf{Z}_l\mathbf{I}_m = \mathbf{V}_{Array,m}$ by direct method to get $\mathbf{I}_m$, where $m = 1, 2, 3 \ldots M$.

D. Scattering field computation

To save the memory and time of pre-process, we just mesh one local array element as reference since all elements are the same. Thus, the total unknowns N for array is equal to $N_l \times M$, where N_l is the unknowns for the reference element. Actually, it is not necessary to

construct all basis functions for the whole array. $\mathbf{Z}_l$ and $\mathbf{\Lambda}_l$ can be calculated from N_l local basis functions and $\mathbf{G}_{Array}$ is independent of the basis functions. Nevertheless, ignoring the current, the contribution of each element to the scattering field is different due to its different position in the array.

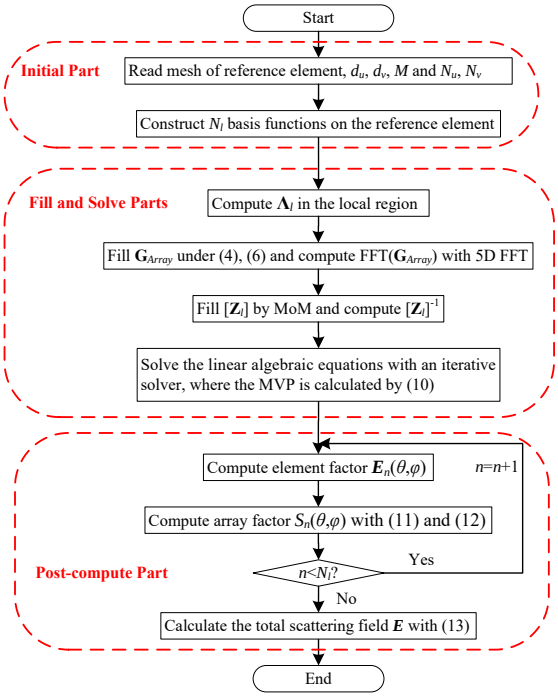

Fig. 2. Flowchart of the array AIM.

This issue could be solved easily with the help of the principle of pattern multiplication. Firstly let $\boldsymbol{E}_n(\theta,\varphi)$ be the scattering electric field of the nth basis functions at the angles of elevation θ and azimuth φ without multiplying the current I_n, where $n \in [1, N_l]$ is an integer. Secondly, the array factor $S_n(\theta,\varphi)$ for the nth basis functions can be evaluated by:

$$S_n(\theta,\varphi) = \sum_{m=1}^{M} I_{n+(m-1)N_l} \exp(-jkd_m), \tag{11}$$

$$d_m = -\left(\Delta N_{u,m} d_u \cos\varphi + \Delta N_{v,m} d_v \sin\varphi\right)\sin\theta, \tag{12}$$

where d_m is the path-difference between the mth element and the reference element. The array factor only includes the current excitations and phase factors of different elements, which is independent of the basis functions. Finally, the total scattering field at (θ,φ) can be expressed as:

$$\boldsymbol{E}(\theta,\varphi) = \sum_{n=1}^{N_l} \boldsymbol{E}_n(\theta,\varphi) S_n(\theta,\varphi), \tag{13}$$

Once the currents are calculated by the proposed method, the scattering field can be evaluated quickly via (11), (12) and (13). To better understand the whole procedure of the proposed method, the flowchart is shown in Fig. 2.

E. Memory requirements and computational complexity

In the proposed method, the memory consumptions are primarily from $\mathbf{Z}_l^{-1}$, $\mathbf{\Lambda}_l$ and $\tilde{\mathbf{G}}_{Array}$. Suppose that each basis function is expanded by K grids and the ratio of idle to local grids along u,v direction are c, thus the memory cost of the proposed method is:

$$\begin{aligned} &16\left(N_l^2 + 2KN_l + N_A\right) \\ &\approx 16\left(N_l^2 + 2KN_l + 32N_u N_v N_x N_y N_z\right) \end{aligned}, \tag{14}$$

where the first and second terms are the memory cost of $\mathbf{Z}_l^{-1}$ and $\mathbf{\Lambda}_l$ respectively. The last term for $\tilde{\mathbf{G}}_{Array}$ is rather larger than the others and 16 means all the matrices are saved in double precision. While the memory cost of AIM is approximated as:

$$16\left(2TMN_l + 2MKN_l + 8(1+c)^2 N_u N_v N_x N_y N_z\right), \tag{15}$$

where T is the average number of the basis functions in the near field. The first term of (15) represents the memory cost by $\mathbf{Z}^{near}$ and the preconditioning matrix, which is much larger than $\mathbf{Z}_l^{-1}$ since $2TM \gg N_l$ for the large-scale array. The second and third terms of (15) denote the memory requirements of $\mathbf{\Lambda}$ and $\tilde{\mathbf{G}}$. Compared with $\mathbf{\Lambda}_l$, $\mathbf{\Lambda}$ is M times larger than $\mathbf{\Lambda}_l$, and the length of $\tilde{\mathbf{G}}$ is determined by the unoccupied ratio c. If c<1, $\tilde{\mathbf{G}}$ is less than $\tilde{\mathbf{G}}_{Array}$, but when c>1 for the array with large spacings, $\tilde{\mathbf{G}}_{Array}$ is less than $\tilde{\mathbf{G}}$ since $\tilde{\mathbf{G}}$ is increased by $(1+c)^2$ times.

On the other hand, the computational complexity of $\mathbf{Z}_l$ and $\mathbf{Z}^{near}$ are $O(N_l^2)$ and $O(TMN_l)$ respectively. This suggests that the speed of filling $\mathbf{Z}_l$ is much faster than filling $\mathbf{Z}^{near}$. The constructing time of preconditioner could also be further reduced. Moreover, it is easy to infer the time cost for calculating $\mathbf{\Lambda}_l$ is M times less than calculating $\mathbf{\Lambda}$. The filling time of $\tilde{\mathbf{G}}_{Array}$ and $\tilde{\mathbf{G}}$ are quite short. Similarly, the improvement on the speed of MVP is determined by c because the computational complexity of $\tilde{\mathbf{G}}_{Array}$ and $\tilde{\mathbf{G}}$ are $O(N_A \log(N_A))$ and $O(N_C \log(N_C))$ respectively, where $N_C = (1+c)^2 N_A/4$.

Therefore, for a given element, the filling time and

memory requirements of $\mathbf{Z}_l^{-1}$ and $\mathbf{\Lambda}_l$ in the proposed method are independent of the size and interval of the array, which are much less than AIM. Significant improvements on memory cost of $\tilde{\mathbf{G}}_{Array}$ and the speed of the MVP would be obtained if c is larger than 1.

III. NUMERICAL RESULTS

To demonstrate the performance of the proposed method, the scattering of 2D arrays are considered. The arrays are supposed to be located at *xoy* plane. A –*x*-polarized plane wave propagation along –*z* direction impinges the array with frequency 0.3GHz. AIM parameters are: the grid interval is 0.05λ, the grid order is 2 and the near threshold is 0.3λ. The iterative solver is the stabilized biconjugate gradient (Bi-CGSTAB) with the relative residual error less than 10^{-4}. All the numerical experiments are performed on the desktop PC of four cores 4790 Intel processors with math kernel library to calculate FFT and IFFT.

A. The accuracy of the proposed method

The first example is a 9×9 conducting cylinder array with the array length $l_{u,v}$=6.5m and the interval $d_{u,v}$=0.7m. The geometry parameters of PEC cylinder are the height h=0.8m and diameter D=0.2m as shown in left side of Fig. 3. Each cylinder is discretized by 334 triangle patches, leading to 501 basis functions, and correspondingly 40581 unknowns for the whole array. The bistatic radar cross section (RCS) are plotted in Fig. 4. Clearly, the results of the proposed method agree well with that of AIM and MLFMA (FEKO). Figure 5 gives the relative error of this example, which is defined as:

$$error = 10\log_{10}\left(\left|\sigma_{proposed} - \sigma_{MLFMA}\right| / \left|\sigma_{MLFMA}\right|\right), \quad (16)$$

where $\sigma_{proposed}$ and σ_{MLFMA} represent the RCS pattern computed by the proposed method and MLFMA respectively. The average relative errors are about -15dB. On some angles, the relative errors exceed -10dB due to the round-off error.

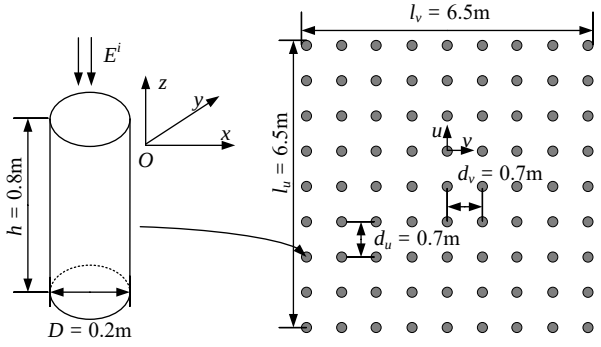

Fig. 3. Geometry and dimension of the 9×9 PEC cylinder periodic array.

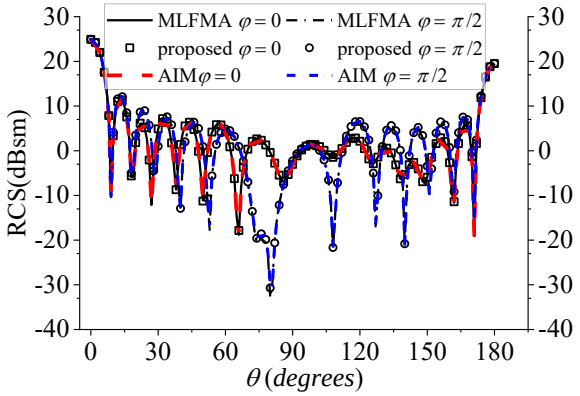

Fig. 4. Bistatic RCS pattern of the 9×9 cylinder array in the vertical plane.

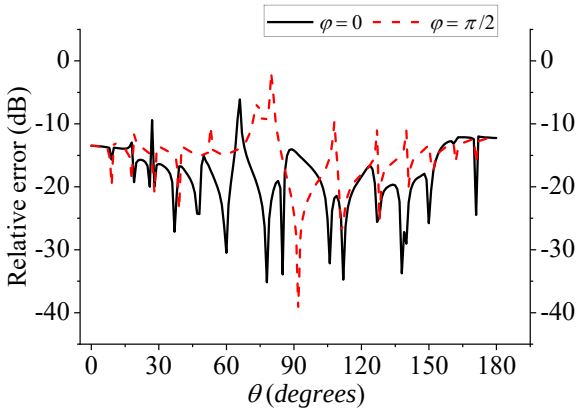

Fig. 5. The relative error of the 9×9 cylinder array in the vertical plane. (MLFMA as reference).

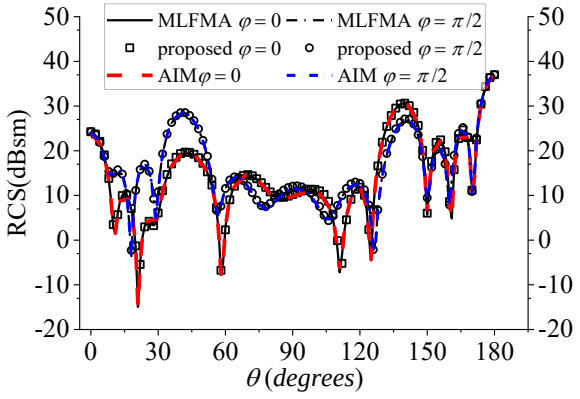

Fig. 6. Bistatic RCS pattern of the 4×4 sphere array in the vertical plane.

The second example is a 4×4 conducting sphere array. The array has length l=5.7m, the interval $d_{u,v}$ =1.5m and the PEC sphere radius r=0.6m. Incident wave is the

same as last example. The geometry of this example is omitted for the similarity with the first one. The unknowns of the sphere and the whole array are 1287 and 20592 respectively. Figure 6 demonstrates that the bistatic RCS of proposed method agrees well with that of AIM and MLFMA.

B. The performance of the proposed method for different unoccupied ratio *c*

To investigate the influence of the unoccupied ratio c, the interval $d_{u,v}$ of the 9×9 cylinder array above are chosen as 0.5m, 0.6m, 0.8m, 1.2m and 2m, which are corresponding to c=0.42, 0.71, 1.28, 2.42 and 4.7 respectively. The number of the local grids for the element is N_x=N_y=7, N_z=19 and the rest parameters of the array are the same as Fig. 3.

Table 1 summarizes the performance of the proposed method and AIM in different intervals. We can see from Table 1 that the filling time and memory requirements of the proposed method are independent of c. While in AIM the memory requirement of **G** and the per iteration time increase dramatically with the increasing of c. It can be observed that the proposed method could achieve more than 99.6% reduction in filling time.

In addition, in terms of the memory and per iteration time, AIM performs a better performance for c<1. But when c>1, the proposed method are more efficient than AIM, especially for d=2m, about 10 times improvements are achieved.

Table 1: CPU time and memory requirements of the proposed and conventional AIM for the 9×9 cylinder array in different intervals

Interval d(m)	Unoccupied Ratio c	Memory (MB)		Filling Time(s)		Each Iteration Time(s)	
		$\mathbf{G}_{Array}$	**G**	**Proposed**	**AIM**	**Proposed**	**AIM**
0.5	0.42	27.57	16.25	0.465	74.53	0.544	0.47986
0.6	0.71	27.57	22.86	0.417	73.356	0.544	0.53645
0.8	1.28	27.57	39.45	0.461	75.217	0.566	1.05973
1.2	2.42	27.57	86.14	0.435	78.098	0.586	1.33586
2	4.7	27.57	233.51	0.464	78.696	0.586	7.848

Table 2: CPU time and memory requirements of the proposed and conventional AIM for the cylinder array in different sizes

Array size	Unknowns	Total Memory (MB)		Filling Time(s)		Total Time(s)	
		Proposed	**AIM**	**Proposed**	**AIM**	**Proposed**	**AIM**
9×9	40581	31.81	761.95	0.465	81.20	10.614	98.16
16×16	128256	95.93	2468.38	0.465	523.53	57.582	596.61
27×27	365229	272.25	8397.46	0.465	1652.4	271.09	2000.85
40×40	801600	599.71	20663.87	0.465	12404.23	3448.8	17186.4

C. The performance of the proposed method for the different array sizes

In this part, the array AIM and conventional AIM are applied to solve the scattering problem of the cylinder array with different sizes. The sizes of the array are selected as 9×9, 16×16, 27×27 and 40×40, the rest parameters of the array are the same as Fig. 3. The unknowns of the four arrays are 40581, 128256, 365229 and 801600, respectively. RCS patterns of these arrays are omitted for redundancies.

Table 2 lists the CPU time and memory requirements of the proposed method and AIM for the four cases. It can be observed from Table 2 that the proposed method could reduce more than 96% total memory requirements in comparison with the conventional AIM. The reason of the memory reduction is that the local impedance matrix and the BJ preconditioner only consume a little memory.

Furthermore, the filling time of AIM rises dramatically as the array size increases, while the proposed method holds. Thus for the largest array size 40×40, the filling speed of the proposed method is about 26000 times faster than AIM. As a result, the total solution time of the proposed method is greatly less than that of AIM. It should be pointed that the solving time of the two methods are nearly the same since interval d=0.7m means c=1 for all the cases.

Therefore, for the large-scale array with large spacings, the array AIM is much more efficient than the conventional AIM both on computational complexity and memory requirements.

IV. CONCLUSION

In this paper, a modified AIM has been proposed for the fast analysis of the electromagnetic scattering problem of the large-scale finite array. The whole array

is divided into array and local parts. In array part, a 5-level block-toeplitz $\mathbf{G}_{Array}$ is constructed to calculate the interactions between different elements, because $\mathbf{G}_{Array}$ could reduce memory requirement by eliminating the idle grids. In local part, the local translation matrix $\mathbf{\Lambda}_l$ and self-impedance matrix $\mathbf{Z}_l$ are shared by all elements to reduce the computational source. Through filling zeros into the diagonal submatrices of $\mathbf{G}_{Array}$, the local and array parts are isolated to eliminate the near correction. The numerical simulations have demonstrated that, without losing accuracy, the proposed method combined with block Jacobi preconditioning could not only accelerate the speed of filling matrix and iteration tremendously but also reduce the whole memory requirements dramatically, especially for the large-scale array with large spacings.

Furthermore, the proposed method is suitable for both periodic or non-periodic array. To form a non-periodic array, some periodic elements would be masked by adjusting translation matrix $\mathbf{\Lambda}'_q$ of (5). This work will be studied in the future.

REFERENCES

[1] L. Liu and Z. Nie, "An efficient numerical model for the radiation analysis of microstrip patch antennas," *ACES Journal*, vol. 34, no. 10, p. 6, 2019.

[2] R. F. Harrington, *Field Computation by Moment Methods*. New York, 1993.

[3] J. Song, C.-C. Lu, and W. C. Chew, "Multilevel fast multipole algorithm for electromagnetic scattering by large complex objects," *IEEE Trans. Antennas Propagat.*, vol. 45, no. 10, pp. 1488-1493, 1997.

[4] B. J. Fasenfest, F. Capolino, D. R. Wilton, D. R. Jackson, and N. J. Champagne, "A fast MoM solution for large arrays: Green's function interpolation with FFT," *IEEE Antennas Wireless Propag. Lett.*, vol. 3, no. 1, pp. 161-164, Dec. 2004.

[5] S. M. Seo and J.-F. Lee, "A fast IE-FFT algorithm for solving PEC scattering problems," *IEEE Trans. Magn.*, vol. 41, no. 5, pp. 1476-1479, 2005.

[6] E. Bleszynski, M. Bleszynski, and T. Jaroszewicz, "AIM: Adaptive integral method for solving large-scale electromagnetic scattering and radiation problems," *Radio Sci.*, vol. 31, no. 5, pp. 1225-1251, Sep. 1996.

[7] S. M. Seo, "A fast IE-FFT algorithm to analyze electrically large planar microstrip antenna arrays," *IEEE Antennas Wireless Propag. Lett.*, vol. 17, no. 6, pp. 983-987, June 2018.

[8] B. J. Rautio, V. I. Okhmatovski, A. C. Cangellaris, J. C. Rautio, and J. K. Lee, "The unified-FFT algorithm for fast electromagnetic analysis of planar integrated circuits printed on layered media inside a rectangular enclosure," *IEEE Trans. Microw. Theory Tech.*, vol. 62, no. 5, pp. 1112-1121, May 2014.

[9] X. Wang, D. H. Werner, and J. P. Turpin, "Application of AIM and MBPE techniques to accelerate modeling of 3-D doubly periodic structures with nonorthogonal lattices composed of bianisotropic media," *IEEE Trans. Antennas Propagat.*, vol. 62, no. 8, pp. 4067-4080, Aug. 2014.

[10] P. De Vita, A. Freni, F. Vipiana, P. Pirinoli, and G. Vecchi, "Fast analysis of large finite arrays with a combined multiresolution-SM/AIM approach," *IEEE Trans. Antennas Propagat.*, vol. 54, no. 12, pp. 3827-3832, Dec. 2006.

[11] P. D. Vita, F. D. Vita, A. D. Maria, and A. Freni, "An efficient technique for the analysis of large multilayered printed arrays," *IEEE Antennas Wireless Propag. Lett.*, vol. 8, pp. 104-107, 2009.

[12] A. Freni, P. D. Vita, P. Pirinoli, L. Matekovits, and G. Vecchi, "Fast-factorization acceleration of MoM domain-decomposition: SFX-AIM and general," in *2012 6th European Conference on Antennas and Propagation (EUCAP)*, pp. 276-277, 2012.

[13] X. Wang, D. H. Werner, and J. P. Turpin, "Investigation of scattering properties of large-scale aperiodic tilings using a combination of the characteristic basis function and adaptive integral methods," *IEEE Trans. Antennas Propagat.*, vol. 61, no. 6, pp. 3149-3160, June 2013.

[14] C. C. Ioannidi and H. T. Anastassiu, "Circulant adaptive integral method (CAIM) for electromagnetic scattering from large targets of arbitrary shape," *IEEE Trans. Magn.*, vol. 45, no. 3, pp. 1308-1311, Mar. 2009.

[15] X. Wang, S. Zhang, Z.-L. Liu, and C.-F. Wang, "A SAIM-FAFFA method for efficient computation of electromagnetic scattering problems," *IEEE Trans. Antennas Propagat.*, vol. 64, no. 12, pp. 5507-5512, Dec. 2016.

[16] W.-B. Ewe, L.-W. Li, Q. Wu, and M.-S. Leong, "Preconditioners for adaptive integral method implementation," *IEEE Trans. Antennas Propagat.*, vol. 53, no. 7, pp. 2346-2350, July 2005.

[17] M. Zhang, T. S. Yeo, and L. W. Li, "Thresholdbased incomplete LU factorization preconditioner for adaptive integral method," *Proc of 2007 Asia Pacific Microwave Conference*, Bangkok, Thailand, pp. 913-916, Dec. 11-14, 2007.

[18] J. Q. Chen, Z. W. Liu, K. Xu, D. Z. Ding, Z. H. Fan, and R. S. Chen, "Shifted SSOR preconditioning technique for electromagnetic wave scattering problems," *Microw. Opt. Tech. Lett.*, vol. 51, no. 4, pp. 1035-1039, 2009.

[19] M. Li, M. Chen, W. Zhuang, Z. Fan, and R. Chen, "Parallel SAI preconditioned sdaptive integral

method for analysis of large planar microstrip antennas," *ACES Journal*, vol. 25, no. 11, p. 10, 2010.

[20] B. E. Barrowes, F. L. Teixeira, and J. A. Kong, "Fast algorithm for matrix–vector multiply of asymmetric multilevel block-Toeplitz matrices in 3-D scattering," *Microw. Opt. Technol. Lett.*, vol. 31, no. 1, pp. 28-32, 2001.

Improving the Efficiency of Hybrid Boundary Element Method for Electrostatic Problems Solving

Mirjana T. Perić, Saša S. Ilić, Ana N. Vučković, and Nebojša B. Raičević

Department of Theoretical Electrical Engineering
University of Niš, Faculty of Electronic Engineering, 18000 Niš, Serbia
{mirjana.peric, sasa.ilic, ana.vuckovic, nebojsa.raicevic}@elfak.ni.ac.rs

Abstract ― This paper describes a modification of the Hybrid Boundary Element Method (HBEM) for electrostatic problems solving. Such improved method is applied for transmission lines analyses. By taking a quasi-static TEM approach, the Hybrid Boundary Element Method is applied to determine the effective relative permittivity and the characteristic impedance of different stripline structures. Comparisons with already published numerical results and software simulation have been also performed with an aim to test the validity of the proposed approach. A close results match can be noticed. The main novelties of the proposed HBEM modification are better accuracy and ability to determine the polarization charges distribution on the separating surface between a strip and a dielectric layer. This was not possible before, using the previous version of the method.

Index Terms ― Characteristic impedance, effective relative permittivity, finite element methods, hybrid boundary element method, stripline.

I. INTRODUCTION

The Hybrid Boundary Element Method (HBEM) is a semi-numerical method, [1]. This method presents a combination of several other methods: the boundary element method (BEM) [2, 3], the equivalent electrodes method (EEM) [4] and the point-matching method (PMM) for the potential of the perfect electric conductor electrodes and for the normal component of the electric field at the boundary surface between any two dielectric layers.

Different electromagnetic problems have been solved using this method up to now. The electromagnetic field distribution in the vicinity of cable joints and terminations is determined in [5], the calculation of permanent magnets magnetic force is performed in [6] and characteristic parameters of transmission lines have been calculated in [7-9]. Also, in [10] a two-wire line with a magnetic material in its vicinity is analysed and the line inductance is calculated. The grounding systems are analysed in [11] using the HBEM.

The main idea of this method is that each conductor surface and the boundary surfaces between any two dielectric layers should be divided into a large number of segments as in the EEM's application, [1]. Each of these segments is replaced by the equivalent electrodes (EEs), placed at the segment's centres. In the case of single layer problems, the HBEM application is identical to the EEM. But, for the multilayered systems, the HBEM application comes to the fore. At the boundary surfaces between any two dielectric layers only polarization (bound) charges exist, [12]. According to the HBEM, the segments at these surfaces are replaced by discrete equivalent polarization charges placed in the air. The boundary surfaces between the perfect electric conductor and the dielectric layers consist of total charges, i.e., free and polarization charges. In the previous HBEM application, an approximation was done – only the free charges on those boundary surfaces, placed in the corresponding dielectric layer, were considered, [7-9]. Such approximation gave satisfactory results for majority of solved problems. The results verification shows that the error rate is less than 1%, [6-10]. Using this approximation, it is not possible to determine the polarization charges distribution at the conductor-dielectric layer separating surfaces, but only at the separating surfaces of two dielectric layers, [7-9]. This paper attempts to address this issue and improve existing method.

The advantages of the improved HBEM are illustrated by numerical results. The computation time is shown, as well as the results convergence. The characteristic impedance and effective relative permittivity of single and coupled striplines are analysed. The computed results will be verified with the corresponding results obtained by the finite element method (FEM), [13] and data available in the literature.

II. HBEM MODIFICATION AND APPLICATION

The geometry of a system which consists of conductors and arbitrary number of dielectric layers is depicted in Fig. 1.

Submitted On: January 27, 2020
Accepted On: May 25, 2020
https://doi.org/10.47037/2020.ACES.J.350804

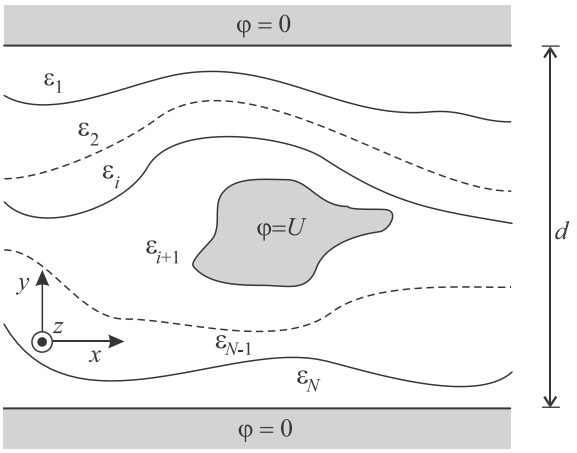

Fig. 1. Geometry of the problem.

The shapes of the conductor and layers are also arbitrary. The infinite parallel planes are on the zero potential and the conductor is on the potential U.

A similar system was already presented in [9] as well as corresponding HBEM model. Having the goal to improve the existing HBEM model in mind, as it is mentioned in the previous section, the total charges on the separating surface between the dielectric layer and conductor are taken into account now. They consist of free and polarized charges placed in the air. Only the polarized charges, placed also in the air, exist on the separating surfaces between dielectric layers.

That leads to the modification of the HBEM model, so the improved version is shown in Fig. 2.

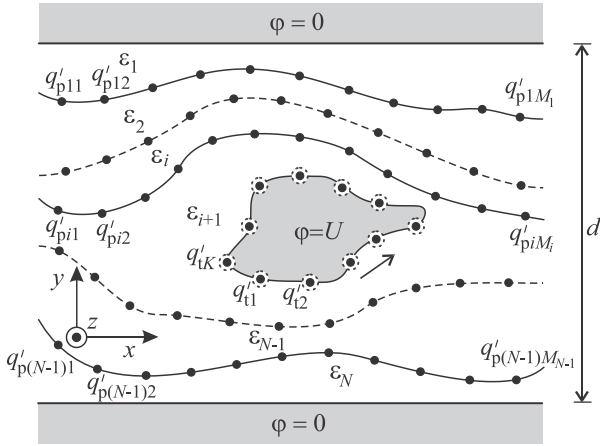

Fig. 2. Modified HBEM model.

In order to determine the potential at any point in the $x0y$ plane, it is necessary to use the Green's function for the line charge placed in dielectric of permittivity ε, between two infinite parallel grounded planes, at distance h from the bottom plane, given in [14]. The function is:

$$G(x,y)=\frac{1}{2\pi\varepsilon}\ln\sqrt{\frac{\cosh\left[\frac{\pi}{d}x\right]-\cos\left[\frac{\pi}{d}(y+h)\right]}{\cosh\left[\frac{\pi}{d}x\right]-\cos\left[\frac{\pi}{d}(y-h)\right]}}, \quad (1)$$

where d is a distance between two infinite parallel grounded planes. Therefore, it is possible to form an expression for the potential at any point of the system given in Fig. 2:

$$\varphi=\sum_{k=1}^{K}\frac{q'_{\mathrm{t}k}}{2\pi\varepsilon_0}\ln\sqrt{\frac{\cosh\left[\frac{\pi}{d}(x-x_{\mathrm{t}k})\right]-\cos\left[\frac{\pi}{d}(y+y_{\mathrm{t}k})\right]}{\cosh\left[\frac{\pi}{d}(x-x_{\mathrm{t}k})\right]-\cos\left[\frac{\pi}{d}(y-y_{\mathrm{t}k})\right]}}+$$

$$+\sum_{i=1}^{N-1}\sum_{m=1}^{M_i}\frac{q'_{\mathrm{p}im}}{2\pi\varepsilon_0}\ln\sqrt{\frac{\cosh\left[\frac{\pi}{d}(x-x_{\mathrm{p}im})\right]-\cos\left[\frac{\pi}{d}(y+y_{\mathrm{p}im})\right]}{\cosh\left[\frac{\pi}{d}(x-x_{\mathrm{p}im})\right]-\cos\left[\frac{\pi}{d}(y-y_{\mathrm{p}im})\right]}}, \quad N\geq 2. \quad (2)$$

With $q'_{\mathrm{t}k}=q'_{\mathrm{f}k}+q'_{\mathrm{p}k}$ $(k=1,...,K)$ the total EEs charges, which consist of free (f) and polarized (p) line charges, placed at the conductor surface, are denoted. These charges are at the same positions $(x_{tk},y_{\mathrm{t}k})$. The polarized line charges, placed at the boundary surfaces between any two dielectric layers, are denoted with $q'_{\mathrm{p}im}$ $(m=1,...,M_i,\ i=1,...,N-1)$.

The total number of unknowns is:

$$N_{\mathrm{tot}}=2K+\sum_{i=1}^{N-1}M_i\ . \quad (3)$$

At the boundary surfaces, between two dielectrics, the boundary condition, should be satisfied, [12]:

$$\hat{\boldsymbol{n}}_{im}\cdot\boldsymbol{E}_{im}^{(0+)}=\frac{-\varepsilon_{i+1}}{\varepsilon_0(\varepsilon_i-\varepsilon_{i+1})}\eta_{\mathrm{p}im}, \quad (4)$$

while between the conductor and $(i+1)$-th dielectric, the boundary condition has a form:

$$\hat{\boldsymbol{n}}_k\cdot\boldsymbol{E}_{(i+1)k}^{(0+)}=\frac{-\varepsilon_0}{\varepsilon_0(\varepsilon_{i+1}-\varepsilon_0)}\eta_{\mathrm{p}k}\ . \quad (5)$$

$\boldsymbol{E}=-\mathrm{grad}(\varphi)$ represents the electric field strength; $\eta_{\mathrm{p}im}=q'_{\mathrm{p}im}/\Delta l_{im}$ and $\eta_{\mathrm{p}k}=q'_{\mathrm{p}k}/\Delta l_k$ are the surface charges on the segments of the lengths Δl_{im} and Δl_k, respectively, ($m=1,...,M_i$, $i=1,...,N-1$, $k=1,...,K$); $\hat{\boldsymbol{n}}_{im}$ and $\hat{\boldsymbol{n}}_k$ are the unit normal vectors oriented from the layer ε_{i+1} towards the layer ε_i and from the conductor towards the layer ε_{i+1}, respectively.

In order to calculate the characteristic impedance and effective relative permittivity, the following procedure, described in detail in [9], should be applied:

a) Form the HBEM model (EE's positioning);
b) Form the system of linear equations matching

the potential of the conductor using (2) and boundary condition at the separating surfaces using (4) and (5);

c) Solve the formed system of linear equation;

d) Calculate the characteristic parameters.

III. NUMERICAL ANALYSIS

To validate and demonstrate the accuracy and efficiency of the proposed, improved version of HBEM, two types of striplines will be illustrated in this section. The analysis refers to the striplines, where the substrates are of infinite width, made of isotropic material. The parallel planes are also infinite with zero potential. These geometries are shown in Figs. 3 and 4.

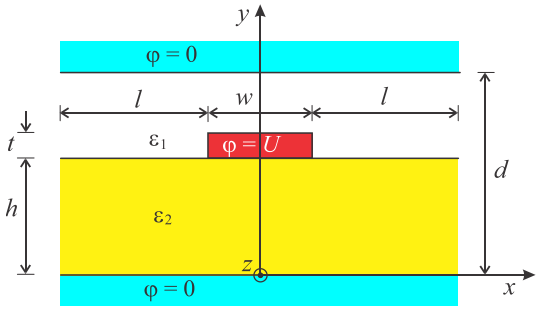

Fig. 3. Stripline.

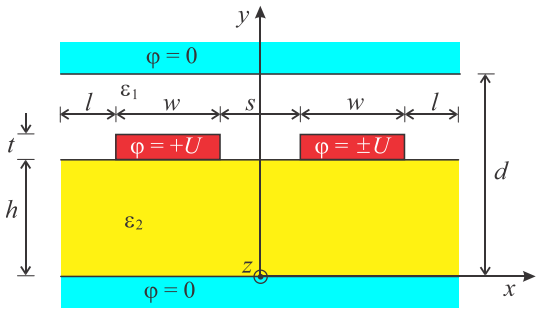

Fig. 4. Coupled stripline.

Therefore, the HBEM will be applied, unknown charges determined and the characteristic parameters calculated. Afterwards, we will compare the results with those obtained using the FEMM software, [13]. All calculations are performed on a 4 Core CPU (Intel i5) running at 3.1 GHz and 4GB RAM in double precision.

A. Results convergence and computation time

The influence of number of unknowns, N_{tot}, to the characteristic impedance results and computation time, is given in Fig. 5 for the problem from the Fig. 3. Increasing the number of EEs, a fast results convergence is obtained in a short period of time. For over 1000 unknowns the characteristic impedance value is almost constant.

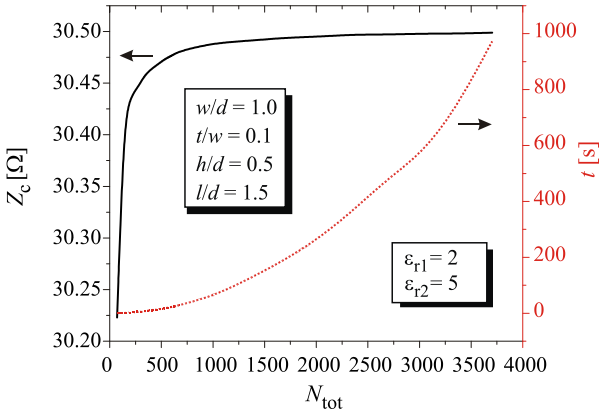

Fig. 5. Convergence of results and computation time.

In regards the computation time, (denoted with the red dotted line), it is visible that the time, necessary to place equivalent electrodes, then to form and solve the system of equations and to calculate characteristic impedance, significantly increases with the number of unknowns. For 1000 unknowns the computation time is less than 100 seconds. In all following calculations the number of unknowns will be 1500, so the computation time is about two minutes.

B. Influence of substrate width on characteristic impedance and effective relative permittivity

Considering that the substrates from the Fig. 3 and 4 are of the infinite width, it was necessary to analyse the influence of substrate width on characteristic impedance and effective relative permittivity values. What is the minimum substrate width above which the characteristic parameters do not change?

This analysis is performed for: $w/d = 1.0$, $h/d = 0.5$, $t/w = 0.1$, $\varepsilon_{r1} = 2$, $\varepsilon_{r2} = 5$ (for the stripline from Fig. 3) and $w/d = 1.0$, $h/d = 0.5$, $s/d = 0.5$, $t/w = 0.1$, $\varepsilon_{r1} = 2$, $\varepsilon_{r2} = 5$ (for both modes of the coupled stripline from Fig. 4), and shown in Figs. 6 and 7.

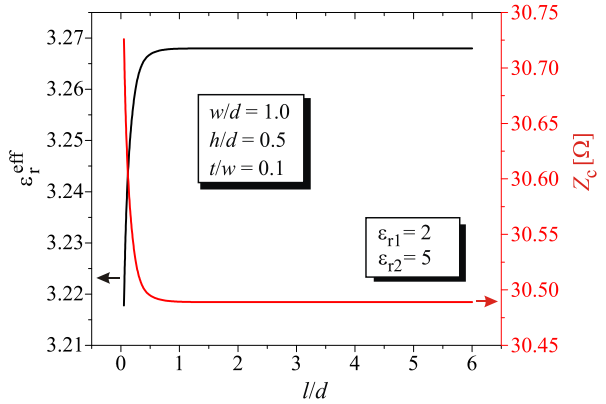

Fig. 6. Influence of parameter l/d on characteristic impedance and effective relative permittivity of stripline.

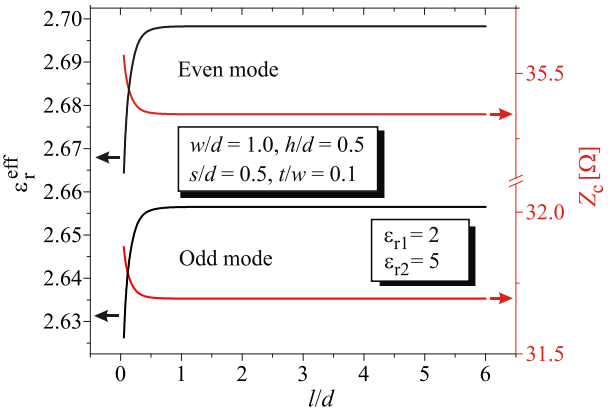

Fig. 7. Influence of parameter l/d on characteristic impedance and effective relative permittivity of coupled stripline.

As it can be noticed, for $l/d > 1.0$ the values for both characteristic parameters are constant. These led us to conclude that, in all following calculations, the value $l/d = 1.5$ can be used.

IV. RESULTS AND DISCUSSION

The analysed problems from Figs. 3 and 4 are on the left and right sides unbounded, i.e., "open". That means that electromagnetic fields should extend towards infinity. In order to simulate considered striplines with the finite element method solver such as FEMM [13] it was necessary to close the simulation domain "far enough". In that way, the influence of the terminating boundary conditions at the far end becomes negligible. This is the common and easiest used approach as it is mentioned in [15] and [16].

FEMM simulation will be done with about 400.000 finite elements. So, the verification of the results can be made.

In Tables 1 and 2 the effective relative permittivity and characteristic impedance versus the strip thickness, calculated using HBEM as well as using FEMM simulation, are given for the stripline from Fig. 3. The dimensions of the analysed stripline are: $w/d = 1.0$, $h/d = 0.5$, $l/d = 1.5$, $\varepsilon_{r1} = 2$ and $\varepsilon_{r2} = 5$.

In those tables, the values obtained using the "old" version of HBEM (oHBEM) are also presented.

Table 1: Effective relative permittivity distribution versus parameter t/w

t/w	HBEM	oHBEM	FEMM
0.1	3.2680	3.1737	3.2777
0.05	3.3692	3.2867	3.3801
0.02	3.4314	3.3714	3.4466
0.01	3.4555	3.4080	3.4716

Table 2: Characteristic impedance distribution versus parameter t/w

t/w	HBEM	oHBEM	FEMM
0.1	30.489	30.955	30.437
0.05	32.549	32.969	32.481
0.02	33.907	34.219	33.809
0.01	34.405	34.653	34.291

It is visible that the results of the new and improved HBEM are close to the FEMM results. Also, it can be concluded that, when the strip thickness decreases, the analysed characteristic parameters increase.

Figure 8 presents a distribution of characteristic impedance versus parameter w/h, incorporating the effect of strip thickness. The stripline is without dielectric, placed in the centre of the system at equal distance from the parallel planes. In this figure the results from [17] are also shown. They are obtained using formulas given in [17] and [18] and the good results match is obtained. Also, it is evident that increasing the strip width, characteristic impedance decreases.

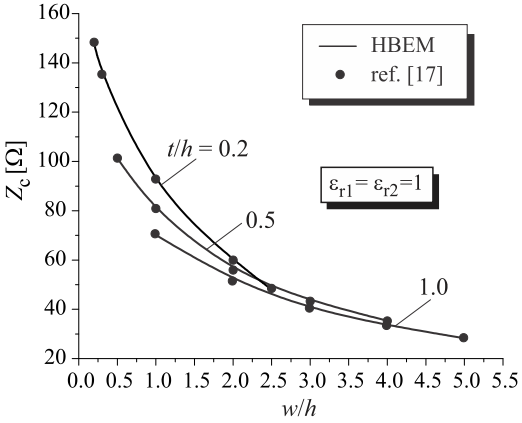

Fig. 8. Characteristic impedance of a stripline without dielectric.

The main advantage of the improved version of HBEM, besides the better accuracy, is a possibility to determine the polarized charges distribution on the separating conductor-dielectric surfaces. The attempt to apply this modified approach and show the normalized distribution is visible in Fig. 9 for stripline from Fig. 3, for parameters: $w/d = 1.0$, $h/d = 0.5$, $l/d = 1.5$, $\varepsilon_{r1} = 2$ and $\varepsilon_{r2} = 5$. Considering that the strip is on the positive potential, those charges are negative.

The normalized polarized charges distribution if one of the layers is the air, $\varepsilon_{r1} = 1$, is presented in Fig. 10 for stripline from Fig. 3. Also in Figs. 11 and 12 the analyse was done for both modes of coupled stripline from Fig. 4 for parameters: $w/d = 1.0$ $h/d = 0.5$, $s/d = 0.5$,

$l/d = 1.5$, $t/w = 0.1$, $\varepsilon_{r1} = 1$, $\varepsilon_{r2} = 5$.

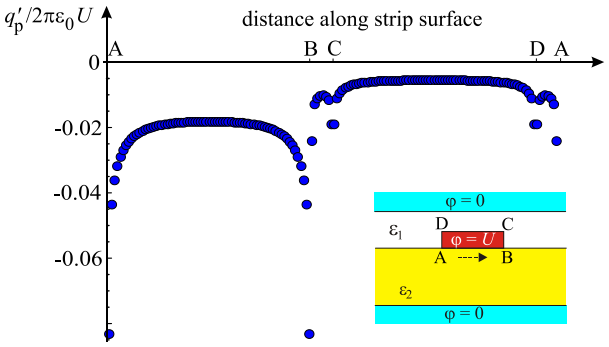

Fig. 9. Polarized charges distribution along strip surface.

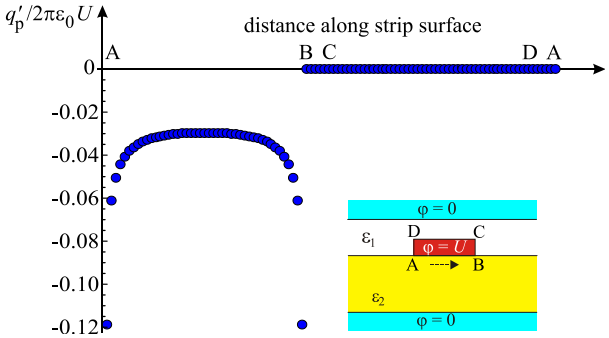

Fig. 10. Polarized charges distribution along strip surface of stripline for $\varepsilon_{r1} = 1$.

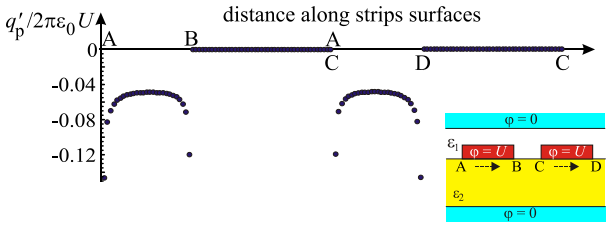

Fig. 11. Polarized charges distribution along strips surfaces of coupled stripline for $\varepsilon_{r1} = 1$ (even mode).

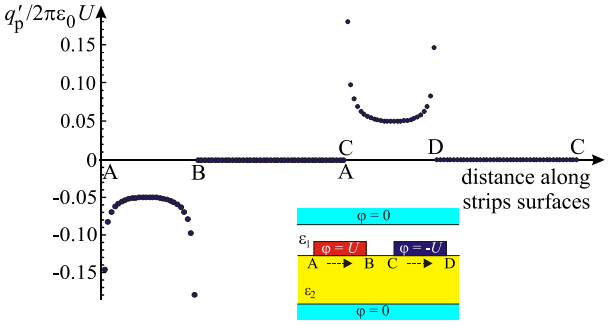

Fig. 12. Polarized charges distribution along strips surfaces of coupled stripline for $\varepsilon_{r1} = 1$ (odd mode).

As expected, the polarized charges do not exist on the air-strip boundary surfaces. Also, from those figures can be confirmed that the polarized charges are negative when the strips are on the positive potential and vice versa.

V. CONCLUSION

In this paper, an improved version of HBEM is applied to quasi-static analysis of different stripline structures. The presented numerical results demonstrate the accuracy and efficiency of the method. Applying the HBEM, the system matrix has the greatest elements on the main diagonal. This leads to a better conditioned system of linear equations and computation time is shorter. The method can be used to determine the polarized charges distribution on the separating surfaces of any two layers as well as conductor-dielectric separating surfaces. Also, using presented methodology, the strips of infinitely thin metallization thickness can be also modelled and analysed.

ACKNOWLEDGMENT

This work has been supported by the Ministry of Education, Science and Technological Development of the Republic of Serbia.

REFERENCES

[1] N. B. Raičević, S. R. Aleksić, and S. S. Ilić, "A hybrid boundary element method for multi-layer electrostatic and magnetostatic problems," *Journal of Electromagnetics*, no. 30, pp. 507-524, 2010.

[2] C. A. Brebbi, J. C. F. Telles, and L. C. Wrobel, *Boundary Element Techniques. Theory and Applications in Engineering*, Berlin: Springer, 1984.

[3] D. Li and L. Di. Rizenzo, "Boundary element computation of line parameters of on-chip interconnects on lossy silicon substrate," *ACES Journal*, vol. 26, no. 9, pp. 716-722, 2011.

[4] D. M. Veličković, "Equivalent electrodes method," *Scientific Review*, no. 21-22, pp. 207-248, 1996.

[5] N. B. Raičević, S. S. Ilić, and S. R. Aleksić, "Application of new hybrid boundary element method on the cable terminations," *14th International IGTE Symposium*, Graz, Austria, pp. 56-61, 2010.

[6] A. Vučković, N. Raičević, and M. Perić, "Radially magnetized ring permanent magnet modelling in the vicinity of soft magnetic cylinder," *Safety Engineering*, vol. 8, no. 1, pp. 33-37, 2018.

[7] S. Ilić, M. Perić, S. Aleksić, and N. Raičević, "Hybrid boundary element method and quasi TEM analysis of 2D transmission lines – generalization," *Electromagnetics*, vol. 33, no. 4, pp. 292-310, 2013.

[8] M. Perić, S. Ilić, S. Aleksić, and N. Raičević, "Application of hybrid boundary element method to 2D microstrip lines analysis," *International*

Journal of Applied Electromagnetics and Mechanics, vol. 42, no. 2, pp. 179-190, 2013.

[9] M. Perić, S. Ilić, S. Aleksić, and N. Raičević, "Characteristic parameters determination of different striplines configurations using HBEM," *ACES Journal*, vol. 28, no. 9, pp. 858-865, 2013.

[10] S. Ilić, D. Jovanović, A. Vučković, and M. Perić, "External inductance per unit length calculation of two wire line in vicinity of linear magnetic material," *14th International Conference on Applied Electromagnetics – IIEC 2019*, Niš, Serbia, CD proceeding, Aug. 26-28, 2019.

[11] S. S. Ilić, N. B. Raičević, and S. R. Aleksić, "Application of new hybrid boundary element method on grounding systems," *14th International IGTE Symposium*, Graz, Austria, pp. 160-165, 2010.

[12] E. Rothwell, M. Cloud, *Electromagnetics*, Chapter 2, CRC Press, 2001.

[13] D. Meeker, FEMM, ver. 4.2, available at: http://www.femm.info/wiki/Download.

[14] S. S. Ilić, S. R. Aleksić, and N. B. Raičević, "TEM analysis of vertical broadside symmetrically coupled strip lines with anisotropic Substrate," *International Journal of Applied Electromagnetics and Mechanics*, IOS Press, vol. 37, no. 2-3, pp. 207-214, 2011.

[15] S. M. Musa and M. N. O. Sadiku, "Quasi-TEM analysis of multiconductor transmission lines embedded in layered dielectric region," *CD Proc. of COMSOL Conference*, Boston, USA, 2009.

[16] Q. Chen, A. Konrad, and P. Biringer, "Computation of static and quasistatic electromagnetic fields using asymptotic boundary conditions," *ACES Journal*, vol. 9, no. 2, pp. 37-42, 1994.

[17] H. A. Wheeler, "Transmission-line properties of a strip line between the parallel plates," *IEEE Trans. Microwave Theory Tech.*, vol. 26, no. 11, pp. 866-876, 1978.

[18] H. A. Wheeler, "Transmission-line properties of a strip on a dielectric sheet on a plane," *IEEE Trans. Microwave Theory Tech.*, vol. 25, no. 8, pp. 631-647, 1977.

Mirjana Perić received the Dipl.–Ing., M.Sc. and Ph.D. degrees from the Faculty of Electronic Engineering (FEE) of Niš, Serbia. In 2001 she joined the Department of Theoretical Electrical Engineering at the FEE. She is currently the assistant professor at the same faculty. Her researching interests are: electromagnetic field theory, analytical and numerical methods for electromagnetic field calculations, electromagnetic compatibility and transmission line analysis.

She is a member of the ACES, IEEE MTT and IEEE EMC societies.

Saša S. Ilić received Dipl.–Ing. degree in Electronics and Telecommunications in 1995 from the Faculty of Electronic Engineering (FEE) of Niš, Serbia. At the same faculty he received M. Sc. and Ph.D. degree in Theoretical Electrical Engineering in 2001 and 2014, respectively. From January 1998 up to now, he has engaged to the Department of Theoretical Electrical Engineering, at the FEE. His researching areas are: lightning protection systems, low-frequency electromagnetic fields penetrated into human body and microstrip transmission lines analysis with isotropic, anisotropic and bianisotropic media.

Ana Vučković received the Dipl.–Ing., M.Sc. and Ph.D. degrees from the Faculty of Electronic Engineering (FEE) of Niš, Serbia. In 2003 she joined the Department of Theoretical Electrical Engineering at the FEE. She works as the Assistant Professor at the same faculty. Her main research area is computational electromagnetics (electromagnetic field theory, analytical and numerical methods for electromagnetic field calculations, electromagnetic compatibility and permanent magnet analysis). Also, she took part in numerous international projects and projects supported by the Serbian Ministry of Education and Science.

Nebojša Raičević received his Dipl.–Ing., M.Sc. and Ph.D. degrees at the FEE of Niš, Serbia, in 1989, 1998 and 2010, respectively. He received the Dr.-Ing. degree with a PhD-thesis dealing with the numerical electromagnetic field calculations.

He is currently an Associate Professor at the FEE. His research interests include: cable terminations and joints, numerical methods for EM problems solving, microstrip transmission lines with isotropic, anisotropic and bianisotropic media, metamaterial structures, EMC, nonlinear electrostatic problems, magnetic field calculation of coils and permanent magnets. Prof. Raičević is a member of the IEEE AP Society, IEEE EMC Society, IEEE Dielectrics and Electrical Insulation Society and IEEE Magnetics Society.

Comprehensively Efficient Analysis of Nonlinear Wire Scatterers Considering Lossy Ground and Multi-tone Excitations

Amir Bahrami and Saeed Reza Ostadzadeh

Department of Electrical Engineering,
Arak University, Arak, Iran
bahrami94amir@gmail.com, s-ostadzadeh@araku.ac.ir.

Abstract ─ In this paper based on intelligent water drops algorithm (IWD), comprehensively nonlinear analysis of nonlinearly loaded wire scatterers are carried out. The analyses involve two stages. First, the problem is modeled as a nonlinear multi-port equivalent circuit and it is then reformulated into an optimization problem which is solved by the IWD. The simulation results are compared with harmonic balance (HB), arithmetic operator method (AOM), approximate methods and experiment. Analysis of the problem under strongly nonlinear loads, presence of lossy ground, multi-port structures, and multi-ton excitations are included to cover all the complex aspects. In one hand, the proposed modeling approach is in excellent agreement with other conventional techniques. On the other hand, the run time is considerably reduced.

Index Terms ─ IWD, lossy ground, multi-tone excitation, nonlinear load, wire scatterers.

I. INTRODUCTION

As known, nonlinearly loaded wire scatterers in single and multi-port structures can be used in applications such as control of scattering response, microwave imaging and protecting against high-valued signals such as lightning return strokes [1-10].

In this paper, nonlinearly loaded wire scatterers as single-port and multi-port are investigated as shown in Fig. 1. Such structures are used to control scattering response at frequency harmonic of interest using tuning the spacing among antennas and respective nonlinear load. From now on, the mentioned scatterers are called nonlinear wire scatterer for simplicity. The analyses of such structures are carried out in the frequency domain [1-5], time domain [6, 7], and mixed time-frequency domain [8-10]. Although the frequency-domain methods are suitable for inclusion of frequency dependence of the lossy ground, they are limited to weakly nonlinear loads [1-3] and suffering from drawbacks of Newton Raphson algorithm [4, 5] which yields unacceptable results [5]. Time domain methods, on the other hand, are easily used to treat nonlinearity effect of arbitrary order, however, inclusion of frequency dependence effect of the lossy ground is difficult. To include both effects, the mixed time-frequency domain methods such as harmonic balance technique (HB) should be used [8-10]. In the last method, all the mentioned scatterers depending upon the number of ports are modelled as a nonlinear equivalent circuit as shown in Fig. 2. In this figure, the nonlinear circuits consists of two parts. The first part is the linear part representing Norton circuit viewed across the nonlinear load. This part includes I_{sc} as the short circuit current which is due to the applied excitation, Y_{in} and $\overline{\overline{Y}}$ as the input admittance matrix viewed across the nonlinear load at mixing frequencies respectively for single-port and multi-port scatterers. The three mentioned quantities are conventionally computed using numerical methods such as method of moments (MoM). The second part in Fig. 2 is a nonlinear part which is used for modelling the nonlinearity effects of the device connected to the wire scatterer.

The HB technique is suitable for strongly nonlinear loads, but it is inefficient in analyzing multi-port wire scatterers under multi-tone excitations. Also, it suffers from initial guess and gradient operation in the Newton Rophson iteration algorithm. To remove these drawbacks, a number of optimization techniques [11-13] such as genetic algorithm (GA) [11], and particle swarm optimization (PSO) [12]] for analysis of nonlinear wire scatterers under single tone excitation were proposed. Such approaches, although yield near global solutions, they are time-consuming especially for multi-port structures under multi-tone exciations. In addition, the mentioned Norton circuits are computed via MoM which is time consuming. To remove this complexity, Ostadzadeh et al. proposed a model based on fuzzy inference (MoF) to compute Norton circuit very efficiently [14-16]. The rest challenge is that to compute the induced voltage across the nonlinear load efficiently.

Submitted On: March 23, 2020
Accepted On: May 4, 2020

https://doi.org/10.47037/2020.ACES.J.350805

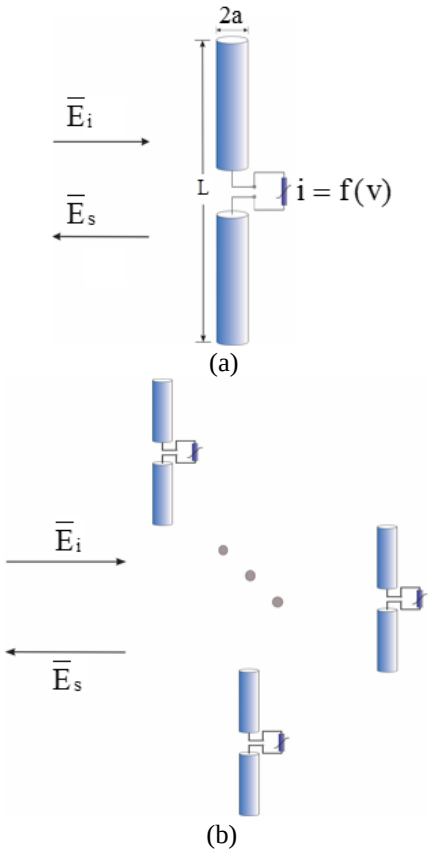

Fig. 1. Nonlinearly loaded wire scatterer as: (a) single port and (b) multi-port structures.

In our previously published literature [17], the IWD algorithm has been used for computing scattering response from Gun diode-loaded antenna array under single-tone excitation but its efficiency in the presence of lossy ground, strongly nonlinear loads and multi-tone excitations was not addressed. In this study, comprehensive analysis of nonlinear wire scatterers based on IWD algorithm considering the mentioned aspects is carried out. The simulation results show that the IWD-based results are in excellent agreement with the HB, AOM, experiment and approximate methods while the run-time is considerably reduced.

This paper is organized as follows. Section II is focused on formulation principles of the nonlinear wire scatterers. IWD algorithm is briefly explained in Section III. Section IV applies the IWD on the multi-port nonlinear wire scatterers considering different complex aspects. Finally conclusion is given in Section V.

II. ANALYSIS OF NONLINEAR WIRE SCATTERERS

As known, the main problem in analyzing nonlinear wire scatterers is compution of the induced voltage across the nonlinear load. To this end, the following cost function should be zero [8]:

$$\left|\bar{\varepsilon}\right| = \left|\bar{\bar{Y}}_{in}\bar{V}_s - \bar{I}_{sc} + \bar{\bar{D}}f\left(\bar{\bar{T}}\bar{V}_s\right)\right| \to \bar{0}. \qquad (1)$$

All quantities in (1) are defined as below:

$\bar{I}_{sc}$ is a vector of short-circuit currents due to the excitations which is computed only at M excitation frequencies, that is,

$$\bar{I}_{sc} = [I_0 \quad I_{1r} \quad I_{1i} \quad \cdots \quad I_{Mr} \quad I_{Mi}]. \qquad (2)$$

$\bar{\bar{Y}}_{in}$ is a matrix containing input admittance viewed across the nonlinear load at N mixing frequencies (N>M), that is,

$$\bar{\bar{Y}}_{in} = \begin{bmatrix} 0 & 0 & 0 & \dots & 0 & 0 \\ 0 & G_{in1} & B_{in1} & 0 & \vdots & 0 \\ 0 & -B_{in1} & G_{in1} & \ddots & 0 & \vdots \\ \vdots & 0 & 0 & \ddots & & 0 \\ 0 & \vdots & \vdots & 0 & G_{inN} & B_{inN} \\ 0 & 0 & \cdots & 0 & -B_{inN} & G_{inN} \end{bmatrix}. \qquad (3)$$

$\bar{\bar{D}}$ and $\bar{\bar{T}}$ are respectively transformation matrix from the frequency domain to the time domain and vice versa. Also, f(.) is the (i-v) characteristic of the nonlinear load. All the above quantities are known, except $\bar{V}_s$, which is an unknown vector including induced voltages across nonlinear load at N mixing harmonic frequencies as follows:

$$\bar{V}_{sc} = [V_0 \quad V_{1r} \quad V_{1i} \quad \cdots \quad V_{Nr} \quad V_{Ni}]. \qquad (4)$$

The vectors of $\bar{V}_s$ and $\bar{I}_{sc}$ are Fourier coefficients of the time-domain signals $i_{sc}(t)$ and $v(t)$, i.e.,

$$i_{sc}(t) = I_0 + \sum_{j=1}^{M}\left\{I_{jr}\cos(\omega_j t) + I_{ji}\sin(\omega_j t)\right\}, \qquad (5)$$

$$v(t) = V_0 + \sum_{j=1}^{N}\left\{V_{jr}\cos(\omega_j t) + V_{ji}\sin(\omega_j t)\right\}. \qquad (6)$$

In dealing with Multi-port nonlinear wire scatterers, the input admittance matrix $\bar{\bar{Y}}_{in}$ is replaced with the admittance matrix $\bar{\bar{Y}}$ as (7) in which diagonal elements are self-admittances which are approximately the one in single-port nonlinear wire scatterers, whereas off-diagonal ones are mutual admittances between among scatterers.

To solve Eq. (1) with guaranteed convergence, we resort to the intelligent water drop algorithm (IWD):

$$\bar{\bar{Y}} = \begin{bmatrix} Y_{11} & \cdots & Y_{1M} \\ \vdots & \ddots & \vdots \\ Y_{M1} & \cdots & Y_{MM} \end{bmatrix}. \qquad (7)$$

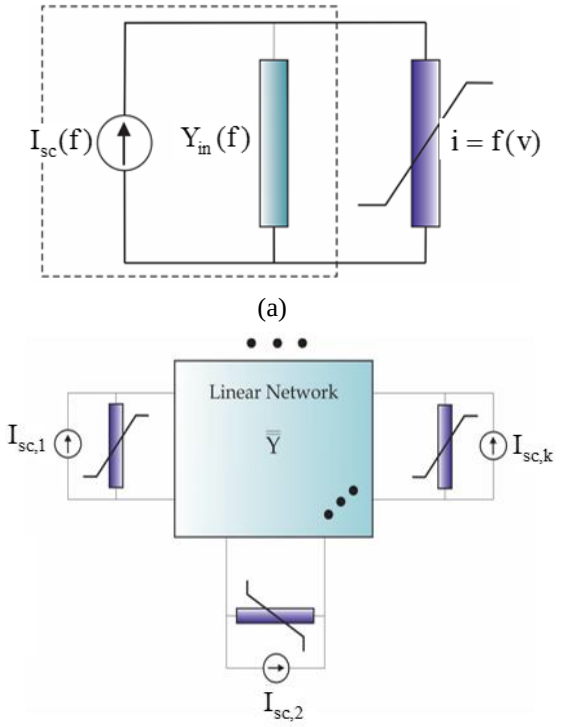

Fig. 2. Equivalent circuit of nonlinear wire scatterer as: (a) single-port and (b) multi-port structures.

III. IWD-BASED ALGORITHM

In this section, a succinct but nevertheless comprehensive explanation of the IWD algorithm is provided. The IWD algorithm is a constructive-based method, where a set of water drops move from one node to the next until a complete population of the solution is reached. This algorithm is based on the observation of the flow of water in rivers. The water in rivers is seen as a collection of water drops that flow from point in high terrain (source) to point in low terrain (destination) with a certain velocity. The water drops also carry some amount of soil with them while flowing along a path. Therefore, water drops are able to transport an amount of soil from one place to another. The parameters involved in this algorithm are classified into two kinds of static and dynamic parameters. Static parameters should be initialized before the algorithm starts, while dynamic parameters, as their name suggests, will vary as the algorithm iterates. By taking these two properties of water drops into account, IWD algorithm has been developed.

In summary, the algorithm of IWD as step by step is as follows:

1. Initialize the static parameters. The graph (V, E) of the problem is given to the algorithm. The value of the total-best solution T^{TBest}, is initially assigned to the worst value:

$$q(T^{TBest}) = -\infty . \quad (8)$$

The value of it_{max} is specified by the user. The initial value of the iteration counter is set to zero. That is it_{count}=0. The algorithm terminates when it_{count}=it_{max}.

The value of N_{IWD} (number of water drops) is set to a positive integer value, which is normally set to the number of nodes N_C in the graph. The location vector of each water drop represents the induced voltage at scatterer terminal in our problem. For soil updating a_s, b_s and c_s for velocity updating, the parameters are a_v, b_v and c_v. The local soil updating parameter ρ_n, which is a small positive number less than one, is set as ρ_n =0.99. The global soil updating parameter ρ^{IWD}, which is selected from [0, 1], is set as ρ^{IWD} =0.99. Furthermore, the initial soil on each path (edge) is denoted by the constant InitialSoil such as the soil of the path within every two nodes i and j, that is set by soil(i,j)=InitialSoil. The initial velocity value of each IWD is set to InitialVel. Both parameters InitialSoil and InitialVel are users choose and they should be tuned experimentally for the application.

2. Initialize the dynamic parameters. Every IWD has a visited node list V_c(IWD), which is initially empty: V_c(IWD)={ }; Each IWD's velocity is set to InitialVel.
3. Spread the intelligent water drops randomly on the nodes of the graph as their first visited nodes.
4. Update the visited node list for each intelligent water drop to include the nodes that just visited.
5. Repeat steps 5.1 to 5.4 for those IWDs with partial solutions. Worth mentioning that partial solutions are solutions with certain degree of undesirability. Although partial solutions are not local solutions and are merely acceptable, they are not the optimum solution.

5.1) Consider water drop k residing at the current node (node i) intends to move to the next node (node j) through an edge e(i,j). The edge selection is done through a probability function, determined by $P_i^{IWD}(j)$, as defined in (2). Then, the water drop visits node j by adding to V_c(IWD):

$$P_i^{IWD}(j) = \frac{d(soil(i,j))}{\sum_{k \notin V_c(IWD)} soil(i,k)}, \quad (9)$$

$$d(i,j) = \frac{1}{\varepsilon + g(soil(i,j))}, \quad (10)$$

where ε is a small positive number used to prevent the division by zero in function d(.), and,

$$g(soil(i,j)) = \begin{cases} soil(i,j) & \text{if } \min_{l \notin V_c(IWD)}(soil(i,j)) \geq 0 \\ soil(i,j) - \min_{l \notin V_c(IWD)}(soil(i,h)) & \text{else} \end{cases}, \quad (11)$$

where soil(i, j) refers to the amount of soil within the local path between nodes i and j. Then, add the newly visited node j to the list V_c(IWD).

5.2) For each IWD moving from node i to node j, update

its velocity $velocity^{IWD}(t)$ by:

$$velocity^{IWD}(t+1) = velocity^{IWD}(t) + \frac{a_v}{b_v + c_v soil^2(i,j)}, \quad (12)$$

where a_v, b_v and c_v are the static parameters used to represent the nonlinear relationship between the velocity of water drop, i.e. $velocity^{IWD}$, and $velocity^{IWD}(t+1)$ is the updated velocity for the IWD.

5.3) For the intelligent water drop (IWD) moving on the path from node i to j, compute the change of soil $\Delta Soil(i, j)$ that the intelligent water drop (IWD) loads from the path by:

$$\Delta soil(i,j) = \frac{a_s}{b_s + c_s time(i,j;Vel^{IWD})}, \quad (13)$$

where, a_s, b_s, and c_s are the static parameters used to represent the nonlinear relationship between $\Delta Soil(i, j)$ and the inverse of vel^{IWD}.

Note that $time(i,j;vel^{IWD})$ refers to the time needed for water drop to transit from node i to node j at time t + 1. It is defined as follows:

$$time(i,j;Vel^{IWD}) = \frac{HUD}{\max(\varepsilon, Vel^{IWD})}, \quad (14)$$

where $HUD(.)$ is a local heuristic function defined to measure the degree of the undesirability of IWD to move between nodes i and j. In our application, it is chosen to be unity.

5.4) Update the soil Soil(i, j) of the path from node i to j traversed by that IWD and also update the soil that the IWD carries $Soil^{IWD}$ by:

$$soil(i,j) = (1-\rho).soil(i,j) - \rho.soil(i,j), \quad (15)$$

$$soil^{IWD} = soil^{IWD} - \Delta soil(i,j), \quad (16)$$

where ρ is a small positive constant between zero and one.

6) Find the iteration best solution T^{TBest} from all the solutions T^{IWD} found by the IWDs using:

$$T^{TBest} = \arg\max_{\forall T^{IWD}} q(T^{IWD}). \quad (17)$$

7) Update the soils on the paths that form the current iteration best solution T^{TBest} by:

$$soil(i,j) = (1-\rho)soil(i,j) + \rho\frac{2soil^{IWD}}{N_c(N_c-1)}$$
$$\forall (i,j) \in T_M. \quad (18)$$

Update the total best solution T^{TBest} by the current iteration best solution T^{TBest} using:

$$T^{TBest} = \begin{cases} T^{1Best} & \text{if} \quad q(T^{TBest}) \geq q(T^{1Best}) \\ T^{TBest} & \text{else} \end{cases}. \quad (19)$$

8) Increment the iteration value by:

$$It_{count} = It_{count} + 1, \quad (22)$$

Then, go to Step 2 if:

$$It_{count} < It_{max}. \quad (21)$$

9) The algorithm stops here with the total best solution T^{1Best}.

Here T^{TBest} is the best value for harmonics voltages. It_{count} is the number of iterations when the algorithm has converged. The static and dynamic parameters in this paper are listed in Table 1 in [17].

IV. NUMERICAL SIMULATION AND DISCUSSION

A. Comparison with AOM

A.1. Strongly nonlinear load

To show the capability of the algorithm on the order of load nonlinearity, a single-port wire scatterer having length to diameter ratio L/2a=74.2, and one meter length (L=1 m) is selected. Also, the scatterer is illuminated by an incident plane wave of magnitude E_i=1(V/m) and centrally loaded with a very strongly nonlinear device, which is characterized by (22):

$$i=10^{11}\times v^{13}. \quad (22)$$

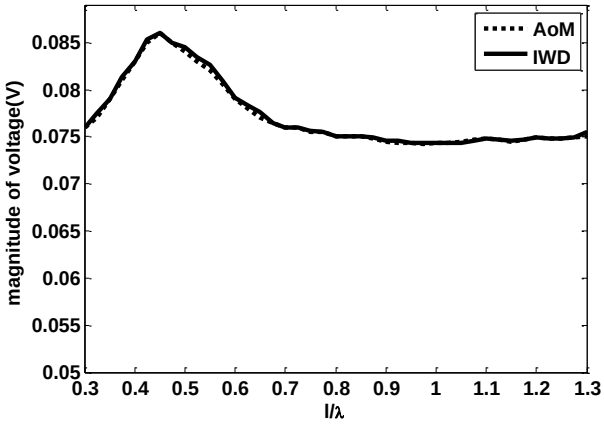

Fig. 3. The induced voltage across the strongly nonlinear load at the fundamental harmony under single-tone excitation.

Prior to analysis, the Norton circuit in Fig. 2 is efficiently computed based on [14, 15]. The voltage magnitudes for various values of length to wavelength are shown in Fig. 3. A comparison of IWD results with those obtained by the AOM [4] substantiates the high accuracy of the algorithm while the run-time is considerably reduced which will be discussed in next sections.

A.2. Lossy ground

In the second example, the versatility of the method considering lossy ground is tested. Hence, a single–port nonlinear wire scatterer is situated 0.4 m above a lossy ground, while it is illuminated by a plane wave with the polar angle of incidence θ=60 deg. The ground is characterized by a relative permittivity of ε_r=10 and

conductivity of σ=0.003S/m. The nonlinear load has a (i-v) characteristic as below:

$$i = \frac{1}{75}v + 4v^3 . \quad (23)$$

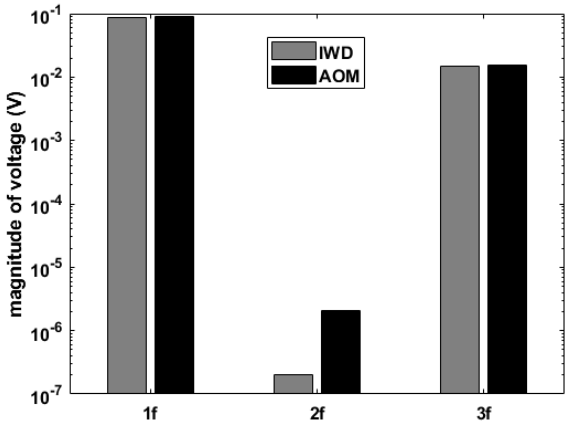

Fig. 4. Spectral content across the nonlinear load of single-port nonlinear wire scatterer over lossy ground.

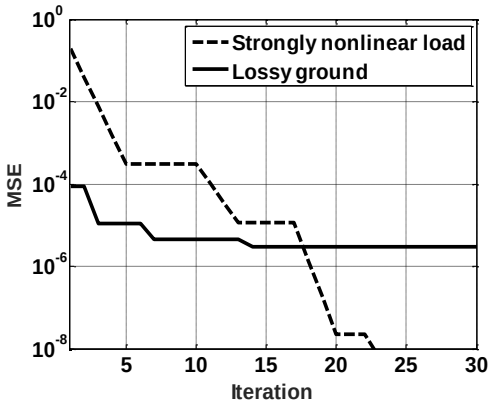

Fig. 5. Mean square error (MSE) versus iteration by the IWD approach for single nonlinear scatterer considering the lossy ground and strongly nonlinear load.

At first, the Norton circuit is efficiently computed based on the MoF in [16] and the IWD is then applied to Eq. (1). The voltage magnitudes are depicted in Fig. 5. A comparison of our results with those obtained by AOM [4] corroborates the accuracy of the proposed method. It should be mentioned that in this examples, the suppression of even harmonics are due to the cubic nature of the load's nonlinearity. As shown in Fig. 4, this even harmonic suppression is better demonstrated by the proposed method with respect to AOM. The mean square errors (MSEs) by the IWD, for the two mentioned cases are also provided in figure 5 for the first 30 iterations with deactivated stopping criteria (1.E-8). It shows that iteration process larger than 30 gives excellent agreement in the two examples.

B. Comparison with HB and NC

B.1. Single-port

In this sub-section, capability of the IWD method in comparison with HB technique [8] is investigated. Hence, a single-port wire scatterer the same as previous sections is exposed to multiple plane waves of the same amplitude (E_i=1(V/m)) and different frequencies, i.e., 140MHz, 160MHz.

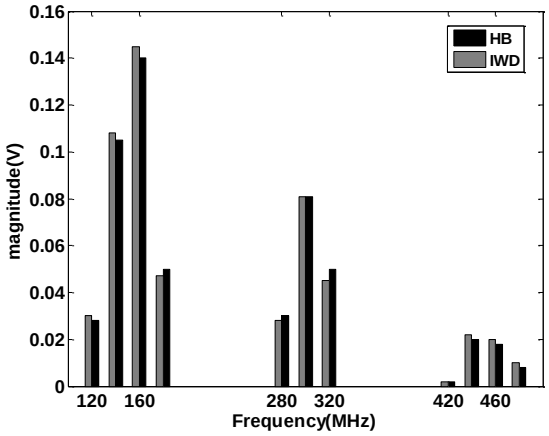

Fig. 6. Induced voltage using IWD and HB-based methods for single-port nonlinear wire scatterers.

The scatterer is centerally loaded with a p-n junction diode with the following (i-v) characteristic:

$$i = I_s(e^{v/v_T} - 1), \quad (24)$$

where $I_s = 10\,\text{nA}$, and $v_T = 26\,\text{mV}$. The induced voltage across the diode at different harmonic frequencies using the IWD, HB, and NC methods are shown in Fig. 6. From this figure, IWD and HB-based results are in good agreement, whereas the NC-based results are considerably violated.

B.1. Multi-port

In this section to show capability of the IWD in analyzing multi-port wire scatterer under multi-ton excitation, an infinite planar array of nonlinear wire scatterers is chosen. The scatterers in the array are equally spaced in vertical and horizontal directions. The nonlinear wire scatterers in the array are the same as the previous sub-sections. The induced voltage across the p-n junction diode are computed for the vertical and horizontal spacing 1 m and shown in Fig. 7.

The HB and NC-based results are included in the same figure as well. From this figure, IWD-based results are in good agreement with HB-based ones [18]. In

addition, although the approximated method of NC is efficient, it is violated under strong nonlinearity.

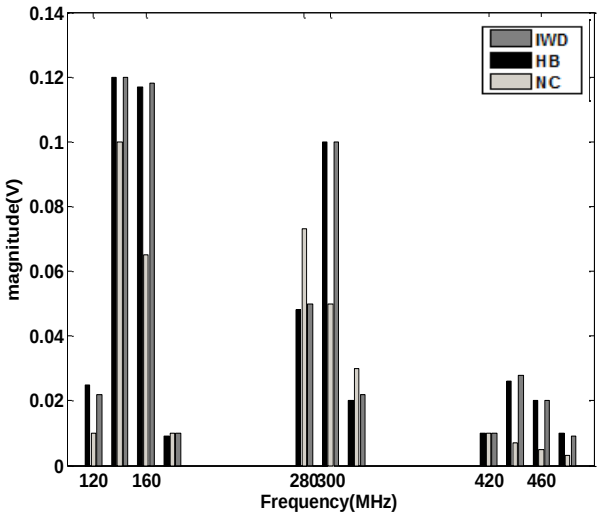

Fig. 7. The induced voltage across the diode at different harmonics for multi-port nonlinear wire scatterers.

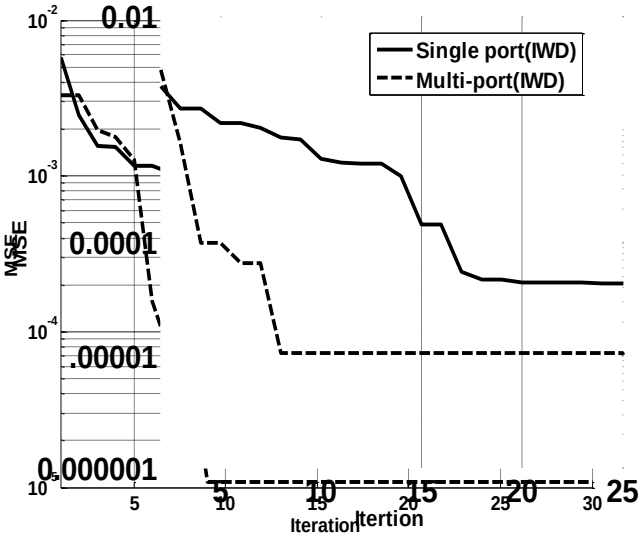

Fig. 8. The MSEs for single and multi-port nonlinear wire scatterer.

To show the efficiency of the proposed approach better, the MSEs for the single and multi-port nonlinear wire scatterers with very fast convergences are shown in Fig. 8. Finally, the relative error percentages of the proosed method for single and multi-port wire scatterers in comparision with the HB technique are listed in Table 1. From this table, the precise of the IWD can be observed.

Table 1: Relative error percentage of the IWD algorithm in comparison with the HB technique at different harmonic frequencies

Relative Error Percentage of Terminal Voltage						
f (MHz)	**120**	**140**	**160**	**180**	**280**	**300**
Single port	6.7	2.7	3.5	6	9	2.2
Multi port	7.2	0.5	2.4	3.5	8.3	0.8
f (MHz)	**320**	**420**	**440**	**460**	**480**	**Dc**
Single port	4	0.8	9	9.5	3.5	0
Multi port	3.5	0.5	8.5	3.5	2.7	0

C. Comparison with measurement

C.1. Single-port

To illustrate another capability of the proposed approach, it is compared with measurement. Figure 9 shows complex wire scatterer namely vertical rod as single-and multi-port structures which are buried in a lossy ground and subjected to the high-valued lightning stroke. In this figure, the nonlinear load represents the ionization phenomenon in the lossy ground. The (i-v) characteristic of the nonlinear load is conventionally is expressed as follows [19]:

$$v = \frac{R}{\sqrt{1+i/I_g}}\,i, \qquad (25)$$

where R is low-frequency resistance of the grounding rod, and I_g is computed as below:

$$I_g = E_c/(2\pi R^2\sigma), \qquad (26)$$

where E_c and σ are respectively critical electric field and conductivity of the lossy ground. Transient analysis of such scatterers has been carried out in time domain [20] where the input admittance is first computed in the frequency domain and then converted to time domain by vector fitting method [21]. Consequently, such analysis demands more run-time. Also, more recently, the ionization phenomenon has been modelled as gradually increasing radius of the rod by the MTL [22-26]. This approach, however, can not include the hystersis effect in the ionization process, whereas, by the proposed model in Fig. 9, it can be easily included [27, 28].

To verify the performance of the IWD in such complex scatterers, a vertical rod with length L=3.05m, and radius a=12.7mm and buried in a lossy ground with conductivity $\sigma = 0.011\,\mathrm{S/m}$, relative permittivity $\varepsilon_r = 10$ and critical electric field $E_c = 127\,\mathrm{kV/m}$ is selected [29]. The lightning stroke is expressed as a current source and shown in Fig. 12 (dotted line). Prior to analysis, such current source is represented as Fourier series, and the input admittance in Fig. 2 (a) is then computed by MoM or the efficient method based on fuzzy inference (MoF) [30, 31]. Finally, applying the IWD method to Fig. 2 (a), the lightning-induced voltage in time domain is

efficiently computed and shown in figure 10 which is in good agreement with measurement [29] (Fig. 6 in [29]). The slight error shown in tail time may be due to truncation error of the Fourier series which is used to obtain the lightning current.

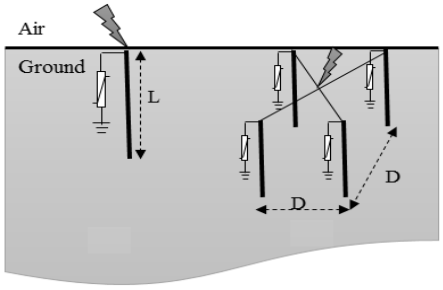

Fig. 9. Two nonlinear wire scatterers under lightning strokes as: (a): single-port rod, and (b): multi-port rod.

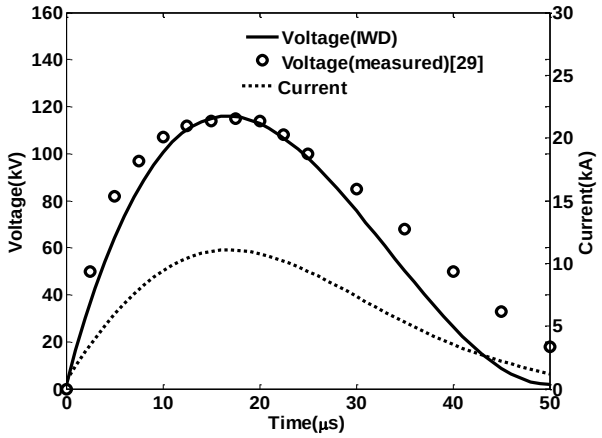

Fig. 10. Lightning-iduced voltage of the single-port vertical rod in time domain.

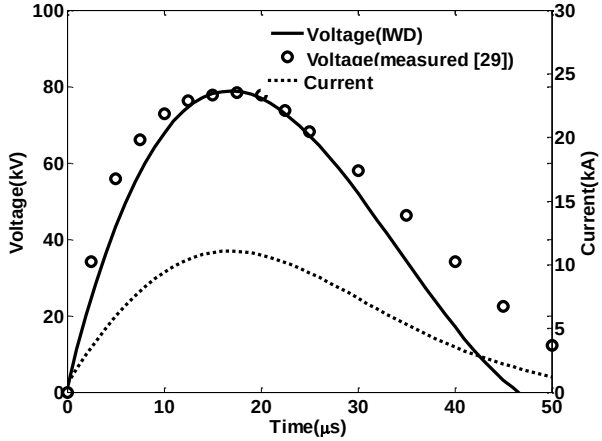

Fig. 11. Lightning-induced voltage of the multi-port vertical rod in time domain.

It's worth mentioning that the HB technique is evidently inefficient for nonlinear multi-port networks under multi-tone excitations [8]. Hence, the single-port nonlinear scatterer only has been analyzed by Shariatinasab et al. [28] and the multi-port one has not been addressed yet, whereas the proposed method can be easily applied.

C.2. Multi-port

The analysis of multi-port rod by the IWD is the same as single port, except that Fig. 2 (b) is used. Each vertical rod has length L=3.05m, and radius a=12.7mm and buried in a lossy ground with $\sigma = 0.016 \mathrm{S/m}$, $\varepsilon_r = 10$ and $E_c = 50 \mathrm{kV/m}$ [29]. The spacing between rods is D=3.09 mand the lightning current is the same as previous sub-section. The lightning-induced voltage by the IWD is shown in Fig. 11 which is in good agreement with the measurement [29] (Fig. 9 in [29]). Note that the validity of the IWD method with commercial packages has been investigated [32].

D. Comparison of run-times

As a final advantage of the IWD method, the its run-time in analyzing single and multi-port nonlinear wire scatterers under multi-tone excitations is compared with the mentioned methods.

D.1. Single-port

In the case of single-port scatterer, the wire scatterer is the one in the sub-section IV-A, and the nonlinear load is as Eq. (23). The run-times of different approaches are listed in Table 2. From this table, when the number of exciting frequencies is increased, the run-time of the IWD method is slightly increased. Moreover, although the run-time of NC-based method is very short, it is restricted to weakly nonlinear loads (Figs. 6 and 7).

D.2. Multi-port

In the case of multi-port nonlinear wire scatterers, the nonlinear load and wire scatterer are the same as previous sub-section, but the different arrangements of wire scatterers are investigated. The run-times of the different arrangements under double-ton excitation are listed in Table 3. From this table, high efficiency of the IWD in comparison with the others is once more proven.

Table 2: Run-time of different methods for single-port nonlinear wire scatterers under multi-tone excitation

Exciting Frequency (MHz)	Run-time (sec)			
	IWD	AOM	HB	NC
150	1	1	62	0.12
140,160	2	2	113	0.14
140,160,180	6	10	163	0.17
140,160,180, 200	17	31	320	0.25
140,160,180, 200,220	29	53	430	0.35

Table 3: Run-time of different methods for multi-port nonlinear wire scatterers under double-tone excitation

Multi-port Scatterer	Run-time (sec)			
	IWD	AOM	HB	NC
1 by 1	2	2	113	0.14
2 by 1	20	30	205	0.20
2 by 2	30	83	445	0.25
3 by 3	53	170	580	0.28

V. CONCLUSION

In this study, an efficient hybrid method for analyzing nonlinear wire scatterers over lossy ground under multi-ton excitations was proposed. The proposed method consists of linear and nonlinear parts. The linear part can be used for inclusion of frequency dependence of the lossy ground, while the nonlinear one considers nonlinearity effects of the device connected to the scatterer so that both effects are considered. The model was validated using extensive examples. Comparative studies show excellent agreement with the existing methods, while run-time is considerably reduced.

It worth noting that although all the nonlinear loads in this study are expressed as analytical models, the (i-v) characteristics of some of devices are based on experimental measurements and are not smooth curves [33, 34] (Fig. 7 in [33] and Table 2 in [34]). In such cases, the HB method which needs initial guess and gradient operation in the iteration process, may yield violated solutions, whereas the artificial intelligent (AI) approaches especially IWD outperforms the HB method.

REFERENCES

[1] T. K. Sarkar and D. D. Weiner, "Scattering analysis of nonlinearly loaded dipole antennas," *IEEE Trans. Antenna Propag.*, vol. 24, no. 2, pp. 125-131, 1976.

[2] T. K. Sarkar and D. D. Weiner, "Analysis of nonlinearly loaded multiport antenna structures over an imperfect ground plane using the Volterra-series method," *IEEE Trans. Electromag. Compat.*, vol. 20, no. 2, pp. 278-287, 1978.

[3] K. C. Lee, "Mutual coupling mechanisms within arrays of nonlinear antennas," *IEEE Trans. Electro. Compat.*, vol. 47, no. 4, pp. 963-970, 2005.

[4] K. Sheshyekani, S. H. Sadeghi, and R. Moini, "A combined MoM-AOM approach for frequency domain analysis of nonlinearly loaded antennas in the presence of a lossy ground," *IEEE Trans. Antennas Propagat.*, vol. 56, no. 6, pp. 1717-1724, 2008.

[5] K. Sheshyekani, S. H. H. Sadeghi, R. Moini, and F. Rachidi, "Frequency-domain analysis of ground electrodes buried in an ionized soil when subjected to surge currents: A MoM–AOM approach," *Electric Power System Research*, vol. 81, pp. 290-296, 2011.

[6] J. A. Landt, "Network loading of thin-wire antennas and scatterers in the time domain," *Radio Sci.*, vol. 16, pp. 1241-1247, 1981.

[7] D. Poljak, C. Y. Tham, and A. McCowen, "Transient response of nonlinearly loaded wire antennas in two-media configuration," *IEEE Trans. Electromag. Compat.*, vol. 46, no. 1, pp. 121-125, 2004.

[8] C. C. Huang and T. H. Chu, "Analysis of wire scatterers with nonlinear or time-harmonic loads in the frequency domain," *IEEE Trans. Antennas Propagat.*, vol. 41, no. 1, pp. 25-30, 1993.

[9] D. Liao, "Generalized wideband harmonic imaging of nonlinearly loaded scatterers," *IEEE Trans. Antennas Propagat.*, vol. 63, no. 5, pp. 2079-2087, 2015.

[10] A. E. Yilmaz, "An envelope tracking hybrid field-circuit simulator for narrow-band analysis of nonlinearly loaded wire antennas," *IEEE Trans. Microw. Theory and Techn.*, vol. 62, no. 2, pp. 208-223, 2014.

[11] M. Teimoori, S. R. Ostadzadeh, and B. Abdoli, "Analysis of frequency selective with nonlinear antenna under radiations of bi-frequency waves based on genetic algorithm," *International Journal of Computer & Technology*, vol. 15, no. 7, pp. 6914-6922, 2016.

[12] K. C. Lee, "Analyses of nonlinearly loaded antennas and antenna arrays using particle swarm algorithm," *IEEE Conference on Antennas Propag.*, 2004.

[13] S. R. Ostadzadeh, "Nonlinear analysis of non-linearly loaded dipole antenna in the frequency domain using fuzzy inference," *Journal of Communication Engineering*, vol. 3, no. 2, pp. 141-152, 2014.

[14] S. R. Ostadzadeh, M. Tayarani, and M. Soleimani, "A fuzzy model for computing input impedance of two coupled dipole antennas in the echelon form," *Progress in Electromagnetics Research*, vol. 78, pp. 265-283, 2008.

[15] S. R Ostadzadeh, M. Tayarani, and M. Soleimani, "A hybrid model in analyzing nonlinearly loaded dipole antenna and finite antenna array in the frequency domain," *International Journal of RF and Microwave*, vol. 19, pp. 512-518, 2009.

[16] S. R Ostadzadeh, "An efficient hybrid model in analyzing nonlinearly loaded dipole antenna above lossy ground in the frequency domain," *Applied Computational Electromagnetic Society (ACES) Journal*, vol. 28, no. 9, pp.780-787, 2013.

[17] A. Bahrami and S. R. Ostadzadeh, "Back scattering response from single, finite and infinite array of nonlinear antennas based on intelligent water drops algorithm," *International Journal for Computation and Mathematics in Electrical and Electronic Engineering*, vol. 38, no. 6, pp. 2040-2056, 2019.

[18] K. C. Lee, "Two efficient algorithms for the analyses of a nonlinearly loaded antenna and antenna array in the frequency domain," *IEEE Trans. Electromag. Compat.*, vol. 45, no. 4, pp. 339-346, 2000.

[19] L. Grcev, "Modeling of grounding electrodes under lightning currents," *IEEE Trans. Electromagn. Compat.*, vol. 51, no. 3, pp. 559-571, 2009.

[20] M. Kazemi, and S. R. Ostadzadeh, "Vector fitting-based models of vertical and horizontal electrodes under lightning strikes to interface with EMTP," *Asian Journal of Fuzzy and Applied Mathematics*, vol.3, no. 1, pp. 11-21, 2015.

[21] S. Mehrabi and S. R. Ostadzadeh, "Impact of ocean-land mixed propagation path on equivalent circuit of grounding rods", *Journal of Communication Engineering*, vol. 8, no. 2, pp. 197-207, 2019.

[22] S. S. Sajjadi and S. R. Ostadzadeh, "Lightning response of multi-port grounding grids buried in dispersive soils: An approximation versus full wave methods and experiment," *Advanced Electromagnetics*, vol. 8, no. 1, pp. 43-50, 2019.

[23] S. S. Sajjadi, V. Aghajani, and S. R. Ostadzadeh, "Transient analyses of grounding electrodes considering ionization and dispersion aspects of soils simultaneously: An improved multiconductor transmission line model (Improved MTL)," *Applied Computational Electromagnetic Society Journal (ACES)*, vol. 34, no. 5, pp. 731-737, 2019.

[24] S. S. Sajjadi, V. Aghajani, and S. R. Ostadzadeh, "Comprehensive formulae for effective length of multiple grounding electrodes considering different aspects of soils: Simplified multiconductor transmission line-intelligent water drop approach," *Int. J Numer Model El.*, 2020. e2721, https://doi.org/10.1002/jnm.2721

[25] S. R. Ostadzadeh, "Validity of improved MTL for effective length of counterpoise wires under low and high-valued lightning currents," *Advanced Electromagnetics*, vol. 9, no. 1, 2020.

[26] V. Aghajani, S. S. Sajjadi, and S. R. Ostadzadeh, "Design of grounding vertical rods buried in complex soils using radial basis functions," *Journal of Communication Engineering*, vol. 7, no. 2, pp. 30-40, 2018.

[27] M. Mokhtari and G. B. Gharehpetian, "Integration of energy balance of soil ionization in CIGRE grounding electrode resistance model," *IEEE Trans. Electromagn. Compat.*, vol. 60, no. 2, pp. 402-413, 2017.

[28] J. G. Safar, R. Shariatinasab, and J. He, "Comprehensive modeling of grounding electrodes buried in ionized soil based on MoM-HBM approach," *IEEE Trans. Power. Del.*, vol. 57, no. 6, pp. 1627-1636, 2019.

[29] A. C. Liew and M. Darveniza, "Dynamic model of impulse characteristics of concentrated earths," *Proc. IEE*, vol. 121, no. 2, 1974.

[30] S. M. Taghavi and S. R. Ostadzadeh, "High frequency analysis of single overhead line terminated to grounding arrester using fuzzy inference models," *Journal of Communication Engineering*, vol. 2, no. 3, pp. 208-221, 2013.

[31] Z. Samiee and S. R. Ostadzadeh, "Transient analyses of grounding systems subjected by lightning surge currents through fuzzy-based models of input impedance in the frequency domain," *Asian Journal of Fuzzy and Applied Mathematics*, vol.3, no. 1, pp. 22-34, 2015.

[32] H. Samiian, S. R. Ostadzadeh, and A. Mirzaie, "Application of intelligent water drops in transient analysis of single conductor overhead lines terminated to grid-grounded arrester under direct lightning strikes," *Journal of Communication Engineering*, vol. 5, pp. 50-59, 2016.

[33] J. C. Salari and C. Portela, "Grounding systems modeling including soil ionization," *IEEE Trans. Power. Del.*, vol. 23, no. 4, pp. 1939-1945, 2008.

[34] A. Geri and E. Garbagnati, "Non-linear behavior of ground electrodes under lightning surge currents: Computer modelling and comparison with experimental results," *IEEE Transactions on Magnetics*, vol. 28, no. 2, pp. 1442-1445, 1992.

Amir Bahrami was born in Esfahan, Iran, on June 22, 1994. He received B.Sc. in Electrical Engineering from Arak University, Arak, Iran, in 2016. His research interests include nonlinear microwaves, nonlinear RF circuits, nonlinear differential equations and nonlinear functional analysis.

Saeed Reza Ostadzadeh was born in Kashan, Iran, on April 13, 1978. He received B.Sc., M.Sc. and Ph.D. in Communication Engineering from the Iran University of Science and Technology (IUST), Tehran, Iran, in 2000, 2002 and 2008, respectively. He is currently an Assistant Professor in the Department of Electrical Engineering at Arak University, Arak, Iran. His research interests include qualitative modeling, grounding systems and power systems under lightning strokes. He has authored more than 50 scientific papers for conferences and international journals. He is a member of Iranian electromagnetic engineering society and Iranian fuzzy systems society.

A Compact Eight-port CPW-fed UWB MIMO Antenna with Band-notched Characteristic

Li-Yan Chen, Wei-Si Zhou, Jing-Song Hong, and Muhammad Amin

Institute of Applied Physics, School of Physical
University of Electronic Science and Technology of China, 610054 Chengdu, China
727683316@qq.com, 1355746335@qq.com, cemlab@uestc.edu.cn, aminssphysics@hotmail.com

Abstract ─ A compact eight-port coplanar waveguide (CPW)-fed ultra-wideband (UWB) multiple-input-multiple-output (MIMO) antenna with band-notched characteristics in a small size of 54×54×0.8 mm^3 is proposed in this paper. The eight-port MIMO antenna consists of four two-port MIMO antennas. For each two-port MIMO antenna, two monopole antenna elements are printed on the FR4 substrate and placed perpendicularly to each other. To increase impedance bandwidth and improve the isolation, a stub is positioned in the middle of two radiating elements. The band-notched characteristic are achieved by etching two L-shaped resonator slots on each radiating elements, respectively. The S_{11} reflection coefficients, coupling isolation, radiation patterns, peak gain and radiation efficiencies of the MIMO antenna are measured. The MIMO performance of the proposed antenna is analyzed and evaluated by the envelope correlation coefficient (ECC) and total active reflection coefficient (TARC).

Index Terms ─ Band-notched, CPW, ECC, MIMO, TARC, UWB.

I. INTRODUCTION

Since the Federal Communication Commission (FCC) assigned an unlicensed 3.1-10.6 GHz bandwidth, ultra-wideband (UWB) devices have been one of the most rapidly developing technologies in wireless applications due to its numerous blessings, including low power, high transmission rate, and so on [1-2]. The multipath fading in UWB system has been becoming more and more serious because of the low power limited by FCC. Multiple-input-multiple-output (MIMO) generation has incomparable advantages in improving the wireless link transmission capacity and reliability [3]. Therefore, combining MIMO technology with UWB technology is an efficient way to decrease multipath fading in UWB system [4]. However, there is a strong mutual coupling among two close radiating elements, which result in the loss of antenna bandwidth and radiating efficiency and make it difficult to design MIMO antenna in a compact dimension. Besides, the UWB overlaps with other wireless frequency bands, especially the wireless local area network (WLAN) frequency band at 5.15-5.85 GHz, which can cause some potential interference and noisy to the UWB system. Thus, it is inevitable to reduce both the mutual coupling among UWB MIMO antenna and the electromagnetic interference caused by WLAN system with some simple and effective methods.

Researchers have proposed various MIMO antennas [5-10]. Using electromagnetic band-gap (EBG) structure [5], or a tree-shaped parasitic structure [6], or a T-shaped protruded ground stub [7] to minimize the mutual coupling between radiating elements, or a complementary split-ring resonator (CSRR) etching on the antenna ground [8]. The MIMO antenna in [9] don't use any decoupling structure, the high isolation performance is achieved by the asymmetrical and complementary structures of the quasi-self-complementary antenna (QSCA). The antenna in [10] has the smallest dimension in those UWB MIMO antennas, etching a T-shaped slot at the antenna ground to enhance the impedance bandwidth and reduce the mutual coupling. However, the antenna in [5] is not suitable for UWB system due to their narrow operation band. The operation band of antennas in [6], [8], [9] and [10] is UWB level, but it can't avoid the noise and interference in WLAN band.

In this paper, a compact eight-port CPW-fed UWB MIMO slot antenna with WLAN band-notched characteristics in a size of 54×54×0.8 mm^3 is presented. The eight-port MIMO antenna consists of four two-port MIMO antennas. Each two-port MIMO antenna consists of two orthorhombic monopole antenna fed by CPW. A ground stub which is protruded at 45° in the middle of two radiating elements acts as a reflector to achieve UWB characteristics and high isolation. To be able to acquire the band-rejected characteristics at WLAN operation band, a L-shaped slot resonators (approximately half wavelength at 5.5 GHz) are etched on each radiating element. The proposed UWB MIMO slot antenna is manufactured and measured, measured outcome show that the designed antenna exhibits S_{11} < -10 dB, high isolation better than 17 dB, peak gain varies 1.524 dBi to

Submitted On: June 17, 2018
Accepted On: May 4, 2020
https://doi.org/10.47037/2020.ACES.J.350806

2.83 dBi, radiation efficiencies varies 74.7% to 85%, ECC < 0.02 and TARC < -15 dB over the whole UWB band except for a notched at 5-6 GHz. Compared to the previous UWB MIMO antennas in [5]-[10], this UWB MIMO slot antenna has the superiority of more ports, a notched band and better MIMO performance.

II. ANTENNA DESGIN

A. Antenna geometry

The geometry and photograph of the proposed eight-port MIMO antenna which consists of four two-port MIMO antennas is illustrated in Fig. 1. The antenna is engraved on a 54×54×0.8 mm^3 square FR4 (dielectric constant of 4.4 and loss tangent of 0.02) substrate. All parameters are in millimeter and optimized by simulating in ANSYS Electromagnetics Suite 17.1, as shown in Fig. 1.

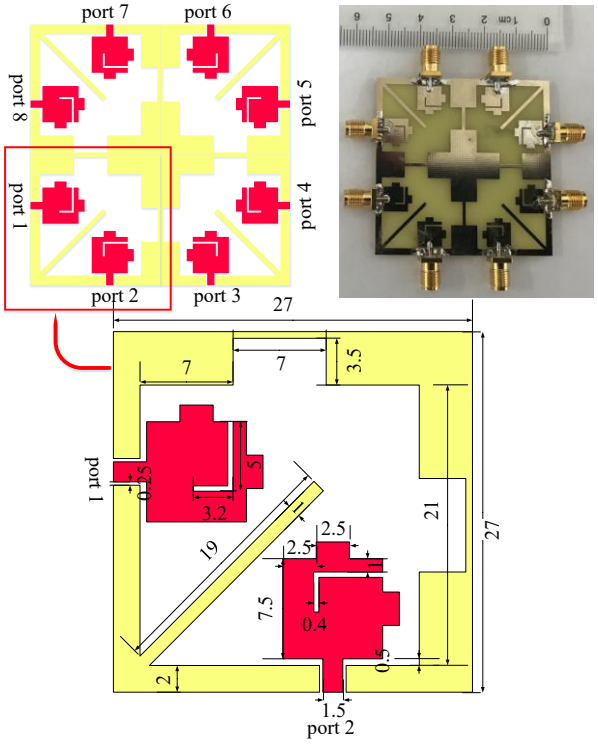

Fig. 1. The geometry and photograph of the proposed UWB MIMO antenna.

B. The two-port MIMO slot antenna

The design process of the presented MIMO slot antenna is demonstrated in Fig. 2, including antennas I-IV. The simulated S-parameters of antenna I-IV are shown in Fig. 3. First, antenna I which consists of two orthorhombic square monopole antennas is presented. A square slot is etched on the ground to obtain a wide operation band. The fundamental resonant frequency f_r of antenna I can be estimated by (1) [11]:

$$f_r = \frac{144}{l_1+l_2+g+\frac{A_1}{2\pi l_1\sqrt{\varepsilon_{re}}}+\frac{A_2}{2\pi l_2\sqrt{\varepsilon_{re}}}}, \quad (1)$$

where l_1 and A_1 denote the length and area of the radiation patch, respectively, l_2 and A_2 denote the length and area of the ground, g is the gap between the ground and the radiation patch. For antenna I, $l_1 = Lb$, $l_2 = La$, $g = g$, $A_1 = Lb \times Lb$ and $A_2 = Lg \times (L/2 - Wf - 2t) + (L - Lg - La) \times La$. ε_{re} is the effective dielectric constant of FR4 and $\varepsilon_{re} = \frac{\varepsilon_r+1}{2}$. The calculated *fr* is 4.8 GHz, the simulated *fr* is about 5 GHz, which is very close to the calculated value using formula (1).

Then, on the basis of antenna I, protruding two parasitic rectangular stubs on square radiation patches and etching two additional rectangular slots on the ground, as illustrated as antenna II. The antenna II exhibits a wider operational bandwidth than antenna I, especially in the low spectrum, but it still can't reach the UWB level. Finally, a ground stub is extended at 45° in the middle of two radiating elements of antenna II to further expand bandwidth, as shown in antenna III. The ground stub acts as a reflector to make the first resonator move from 5.4 GHz to 3.8 GHz, as the blue $S_{11/22}$ curve shown in Fig. 3. Therefore, the UWB characteristics have achieved.

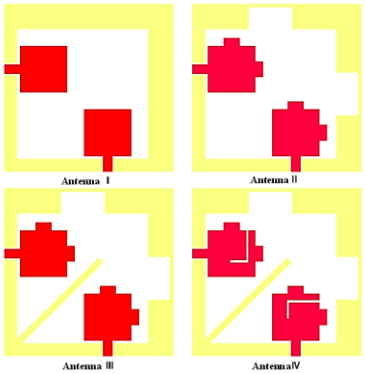

Fig. 2. The design process of proposed UWB MIMO slot antenna.

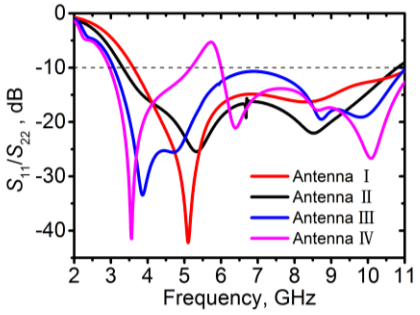

(a)

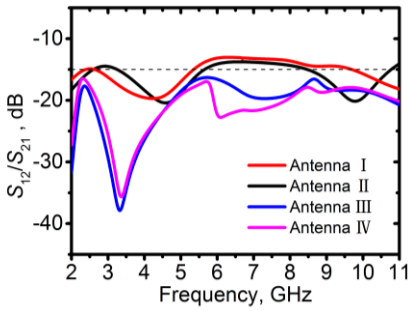

(b)

Fig. 3. Simulated S11/S22 parameters of Antenna I-IV (a), and Simulated S12/S21 parameters of Antenna I-IV (b).

C. Achievement of decoupling

Although the two radiation elements in antenna I and II are placed perpendicularly to one another, the coupling between two excited ports remains worse in middle spectrum. The ground stub in antenna III acts as a reflector which separates the two radiating elements to decrease the mutual coupling between the two ports. The $S_{12/21}$ isolation results are improved to more than 17 dB by the addition of stub, as can be seen from the blue $S_{12/21}$ curve illustrated in Fig. 3.

In order to further understand the function of the ground stub, Fig. 4 shows the surface current distributions at 7 GHz without and with the stub when port 1 is excited. Most of the current is accumulating on the excited port and the stub. The stub prevents current flowing from port 1 to port 2, resulting in high isolation.

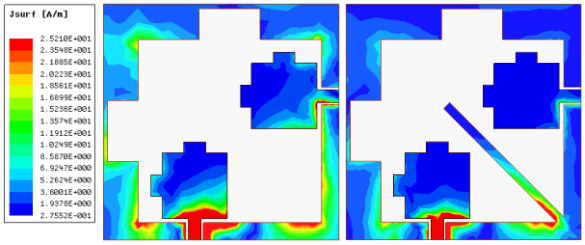

(a) (b)

Fig. 4. Surface current distributions of antenna II (a), and antenna III at 7 GHz (b).

D. Achievement of band-notched characteristics

The band-notched characteristics of WLAN spectrum (5.15 GHz-5.85 GHz) for the presented UWB MIMO antenna is accomplished by etching an L-shaped slot on each radiating element of the antenna III, as shown in antenna IV of Fig. 2. The length of the slot is about quarter wavelength corresponding to 5.5 GHz and estimated by the formula (2) [12]:

$$l1 + w1 = \frac{c}{4f_0\sqrt{\varepsilon_{re}}}, \quad (2)$$

where c is the velocity of the light, $\varepsilon_{re} = \frac{\varepsilon_r+1}{2}$ is the relative dielectric constant of FR4. The calculated $l1 + w1$ is 8.4 mm approximately.

Figure 5 (a) illustrates the simulated S-parameters for different values of $l1 + w1$. The rejected band is shifting to the low frequency with the increase of value of $l1 + w1$, but almost no impact on $S_{12/21}$ isolation. The value of $l1 + w1$ is selected to 8.2 mm for obtaining notched band from 5 GHz to 6 GHz.

Figure 5 (b) shows the surface current distributions at 5.5 GHz of antenna IV when port 1 is excited. A large amount of current has trapped in the L-shaped slot, which acts as a capacitance to obtain the band-notched characteristics.

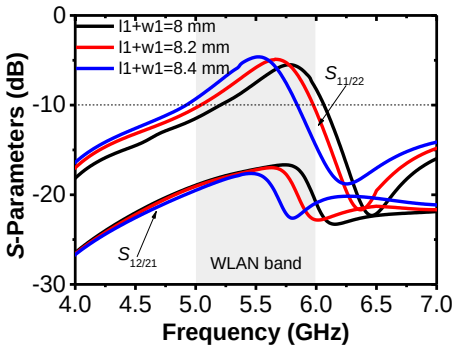

(a)

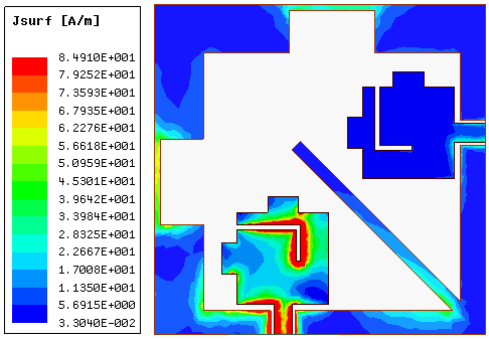

(b)

Fig. 5. Simulated S-parameters for different $l1 + w1$ (a), and surface current distributions of antenna IV at 5.5 GHz (b).

III. MEASURED RESULTS

The proposed eight-port UWB MIMO slot antenna has fabricated and measured to verify the simulation results. The port 1 is measured and other ports ceased with a 50 Ω load during the measurement.

A. S-parameters

The *S*-parameters of the fabricated antenna are presented in Figs. 6-7. There is a superb settlement between simulated and measured results. Some discrepancies

can be seen, which may be caused by the manufacture tolerance, SMA connector and the fluctuation of the dielectric constant of FR4. Measured outcomes show that the proposed MIMO antenna operates from about 3.1 GHz to 11 GHz with $S_{11/22} < -10$ dB except for a notched band from 5 GHz to 6 GHz and $S_{12\text{-}18} < -15$ dB.

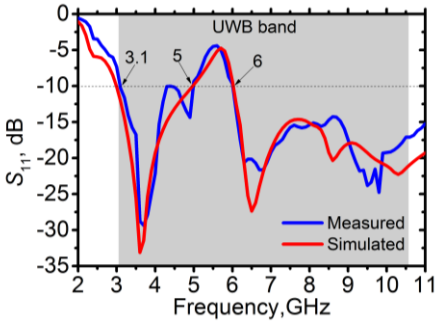

Fig. 6. The measured and simulated S_{11} of the eight-port UWB MIMO antenna.

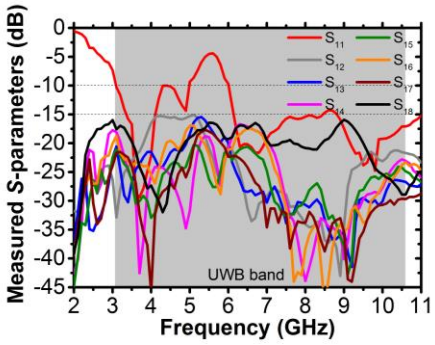

Fig. 7. The measured *S*-parameters of the eight-port UWB MIMO antenna.

B. Radiation performance

Three frequency points (4 GHz, 7 GHz, and 10 GHz) are selected to indicate the radiation pattern for low frequency, middle frequency and high frequency in the UWB band, respectively. Figures 8 (a-c) illustrate the radiation pattern of UWB MIMO antenna in E-plane (xoz-plane) and H-plane (xoy-plane). It can be realized that the radiation pattern in both E-plane and H-plane are quasi-omnidirectional. Besides this, the peak gain and radiation efficiencies of the proposed MIMO antenna is shown in Fig. 8 (d). The peak gain varies 1.524 dBi to 2.83 dBi and radiation efficiencies varies 74.7% to 85% over the UWB spectrum except for the notched band. At the notched band (5.15 GHz-5.85 GHz), there is a deep drop in Peak Gain, this dramatical drop in gain enables the antenna to avoid crosstalk from signals in WLAN band and operate in the high interference surroundings.

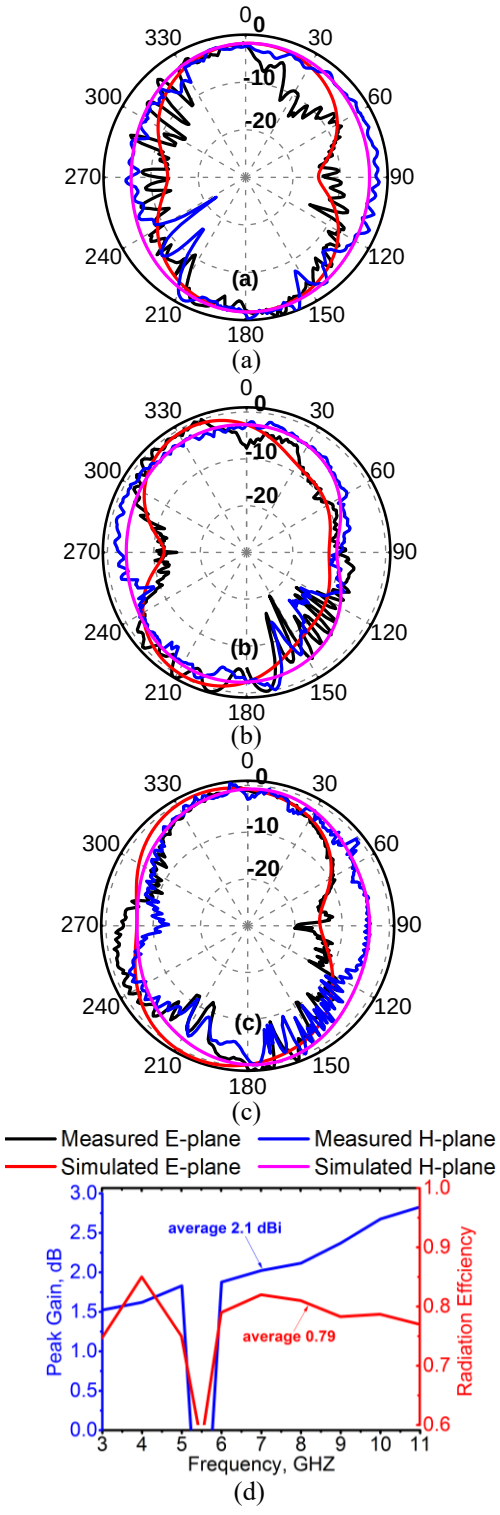

Fig. 8. Simulated and measured radiation pattern of the UWB MIMO slot antenna at: (a) 4 GHz, (b) 7 GHz, (c) and 10 GHz. (d) The measured peak gain and radiation efficiencies of the UWB MIMO slot antenna vs frequency.

C. MIMO performance

The MIMO performance of the proposed antenna is analyzed and figured out by the ECC and TARC. The value of ECC signifies how the two antennas are coupled to each other. For achieving good channel characteristics and antenna diversity, the ECC must be less than 0.05. The ECC between two elements can be calculated from the S-parameters using the formula (3) when the radiation efficiency of the MIMO antenna is high [13]:

$$ECC = \frac{|S_{11}^{*}S_{12}+S_{21}^{*}S_{22}|^2}{(1-|S_{11}|^2-|S_{12}|^2)(1-|S_{21}|^2-|S_{22}|^2)}. \quad (3)$$

For MIMO antenna systems, traditional scattering matrixes are not sufficient to predict the real antenna performance. TARC which take coupling effect into account has been proposed. The TARC for the 8-port MIMO antenna could be described as [14]:

$$TARC = -\sqrt{(\sum_{i=1}^{8}(\sum_{k=1}^{8}S_{ik})^2)/8}. \quad (4)$$

As depicted in Fig. 9, the measured ECC is less than 0.02 and TARC is less than -20 dB for the UWB band.

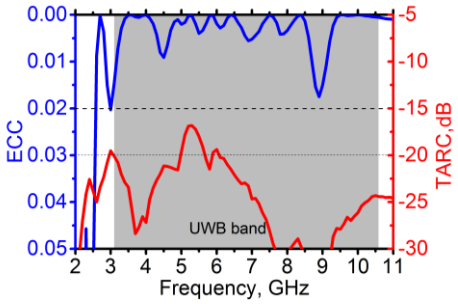

Fig. 9. Measured ECC and TARC of the proposed UWB MIMO antenna against frequency.

IV. CONCLUSION

In this paper, a compact eight-port UWB MIMO antenna with WLAN band-notched characteristics in a size of 54×54×0.8 mm^3 has been designed successfully. Measured outcomes show that the designed antenna exhibits S_{11} < -10 dB, high isolation better than 15 dB, peak gain varies 1.524 dBi to 2.83 dBi, radiation efficiencies varies 74.7% to 85%, ECC < 0.02 and TARC < -20 dB over the UWB band except for a notched band at 5-6 GHz. In addition, the proposed scheme retains full planarity of the UWB MIMO antenna, involves simple and straightforward fabrication process. All the measured, simulated and calculated results indicate the proposed eight-port MIMO antenna is a good candidate for UWB system.

REFERENCES

[1] Federal Communication Commission, "First report and order Revision of part 15 of the Commission's rules regarding ultra-wideband transmission system," *FCC 02 48*, 2002.

[2] I. Oppermann, M. Hamalainen, and J. Iinatti, *UWB Theory and Applications.* New York: Wiley, ch. 1, pp. 3-4, 2004.

[3] A. J. Paulraj, D. A. Gore, R. U. Nabar, and H. Bolcskei, "An overview of MIMO communications-A key to gigabit wireless," *Proceedings of the IEEE*, vol. 92, pp. 198-218, 2004.

[4] T. Kaiser, F. Zheng, and E. Dimitrov, "An overview of ultrawide-band systems with MIMO," *Proceedings of the IEEE*, vol. 97, pp. 285-312, 2009.

[5] Q. Li, A. P. Feresidis, M. Mavridou, and P. S. Hall, "Miniaturized double-layer EBG structures for broadband mutual coupling reduction between UWB monopoles," *IEEE Transactions on Antennas & Propagation*, vol. 63, no. 2, pp. 1168-1171, 2015.

[6] S. Zhang, Z. Ying, J. Xiong, and S. He, "Ultra-wideband MIMO/diversity antennas with a tree-like structure to enhance wideband isolation," *IEEE Antennas Wireless and Propagation Letters*, vol. 8, pp. 1279-1282, 2009.

[7] L. Liu, S. W. Cheung, and T. I. Yuk, "Compact MIMO antenna for portable UWB applications with band-notched characteristic," [J]. *IEEE Transactions on Antennas & Propagation*, vol. 63, no. 3, pp. 1917-1924, 2015.

[8] M. S. Khan, A. Capobianco, S. M. Asif, D. E. Anagnostou, R. M. Shubair, and B. D. Braaten, "A compact CSRR enabled UWB diversity antenna," *IEEE Antennas & Wireless Propagation Letters*, 2016.

[9] X. L. Liu, Z. D. Wang, Y. Z. Yin, J. Ren, and J. J. Wu, "A compact ultra-wideband MIMO antenna using QSCA for high isolation," [J]. *IEEE Antennas & Wireless Propagation Letters*, vol. 13, pp. 1497-1500, 2014.

[10] C. M. Luo, J. S. Hong, and L. L. Zhong, "Isolation enhancement of a very compact UWB-MIMO slot antenna with two defected ground structures," [J]. *IEEE Antennas & Wireless Propagation Letters*, vol. 14, pp. 1766-1769, 2015.

[11] K. G. Thomas and M. Sreenivasan, "A simple ultrawideband planar rectangular printed antenna with band dispensation," *IEEE Trans. Antennas Propag.*, vol. 58, no. 1, pp. 27-34, Jan. 2010.

[12] R. Chandel, A. K. Gautam, and K. Rambabu, "Tapered fed compact UWB MIMO-diversity antenna with dual band-notched characteristics," *IEEE Transactions on Antennas & Propagation*, vol. 1, no. 1, pp. 99-107, 2018.

[13] S. Blanch, J. Romeu, and I. Corbella, "Exact representation of antenna system diversity performance from input parameter description," *Electron. Lett.*, vol. 39, no. 9, pp. 705-707, 2003.

[14] S. I. Jafri, R. Saleem, M. F. Shafique, and A. K. Brown, "Compact reconfigurable multiple-input

multiple-output antenna for ultra wideband applications," *IET Microwaves, Antennas & Propagation*, vol. 10, pp. 413-419, 2015.

Jing-song Hong received the B.Sc. degree in Electromagnetics from Lanzhou University, China, in 1991, and the M.Sc. and Ph. D. degrees in Electrical Engineering from the University of Electronic Science and Technology of China (UESTC), in 2000 and 2005, respectively. From 1999 to 2002, he was a Research Assistant with the City University of Hong Kong. He is now a Professor with UESTC. His research interest includes the use of numerical techniques in electromagnetics and the use of microwave methods for materials characterization and processing.

Li-yan Chen was born in Wuhan, China. He received his B.S. degree from Shanxi University in 2016. He is now working towards his M.S. degree in Radio Physics at the University of Electronic Science and Technology of China (UESTC). His interests include MIMO antenna and MIMO system.

Wei-si Zhou was born in Anqing, China. He received his Bachelor degree from Shandong University of Technology in 2018. Since September 2018 he is a master student in the major of Electronics and Communications Engineering at the University of Electronic Science and Technology of China (UESTC). His interests include MIMO antenna and UWB antenna.

Muhammad Amin was born in D.I.Khan, Pakistan. He received his master degree from Gomal University D.I.Khan Pakistan in 2003. Since September 2014 he is a Ph.D. student in the major of Radio Physics at the University of Electronic Science and Technology of China (UESTC). His interests include antenna technology and wireless communication technology.

Design of Polarization Reconfigurable Patch Antenna for Wireless Communications

A. Priya [1*], S. Kaja Mohideen [1], and Manavalan Saravanan [2]

[1] Department of Electronics and Communication Engineering
[1] B.S. Abdur Rahman Crescent Institute of Science and Technology, Chennai, India
priyamarish@crescent.education*, kajamohideen@crescent.education

[2] Department of Electronics and Communication Engineering
Vel Tech Rangarajan Dr. Sagunthala R&D Institute of Science and Technology, Chennai, India
msarawins@ieee.org

Abstract — A single fed circularly polarized reconfigurable patch antenna is proposed. The antenna consists of a radiating patch incorporated with an H-shaped slot at its center. Four ultra-miniature switches are used for polarization reconfiguration. The antenna is designed to operate at the center frequency of 2.357 GHz. The antenna achieves either left-hand polarization or right-hand polarization depending upon switching of corresponding switches. The antenna parameters are simulated using Ansoft high-frequency structure simulator and are validated using an Agilent network analyzer (N9925A) and antenna test systems. The antenna achieves a good impedance match of 120MHz between 2.26GHz – 2.38GHz band and achieves low cross-polarization isolation of -22.82 dB for RHCP and -21.77 dB for LHCP configurations at its operating frequency. The antenna finds application in areas of modern wireless communication.

Index Terms — Antenna feeds, antenna radiation patterns, circular polarization, microstrip antennas, slot antennas.

I. INTRODUCTION

Polarization reconfigurable antenna plays a major role in modern wireless communication system due to antenna orientation restriction and to enhance channel capacity and suppression of multipath interference. Therefore designing such antennas are highly desirable for wireless communications. In general, polarization reconfiguration is achieved by reconfiguring radiating element by means of pin diodes, RF switches or by reconfiguring feed network. Lin and Wong [1] demonstrated polarization reconfigurable antenna by reconfiguring feeding network through sequential excitation by means of pin diodes in the feed network. In [2], an aperture coupled polarization reconfigurable antenna is proposed which consists of controllable RF switches on a cross aperture to excite radiating element. A most common method of achieving polarization reconfiguration is by etching a slot on radiating element and reconfiguring it by means of pin diodes [3]-[4] to bridge the gap between the slots. A reconfigurable monopole antenna integrated with mushroom like meta-surface to improve antenna performance is presented in [5]. Panahi et al. [6] demonstrated a simple reconfigurable antenna using two pin diodes. Though the antenna achieves polarization diversity with minimum number of diodes, the axial ratio bandwidth of the antenna is far moved from resonant frequency of the antenna. Further the use of pin diodes in polarization reconfiguration requires additional biasing circuit and has to be carefully designed in such a way that it should not affect antenna performance characteristics.

Another approach for changing polarization states is achieved by modifying the feed network by means of PIN diodes, RF switches or by using varactor diodes. H.Sun and S.Sun [7] proposed reconfigurable antenna by reconfiguring feed network to induce phase difference in the output ports. In [8], polarization diversity is achieved by modifying feed network which gives outputs of different phases by means of v shaped coupling strip loaded in the feed network. This technique of reconfiguring feed network to achieve polarization diversity requires additional space for feeding network and also it is highly dependent on performance characteristics and affects its performance drastically when it is not properly designed. Recently liquid dielectric materials are widely studied for polarization reconfiguration [9]-[12]. Though these methods give linear control over polarization, it is difficult to integrate with most of the miniature devices due to its complexity in their control mechanism and requires additional space for the fluid tank. Varactor diode is used recently to reconfigure the characteristics of the antenna [13]. By varying the bias voltage, the capacitance of the varactor

Submitted On: January 3, 2020
Accepted On: May 21, 2020
https://doi.org/10.47037/2020.ACES.J.350807

diode is changed and thereby tuning the performance of the antenna. Polarization reconfigurability is achieved using ultra miniature diodes as in [14] and [15] where two diodes are placed in the symmetrical slots of the patch antenna to get reconfigurability in polarization.

In this paper, a compact polarization reconfigurable patch antenna operating at 2.3 GHz band with a center frequency of 2.357 GHz is proposed. An H-shaped slot is etched in the radiating patch. Four miniature tactile switches (2mm x 3mm x 0.6mm) are used for switching the nature of polarization. The use of tactile switch eliminates the need of biasing circuit and hence reduces the antenna complexity and fabrication cost. The antenna achieves good 3-dB axial ratio beamwidth and better cross polarization isolation in operating band. The antenna is modeled using ansys electromagnetic tool and is fabricated over FR_4 substrate. The antenna performance is validated using network analyzer and antenna radiation pattern test system. The measured results are in good agreement with the simulated results and are compared with other traditional techniques.

II. ANTENNA DESIGN CONSIDERATIONS

Initially a rectangular Microstrip antenna as shown in Fig. 1 (a) is modelled and its dimensions are calculated from equation (1)-(2):

$$W = \frac{c}{2f_0\sqrt{\frac{(\varepsilon_r+1)}{2}}}, \quad (1)$$

$$L_{eff} = \frac{c}{2f_0\sqrt{\varepsilon_{eff}}}. \quad (2)$$

A slot of appropriate dimension is made along diagonal axis as shown in Figs. 1 (b) and 1 (c) to induce 90 degree phase difference between two orthogonal field components E_x and E_y and generates hand circular polarization. Parametric analysis of slot dimensions are carried to optimize antenna axial ratio performance to achieve better circular polarization purity at its operating band. Switches are used at appropriate places to switch between two geometries (Figs. 1 (b) and 1 (c)).

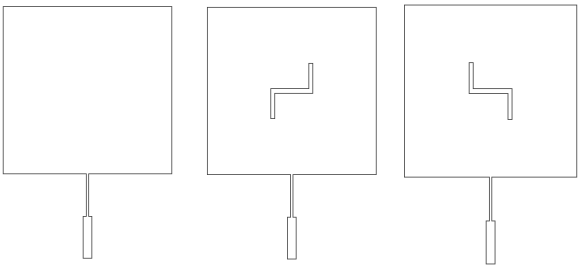

(a) LP (b) LHCP (c) RHCP

Fig. 1. Design geometries.

Figure 2 shows antenna model with H-shaped slot incorporated in the radiating element. The antenna is fabricated on fire retardant dielectric substrate (FR4) having a relative permittivity of $\varepsilon_r = 4.4$. In order to have low profile thickness, the substrate is chosen to have a thickness of 1.6 mm and overall length and width of the substrate is 57 mm x 57mm.

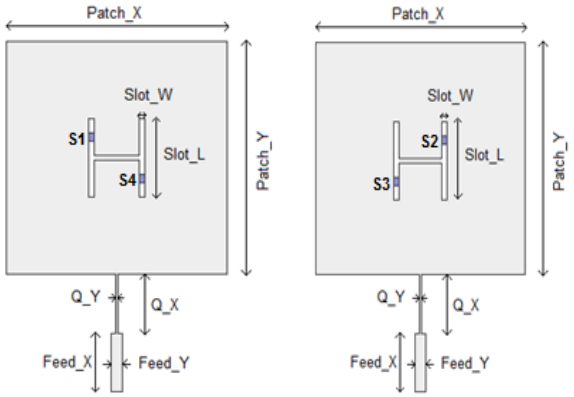

(a) RHCP (b) LHCP

Fig. 2. Geometry of proposed antenna.

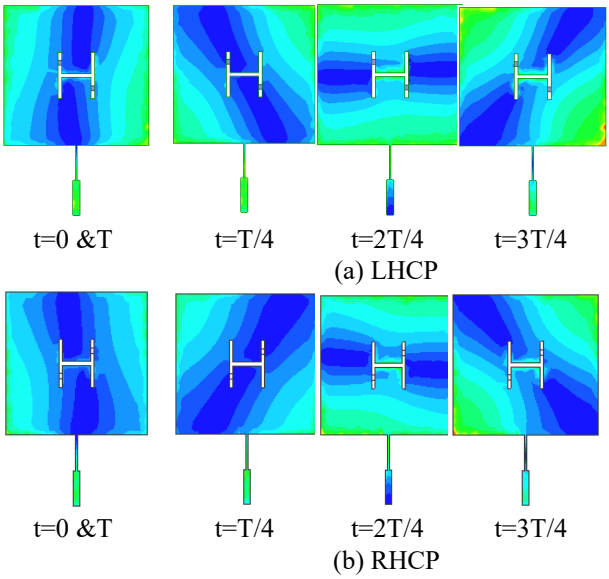

(a) LHCP (b) RHCP

Fig. 3. Simulated surface current distribution.

Four ultra-miniature tactile switches (TL3780) are used to reconfigure the polarization characteristics of the antenna. The switches are placed in the H-slot and establish a contact between the slot regions by pressing (100 gram-force) the switch which indicates ON state. According to the datasheet given by the manufacturer, the switch gives 500 mΩ initial contact resistance when in contact (ON state) and 50 MΩ when it is open (OFF state).The polarization reconfiguration is achieved by switching the appropriate pair of switches and thereby reconfiguring antenna geometry. Compared to traditional techniques to reconfigure polarization, the proposed

method doesn't require any additional biasing circuit (as in pin diodes) or additional space for feeding network to achieve polarization diversity, and hence it is easy to integrate with other high frequency circuit components. Figure 3 shows the current distribution over the surface of the radiating patch element. The polarization reconfiguration is achieved by suitably switching ON the ultra-miniature tactile switch pair which produces two orthogonal modes which are spatially orthogonal, have equal magnitude and are in phase quadrature. Switch S2 and S3 is switched ON to get Left Hand Circular Polarization (LHCP) as shown in Fig. 3 (a) and Switch S1 and S4 is Switched ON to get Right Hand Circular Polarization (RHCP) as shown in Fig. 3 (b).

III. PARAMETRIC ANALYSIS

Parametric analysis is carried on the slot dimension of the antenna and its performance is discussed. The length of the slot is given as primary importance since it greatly affects the operating frequency and also the purity of polarization. Figure 4 shows a variation of slot length and its effect on the performance of reflection coefficient (dB). It is observed that the reflection coefficient curve moves towards to the lower band with an increase in slot length. This is due to the fact that, an increase in the length of slot increases the electrical length of the antenna and hence the antenna resonates at lower bands. The increase in the length of the slot also affects the purity of polarization. The length of the slot is chosen in such a way that, the electric field component E_x has 90 degree phase delay with respect to E_y field component.

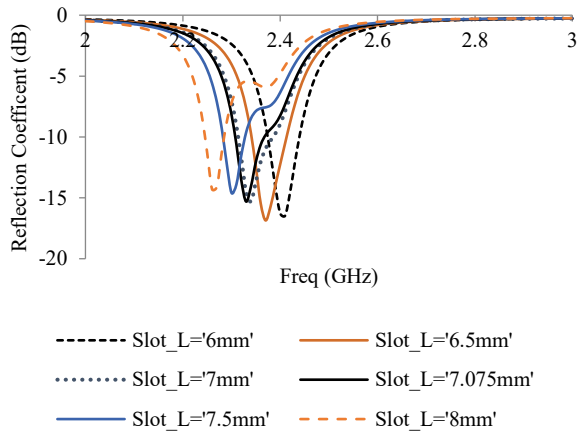

Fig. 4. Variation of reflection coefficient with respect to slot length.

IV. RESULTS AND DISCUSSIONS

Based on the parametric analysis discussed above, the optimum slot length, the dimension of antenna model is obtained and is given in Table 1.

Table 1: Antenna specification

Parameters	Specifications
Operating Frequency	2.34 GHz
Sub_X*Sub_Y*Sub_Z	57mm*57mm*1.6mm
Patch_X*Patch_Y	28.3mm * 28.3mm
Slot_L*Slot_W	7.075mm*0.705mm
Q_X*Q_Y	7.075mm*0.353mm
Feed_X*Feed_Y	7.075mm*1.415mm

The proposed model is fabricated on FR4 substrate as shown in Fig. 5. The model is integrated with switches at appropriate gap regions and are connected with 50 ohm SMA connector.

Fig. 5. Fabricated antenna.

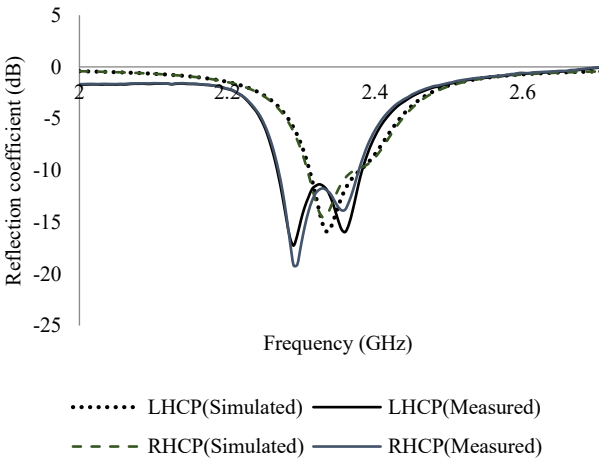

Fig. 6. Reflection coefficient (dB).

The reflection coefficient curve measured for both LHCP and RHCP polarization is compared with corresponding simulation results and are shown in Fig. 6 and shows that the antenna achieves a -10dB impedance bandwidth of 120 MHz (2.26GHz-2.38GHz) for both LHCP configuration and RHCP configuration and is much suitable for WLAN/WiMAX applications. The simulated and measured radiation pattern for the proposed antenna model operating at 2.34 GHz is shown in Fig. 7. The LHCP radiation pattern is taken by turning on switches S2 and S3 and RHCP radiation pattern is

taken by turning on switches S1 and S4. The simulation results agree with measured results for both LHCP and RHCP configurations. The antenna gives symmetrical radiation performance around the zenith. The small difference in pattern between simulated and measured results is due to additional resistance created by the switches during on state and also due to fabrication loss and antenna alignment losses.

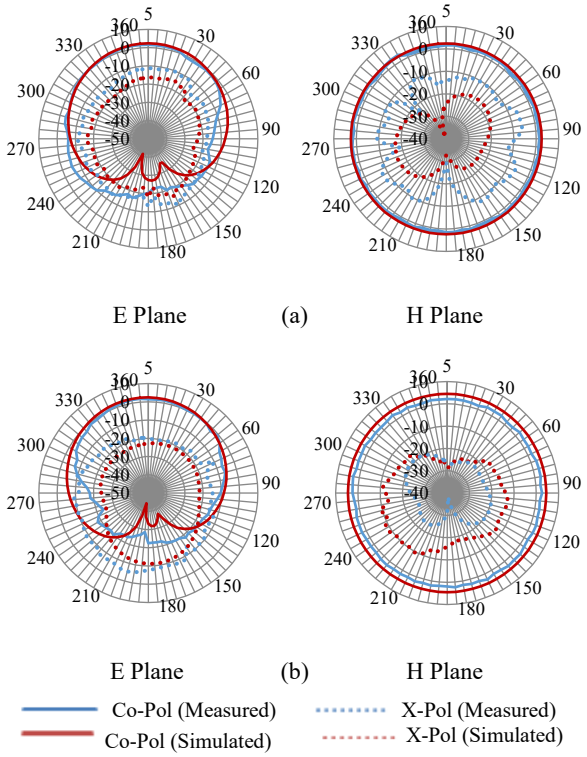

Fig. 7. Simulated and measured radiation pattern of (a) LHCP and (b) RHCP.

Figure 8 shows a variation of axial ratio against frequencies for both LHCP and RHCP configurations. The antenna gives minimum axial ratio at operating frequency for both the configurations and achieves a 3-dB axial ratio bandwidth of 60MHz (2.32GHz – 2.38GHz) for LHCP and 50MHz (2.32GHz – 2.37 GHz) for RHCP configuration.

Figure 9 shows axial ratio beamwidth characteristics of both LHCP and RHCP configurations. It is observed that the antenna achieves a good axial ratio over a wide beam angle of -50^0 to 40^0 for LHCP and -50^0 to 45^0 for RHCP.

The antenna gives a simulated gain of around 6.92dBic for LHCP and 6.84dBic for RHCP.

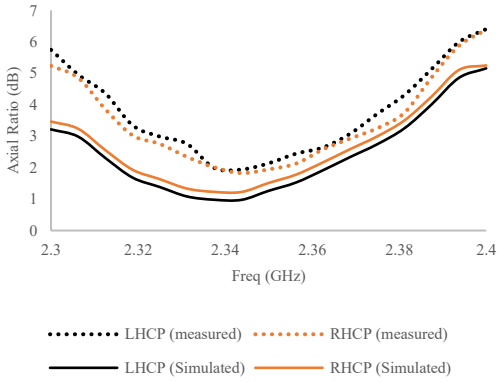

Fig. 8. Variation of axial ratio (dB) against operating band (GHz).

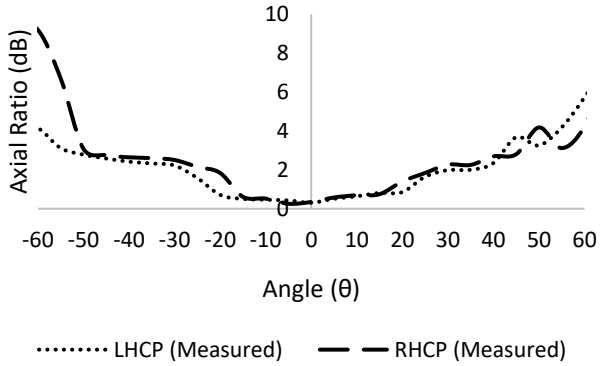

Fig. 9. Variation of axial ratio (dB) against beam angle (θ).

Figure 10 shows the setup used to measure antenna radiation pattern for the proposed model. The antenna is placed inside anechoic chamber and mounted over rotating turn table controlled by precision stepper motor whose control angles are given form antenna measurement software. The measured gain is calculated using two antenna method. A standard pyramidal horn antenna having a gain of 9dB is used as a reference antenna. The distance between two antennas (R) is measured and the gain is calculated using Friis transmission equation given below:

$$\frac{P_r}{P_t} = \left(\frac{\lambda}{4\pi R}\right)^2 G_t G_r. \qquad (3)$$

Figure 11 presents the measured gain across the operating bandwidth for both modes. The antenna achieves a peak gain of 5.19 dBic for LHCP mode with efficiency of 50.1% and 5.17 dBic for RHCP mode with efficiency of 47.3%. The antenna also achieves cross

polarization isolation of -22.82 dB for RHCP and -21.77 dB for LHCP configurations at its operating frequency.

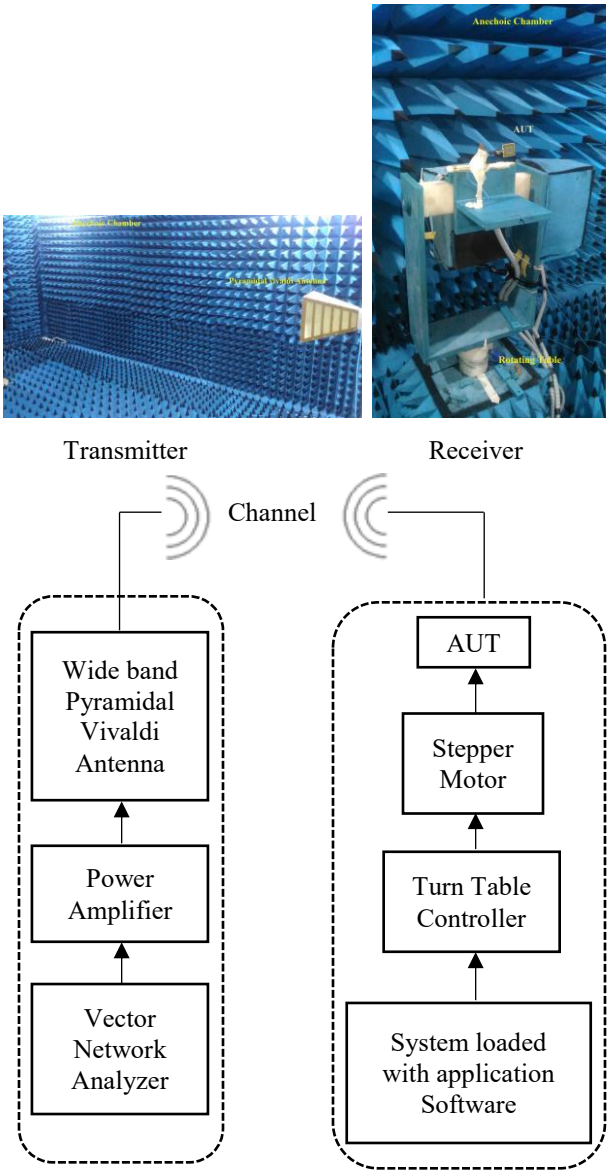

Fig. 10. Antenna measurement setup.

Table 2 gives performance comparison of proposed antenna with some of the conventional antenna. It is observed that the proposed antenna is compact and achieves good beam width characteristics with minimum number of switching elements and also achieves better cross polarization isolation in the operating band. However the proposed model operates at narrow band width and reduced radiation efficiency which can further improved by utilizing low loss dielectric substrate in place of FR_4 substrate.

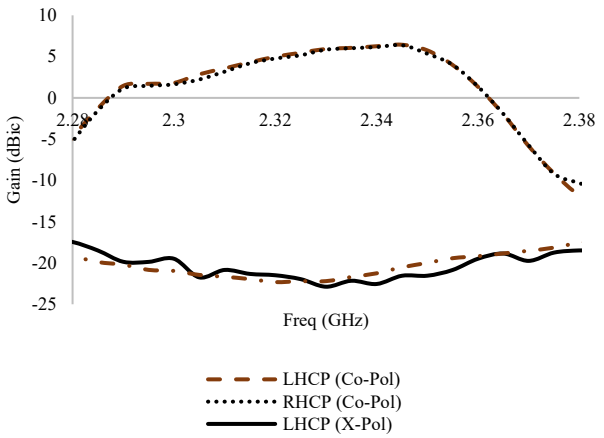

Fig. 11. Measured gain across the operating band for both modes.

Table 2: Performance comparison of proposed antenna

Parameters	[1]	[2]	[3]	[5]	Proposed Model
Size	0.80 λ x 0.80 λ x 0.26 λ	0.70 λ x 0.55 λ x 0.16 λ	7.28 λ x 2.08 λ x 0.06 λ	0.19λ x 0.19λ x 0.14λ	0.43 λ x 0.43 λ x 0.01 λ
Switching Element	8 Pin diodes	9 DPDT	2 Pin diodes	8 pin diodes	4 tactical Switches
3dB AR Band width (GHz)	(1.5 – 1.9) GHz	(1.42-1.88) GHz	(2.25-2.47) GHz	(5.68-5.9) GHz	(2.26 – 2.36) GHz
3dB AR Beam width	90^0 (LHCP, RHCP)	64^0 (LHCP) 46^0 (RHCP)	53^0 ($+45^0$ LP), 50^0 (-45^0 LP),	60^0 (LHCP, RHCP)	90^0 (LHCP) 95^0 (RHCP)
Cross Polarization Isolation	-20 dB (LHCP, RHCP)	-13 dB (LHCP, RHCP)	-10 dB (LHCP, RHCP)	-15 dB (LHCP, RHCP)	-21.77 dB (LHCP) -22.82 dB (RHCP)

V. CONCLUSION

In this paper, a compact H shaped slot circularly polarized reconfigurable antenna has been developed. The antenna is designed to operate at 2.3 GHz band. The proposed antenna achieves polarization diversity by means of miniature tactile switches which eliminates the need of additional biasing circuit or feed network for switching polarization state. The antenna achieves better cross polarization isolation of -22.82 dB for RHCP and -21.77 dB for LHCP configurations and also a wide 3-dB axial ratio beam width of 90^0 ($-50^0 \leq AR \leq 40^0$) for LHCP and 95^0($-50^0 \leq AR \leq 45^0$) for RHCP configurations, and hence it better suitable for modern wireless application which prefer CP antenna characteristics.

REFERENCES

[1] W. Lin and H. Wong, "Wideband circular polarization reconfigurable antenna," in *IEEE Transactions on Antennas and Propagation*, vol. 63, no. 12, pp. 5938-5944, Dec. 2015. doi: 10.1109/

TAP.2015.2489210.

[2] W. Lin and H. Wong, "Polarization reconfigurable aperture-fed patch antenna and array," in *IEEE Access*, vol. 4, pp. 1510-1517, 2016. doi: 10.1109/ACCESS.2016.2552488.

[3] B. Anantha, L. Meruguand, and P. V. D. S. Rao, "A novel single feed frequency and polarization reconfigurable microstrip patch antenna," in *AEU - International Journal of Electronics and Communications*, vol. 72, pp. 8-16, Feb. 2017.

[4] A. Priya, S. K. Mohideen, and M. Saravanan, "Multi-state reconfigurable antenna for wireless communications," *Journal of Electrical Engineering & Technology*, vol. 15, pp. 251-258, 2020. https://doi.org/10.1007/s42835-019-00321-8.

[5] Y. F. Cao, S. W. Cheung, and T. I. Yuk, "Dual-cap mushroom-like metasurface used in CP reconfigurable monopole antenna for performance enhancement," in *IEEE Transactions on Antennas and Propagation*, vol. 63, no. 12, pp. 5949-5955, Dec. 2015. doi: 10.1109/TAP.2015.2489682.

[6] A. Panahi, X. L. Bao, K. Yang, O. O'Conchubhair, and M. J. Ammann, "A simple polarization reconfigurable printed monopole antenna," in *IEEE Transactions on Antennas and Propagation*, vol. 63, no. 11, pp. 5129-5134, Nov. 2015. doi: 10.1109/TAP.2015.2474745.

[7] H. Sun and S. Sun, "A novel reconfigurable feeding network for quad-polarization-agile antenna design," in *IEEE Transactions on Antennas and Propagation*, vol. 64, no. 1, pp. 311-316, Jan. 2016. doi: 10.1109/TAP.2015.2497350.

[8] J. S. Row, W. L. Liu, and T. R. Chen, "Circular polarization and polarization reconfigurable designs for annular slot antennas," in *IEEE Transactions on Antennas and Propagation*, vol. 60, no. 12, pp. 5998-6002, Dec. 2012.

[9] Y. H. Qian and Q. X. Chu, "A polarization-reconfigurable water-loaded microstrip antenna," in *IEEE Antennas and Wireless Propagation Letters*, vol. 16, pp. 2179-2182, 2017. doi: 10.1109/LAWP.2017.2703821.

[10] Z. Chen, H. Wong, K. Wang, and J. Xiang, "Polarization-reconfigurable antennas with different liquid solutions," *2019 IEEE Conference on Antenna Measurements & Applications (CAMA)*, Kuta, Bali, Indonesia, pp. 138-140, 2019. doi: 10.1109/CAMA47423.2019.8959630.

[11] M. Khan, G. Hayes, S. Zhang, M. Dickey, and G. Lazzi, "A pressure responsive fluidic microstrip open stub resonator using a liquid metal alloy," *IEEE Microw. Wireless Compon. Lett*., vol. 22, no. 11, pp. 577-579, Nov. 2012.

[12] G. Xu, J. Shu, H. Peng, Y. Zhang, W. Yin, and J. Mao, "Liquid crystal-based polarization reconfigurable cross-slot fed patch antenna," *2019 IEEE International Conference on Computational Electromagnetics (ICCEM)*, Shanghai, China, pp. 1-3, 2019. doi: 10.1109/COMPEM.2019.8779107.

[13] B. Liang, B. Sanz-Izquierdo, E. A. Parker, and J. C. Batchelor, "A frequency and polarization reconfigurable circularly polarized antenna using active EBG structure for satellite navigation," in *IEEE Transactions on Antennas and Propagation*, vol. 63, no. 1, pp. 33-40, Jan. 2015. doi: 10.1109/TAP.2014.2367537.

[14] M. Saravanan and M. J. S. Rangachar," Design of pin loaded reconfigurable patch antenna for wireless communications," *ACES Journal*, vol. 34, no. 10, pp. 1535-1541, Oct. 2019.

[15] Q. Chen, J. Li, G. Yang, B. Cao, and Z. Zhang, "A polarization-reconfigurable high-gain microstrip antenna," in *IEEE Transactions on Antennas and Propagation*, vol. 67, no. 5, pp. 3461-3466, May 2019. doi: 10.1109/TAP.2019.2902750.

Design of Dual-Band Printed-Dipole Array Antenna with Omni-directional Radiation Behaviour

Jean-Marie Floch [1,2], Ameni Mersani [3], Bandar Hakim [1], Khaled Sedraoui [1], and Hatem Rmili [1]

[1] King Abdulaziz University, Electrical and Computer Engineering Department
P.O. Box 80204, Jeddah 21589, Saudi Arabia

[2] IETR, INSA, 20 avenue des Buttes de Coësmes, 35708 Rennes, France
hmrmili@kau.edu.sa

[3] University of Tunis El Manar, Faculty of Sciences Tunisia
Microwave Electronics Research Laboratory, LR18ES43, 2092 Tunis, Tunisia

Abstract – In this paper, we present a compact array of 4 printed dipole antennas with ground plane, operating at 2.7 GHz and 5.2 GHz, designed for base station applications. First, the elementary printed dipole antenna, selected for its small size and good performances, is described. However, this kind of structures cannot cover two bands at the same time, which justify our proposal of a 4-elemnts network. Next, the 4-elements array is simulated, optimized, and measured to proof its performances with good agreement between the measurements and simulations. The measured gain of the 4-dipoles array is 4.21 dBi and 6.15 dBi for both operating frequencies 2.7 GHz and 5.2 GHz, respectively.

Index Terms – Dual-band array, horizontal polarization, Omnidirectional radiation pattern, printed dipole.

I. INTRODUCTION

The last few years have seen the emergence of a wide variety of wireless networks, and a new need has arisen: that of being permanently connected to a network wherever you are [1]. We then see the appearance of many types of networks: telephony networks, broadband broadcasting, local or very extensive via terrestrial or space communications. Thus, the development of these wireless networks requires technological advances in electronic components, computer software, coding techniques and antennas. Indeed, the antenna is one of the key points of wireless networks since this element is the last link in the chain allowing transmission and reception of the signal and therefore of the information contained therein [2-7]. The base station antenna must be adapted to each link according to the desired coverage. The antenna must not only cover standard but must also keep a compact size and good efficiency. Different types of antennas can be used such as patch antennas, dielectric resonator antennas and dipole antennas.

The printed dipole is one of the most used antenna structures in wireless communication systems, thanks to its advantages (low cost, low profile, easy to integrate with other electronics and omnidirectional radiation pattern) with several designs presented in the literature [8]. For a dipole, a natural resonance appears when the dimension of the antenna is close to half the wavelength. The size of the dipole antenna can be reduced with the ground plane effect. According to image theory [9], the ground plane creates an image of the antenna; the combination of the antenna and its image plays an identical role to that of a dipole. Nowadays we are also seeing more and more multi-standard wireless communication devices, especially with the evolution of technologies like 4G, LTE, 5G, which requires multi-band antennas for good coverage at multi-operating frequencies. Some techniques used to design these types of antenna have also been described in the literature. Among these techniques, we mention the addition of slots [10,11] and parasites [12,13]. To meet this growing need to integrate several standards and new applications in the same device, new concepts of miniature and multi-frequency antennas are the subject of much research. Several techniques identified in the literature to achieve significant directivities with compact antennas. These techniques include adding a reflector [14,15], Huygens sources [16,17], integrating charges [18], using parasitic elements within the Alford loop antennas [3] or antenna arrays [19,20].

Antenna networks represent one of the methods for obtaining miniature structures. This technique is based on the combination of radiation of multiple compact sources to increase the directivity of the network. Optimizing the network factor by controlling the coupling phenomena makes it possible to increase the

Submitted On: February 14, 2020
Accepted On: May 17, 2020
https://doi.org/10.47037/2020.ACES.J.350808

directivity. In [20], a 4 × 4 array of compact wideband dual-polarized printed dipole antenna for 5G base station application was presented with a dimension of 200 mm × 200 mm. A rectangular-shaped reflector is also used to enhance the stability of its radiation patterns over the operating frequencies. It achieves a 22% size reduction compared to the conventional printed half-wavelength cross-dipole. A dual-broadband printed dipole antenna for 2G/3G/4G base station applications is proposed in [21]. The dimension of the antenna is 144mm×132mm× 2mm. The gains are about 4-5 dBi and 5-6 dBi for both resonance frequencies.

In this paper, a compact network that can operate on two different frequencies is presented as summarised in Table 1. The proposed antenna employs an array structure which allows to obtain compactness and high directivity and therefore ease of integration in base stations. First, we describe the elementary dipole which will serve as the basis for the realization of the network. In the second part, we present the design and realization of the network composed of 4 dipoles. Finally, we propose a realistic application of the network for a compact base-station. The simulation has been done using HFSS ANSYS and the measurements are made in a near field anechoic chamber (Starlab from MVG).

Table 1: Summary of the dimension and the gain of the dipole antenna of the literature

References	Application	Dimension (mm^2)	Maximum Gain (dBi)
[19]	5G	200 ×200	6
[20]	2G/3G/4G	144 × 132	6
This work	4G/5G	90 × 90	6.15

II. ELEMENTARY SOURCE

The elementary antenna consists on a printed dipole as shown in Fig. 1 [2]. The design parameters of the structure were optimized to operate at 2.7 GHz and 5.2 GHz. The printed dipole is made of two identical arms of length W2 and width b, printed on both sides of a Neltec NY9220 substrate of size 33 × 55 mm, thickness h = 0.8 mm, and relative permittivity ε_r = 2.2.

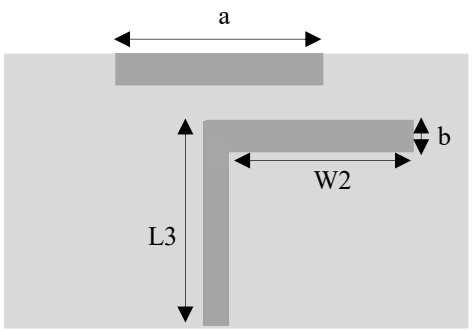

(a)

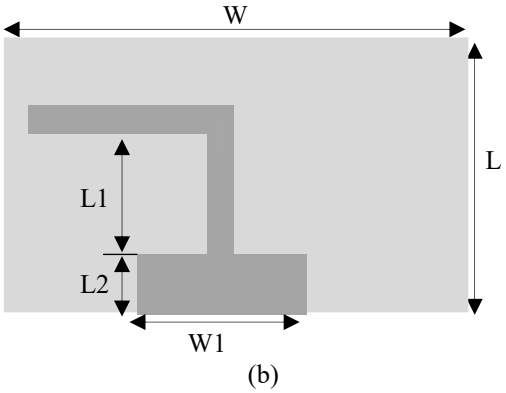

(b)

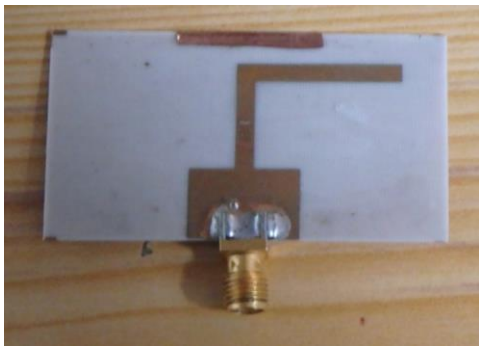

(c)

Fig. 1. Schema of the elementary printed dipole: (a) front view and (b) back view. (c) Photograph of the proposed antenna.

The two arms of the dipole of length approximately λ/2 are placed at λ/4 from of a small rectangular ground plane where the SMA connector is soldered. A parasitic strip of length λ/2 is placed at a distance of 2 mm from the dipole to operate at 5.2 GHz. Table 1 presents the dipole antenna dimensions. These dimensions were optimized to get good impedance matching, by using HFSS software.

Table 2: The elementary printed dipole antenna dimensions

Parameters	Values (mm)	Parameters	Values (mm)
W	55	a	20
L	33	b	2
L1	12	W1	8
L2	4	h	0.8
L3	18	W2	20

Both simulated and measured reflection coefficients of the antenna are shown in Fig. 2.

The simulated return loss of the dipole antenna shows a first resonating band which extends from 2.7 GHz to 3.4 GHz and a second one from 5.2 GHz to 5.4 GHz. However, the same performance was obtained in

simulation with a small frequency shift towards low frequencies, this may be due to the rapid realization of the prototype with copper ribbon.

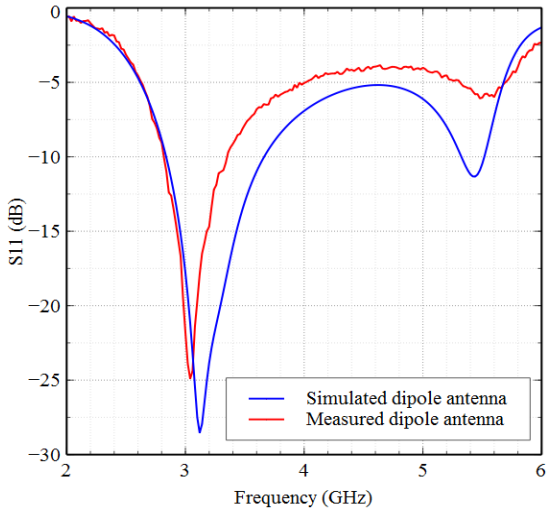

Fig. 2. Measured and simulated $|S_{11}|$ values of the dipole antenna versus the source frequency.

The radiation patterns were measured at resonance frequencies 2.7 GHz and 5.2 GHz, at the IETR institute, buy using the STARLAB MVG anechoic room facilities. At the resonance frequency, the radiation pattern is omnidirectional in the x-z plane with null along the dipole y-axis as shown in Fig. 3. The maximum simulated realized gain is about 2.75 dBi while the measurements show a gain of 2.7dBi.

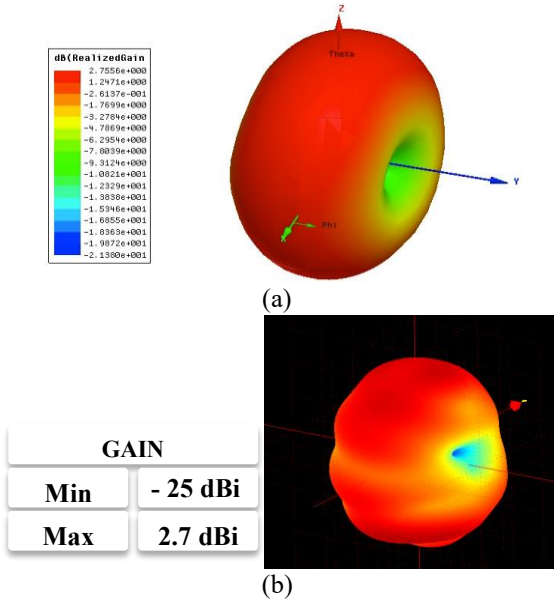

(a)

(b)

Fig. 3. 3D-radiation pattern at the resonance frequency 2.7 GHz: (a) simulation and (b) measurement.

As shown in Fig. 4 with the red simulated curve, ripples of ± 0.8 dBi in the H-plane are observed, much larger than in the blue measured curve.

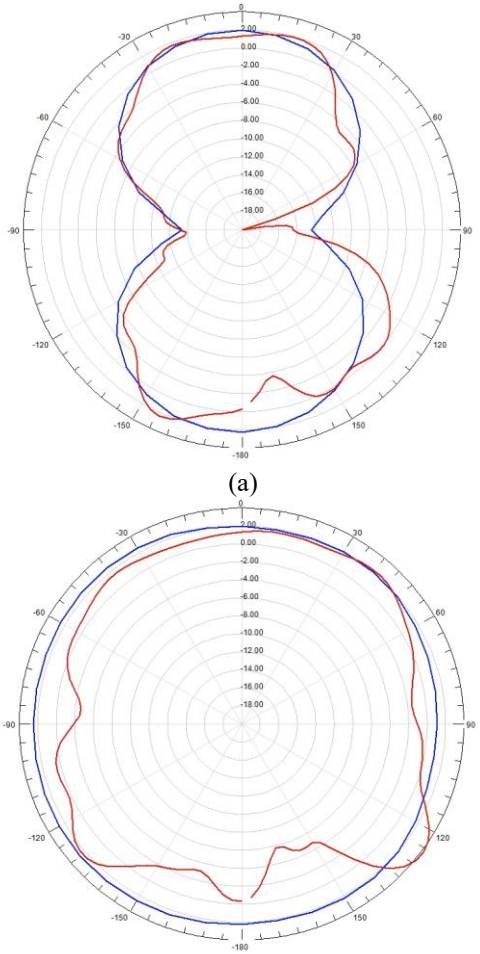

(a)

(b)

Fig. 4. Simulated and measured gain: (a) E-plane and (b) H-plane at 2.7 GHz (simulation in red and measurements in blue).

III. DIPOLE ARRAY

A. Dipole array design

Antenna networks represent one of the methods for obtaining miniature and directive structures. This technique is based on the combination of radiation from multiple compact sources to increase the directivity of the network [22]. Optimizing the network factor by mastering the coupling phenomena [23] makes it possible to increase the directivity. For this reason, a complete network of a 4-dipole array is designed as shown in Fig. 5.

The 4 dipoles with their parasitic elements are positioned at the 4 corners of a 60-mm diameter circular substrate. The power is supplied to the center of the

network with an SMA-connector welded on a small ground plane. The dipoles are positioned approximately at 12 mm from the small ground plane, which corresponds substantially to λ/4.

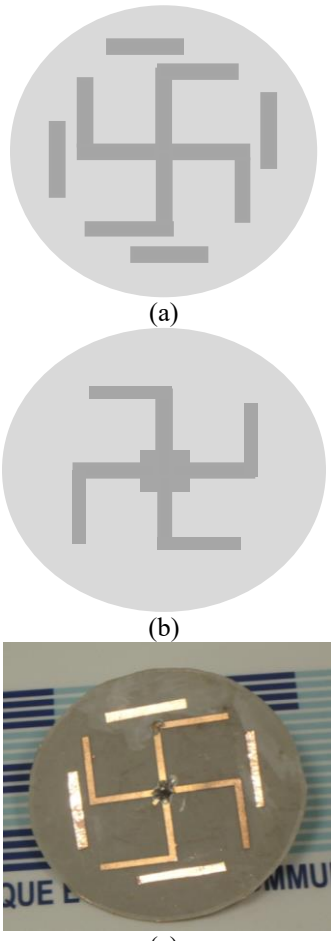

(a) (b) (c)

Fig. 5. Structure of proposed 4-dipole array: (a) front view and (b) back view. (c) Photograph of the manufactured prototype.

B. Reflection coefficient

Figure 6 shows the reflection coefficient of the 4-dipole array. There is a good agreement between the measurements and the simulation. The resonance frequency of the low band is located at 2600 MHz with a bandwidth of -10 dB between 2550 and 2700 MHz. For the higher band, the resonance frequency is at 5200 MHz with a bandwidth of -10 dB between 5100 MHz and 5520 MHz.

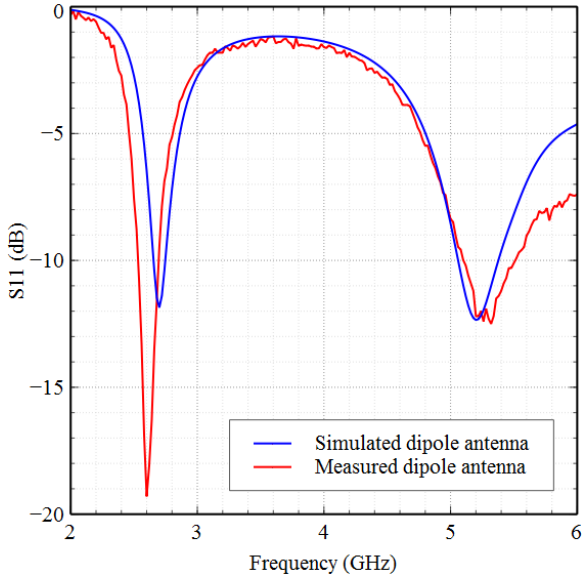

Fig. 6. Simulated and measured $|S_{11}|$ values of the 4 dipoles array versus the source frequency.

C. Gain and Directivity

The radiation patterns at the resonance frequencies are shown in Figs. 7, 8 and 9. Figures 7 and 8 show the simulated and measured 2-D radiation patterns of the proposed 4-dipoles array at 2.7 GHz and 5.2 GHz, in the E- plane and H- plane. The radiation patterns show good agreement between measurements and simulations for the two operating resonance frequencies. The structure has a directive radiation pattern with horizontal polarization.

At 2.7 GHz, we obtain a maximum gain of 2.5 dB in simulation and 2.4 dB in measurement. At the high operating frequency, we obtain 2.7 dB in simulation and 1.95 dB in measurement as shown in Figs. 7, 8 and 9.

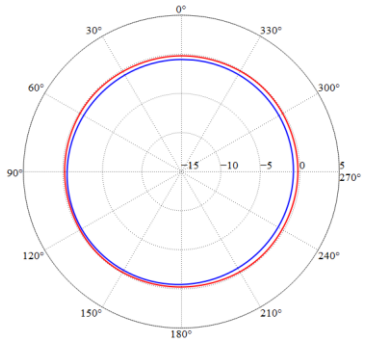

(a)

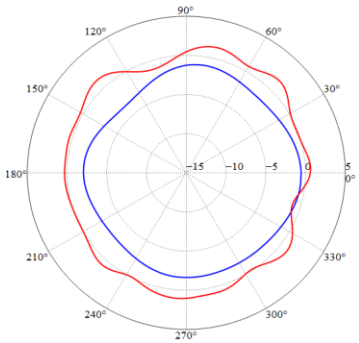

(b)

Fig. 7. Simulated and measured radiation patterns of the 4-dipoles array in the H-plane: (a) at 2.7 GHz and (b) at 5.2 GHz. (Simulation in red and measurements in blue).

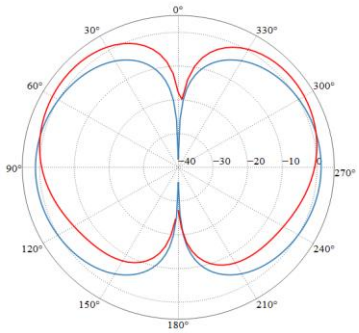

(a)

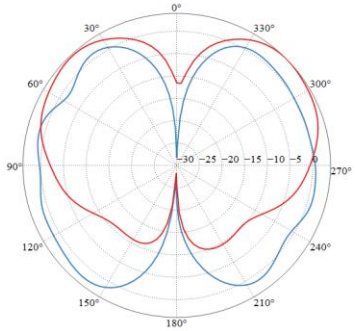

(b)

Fig. 8. Simulated and measured radiation patterns of the 4-dipole array in the E-plane: (a) at 2.7 GHz and (b) at 5.2 GHz. (Simulation in red and measurements in blue).

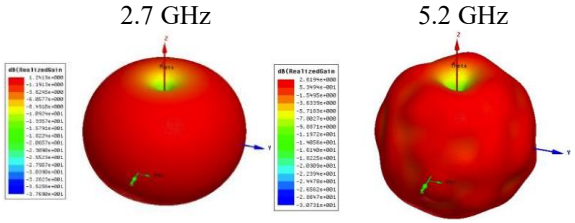

(a)

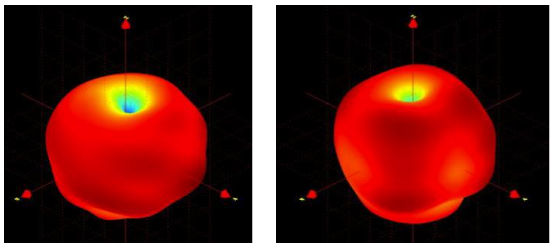

(b)

Fig. 9. 3D-radiation patterns at 2.7 GHz and 5.2 GHz: (a) simulation and (b) measurement.

Figure 10 shows the measured efficiency of the 4-dipole arrays. As we can see it about 88% for both resonance frequency of 2.7 GHz and 5.2 GHz.

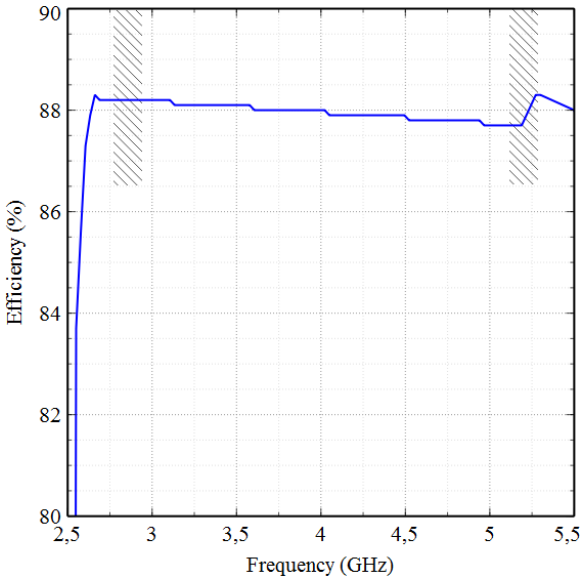

Fig. 10. Maximum measured efficiency of the 4-dipole arrays.

IV. APPLICATION FOR COMPACT BASE STATION

The base station antennas have undergone several changes. The first versions were simple single-band antennas. The deployment of new standards has been accompanied by new frequency bands. The antennas have been multiband since that time [24].

In this section, we propose a 4-dipoles array structure with a ground plane to operate in a compact base station. The simulated and fabricated structure is shown in Fig. 11. A circular ground plane of 45 mm diameter is placed at 21 mm from the 4-dipoles array. In this way, a compact structure is obtained where the electronic part can thus be placed on the other side of the ground plane.

The measured reflection coefficient of the 4-dipoles array with a ground plane is in good agreement with the simulation results as we can see in Fig. 12 with a small frequency shift of 100 MHz. The bandwidth obtained in the low frequency band is 200 MHz between 2620 and 2820 MHz for an |S11| <-6 dB, whereas for the high frequency band, a bandwidth 820 MHz between 4860 and 5680 MHz is obtained.

The maximum measured gain of the 4-dipole array with a ground plane is shown in Fig. 13.

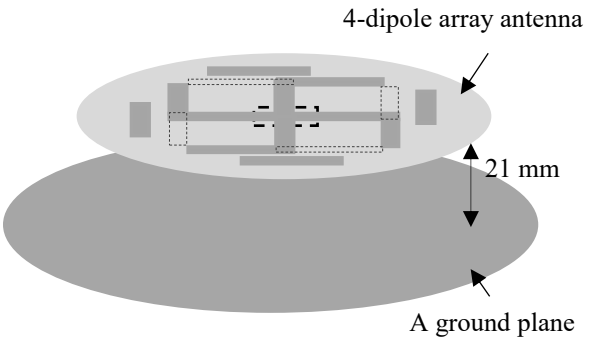

(a)

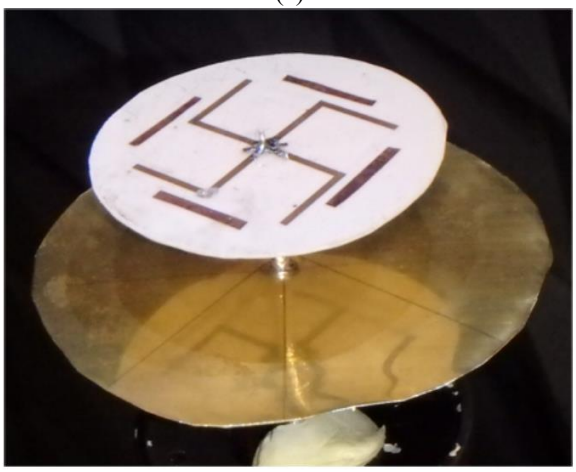

(b)

Fig. 11. Structure of the 4-dipoles array with ground plane: (a) simulated structure and (b) fabricated structure.

The proposed structure has a gain which can reach 2.6 dB for the first resonance frequency and 4.03 dB for the second resonance frequency. The gain seems to increase with the frequency as it is known. It is depending more on the shape (size of the structure), whereas the efficiency is related to the loses in the antennas (metals and dielectric (substrate)).

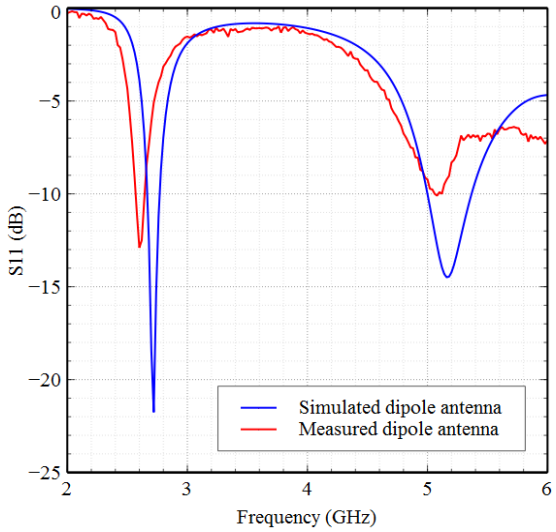

Fig. 12. Reflection coefficient of the 4-dipoles array with ground plane versus frequency.

Moreover, the prototype structure showed good measured efficiency which can reach 83% for both resonance frequencies as shown in Fig. 14. Figures 15, 16 and 17 show the 2-D and 3-D simulated and measured radiation patterns of the proposed structure in the H-plane at 2.7 GHz and 5.2 GHz. At both resonant frequencies, the radiation pattern of the 4-dipoles array with a ground plane is more directive in the orthogonal plane of the antenna and has a null along the dipole axis.

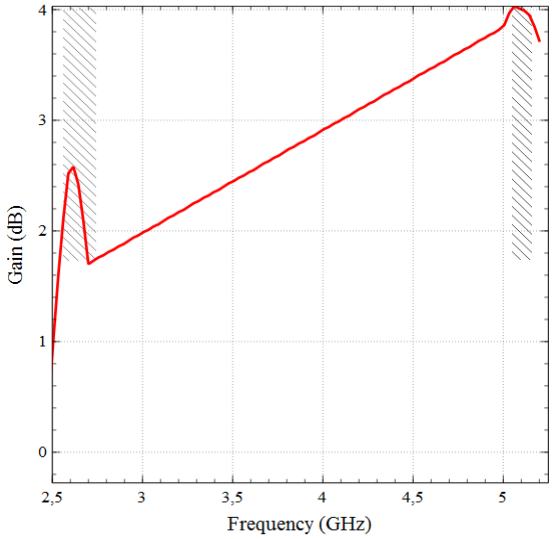

Fig. 13. Maximum measured gain of the proposed structure.

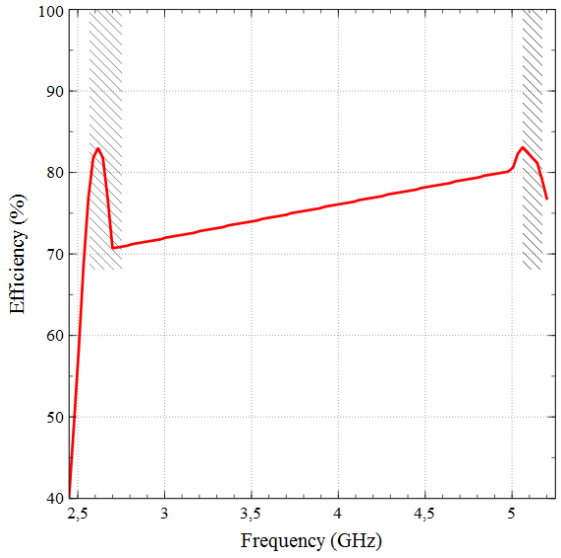

Fig. 14. Maximum measured efficiency of the proposed structure.

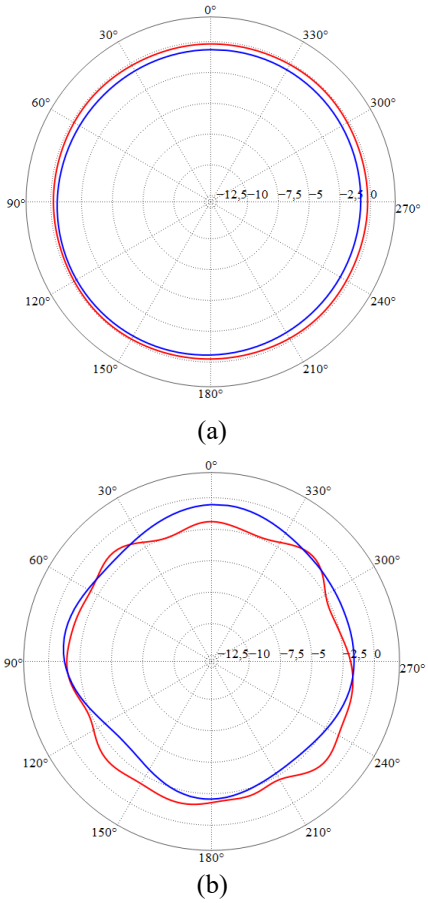

Fig.15. 2-D simulated and measured gain of the 4-dipoles array with ground plane in the E-plane: (a) 2.7 GHz and (b) 5.2 GHz. (simulation in red and measurements in blue).

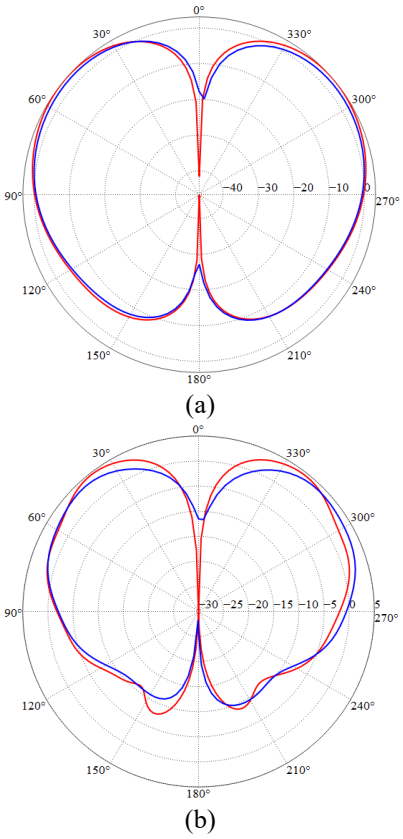

Fig. 16. 2-D simulated and measured gain of 4-dipoles array with ground plane in the H-plane: (a) 2.7 GHz and (b) 5.2 GHz. (simulation in red and measurements in blue).

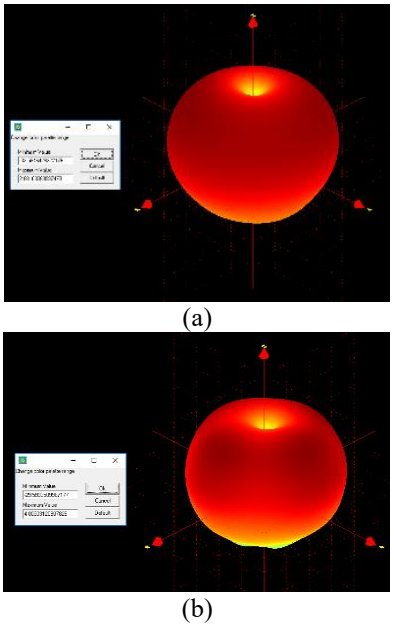

Fig. 17. 3-D measured gain of 4-dipoles array with a ground plane at: (a) 2.7 GHz and (b) 5.2 GHz.

V. CONCLUSION

In this paper, we have designed a 4-dipoles antenna array based on the printed dipole structure. The proposed compact array, operating around 2.7 and 5.2 GHz, is characterized with omnidirectional radiation patterns, and high efficiency (about 88%). These good radiation properties allow it to be a potential candidate for compact-antenna used in wireless base stations used in satellite telecommunications.

ACKNOWLEDGMENT

This project was funded by the Deanship of Scientific Research (DSR), King Abdulaziz University, under Grant No. RG-8-135-40. The authors gratefully acknowledge technical and financial support of KAU.

REFERENCES

[1] H. Arslan, Z. N. Chen, and M.-G. Di Benedetto, *Ultra Wideband Wireless Communication*. John Wiley & Sons, Inc. ISBN 0-471-71521-2, 2006.

[2] J. M. Floc'h and H. Rmili, "Design of multiband dipole antennas using parasitic elements," *Microwave and Optical Technology Letters*, ISSN: 0895-2477, vol. 48, no. 8, pp. 1639-1645, Aug. 2006.

[3] J. W. Jervis, A. Khidre, and S. Ponnuswamy, "Alford loop antennas with parasitic elements," *US Patent USOO9509062B2*, Nov. 2016.

[4] J.-M. Floc'h, A. El Sayed Ahmad, A. C. Tarot, R. Loison, S. Thizon, and J.-Y. Daden, "On the design of planar printed dipole array antennas," *Wireless Engineering and Technology*, vol. N°3, pp. 203-209, 2012.

[5] K.-L. Wong, F.-R. Hsiao, and T.-W. Chiou, "Omnidirectional planar dipole array antenna," *IEEE Transactions on Antennas and Propagation*, vol. 52, no. 2, Feb. 2004.

[6] J. D. Morrow, "Polarization-adjustable omni-directional dipole array," *IEEE Antennas and Wireless Propagation Letters*, vol. 2, 2003.

[7] C. Phongcharoenpanich, W. Polkaew, B. Luadang, and P. Akkaraekthalin, "A horizontally polarized omnidirectional antenna using stacked curve dipoles for DTV reception," *International Journal of Antennas and Propagation*, vol. 2015, Article ID 107148, 2015.

[8] L. Shafai, S. K. Sharma, and S. Rao, *Handbook of Reflector Antennas and Feed Systems*. Artech House: London, 2013.

[9] C. A. Balanis, *Antenna Theory: Analysis and Design*. 3rd ed., Hoboken, NJ: John Wiley, 2005.

[10] C.-Y. Chiu, C.-H. Cheng, R. D. Murch, and C. R. Rowell, "Reduction of mutual coupling between closely-packed antenna elements," *IEEE Transactions on Antennas and Propagation*, vol. 55, no. 6, pp. 1732-1738, June 2007.

[11] Y. Ding, Z. Du, K. Gong, and Z. Feng, "A novel dual-band printed diversity antenna for mobile terminals," *IEEE Transactions on Antennas and Propagation*, vol. 55, no. 7, pp. 2088-2096, July 2007.

[12] R. Vaughan, "Switched parasitic elements for antenna diversity," *Antennas and Propagation, IEEE Transactions on*, vol. 47, pp. 399-405, 1999.

[13] N. Boisbouvier, F. Le Bolzer, and A. Louzir, "A compact radiation pattern diversity antenna for WLAN applications," *in Antennas and Propagation Society International Symposium, 2002, IEEE*, pp. 64-67, vol. 4, 2002.

[14] R. W. Ziolkowski, J. Peng, and L. Chia-Ching, "Metamaterial-inspired engineering of antennas," *Proceedings of the IEEE*, vol. 99, no. 10, pp. 1720-1731, 2011.

[15] N. Engheta and R. W. Ziolkowski, *Metamaterials: Physics and Engineering Explorations*. Wiley, 2006.

[16] A. D. Yaghjian, "Increasing the supergain of electrically small antennas using metamaterials," *Proceeding of the 4th European Conference on Antennas and Propagation (EUCAP)*, Apr. 2010.

[17] S. R. Best, "Progress in the design and realization of an electrically emall Huygens source," *IEEE*, 2010.

[18] P. Jin and R. W. Ziolkowski, "Metamaterial-inspired, electrically small Huygens sources," *IEEE Antennas and Wireless Propagation Letters*, vol. 9, 2010.

[19] H. Wang, H. Yang, L. Gu, and F. Zhao, "An improved design of dipole antenna array for base station applications," *6th International Conference on Advanced Design and Manufacturing Engineering (ICADME 2016)*, 2016.

[20] C. Tang, H. Cao, and J. Ho, "A scalable compact wideband dual-polarized printed dipole antenna for base station applications," *Progress In Electromagnetics Research C*, vol. 75, pp. 203-217, 2017.

[21] X. Z. Zhu, J. L. Zhang, T. Cui, and Z. Q. Zheng, "A dual-broadband printed dipole antenna for 2G/3G/4G base station applications," *International Journal of Antennas and Propagation*, vol. 2019, Article ID 4345819, 2019. https://doi.org/10.1155/2019/4345819

[22] S. R. Best, E. E Altshuler, A. D Yaghjian, J. M. McGinthy, and H. O'Donnel, "An impedance-matched 2-element superdirective array," *IEEE Antennas and Wireless Propagation Letters*, vol. 7, pp. 302-305, 2008.

[23] J. Weber, C. Volmer, K. Blau, R. Stephan, and M. A. Hein, "Miniaturized antenna arrays with an element separation down to λ/10," *IEEE Antennas and Propagation Society International Symposium, IEEE*, pp. 5897-5900, 2007.

[24] L. Martin, "Conception of a compact antenna for

base station used in cellular network," *Thesis, Nantes University*, 2017.

Jean Marie Floch received his Ph.D. in Electronics and Telecommunication Sciences in 1992 from the INSA Rennes, France. He joined the IETR institute as Research Engineer where he supervised Master and Ph.D. Students, in addition to the execution of many research projects with collaboration of the industry. His research interests concern the design of different type of antennas for wireless applications.

Ameni Mersani received a degree in Electronics, Computer and Information Science from the University Tunis El Manar, Tunisia in 2009 and the master thesis in Electronics from the Faculty of Science of Tunis, Tunisia in 2012. She received the Ph.D. in Engineering Sciences (Electronics) from the University of Tunis El Manar, 2018. From September 2018, she was a Research Assistant in ISET'COM (Department of Telecommunication). From December 2019, she was a Post-Doctoral Researcher with King Abdulaziz University, Saudi Arabia. Her research mainly focuses on the development of design of wearable antennas for wireless applications and metamaterial.

Bandar Hakim is an Assistant Professor of Electrophysics at KAU. He received his Ph.D. degree in Electrophysics from the University of Maryland. He worked with the Medical Robotics group at the École Polytechnique Fédérale de Lausanne in Switzerland, the Center for Devices and Radiological Health at the Food and Drug Administration in Washington DC and the Neurology Department at Mount Sinai School of Medicine in the New York NY. He served as an industrial consultant in the US, Switzerland and Germany.

Khaled Sedraoui received the B.S. degree in Electrical Engineering from the Institute of Technology and Sciences Tunis (ESSTT), Tunis, Tunisia, in 1989 and the M.Sc. degree in Electrical Engineering from ETS (Ecole de Technologie Superieure), Quebec University, Montreal, Canada, in 1994 and Ph.D. degree in Electrical Engineering from the Institute of Technology and Sciences Tunis (ESSTT), Tunisia, in 2010. Since 1997, he has been a Faculty Member of College of Technology, Jeddah, KSA. He is currently an Assistant Professor of Electrical and Computer Engineering, College of Engineering, King Abdulaziz University, Jeddah, Saudi Arabia. His research interests include, renewable energies integration and Power quality improvement, design and control strategy for Flexible AC Transmission System (FACTS), Electric energy storage for R.E. systems and E.V., and Optimization for smart grid.

Hatem Rmili received the B.S. degree in General Physics from the Science Faculty of Monastir, Tunisia in 1995, and the DEA diploma from the Science Faculty of Tunis, Tunisia, in Quantum Mechanics, in 1999. He received the Ph.D. degree in Physics (Electronics) from both the University of Tunis, Tunisia, and the University of Bordeaux 1, France, in 2004. From December 2004 to March, 2005, he was a Research Assistant in the PIOM Laboratory at the University of Bordeaux 1. During March 2005 to March 2007, he was a Postdoctoral Fellow at the Rennes Institute of Electronics and Telecommunications, France. From March to September 2007, he was a Postdoctoral Fellow at the ESEO Engineering School, Angers, France. From September 2007 to August 2012, he was an associate professor with the Mahdia Institute of Applied Science and Technology (ISSAT), department of Electronics and Telecommunications, Tunisia. Actually, he is Full Professor with the Electrical and Computer Engineering Department, Faculty of Engineering, King Abdulaziz University, Jeddah, Saudi Arabia.

Rmili's research interests concern applied electromagnetic applications involving antennas, metamaterials and métasurfaces. The main targeted applications are reconfigurable antennas for multi-standard wireless communications systems, security of chipless RFID systems with fractal tags, terahertz photoconductive antennas for infra-red energy harvesting, UWB nano rectennas for collection of solar energy, phase shifters for low-cost 5G communication systems, and microwave absorbing materials for stealth technologies.

Multi-Mode Narrow-Frame Antenna for 4G/5G Metal-Rimmed Mobile Phones

M. Yang [1,2], Y. F. Sun [1*], and T. Q. Liao [1]

[1] Key Lab of Intelligent Computing and Signal Processing, Ministry of Education
Anhui University, Hefei 230601, China
myang@ahu.edu.cn, *yfsun_ahu@sina.com, t.liao@ahu.edu.cn

[2] Electronics and Information Engineering Department
Bozhou University, Bozhou 236800, China

Abstract ─ A novel multi-mode narrow-frame antenna is presented for 4G/5G metal-rimmed mobile phones in this paper. The proposed antenna is constituted by a monopole antenna and a coupling strip, which is printed on FR4 substrate with thickness of 0.8 mm. The overall area occupied by the antenna is only 60 × 10.4 mm^2, which can be used as a promising narrow-frame antenna. The simulated results shows that the return loss of the antenna can provide four operating bandwidths of 822–961 (band 1), 1697–3075 (band 2), 3280–3835 (band 3) and 4475–5050 MHz (band 4), which respectively cover 824–960, 1710–2690, 3300–3600 and 4800–5000 MHz in 4G/5G communication systems. In order to verify the accuracy of theoretical analysis and simulated results, the proposed antenna is fabricated and measured. The experimental results are basically consistent with the simulated results, suggesting that the presented antenna has attractive performance for mobile phones.

Index Terms ─ Frame antenna, metal rim, multi-mode, nona-band operation.

I. INTRODUCTION

As the radio access technologies develop rapidly, an increasing number of portable devices can support the LTE function [1–2], especially metal-framed smartphones have evolved into fashionable and popular products for consumers [3–4]. Nevertheless, the metal characteristics of the bezel of the smartphone affect the internal antenna's performance to a certain extent. Recently, designing the metal frame of a mobile phone with a novel structure has become the key to solving the problem. In [5–6], grounded patches and gaps are utilized to compensate for the performance loss due to the antenna being mounted internally. A novel method which takes part or the whole of the metal rim as antenna elements is proposed in [7–9] to simplify the antenna design. Although these antennas based on metal rim have been successfully implemented, none of them cover the entire 4G/5G frequency bands.

The 5G operating license of domestic mobile phones was promulgated and thLe band division of a new generation of mobile communication was defined by China's Ministry of Industry and Information Technology in November 2017 [10]. The 3300–3600 MHz and 4800–5000 MHz bands are set as 5G wireless communication frequency bands. At the same time, some innovative 5G technologies are also proposed in other countries to obtain faster transmission rates [11-12]. Therefore, the antenna with high-performance and narrow-frame can be applied to 5G wireless communications.

In recent years, a variety of methods are employed to design antenna for 4G/5G mobile phones. On the basis of loop antenna structure, the frame antennas are designed in [13–17], but amounts of inductors and capacitors are used which markedly increase these antennas' complexity. In [18], a dual-band eight-antenna array is proposed for multiple input and multiple output (MIMO) applications in 5G mobile terminals. But, it cannot fully satisfy the requirement of 4G/5G multiband communications. In [19], a hybrid antenna is designed for 4G/5G MIMO application, which is made up of two antenna modules, namely 4G and 5G antenna modules. However, it is difficult for such a hybrid antenna to miniaturize a mobile phone antenna. Four MIMO antennas are also designed in [20-23], and the metamaterial structures are introduced to reduce the coupling between the antenna element, but the decoupling structures are not conducive to the low profile and miniaturization of the antenna.

In this paper, the characteristics of multi-mode, ultra-wideband and multi-band are integrated into an antenna which applied in the 4G/5G fields. Furthermore, the designed antenna has compact structure without any lumped elements. The wider bandwidth is also easily achieved by using an I-shaped feeding strip and a stereoscopic coupled grounding strip, which are printed on the back side of the substrate as a part of mobile phone

Submitted On: March 6, 2020
Accepted On: May 24, 2020
https://doi.org/10.47037/2020.ACES.J.350809

shells.

II. STRUCTURE AND DESIGN OF THE PROPOSED ANTENNA

2.1. Structure of Antenna

The complete geometry of the proposed antenna is shown in Fig. 1. As plotted in Fig. 1 (a), a 0.8 mm thick FR4 substrate which has a relative permittivity of 4.4 and a loss tangent of 0.02 is utilized as the mobile phone housing. The housing has a volume of 120 × 60 × 5 mm^3, and a ground plane with the size of 109.6 × 60 mm^2 is printed on the housing. A 50 Ω mini coaxial line which is connected to the feeding point (Point A) and the PCB grounding point (Point C), is employed to excite the antenna.

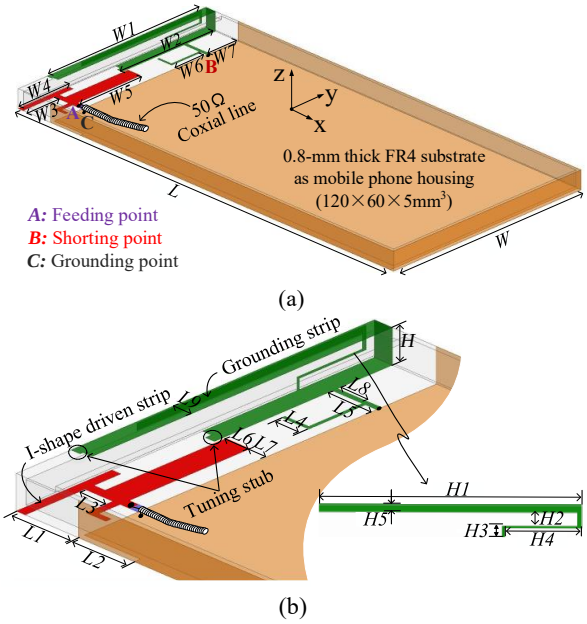

Fig. 1. (a) Configuration of proposed antenna. (b) Detail dimensions of the antenna modules (Unit: mm).

As can be seen in Fig. 1 (a), the three-branch coupled parasitic ground strip (including a long branch and two short branches) and several tuning stubs are used to excite the multiple modes which work at band 1 and band 2. The two bands can cover the 824 – 960 MHz and 1710 – 2690 MHz bands effectively. That shown in Fig. 1 (b) is the proposed antenna with detailed dimensions. In addition, the I-shape driven strip and a rectangular slot are used to excite the multiple modes which work at band 3 and band 4. The two bands can cover the 3300–3600 MHz and 4800–5000 MHz bands effectively. The working mechanism of the proposed antenna is analyzed in detail in the section 2.2.

2.2 Antenna Design and Analysis

A. Slotted loading method for the high band

In this section, the S_{11} and the evolution processes for different antennas are investigated to clearly explain the operating mechanism and design procedure of the proposed antenna. As illustrated in Fig. 2 (a), a ground clearance of 60 × 10.4 mm^2 is reserved for the band 3 and band 4. An I-shape strip (Ant1) is introduced as the monopole antenna. As shown in Fig. 2 (c), Ant1 creates two 0.25λ resonant modes respectively around 3500 MHz and 2100 MHz. The rectangular slot with 1 mm width is inserted between points *D* and *E* (Ant2) to widen the bandwidth of band 3 and band 4, which improves the impedance matching through capacity coupling and creates a 0.25λ resonant mode at around 4850 MHz.

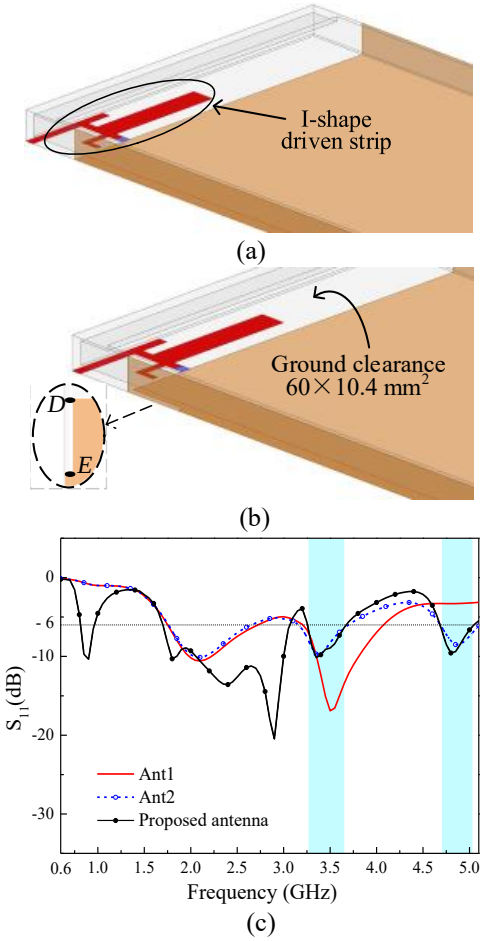

Fig. 2. Comparison of Ant1, Ant2 and simulated S_{11}. (a) Ant1, (b) Ant2, and (c) Simulated S_{11}.

For Ant2, bandwidths of 14.6% (3180–3680 MHz) and 8.6% (4680–5100 MHz) are obtained, which can meet the requirements for 5G mobile phones.

B. Technologies for the low band

According to the above analysis in section 2.2A, Ant2 can cover 3300–3600 MHz and 4800–5000 MHz. This antenna cannot cover 824–960 MHz and 1710–2690 MHz from Fig. 2 (c). An effective solution is introduced to merge multiple modes through utilizing multiple strips. Here, we will introduce the evolution process in order to cover the low band. In Figs. 3 (a)–(c), there are three types of configuration, which represent three important states during the evolution. The corresponding simulated S_{11} is also given in Fig. 3 (d).

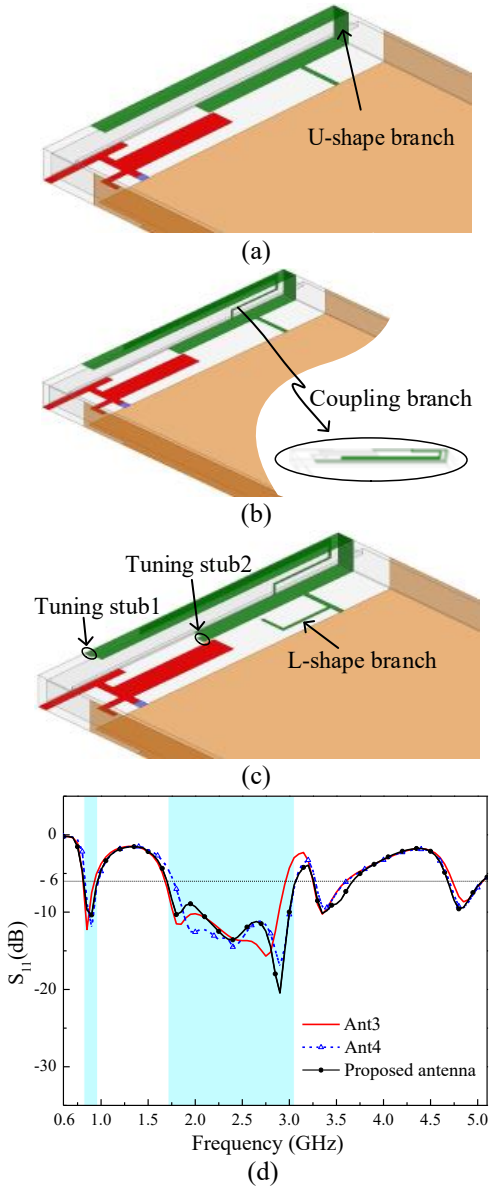

Fig. 3. Comparison of An3, Ant4, proposed antenna and simulated S_{11}: (a) Ant3, (b) Ant4, (c) the proposed antenna, and (d) simulated S_{11}.

As shown in Fig. 3 (a), a U-shape branch is inserted into Ant2 to form Ant3. The U-shape branch is disposed on the right side of the system ground plane, the length of which is 84.1 mm. Ant3 creates a 0.25λ resonant mode at around 850 MHz. In order to broaden the bandwidth of the band 1, a coupling branch is added to Ant3 to form Ant4, as shown in Fig. 3 (b). Thus, the resonance point at 850 MHz is shifted to 900 MHz, and its bandwidth is 820–973 MHz. To obtain a characteristic of broadband which coverage in the 1710 MHz frequency band, an L-shape branch and two tuning stubs are inserted into Ant4 to form the proposed antenna. As illustrated in Fig. 3 (d), by inserting the L-shape branch and two tuning stubs, the band 2 is enhanced. The simulated results show that the S_{11} of the frequency band 1700–3061 MHz is less than -6 dB. So, the proposed antenna can cover LTE/WWAN (4G) bands.

The antenna configuration is modeled by HFSS full-wave simulator and optimized design parameters are listed in Table 1.

Table 1: Geometric parameters of the proposed antenna (Unit: mm)

Parameter	Value	Parameter	Value
W	60.0	H_1	38.4
L	120.0	H_2	2.0
H	5.0	H_3	1.8
W_1	50.8	W_5	20.2
W_2	29.8	W_6	9.5
W_3	10.0	W_7	9.2
L_1	10.4	L_6	4.0
L_2	9.4	L_7	3.0
L_3	4.7	H_4	11.2
W_4	16.0	H_5	1.0
L_4	4.5	L_8	5.0
L_5	7.4	L_9	3.0

C. Operating principle

The surface current distributions of the proposed antenna at 900, 1800, 2400, 3350 and 4800 MHz are simulated as depicted in Figs. 4 (a)–(e). As shown in Fig. 4 (a), the strong surface current distributions at U-shape branch, attribute to the length of U-shape branch is 85.6 mm, which corresponds to about 0.25λ at 900 MHz. Figure 4 (b) plots that the surface current at the 1800 MHz is mainly distributed on U-shape branch and coupling branch, which infers that the coupling branch generates a lower-frequency resonant mode around 1800 MHz. In Fig. 4 (c), it can be seen that the surface currents concentrate upon L-shape branch and I-shape driven strip. Figure 4 (d) shows that strong current flows along the I-shape driven strip, which demonstrates that driven strip can provide a 0.25λ resonant mode at about 3350 MHz. Furthermore, the simulated surface current

distribution excited at 4800 MHz is illustrated in Fig. 4 (e), in which intense and uniform current distributions can be observed around the rectangular slot. In addition, it can be confirmed from Fig. 4 (e) that the higher-frequency resonant mode at about 4800 MHz is mainly contributed to the rectangular slot of the system ground plane, owing to the path (length 18.4 mm) corresponding to about 0.25λ at 4800 MHz.

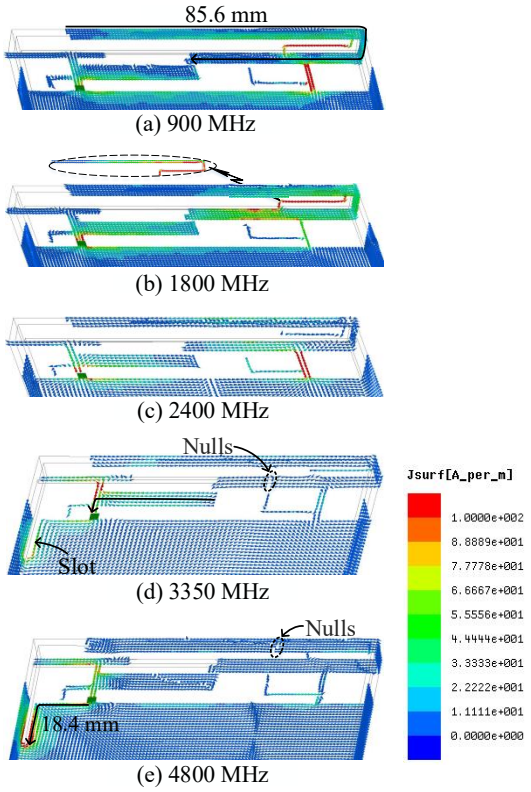

Fig. 4. Simulated surface current distributions at: (a) 900 MHz, (b) 1800 MHz, (c) 2400 MHz, (d) 3350 MHz, and (e) 4800 MHz.

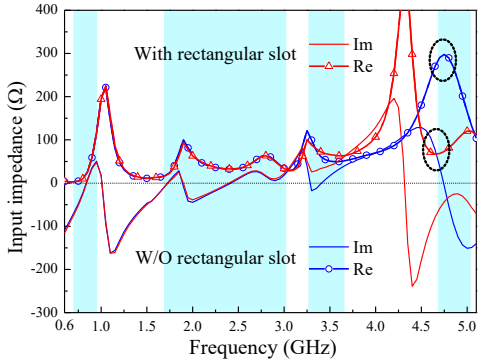

Fig. 5. Effects of the rectangular slot on input impedance.

The rectangular slot has a positive effect on the impedance matching of the proposed antenna in band 4. Figure 5 shows the input impedances with and without the rectangular slot. In band 4, the addition of the rectangular slot decreases the reactance to improve the impedance matching. Therefore, the bandwidth of the band 4 is widely enlarged, covering the 4680–5050 MHz band.

D. Parametric study

In the design of this antenna, changing the length of W_5 and W_1 respectively, the corresponding effects on the resonant mode are depicted at Fig. 6 and Fig. 7. When the length W_5 varies from 17.7 to 22.7 mm, it can be seen from Fig. 6 that the change of antenna's bandwidth is relatively remarkable in band 2 and band 3.

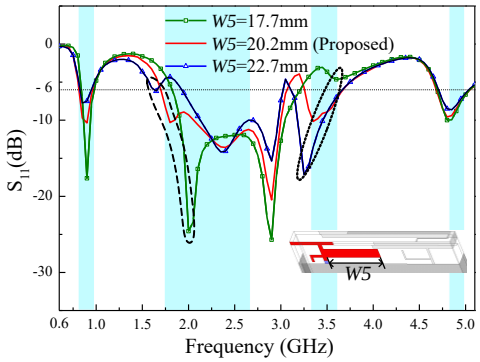

Fig. 6. Simulated S_{11} as a function of the length W_5.

Figure 7 shows the simulated S_{11} as a function of the length W_1 of the U-shape branch. It can be seen from Fig. 7 that when the value of W_1 increases, the antenna bandwidth becomes narrower in band 1. This indicates that the length of the U-shape branch is an important parameter of the designed antenna.

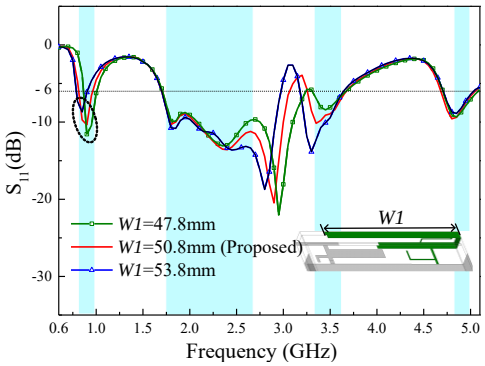

Fig. 7. Simulated S_{11} as a function of the length W_1.

III. EXPERIMENTAL RESULTS AND DISCUSSION

Figure 8 shows the fabricated prototype of the proposed antenna, which is excited by a 50 Ω mini coaxial line. What was used for testing the S-parameters is an Agilent N5247A vector network analyzer. Figure 9 presents the measured results of S_{11}, which is consistent with the simulated results. The measured bandwidths are 822–961 MHz, 1697–3075 MHz, 3280–3835 MHz and 4475–5050 MHz, respectively, and they can cover 824–960 MHz, 1710–2690 MHz, 3300–3600 MHz and 4800–5000 MHz which is widely used as the design specification for 4G/5G mobile antennas.

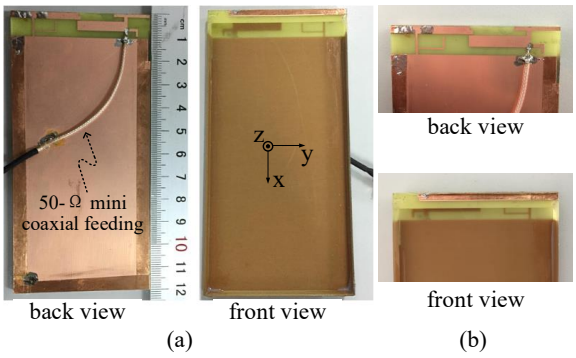

Fig. 8. Photographs of the fabricated antenna. (a) Overall view and (b) enlarged view.

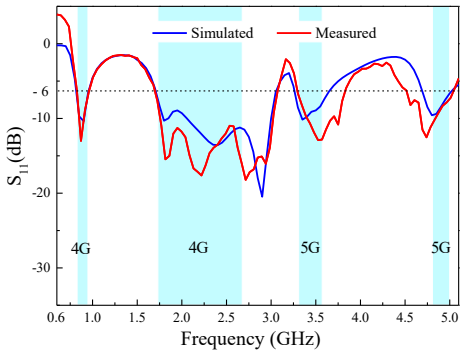

Fig. 9. Comparison between the measured and simulated S_{11} of the proposed antenna.

Figure 10 shows the 2-D radiation patterns of the fabricated prototype at 900, 2400, 3350 and 4800 MHz. As shown in the placement direction of the antenna in Fig. 1, the copol (E_θ) and cross-pol (E_ϕ) in the *xoy*, *yoz* and *zox*-planes are simulated and measured, and it can be concluded from Fig. 10, the E_θ varies smoothly in *yoz*-plane, which is beneficial to actual smartphone applications.

Figure 11 shows the simulated and measured results of the gain and efficiency. It can be concluded from Fig. 11 that the measured results are basically consistent with the simulated results. At the 4G frequency bands, the measured antenna's gain is around 3.2 dBi, and the measured radiation efficiency varies from 51% to 70% measured. In the 5G frequency bands, the measured gain fluctuates from 2.5 dBi to 3.1 dBi. Meanwhile, the efficiency of the proposed antenna fluctuates from 53% to 61%, which can satisfy the requirement of wireless communication for mobile devices. In addition, a comparison between the proposed antenna and the typical reported mobile phones according to the dimensions, frequency bands, bandwidth, and efficiency is shown in Table 2. Thus it can be concluded that the proposed antenna is more suited to 4G/5G metal-rimmed mobile phones.

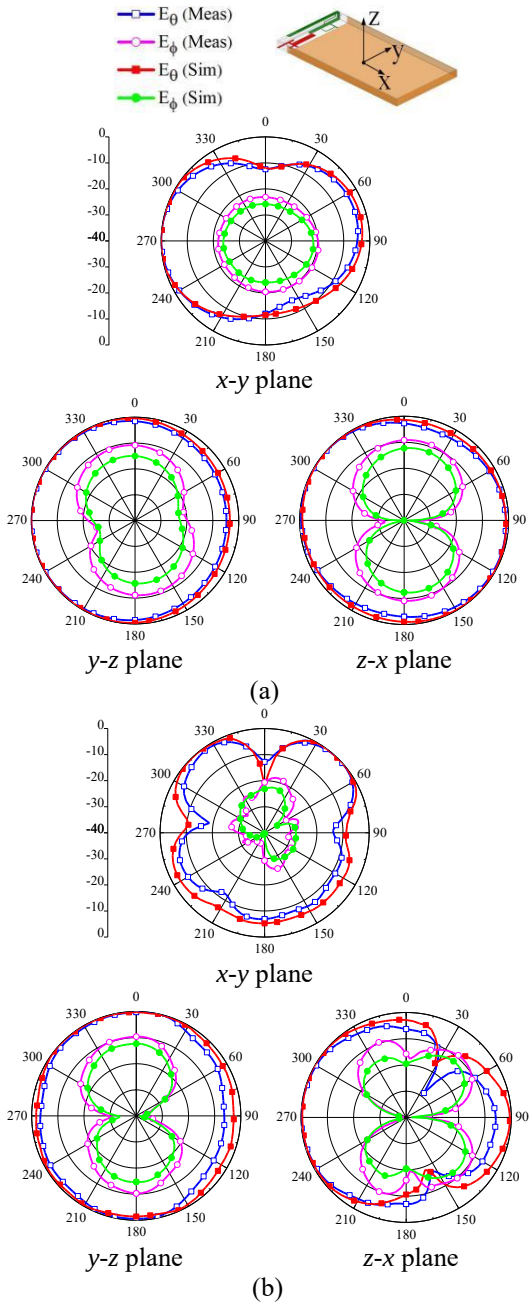

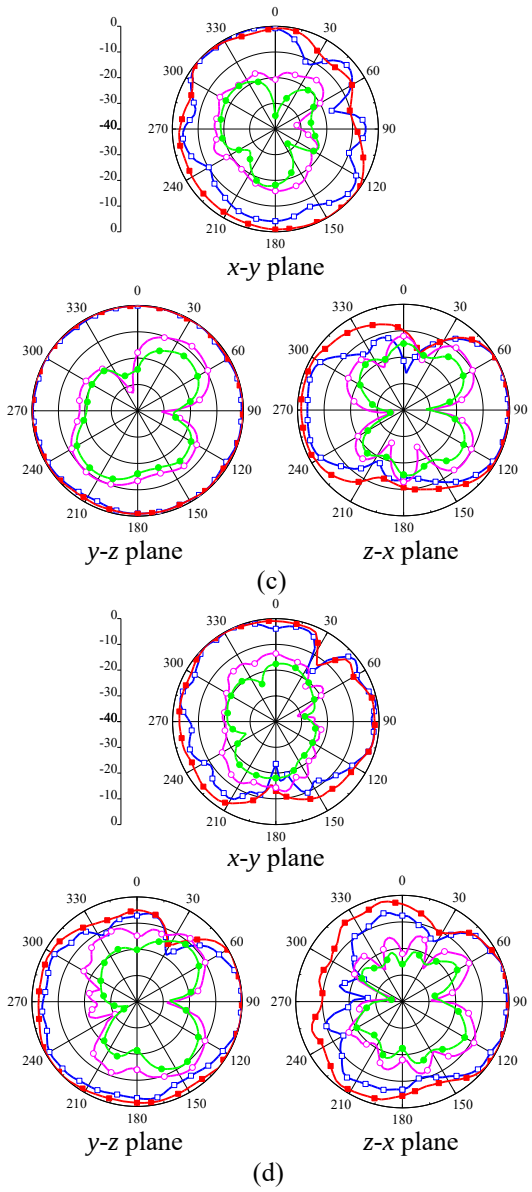

Fig. 10. Simulated and measured 2-D radiation patterns at: (a) 900 MHz, (b) 2400 MHz, (c) 3350 MHz, and (d) 4800 MHz.

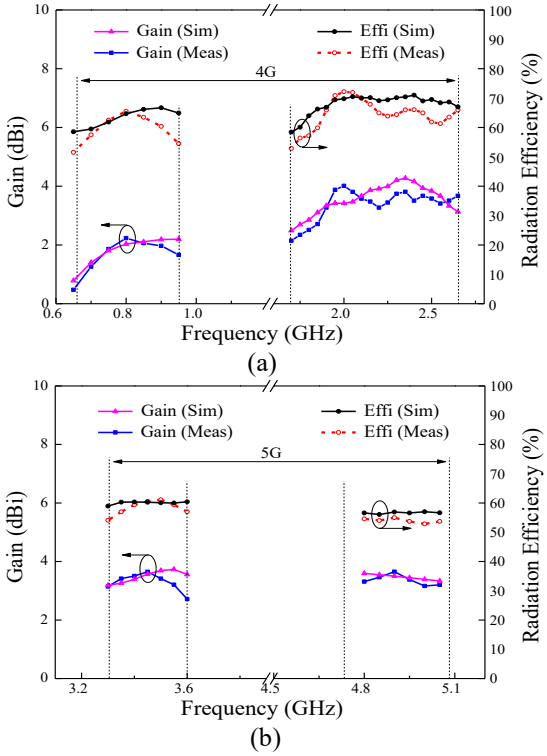

Fig. 11. Simulated and measured gain and efficiency of the proposed antenna: (a) 4G and (b) 5G.

IV. CONCLUSION

A novel multi-mode narrow-frame antenna for 4G/5G metal-rimmed mobile phone is proposed in this paper. The proposed antenna with compact size of 10.4 × 60 mm^2 is integrated on a metal-rimmed mobile phone with size of 120 × 60 × 5 mm^3, which meet the volume requirements of handheld terminals. The bandwidth of the antenna is widened by using meander technologies for the operating band of 822–961 MHz, 1697–3075 MHz which can cover 824–960 MHz, 1710–2690 MHz. The bands of 3280–3835 MHz, 4475–5050 MHz are obtained by slotted loading method which can cover 3300-3600 MHz, 4800-5000 MHz. Therefore, this antenna can satisfy the requirements for smartphone systems without matching circuits or lumped elements.

Table 2: Comparison of proposed antenna and reference antennas

Reference	Dimension (mm^3)	Frequency Band	Bandwidth (MHz)	Gain (dBi)	Efficiency (%)
[1]	72×6.5×5.8	Octa-band	700–1030/1700–2690	1.56/2.38	>46.5/45.5–81.75
[3]	70×9×5	Octa-band	704–960/1700–2830	0.2–2.49/1.18–4.24	44–75/43–76
[7]	71×5×6	Hepta-band	800–1000/1700–2780	–/–	62–85.7/66.9–91
[9]	71.6×10×5	Hepta-band	801–1002/1695–3000	0.7–3.4/2.0–5.0	31–38/42–69
[10]	27×10.8×0.8	Deca-band	685–960/1710–2170/3288–3613	1.4–2.5	40–65/60–92
[16]	120×70×6	Octa-band	675–1050/1600–2800	0–2.1/1.6–3.6	52.7–78.7/45.6–81
[17]	72×8×5	Hepta-band	824–960/1710–2690	0.98–2.1/2.45–5.1	41–48/49–76
[18]	140×70×1	di-band	3300–3600/5150–5925	–/–	51–59/62–80
[20]	100×60×0.5	di-band	2500–2700/3400–3600	–/–	72–88/53–68
Proposed	**60×10.4×5**	**Nona-band**	**822–961/1697–3075/ 3280–3835/4475–5050**	**3.4/2.5–3.1**	**51–70/53–61**

ACKNOWLEDGMENT

This work was supported by the National Natural Science Foundation of China under Grant No. 61172020, the Project of Anhui Local High-level University Construction under Grant No. 2013gx001 and the Key Project of Natural Science Research of Colleges and Universities in Anhui Province under Grant No. KJ2018A0818.

REFERENCES

[1] P. Wang, Y. Shao, D. Huang, and M. A. Basit, "A compact coupled-fed loop antenna for mobile LTE smartphones," *International Journal of Antennas and Propagation*, vol. 2018, Article ID 8426574, 8 pages, 2018.

[2] Y. Wang and Z. W. Du, "Wideband monopole antenna with less nonground portion for octa-band WWAN/LTE mobile phones," *IEEE Transactions on Antennas and Propagation*, vol. 64, no. 1, pp. 383-388, 2016.

[3] P. Y. Qiu and Q. Y. Feng, "Low-profile compact antenna for octa-band metal-rimmed mobile phone applications," *IEEE Transactions on Antennas and Propagation*, vol. 68, no. 1, pp. 54-61, Jan. 2020.

[4] Q. G. Chen, H. W. Lin, and J. P. Wang, L. Ge, Y. Li, T. Pei and C. Y. D. Sim, "Single ring slot-based antennas for metal-rimmed 4G/5G smartphones," *IEEE Transactions on Antennas and Propagation*, vol. 67, no. 3, pp. 1476-1487, Mar. 2019.

[5] K. L. Wong and C. Tsai, "Half-loop frame antenna for the LTE metal-casing tablet device," *IEEE Transactions on Antennas and Propagation*, vol. 65, no. 1, pp. 71-81, Jan. 2017.

[6] J. W. Lian, Y. L. Ban, Y. L. Yang, L. W. Zhang, C. Y. D. Sim, and K. Kang, "Hybrid multi-mode narrow-frame antenna for WWAN/LTE metal-rimmed smartphone applications," *IEEE Access*, no. 4, pp. 3991-3998, Aug. 2017.

[7] Y. Liu, J. K. Zhang, A. D. Ren, H. Wang, and C. Y. D. Sim, "TCM-based hepta-band antenna with small clearance for metal-rimmed mobile phone applications," *IEEE Antennas and Wireless Propagation Letters*, vol. 18, no. 4, pp. 714-721, Apr. 2019 .

[8] K. L. Wong, C. Tsai, and J. Y. Lu, "Two asymmetrically mirrored gap-coupled loop antennas as a compact building block for eight-antenna MIMO array in the future smartphone," *IEEE Transactions on Antennas and Propagation*, vol. 65, no. 4, pp. 1765-1778, 2017.

[9] L. W. Zhang, Y. L. Ban, and C. Y. D. Sim, J. Guo, and Z.-F. Yu, "Parallel dual-loop antenna for WWAN/LTE metal-rimmed smartphone," *IEEE Transactions on Antennas and Propagation*, vol. 66, no. 3, pp. 1217-1226, Mar. 2018.

[10] M. Yang, Y. F. Sun and F. Li, "A compact wideband printed antenna for 4G/5G/WLAN wireless applications," *International Journal of Antennas and Propagation*, ID: 3209840, 2019.

[11] Cursor, "New antenna technology for extremely fast 5G and 6G," May 11, 2019. [Online]. Available: https://www.cursor.tue.nl/en/news/2019/november/week-1/new-antenna-technology-for-extremely-fast-5g-and-6g/

[12] J. Happich, "5G-ready MIMO 4×4 antenna for indoor applications," Nov. 27, 2019. [Online]. Available: https://www.eenewseurope.com/news/5g-ready-mimo-4x4-antenna-indoor-applications

[13] K. L. Wong and Y. C. Chen, "Small-size hybrid loop/open-slot antenna for the LTE smartphone," *IEEE Transactions on Antennas and Propagation*, vol. 63, no. 12, pp. 5837-5841, Dec. 2015.

[14] K. L. Wong and C. Tsai, "IFA-based metal-frame antenna without ground clearance for the LTE/WWAN operation in the metal-casing tablet computer," *IEEE Transactions on Antennas and Propagation*, vol. 64, no. 1, pp. 53-60, 2016.

[15] J. Choi, W. Hwang, C. You, B. Jung, and W. Hong, "Four-element reconfigurable coupled loop MIMO antenna featuring LTE full-band operation for metallic-rimmed smartphone," *IEEE Transactions on Antennas and Propagation*, vol. 67, no. 1, pp. 99-107, 2019.

[16] D. W. Huang and Z. W. Du, "Eight-band antenna with a small ground clearance for LTE metal frame mobile phone applications," *IEEE Antennas and Wireless Propagation Letters*, vol. 17, no. 1, pp. 34-37, Jan. 2018.

[17] Z. Q. Xu, Q. Q. Zhou, Y. L. Ban, and S. S. Ang, "Hepta-band coupled-fed loop antenna for LTE/WWAN unbroken metal-rimmed smartphone applications," *IEEE Antennas and Wireless Propagation Letters*, vol. 17, no. 2, pp. 311-314, Feb. 2018.

[18] J. X. Li, X. K. Zhang, Z. Wang, X. Chen, J. Chen, Y. Li, and A. Zhang, "Dual-band eight-antenna array design for MIMO applications in 5G mobile terminals," *IEEE Access*, no. 7, pp. 71636-71644, 2019.

[19] Y. L. Ban, C. Li, C. Y. D. Sim, G. Wu, and K. L. Wong, "4G/5G multiple antennas for future multi-mode smartphone applications," *IEEE Access*, no. 4, pp. 2981-2988, July 2016.

[20] F. Liu, J. Y. Guo, L. Y. Zhao, G. L. Huang. Y. S. Li, and Y. Z. Yin, "Dual-band metasurface-based decoupling method for two closely packed dual-band antennas," *IEEE Transactions on Antennas and Propagation*, vol. 68, no. 1, pp. 552-557, 2020.

[21] K. Yu, Y. S. Li, and X. G. Liu, "Mutual coupling reduction of a MIMO antenna array using 3-D novel meta-material structures," *Applied Computational Electromagnetics Society Journal*, vol. 33, no. 7,

pp. 758-763, 2018.

[22] S. Y. Luo, Y. S. Li, Y. F. Xia, and L. Zhang, "A low mutual coupling antenna array with gain enhancement using metamaterial loading and neutralization line structure," *Applied Computational Electromagnetics Society Journal*, vol. 34, no. 3, pp. 411-418, 2019.

[23] J. F. Jiang, Y. F. Xia, and Y. S. Li, "High isolated X-band MIMO array using novel wheel-like metamaterial decoupling structure," *Applied Computational Electromagnetics Society Journal*, vol. 34, no. 12, pp. 1829-1836, 2019.

Ming Yang was born in 1982. He received the B.S. and the M.S degrees from Huaibei Normal University and Anhui University in 2005 and 2010, respectively, and the Ph.D. degree in Electromagnetic Field and Microwave Technology with Anhui University in 2019.

His research interest includes antenna theory and antenna design.

Yu-fa Sun was born in 1966. He received the B.S. and M.S. degrees from Shandong University in 1988 and 1991, respectively, and the Ph.D. degree in Electromagnetic Field and Microwave Technology from the University of Science and Technology of China in 2001.

Since 1991, he has been a faculty member in the Department of Electronic Engineering, Anhui University, China, where he is currently a Full Professor. He was a Visiting Scholar at the Wireless Communication Center at the City University of Hong Kong from February 2002 to January 2003. His research interests include computational electromagnetics and antenna theory and technology. He has authored or coauthored more than 150 journal and conference papers.

Realization of Modified Elliptical Shaped Dielectric Lens Antenna for X Band Applications with 3D Printing Technology

Aysu Belen[1] and Evrim Tetik [2]

[1] Hybrid and Electric Vehicle Technology
Iskenderun Vocational School of Higher Education, Iskenderun Technical University, Hatay, TURKEY
aysu.yldrm07@gmail.com

[2] Department of Electric and Electronic
University of Istanbul Arel, İstanbul, TURKEY
evrimtetik@arel.edu.tr

Abstract ─ Placing dielectric lens structures into an antenna's aperture has proven to be one of the most reliable methods of enhancing its gain. However, the selected material and the prototyping method usually limit their fabrication process. With the advances in 3D printing technology and their applications, the microwave designs that were either impractical or impossible in the past to manufacture using traditional methods, are now feasible. Herein, a novel prototyping method by using 3D-printer technology for low-cost, broadband, and high gain dielectric lens designs has been presented. Firstly, the elliptical lens design has been modeled in the 3D EM simulation environment. Then fused deposition modeling based 3D-printing method has been used for the fabrication of the dielectric lens. The measured results of the 3D printed antenna show that the lens antenna has a realized gain of 17 to 20.5 dBi over 8-12 GHz. Moreover, the comparison of the prototyped antenna with its counterpart dielectric lens antenna in the literature has indicated that the proposed method is more efficient, more beneficial, and has a lower cost.

Index Terms ─ 3D Printer, Lens Antenna, Dielectric Lens, Broadband, Novel Prototyping Methods.

I. INTRODUCTION

One of the essential components in wireless communication systems is antenna stages with high gain characteristics. Although Antenna Arrays are a standard solution for high gain performance, it is known that increasing the array element directivity also increases the complexity of its design, decreases its efficiency, and leads to a higher level of loss in the feeding network. On the other hand, dielectric lens structures, having the ability to focus the incoming electromagnetic waves, provide another solution for high gain performance. Dielectric lens antennas are not only free from the disadvantages of Antenna Arrays but also advantageous due to their low loss and wide operation band. Moreover, these designs have been used in a vast range of applications such as millimeter wave, automotive radar, satellite or indoor communications [1-8], beamforming, and generation of multiple beams [9-10]. However, some of the most commonly used dielectric lens structures such as Luneburg, Einstein, dielectric rod, and Fresnel lens are usually optical or quasi-optical, and they have a 3D design structure that makes them difficult to manufacture by using dielectric materials.

With the advances in 3D printing technology, the application areas of these devices continue to expand. One of the most recent applications of 3D printing technology is the prototyping of microwave designs such as Antennas [11-13]. Due to being fast, highly accurate, and their ability to print even the most complex structures which would become either impractical or high cost using traditional prototyping methods, the usage of 3D printing technology has become more prevalent in microwave design prototyping field [14-20].

In this paper, the design and realization of a modified elliptical lens antenna for X band applications by using 3D printing technology has been presented. To this aim, first, elliptical lens design has been modeled in the 3D EM simulation environment. Then, the optimally designed elliptical lens model has been prototyped by using 3D printing technology. The measurements and the simulations show that the proposed prototyped elliptical lens antenna has a desirable performance where it achieves a gain level of 17 to 20.5 dBi over the operation band of 8-12 GHz. Moreover, when it is compared with its counterpart in literature, it is found that the proposed method is more efficient, has a lower cost, and it is an effective method for prototyping dielectric lens structures with 3D properties.

Submitted On: February 18, 2020
Accepted On: May 21, 2020
https://doi.org/10.47037/2020.ACES.J.350810

II. DESIGN AND SIMULATION OF DIELECTRIC LENS ANTENNA

One of the most commonly used antenna types is a waveguide horn antenna. Although they have relatively good gain characteristics, they are limited by their dimensions as they must have a specific size with respect to the wavelength of their operating frequency. Otherwise, they would have efficiency problems. One of the solutions to go beyond this limitation and improve their performance is to place a dielectric lens structure into their aperture.

In this section, an elliptical lens antenna is designed for X band applications. The elliptical dielectric structure is a modified version of the lens design in [21-22], where the endpoint of the structure is trimmed to increase the performance of the antenna in the X band. The design of the Modified Elliptical Dielectric Lens Antenna (MEDLA) is given in Fig. 1. The primary design considerations of the proposed antenna can be named as follows:

(i) Gain performance of the antenna can be increased/decreased by increasing/decreasing the dielectric diameter of the ellipsoid.

(ii) The operating frequency can be increased/ decreased by decreasing/increasing all dimensions of the model.

(iii) Same phenomena can also be said for the dielectric permittivity of the lens material, which plays an essential role in the performance characteristic of the design.

Furthermore, by adding additional matching layers, the reflections at the antenna surface can be reduced at the expanse of increasing the manufacturing cost.

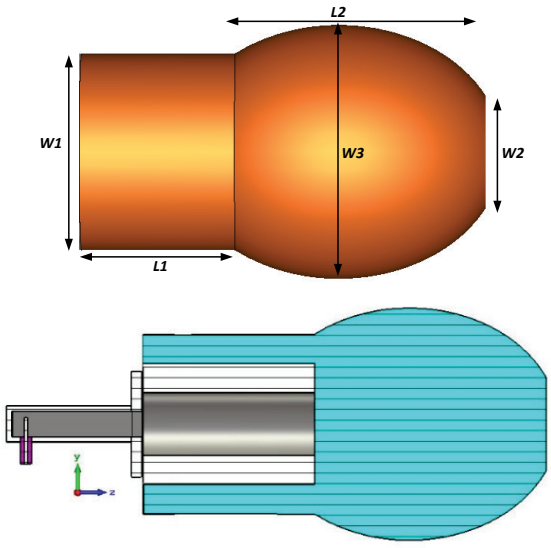

Fig. 1. Schematic of MEDLA.

The variation of Directivity and S_{11} performances of the MEDLA concerning its design parameters are given in Table 1 and Fig. 2.

Table 1: Parametric analyses of design parameters of MEDLA given as (S_{11}/Directivity)

Parameters (mm)		Frequency GHz		
		8	10	12
L_1	50	-13.6/18.9	-17.9/20.1	-19.2/21
	70	-14.1/18.9	-17.7/20.2	-19.7/21
	90	-3/19.1	-5.3/20.2	-20.5/21.4
L_2	80	-6.5/16.8	-9/18.8	-10.7/19
	100	-14.1/18.9	-17.1/20.2	-19.7/21.1
	120	-7.6/17.8	-8.6/19	-9.1/18.1
W_1	50	-14.1/19	-18/20.3	-19.4/21
	70	-14.1/18.9	-17.8/20.2	-19.8/21.1
	90	-14.8/19.1	-17.8/20.3	-20.6/21.1
W_2	10	-15/18.9	-17.8/20.2	-19.8/21.1
	20	-14.1/18.9	-17.7/20.3	-19.8/21.2
	30	-13/18.9	-18/20.3	-20.8/21.2
W_3	60	-6.5/18.8	-8.7/20.2	-9/20.6
	80	-14.1/18.9	-17.7/20.2	-19.7/21.4
	100	-6.1/18.5	-8.9/19.9	-12.7/21.4

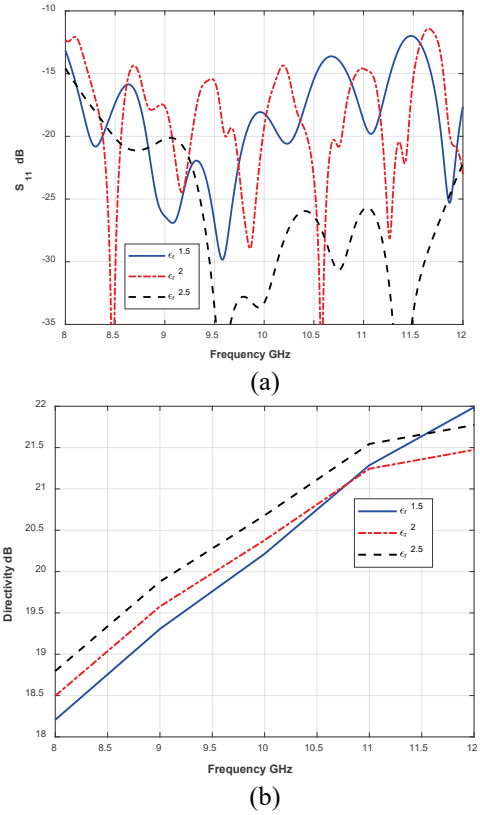

Fig. 2. Simulated performance of: (a) return loss and (b) Directivity; for variant dielectric constant values.

As can be seen from Table 1 and Fig. 2, each design parameter has a unique effect on the performance response of MEDLA design. Thus, the determination of optimal design parameters of antennas geometrical and material parameters can be considered as a multi-objective, multivariable optimization problem. The design parameters of MEDLA can be taken as input variables of the optimization process, and the performance measures of MEDLA, such as S11 and directivity, are taken as outputs or objectives of the optimization problems. In Table 2, optimization variables and their upper and lower constants are presented.

Table 2: Constraints of the variables

Parameter	Constraint	Parameter	Constraint
w_1 (mm)	50~90	L_1 (mm)	50~90
w_2 (mm)	10~30	L_2 (mm)	80~100
w_3 (mm)	60~100	ε_r	1.2~2.7

In our design process, two metaheuristic optimization algorithm that had shown great potential in design optimization of microwave stages; (1) Honey Bee Mating Optimization (HBMO) [23-24], (2) Differential Evolutionary Algorithm (DEA) [25-26], are being used in a hybrid combination of Global (HBMO) and Local (DEA) search tool for finding the optimal design parameters of MEDLA. HBMO algorithm has the capability of searching in ample variables space, which makes it an excellent global optimizer. However, the design optimization of an antenna requires a fine-tuning of design parameters for achieving the ideal performance. For this mean, the DEA optimization method had been used to do a local search around the optimal values obtained by HBMO. Both of the algorithms had been coded in MATLAB environment that can simultaneously work alongside CST simulator [27]. Based on the designer's hardware capabilities, this process can be accelerated via the use of parallel processing methods for reducing the total time required. The cost function that is given in Eq (1) is being used for guiding the hybrid search of HBMO and DEA. The total cost is calculated based on the candidate solution's directivity and S_{11} values at each desired frequency:

$$\text{Cost}_i = \sum_{f=8\text{GHz}}^{12\text{GHz}} \frac{C_1}{Directivity(f)_i} + \frac{C_2}{\left|S_{11}(f)_i\right|}, \qquad (1)$$

where, C is weighted constrained determined by the user (Here in C_1=0.9, C_2= 0.3, which is determined with trial and error method), i is the index of the candidate solution in search space. In Table 3, the optimal design parameters of MEDLA have been presented.

Table 3: Parameters of MEDLA in (mm)

W_1	70	L_1	67.5
W_2	20	L_2	95.8
W_3	84	ε_r	2.5

III. 3D MANUFACTURING AND EXPERIMENTAL RESULTS OF MEDLA

In this section, the CEL Robox® Micro manufacturing platform using PLA material "PLA Filament - Polar White RBX-PLA-WH002" is employed for carrying out the prototyping of the MEDLA designed in Section II. One of the advantages of 3D printers is their ability to adjust the infill rate of the printed material within the structure, which is used by many for creating a design with lower weight values. In addition, making use of this advantage, it is possible to adjust the dielectric properties of the 3D printed structure by increasing or decreasing the infill rate of the design as it is given in Table 4 [28-29]. By using the Eq (2) obtained via regression methods from data in Table 4, the infill rate of the MEDLA is chosen as 70%, which would provide a dielectric constant value of 2.5:

$$\varepsilon_r = -1.3x10^{-6}x^3 + 0.0374x + \frac{6.42}{x} + 0.217, \qquad (2)$$

where x indicates the infill rate in %.

Table 4: Dielectrıc constant value of PLA with respect to the infill rate [28]

Infill Rate %	Dielectric Constant ε_r	Loss Tangent
18	1.24	0.002
33	1.6	0.004
73	2.53	0.006
100	2.72	0.008

The 3D printed MEDLA design is presented in Fig. 3. The measurement results are obtained using the measurement setup given [30-31]. A Network Analyzer with a measurement bandwidth of 9 kHz to 13.5 GHz, and two identical antennas "Rohde—Schwarz RS Zvl13 and LB8180 0.8 to 18 GHz" have been used for measurement of the 3D printed Dielectric Lens antenna.

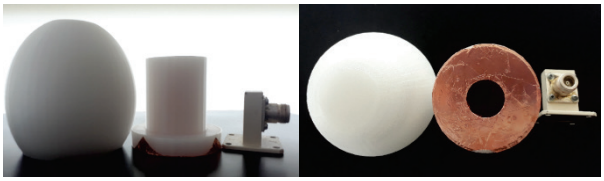

(a) (b)

Fig. 3. Dielectric lens antenna and feed network: (a) side view and (b) top view.

The measured return loss characteristics are given in Fig. 4. It can be observed in Fig. 4 that placing the 3D printed elliptical lens structure into the aperture of the waveguide does not have any distortive effects on the S_{11} characteristics of the system, and the design achieves return loss characteristics of less than -10 dB over the operation band of 8-12 GHz. In addition, it should also

be noted that the main reason for the difference between the simulated and the measured S_{11} characteristics is that the simulations were carried out by assuming an ideal waveguide, whereas non-ideal real waveguides are used for the measurements.

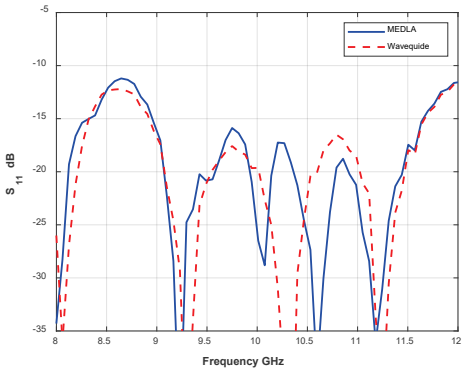

Fig. 4. The measured return loss of MEDLA.

The radiation patterns of the 3D printed MEDLA and the comparison of the maximum gain values between the simulations and the measurements are given in Fig. 5 and Table 5, respectively. It can be concluded from the measurement results shown here that the 3D printed MEDLA structure increases the directivity of the waveguide up to 11 dB over the operation band of 8-12 GHz.

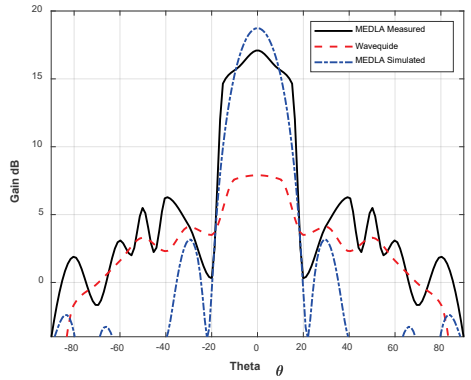

(a)

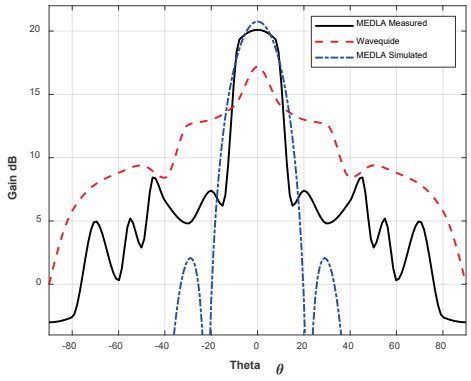

(b)

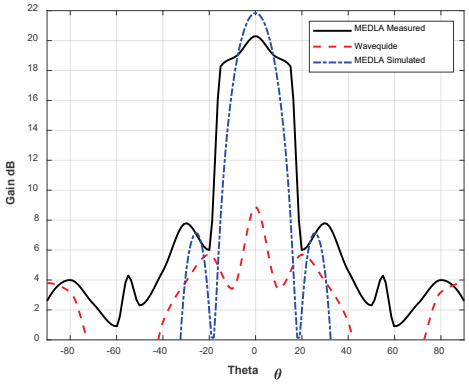

(c)

Fig. 5. Measured and simulated radiation patterns of the MEDLA at: (a) 8 GHz, (b) 10 GHz, and (c) 12 GHz.

Table 5: Maximum hgain (dB) comparison between simulation and measurement

f GHz)	MEDLA		Waveguide
	Simulated	Measured	
8	18.7	17.1	7.9
9	19.8	18.2	8.2
10	20.7	19.8	8.7
11	21.5	20.5	9
12	21.8	20.3	8.9

Furthermore, a gain (dB) comparison of the proposed MEDLA design with similar works in literature [32-35] is given in Table 6. As can be seen from the comparison table, the proposed antenna design achieves a high wideband gain performance compared to the counterpart designs in [32,34], where designs have much larger sizes. In cases of [33, 35] where the designs have much smaller sizes, the gain performance is almost half [35], or much lesser [35] than of the proposed MEDLA design. Thus, it can be said that the proposed MEDLA module achieves a more desirable Gain vs. Volume performance within the requested operating frequency compared to its counterpart designs.

Table 6: Comparison of gain (dB) of typical dielectric loaded antenna modules

	Size (mm)	Volume cm^3	Operation Mand (GHz)				
			8	9	10	11	12
Here	163.3x70x84	960.2	17.1	18.2	19.8	20.5	20.3
[32]	279x244x159	10824	16	18	14.8	17	15
[33]	85.x30.8x15.9	41.62	8.5	9	9	9	10
[34]	90.7x210x210	4013	---	---	17	---	---
[35]	87.4x59.3x80	414.6	14	15.5	16.5	15	17

VII. CONCLUSION

Herein, a modified elliptical lens antenna was designed for X band applications and realized by using

3D printing technology. The optimally designed elliptical lens model was prototyped by using 3D printing technology, and then its simulated and measured performance were compared. The results were found to be desirable, where the proposed prototyped elliptical lens antenna achieves a gain level of 17 to 20.5 dBi over the operation band of 8-12 GHz. In addition, the comparison of the prototyped antenna with its counterpart dielectric lens antenna in literature proved that the proposed method is more efficient, has a lower cost, and it is an effective method for prototyping dielectric lens structures with 3D properties. Thanks to the unique manufacturing capability of 3D printers and varying permittivity values of materials concerning their infill rates, it is possible to have elliptical or non-uniform geometrical designs for dielectric lens stages with multiple layers with different dielectric constant values. Furthermore, with recent developments in 3D printing materials such as conductive filaments, the design of multi-material-lens stages can also be achieved.

REFERENCES

[1] J. R. Risser, *Microwave Antenna Theory and Design*. New York, NY, USA: McGraw-Hill, 1949.

[2] B. Chantraine-Bares, R. Sauleau, L. L. Coq, and K. Mahdjoubi, "A new accurate design method for millimeter-wave homogeneous dielectric substrate lens antennas of arbitrary shape," *IEEE Trans. Antennas Propag*., vol. 53, no. 3, pp. 1069-1082, Mar. 2005.

[3] W. E. Kock, "Metallic delay lens," *Bell System Tech. J*., vol. 27, pp. 58-82, Jan. 1948.

[4] W. E. Kock, "Metal lens antennas," *Proc. IRC*, vol. 34, no. 11, pp. 826-836, Nov. 1946.

[5] B. Schoenlinner, X. Wu, J. P. Ebling, G. V. Eleftheriades, and G. M. Rebeiz, "Wide-scan spherical-lens antennas for automotive radars," *IEEE Trans. Microwave Theory Tech.*, vol. 50, pp. 2166-2175, 2002.

[6] B. Fuchs, O. Lafond, S. Rondineau, M. Himdi, and L. Le Coq, "Off-axis performances of half Maxwell fish-eye lens antennas at 77GHz," *IEEE Trans. Antennas Propag.*, vol. 55, pp. 479-482, 2007.

[7] J. R. Costa, C. A. Fernandes, G. Godi, R. Sauleau, L. Le Coq, and H. Legay, "Compact Ka-band lens antennas for LEO satellites," *IEEE Trans. Antennas Propag*., vol. 56, pp. 1251-1258, 2008.

[8] C. A. Fernandes, "Shaped dielectric lenses for wireless millimeter-wavecommunications," *IEEE Antennas Propag. Mag*., vol. 41, pp. 141-150, 1999.

[9] O. Lafond, M. Caillet, B. Fuchs, S. Palud, M. Himdi, S. Rondineau, and L. Le Coq, "Millimeter wave reconfigurable antenna based on active printed array and inhomogeneous lens," 2008 38th *Eur. Microwave Conf*., Amsterdam, Holland, pp. 147-150, 2008, doi: 10.1109/EUMC.2008.4751409.

[10] B. Fuchs, S. Palud, O. Lafond, M. Himdi, and S. Rondineau, "Système antennaire dont le diagramme de rayonnement est reconfigur-able parmi des diagrammes de rayonnement sectoriels et directifs, etdispositifs émetteur et/ou récepteur correspondant," French Patent 0756664, July 20, 2007.

[11] M. A. Belen and P. Mahouti, "Design and realization of quasi Yagi antenna for indoor application with 3D printing technology," *Microw. Opt. Technol. Lett*., vol. 60, no. 9, pp. 2177-2181, 2018. https://doi.org/10.1002/mop.31319

[12] Y. C. Toy, P. Mahouti, F. Güneş, and M. A. Belen, "Design and manufactering of an X-band horn antenna using 3-D printing technology," *8th International Conference on Recent Advances in Space Technologies*, İstanbul, Turkey, June 19-22, 2017.

[13] J. J. Adams, E. J. Duoss, T. Malkowski, M. Motala, B. Y. Ahn, R. G. Nuzzo, J. T. Bernhard, and J. A. Lewis, "Conformal printing of electrically small antennas on three-dimensional surfaces," *Advanced Materials*, vol. 23, no. 11, pp. 1304-1413, 2011.

[14] G. Shaker, L. Ho-Seon, S. Safavi-Naeini, and M. Tentzeris, "Printed electronics for next generation wireless devices," *IEEE Antenna and Propagation Conference (LAPC)*, pp. 1-5, Nov. 2011.

[15] J. Mei, M. Lovell, and M. Mickle, "Formulation and processing of novel conductive solution inks in continuous inkjet printing of 3-D electric circuits," *IEEE Transactions on Electronics Packaging Manufacturing*, vol. 28, no. 3, pp. 265-273, July 2005.

[16] G. Shaker, S. Safavi-Naeini, N. Sangary, and N. M. Tentzeris, "Inkjet printing of ultrawideband (UWB) antennas on paper based substrates," *Antennas and Wireless Propagation Letters, IEEE*, vol. 10, pp. 111-114, 2011.

[17] J. Hester, S. Kim, J. Bito, T. Le, J. Kimionis, D. Revier, C. Saintsing, W. Su, B. Tehrani, A. Traille, B. S. Cook, and M. Tentzeris, "Additively manufactured nanotechnology and origami-enabled flexible microwave electronics," *Proc. IEEE*, vol. 103, no. 4, pp. 583-606, Apr. 2015.

[18] J. Kimionis, A. Georgiadis, M. Isakov, H. J. Qi, and M. M. Tentzeris, "3D/inkjet-printed origami antennas for multi-direction RF harvesting," *in IEEE MTT-S Int. Microw. Symp. (IMS)*, Phoenix, AZ, USA, pp. 1-4, May 2015.

[19] C. D. Saintsing, K. Yu, H. J. Qi, and M. Tentzeris, "Planar monopole antennas on substrates fabricated through an additive manufacturing process," *2015 IEEE Radio and Wireless Symposium (RWS)*, San Diego, CA, pp. 159-161, 2015. doi: 10.1109/

RWS.2015.7129744.

[20] B. Tehrani, B. S. Cook, and M. M. Tentzeris, "Post-process fabrication of multilayer mm-wave on-package antennas with inkjet printing," in *2015 IEEE Int. Symp. Antennas and Propag. (APSURSI)*, Vancouver, BC, Canada, July 2015.

[21] N. Pohl, "A dielectric lens antenna with enhanced aperture efficiency for industrial radar applications." Available on https://www.cst.com/solutions/article/a-dielectric-lens-antenna-with-enhanced-aperture-efficiency-for-industrial-radar-applications

[22] N. Pohl, "A dielectric lens antenna with enhanced aperture efficiency for industrial radar applications," in *IEEE Middle East Conference on Antennas and Propagation (MECAP 2010)*, pp. 1-5, Oct. 2010.

[23] F. Güneş, S. Demirel, and P. Mahouti, "A simple and efficient honey bee mating optimization approach to performance characterization of a microwave transistor for the maximum power delivery and required noise," *International Journal of Numerical Modelling: Electronic Networks, Devices and Fields*, vol. 29, no. 1, pp. 4-20, 2016.

[24] F. Güneş, S. Demirel, and P. Mahouti, "Design of a front–end amplifier for the maximum power delivery and required noise by HBMO with support vector microstrip model," *Radioengineering*, vol. 23, no. 1, pp. 134-143, 2014.

[25] F. Güneş, M. A. Belen, and P. Mahouti, "Competitive evolutionary algorithms for building performance database of a microwave transistor," *International Journal of Circuit Theory and Applications*, vol. 46, no. 2, pp. 244-258, 2018.

[26] P. Mahouti, "Design optimization of a pattern reconfigurable microstrip antenna using differential evolution and 3D EM simulation-based neural network model," *International Journal of RF and Microwave Computer-Aided Engineering*, vol. 29, no. 8, e21796, 2019.

[27] A. Belen, F. Güneş, and P. Mahouti, "Design optimization of a dual-band microstrip SIW antenna using differential evolutionary algorithm for X and K-band radar applications," *ACES Journal*, Accepted.

[28] S. Zhang, C. C. Njoku, W. G. Whittow, and J. C. Vardaxoglou, "Novel 3D printed synthetic dielectric substrates," *Microw. Opt. Technol. Lett*., vol. 57, pp. 2344-2346, 2015. doi:10.1002/mop.29324.

[29] P. Mahouti, "3 Boyutlu Yazıcı Teknolojisi ile Bir Mikroşerit Yama Antenin Maliyet Etkin Üretimi," *Journal of Engineering Sciences and Design*, Kabul Edildi, 2019 (in Turkish).

[30] F. Güneş, Z. Sharipov, M. A. Belen, P. Mahouti, "GSM filtering of horn antennas using modified double square frequency selective surface," *Int. J. RF Microw. Comput. Aided Eng*., vol. 27, e21136, 2017. https://doi.org/10.1002/mmce.21136

[31] M. A. Belen, F. Güneş, P. Mahouti, and A. Belen, "UWB gain enhancement of horn antennas using miniaturized frequency selective surface," *ACES Journal*, vol. 33, no. 9, Sep. 2018.

[32] A. S. Türk, A. K. Keskin, and M. D. Şentürk, "Dielectric loaded TEM horn-fed ridged horn antenna design for ultrawideband ground-penetrating impulse radar," *Turkish J. Elec. Eng. & Comp. Sci*., vol. 23, pp. 1479-1488, 2015.

[33] R. J. Bauerle, R. Schrimpf, E. Gyorko, and J. Henderson, "The use of a dielectric lens to improve the efficiency of a dual-polarized quad-ridge horn from 5 to 15 GHz," *IEEE Transactions on Antennas and Propagation*, vol. 57, no. 6, June 2009.

[34] J. Tak, D.-G. Kang, and J. Choi, "A lightweight waveguide horn antenna made via 3d printing and conductive spray coating," *Microwave and Optical Technology Letters*, vol. 59, no. 3, Mar. 2017.

[35] M. F. Ain, A. Othman, and Z. A. Ahmad, "Hybrid dielectric resonator integrated pyramidal horn antenna," *Microwave and Optical Technology Letters*, vol. 55, no. 6, June 2013.

Aysu Belen received her M.Sc. degree in Electronics and Communication Engineering from Yıldız Technical University in 2016. She has been currently in the Ph.D. program at Yıldız Technical University. Her main research areas are optimization of microwave circuits, circuits, device modeling, and computer-aided circuit design and microwave amplifiers.

Evrim Tetik received his Ph.D. degree in Satellite Communication and Remote Sensing from Istanbul Technical University in 2015. The main research areas are electromagnetic theory, direct and inverse electromagnetic scattering, and computational electromagnetics.

Slot Filling Factor Calculation and Electromagnetic Performance of Single Phase Electrically Excited Flux Switching Motors

Bakhtiar Khan, Faisal Khan, Wasiq Ullah, Muhammad Umair, and Shahid Hussain

Department of Electrical & Computer Engineering
COMSATS University Islamabad, Abbottabad Campus, Pakistan
engr.bakhtiarkhan@gmail.com

Abstract ─ For variable speed applications, flux controlling capability of electrically excited flux switching motors (EEFSMs) attract researchers' attention. However, low copper slot filling factor of the EEFSM with standard stator slot vitiates the electromagnetic performance and efficiency. This paper has proposed a new Octane Modular Stator (OMS) EEFSM model that has pentagonal stator slot and high copper slot filling factor. Copper slot filling factor is deliberated analytically for the proposed model and designs with standard stator slots, i.e., trapezoidal and rectangular. Electromagnetic performance of the OMS, Rectangular Stator Slot (RSS) and Trapezoidal Stator Slot (TSS) EEFSM designs are evaluated by finite element analysis (FEA) through JMAG v18.1 FEA solver. The proposed OMS EEFSM model has 9% higher copper slot filling factor in comparison with standard stator slots designs under same geometric parameters. The high copper slot filling factor of the proposed OMS EEFSM model has improved performance in term of low electric and magnetic loading.

Index Terms ─ Electrically Excited Flux Switching Motor (EEFSM), Finite Element Analysis (FEA), non-overlapped windings, Octane Modular Stator (OMS), single phase motor, salient rotor.

I. INTRODUCTION

Strong overload capability, high average torque, low torque ripples and high efficiency are the main desired characteristics of every motor and especially for high speed applications [1-4]. In permanent magnet (PM) flux switching motor (FSM), PM as well as armature windings are located at stator and making a robust rotor structure. Furthermore, it has high power density, easy heat dissipation and suitable for high speed applications. Despite these pros, in this type FSM an enormous amount of rare earth permanent magnet is used that overall increases the cost of the machine. The resources of the PM material are depleting day by day and prices to be raised [5-9]. As temperature suddenly increases the performance of the PMFSM is greatly degraded and hence limiting its application at high temperature. The fixed and uncontrolled flux is the undesired characteristic for variable high speed operations [10-11]. The flux of electrically excited (EE) FSM can be controlled electronically, performance is not degraded with increase in temperature and overall cost is low. The simple manufacturing process of single phase EEFSM, easy maintenance, longer lifetime and low cost are the core points that prioritized it for high speed applications [12].

For fan applications, single phase 12Slots-6Poles (12S-6P) EEFSM novel design with trapezoidal slot stator, non-overlapped windings arrangement and segmental rotor has presented in [13]. The key characteristics of this design are low weight, less copper losses and higher efficiency. However, it cannot be used for high speed operations as it has segmental rotor. In [14] authors have presented two novel model 12S-6P and 8S-4P designs of single phase EEFSM with overlapped windings arrangement and both the designs are validated experimentally. In these design overlapped windings arrangement cause high copper losses. Authors have designed a novel model 8S-6P single phase EEFSM with non-overlapped windings arrangement in [15], this design has robust rotor structure and low copper losses. Similarly 24S-10P single phase EEFSM is proposed in [16]. All the designs discussed above have standard trapezoidal slot structure. High power density and efficiency are key factors for motors used in high speed applications. The most desired characteristics for high speed operation are high power density and high efficiency [17-18]. Increasing copper slot filling factor of the stator windings of EEFSM can increase the power density and efficiency [19]. This work has proposed single phase 8S-6P Octane Modular Stator (OMS) EEFSM model and the direction for this design is from [20] as presented by Fig. 1. The proposed model has pentagonal slot structure which has high copper slot filling factor than the trapezoidal stator slot (TSS) and rectangular stator slot (RSS), and this is validated via algorithm [21]. Design methodology, copper slot filling factor calculation, no-load analysis, load analysis and

Submitted On: July 11, 2019
Accepted On: April 5, 2020
https://doi.org/10.47037/2020.ACES.J.350811

conclusion are conferred in Sections II, III, IV, V and VI respectively.

Fig. 1. Poki-Poki model of MITSUBISHI ELECTRIC.

II. DESIGN METHODOLOGY

The three single phase 8S-6P topologies shown in Fig. 2 are designed and analyzed in JMAG v18.1 as per geometric design parameters given in Table 1. The position of the field/armature windings are justified through coils arrangement test.

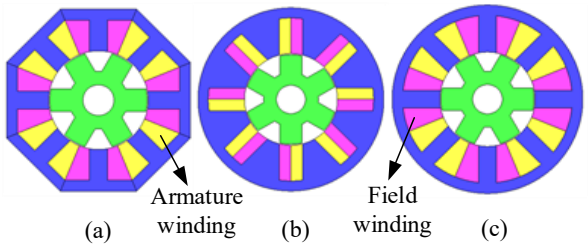

Fig. 2. Electrically excited FSMs: (a) OMS, (b) RSS, and (c) TSS.

Table 1: Single phase 8S-6P EEFSMs parameters

Design Parameter	OMS	TSS	RSS
Stator slot width (mm)	8.2		
Stator yoke height (mm)	5		
Field/armature slots area (mm^2)	430.08	607.12	401.44
Stator outer radius (mm)	45		
Armature/field coil turns	154	180	129
Armature current (A) @ 15A/mm^2	6.57	6.73	6.60
Field excitation current (A) @ 15A/mm^2	4.65	4.75	4.67

III. COPPER SLOT FILLING FACTOR CALCULATION

Copper slot filling factor is calculated by procedure in [21] for the OMS, RSS, TSS EEFSM designs and the results are compared. The input parameters of the algorithm are the slot cross section and dimensions of the wire, where the output is the highest figure of conductors in the slot to be accommodated. Equation (1) is mathematical model for the copper slot filling factor:

$$f_{slot} = \frac{N_w \times A_w}{A_{slot}}. \quad (1)$$

Here f_{slot} is copper slot filling factor, N_w number of copper conductors, A_w cross-sectional area of conductor and A_{slot} slot area. As the copper losses are inversely proportional to copper cross section, so maximizing the copper slot filling factor will minimize the copper losses. Below in Fig. 3 are the slot sections of OMS, TSS and RSS EEFSMs.

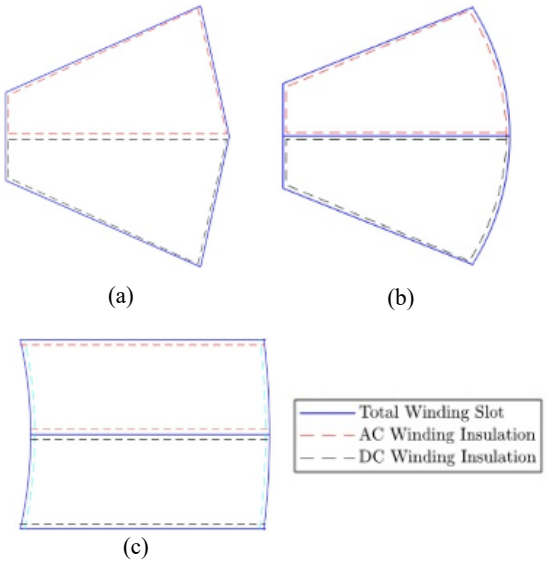

Fig. 3. Slot sections of EEFSM: (a) OMS, (b) TSS, and (c) RSS.

The algorithm for this work has been implemented in MATLAB and geometrical model of the slots are used. Also it is important to select the dimensions and type of the conductor. To insert a conductor in the slot, the conditions below to be satisfied. Here (x_c, y_c) and d_{max} represent the center point and diameter of the circular conductor. The distance of the conductor from y-axis is d_1, x-axis d_2, slop line d_3 and arc d_4 as in Fig. 4. For any conductor to be inside the slot profile, the conditions applied in *xy* frame reference are:

$for\ d_1 \geq 0;$

$$|(x_c - d_{max}/2) - x_{vline}| \geq 0. \quad (2)$$

$for\ d_2 \geq 0;$

$$|(y_c - d_{max}/2) - y_{hline}| \geq 0. \quad (3)$$

$for\ d_3 \geq 0;$
$if\ y_c > 0;$

$$\frac{(y_{pline} - y_c) - s_{line}.(x_{pline} - x_c)}{\sqrt{s^2_{line}+1}} - \frac{d_{max}}{2} \geq 0. \quad (4)$$

$if\ y_c < 0;$

$$\frac{(y_{pline} + y_c) - s_{line}.(x_{pline} - x_c)}{\sqrt{s^2_{line}+1}} - \frac{d_{max}}{2} \geq 0. \quad (5)$$

$for\ d_4 \geq 0;$
$if\ y_c > 0;$

$$\left(r_{1,2} - \frac{d_{max}}{2}\right) - \sqrt{\left(x_c - x_{c,arc}\right)^2 + \left(y_c - y_{c,arc}\right)^2} \geq 0. \quad (6)$$

$if\ y_c < 0;$

$$\left(r_{1,2} - \frac{d_{max}}{2}\right) - \sqrt{\left(x_c - x_{c,arc}\right)^2 + \left(y_{c,arc} - y_c\right)^2} \geq 0. \quad (7)$$

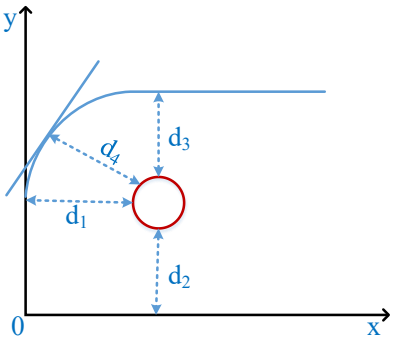

Fig. 4. Conductor placement in slot.

Figure 3 shows the horizontal implementation of slot contour in algorithm. Before starting the algorithm, the placement of first conductor is the first step and coordinate for its center are:

$$x_c = \frac{d_{max}}{2} + d + x_i\,; \quad y_c = -\left(\frac{w + d_{max}}{2}\right) + y_i. \quad (8)$$

For placement the conductors in the remaining part of slot, the slot area is divided into grid of i_{th} columns and j_{th} rows. Circular conductors are always placed in honey comb structure. Equations (9) and (10) are used to determine the maximum number of rows and columns:

$$i_{max} = round\left(\frac{x_E}{\sqrt{3d_{max}/2}}\right), \quad (9)$$

$$j_{max} = round\left(\frac{w}{d_{max}}\right). \quad (10)$$

Round(x) rounds each element of x to nearest integer. Two "for loops" are used here, the outer loop fixes the index i and inner loop varying index j:

$$y_c(i, j+1) = y_c(i,j) + d_{max} + d_w. \quad (11)$$

After the increment in index i, conductor center coordinates are given by equations (12) and (13):

$$x_c(i+1, j) = x_c(i,j) + \sqrt{3/2}\,.(d_{max} + d_w), \quad (12)$$

$$y_c(i+1, j) = y_c(i,j) + mod(i+1, 2)\,.\,d_{max}/2. \quad (13)$$

Where mod(i+1, 2) is a function that returns the module after division between 'i+1' and 2. The results of the algorithm implemented in MATLAB for the arrangement of conductors in slots are in Fig. 5. The dimensions of the conductors in all three designs are selected according to maximum current requirement for the field and armature windings. Copper slot filling factor for each type slot is calculated by the mathematical model (1), results are presented in Fig. 6 and tabulated in Table 2. From the results it can be seen, the copper slot filling factor of OMS slot is 7% higher than that of TSS and 9% higher than that of RSS.

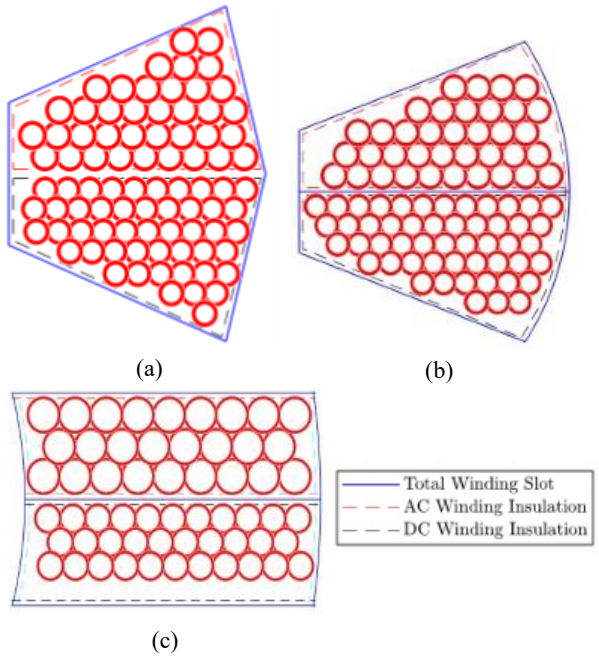

Fig. 5. MATLAB results for copper slot filling: (a) OMS, (b) TSS, and (c) RSS.

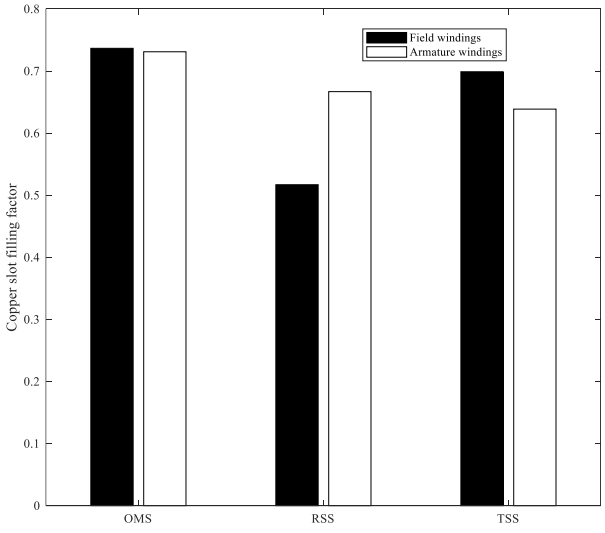

Fig. 6. Comparison of copper slot filling factor for three designs.

Table 2: Single phase 8S-6P EEFSMs copper slot filling factor

Description	Copper Slot Filling Factor		
	OMS	TSS	RSS
Field slot	0.73661	0.69890	0.51686
Armature slot	0.73103	0.63867	0.66682

IV. NO-LOAD ANALYSIS

The no-load analysis key indicators are: flux linkage, cogging torque, back-emf and total harmonic distortion (THD), all these are discussed in subsections.

A. Flux linkage

The operation of single phase 8S-6P OMS, TSS and RSS EEFSMs for non-overlapped windings arrangement is validated via coil test. Equations (14) and (15) are used to calculate the EE coil current density J_e and armature coil current density J_a. For the three designs no-load magnetic flux linkage are analyzed and compared, the EE windings current density is set to 15A/mm^2 and the results are presented in Fig. 7. TSS machine design has the highest flux linkage of 0.069Wb, where OMS has 0.050Wb and RSS design has the lowest 0.029Wb at maximum J_e=15A/mm^2 and J_a=0:

$$J_a = \frac{I_a N_a}{S_a \alpha_a}, \tag{14}$$

$$J_e = \frac{I_e N_e}{S_e \alpha_e}. \tag{15}$$

Where, J, S, N, and α represents current-density, slot-area, number of turns, and winding-factor respectively while subscripts "a" and "e" represent armature and EE coils correspondingly.

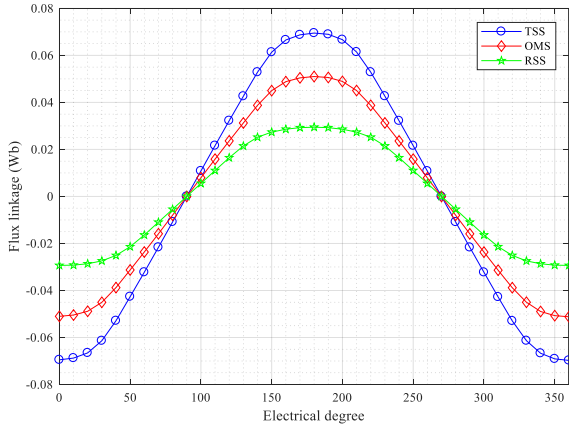

Fig. 7. No-load flux linkage.

B. Cogging torque

The J_e =15A/mm^2 current density of EE coil, J_a=0 armature coil current density and 1000 rpm rotor speed are used for the no-load cogging torque analysis at different rotor position represented by mechanical degree. Figure 8 shows cogging torque comparison of three designs which illustrates that RSS EEFSM design has lowest maximum peak cogging torque value of 0.010Nm as compared to the other designs of this paper. Where TSS has the highest maximum peak cogging torque of 0.136Nm and OMS model has the maximum peak cogging torque value of 0.10Nm.

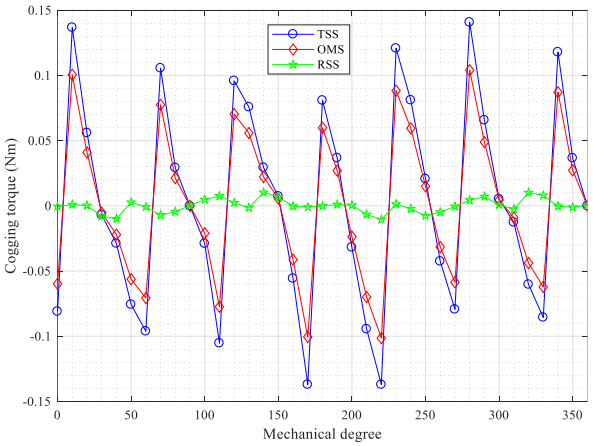

Fig. 8. Single phase no-load cogging torque.

C. Back-emf

2D FEM is used for the investigation of no-load back emf and the designs discussed above are included in this analysis. The no-load parameters were kept the same, i.e., J_e =15A/mm^2 current density of EE coil, J_a=0 armature coil current density and 1000 rpm rotor speed for all no-load tests. The results of the no-load back emf versus rotor position in electrical degree are presented in Fig. 9. In this study, TSS EEFSM design has the highest maximum peak back emf of 39.124 volts, where that of OMS is 28.711 volts. RSS design has the lowest maximum peak back emf value of 1.976 volts but back emf maximum peak values of all three designs are in the range of normal operation and graphs pattern is identical at different field currents.

D. Total harmonic distortion

The performance of conductors and insulators of electrical machines are degraded by harmonics, therefore, the calculation of total harmonic distortion (THD) for the all three designs are obligatory and obtained via equation (16):

$$THD = \frac{\sqrt{3_{rd} harmonic^2 + 5_{th} harmonic^2 + 7_{th} harmonic^2 + \cdots}}{1_{st}\ harmonic}. \tag{16}$$

The calculated THDs from the simulation results are: RSS 8S-6P single phase EEFSM design has the highest THD vale of 4.465%, TSS and OMS models have almost the same THD values of 3%. For better performance and

long lifetime of electrical machines, the THD should be always less than 5%.

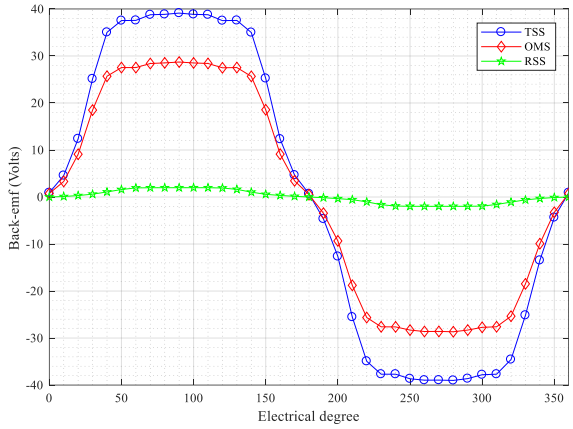

Fig. 9. No-load back-emf.

V. LOAD ANALYSIS

This section comprises analysis of average torque, instantaneous torque, torque and output power versus speed, losses and efficiency. Each one are deliberated in detail in the following subsections.

A. Average torque

The average-torque of single phase 8S-6P OMS, TSS and RSS EEFSM with salient rotor designs are shown in Fig. 10. The current density of EE coil is kept constant at J_e=15A/mm^2 and armature current-density J_a range is varied from 2.5A/mm^2 to 15A/mm^2. From 2D FEM analysis it is observed that increase in armature current density changing the average electromagnetic torque proportionally. TSS design with non-overlapped windings arrangement has the highest average electromagnetic torque value of 0.85 Nm, OMS has average electromagnetic torque 0.77 Nm and RSS has the lowest average electromagnetic torque value 0.58 Nm.

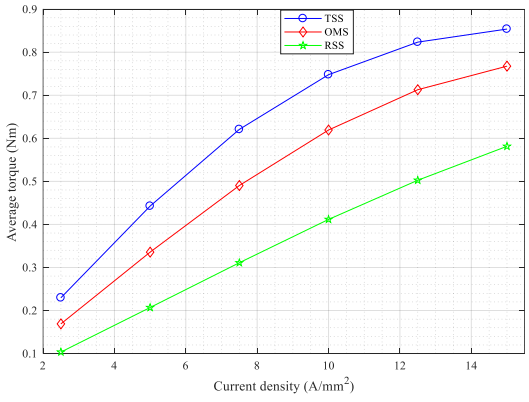

Fig. 10. Average torque vs J_a at J_e=15A/mm^2 plot.

B. Instantaneous torque

Instantaneous torque is the important part of load analysis, simulation results of the 2D FEA for the instantaneous torque at various rotor positions in electrical degree are labeled by different lines in Fig. 11 for the three designs. The TSS model has the highest maximum peak instantaneous torque value of 1.86 Nm and minimum bottom value -0.138 Nm. OMS EEFSM has maximum peak instantaneous torque value of 1.55 Nm and minimum bottom value -0.109 Nm, where RSS design has the lowest maximum peak value of 1.28 Nm and minimum bottom value -0.00002 Nm. This shows that TSS design has the highest peak to peak ripples, RSS design has the lowest and OMS has peak to peak ripples in-between the other two designs.

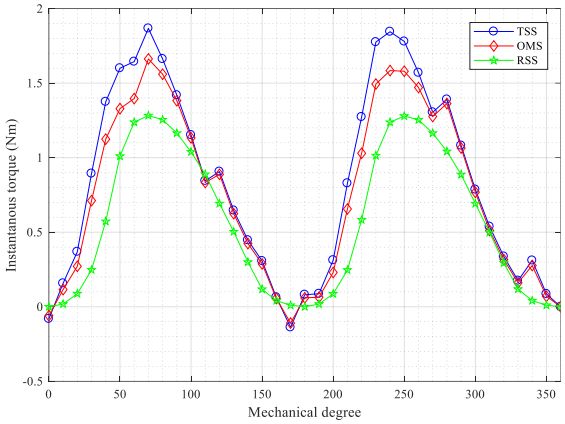

Fig. 11. Instantaneous torque.

C. Average torque and output power versus speed

The torque and power versus speed curves of the initial designs of the EEFSM are plotted in Fig. 12. The maximum torque of OMS, TSS and RSS are 0.83 Nm, 0.94 Nm and 0.59 Nm at speed 1327.5 rpm, 1036.3 rpm and 1913.3 rpm respectively. Similarly, the maximum output power of the above discussed designs are 115.42 watt, 109.5 watt and 119.75 watt at speed 1327.5 rpm, 1362.2 rpm and 1913.3. Below and above these speeds the average torque and output power are reduced. Analysis of the deliberated three EEFSMs show that OMS EEFSM has stable and high average torque and output power at same speed, while for the other two designs either average torque or output power are low. So, OMS EEFSM is the suitable option out of the three designs.

D. Losses and efficiency analysis

Core losses for the three designs are assessed by 2D-FEA via JMAG v18.1 FEA solver, while copper losses are calculated by the following equation [22]:

$$P_c = \rho(2L + 2L_{end}) \times J \times I \times N \times n_{slot}. \quad (17)$$

In (17) P_c copper losses, $\rho = 2.224 \times 10^{-8} \Omega m$ copper resistivity, L stack length, L_{end} calculated end coil length, J current density, I current, N number of turns and n_{slot} number of pairs of slots. OMS-EEFSM has efficiency 76.7% and losses 37.7 watt, the efficiency of TSS-EEFSM is 66.6% and losses are 60.64 watt and RSS-EEFSM has 75.3% efficiency and 34.37 watt losses.

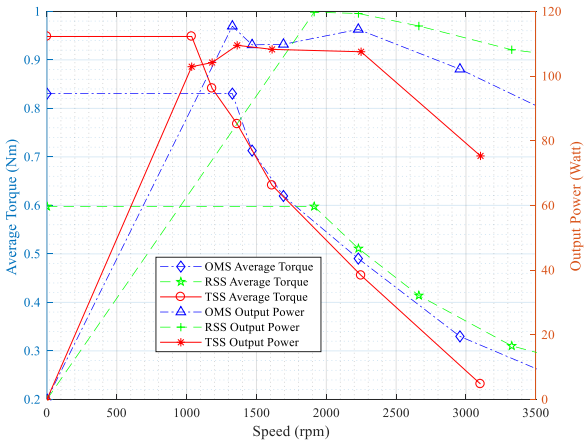

Fig. 12. Average torque and output power vs speed.

VI. CONCLUSION

Single phase OMS 8S-6P, TSS and RSS EEFSM with salient rotor are designed and evaluated in this research work. Copper slot filling factor is calculated for the three designs, the proposed design OMS model has 7% higher copper slot filling factor than TSS design and 9% higher than the RSS with the same geometric specifications, which is the core motive of this work. No-load and load analysis are carried out, the average torque of the proposed un-optimized OMS EEFSM model is 0.90 times of TSS design, at the cost of 17% less number of field and armature windings turns, 3% less field current and 3% less armature current. Besides, the peak to peak value of the instantaneous torque for the proposed design is 20% less than the TSS design, this entails that the proposed design has less peak to peak ripples than the standard trapezoidal slot design. Copper losses OMS EEFSM are 0.62 times that of TSS EEFSM and 1.09 times that of RSS EEFSM. Similarly, efficiency of proposed model is 1.15 times that TSS EEFSM and 1.02 times that of RSS EEFSM. Although the copper losses of RSS EEFSM are less than OMS EEFSM but OMS EEFSM has 1.4 times high average torque than RSS EEFSM and 0.90 times that of TSS EEFSM at the same current density. Based on the analysis, it is concluded that the proposed OMS EEFSM model has better overall performance, copper losses can be reduced, average torque and efficiency of the initial design can be further improved by optimization and is best option for high speed applications.

ACKNOWLEDGMENT

We are thankful to Higher Education Commission (HEC) of Pakistan for supporting financially (No. 8114/KPK/NRPU/R&D/HEC/2017) this work.

REFERENCES

[1] P. Su, W. Hua, M. Hu, Z. Wu, J. Si, Z. Chen, and M. Cheng, "Analysis of stator slots and rotor pole pairs combinations of rotor-permanent magnet flux-switching machines," *IEEE Trans. Ind. Electron.*, vol. 67, no. 2, pp. 906-918, 2019.

[2] N. Ullah, M. K. Khan, F. Khan, A. Basit, W. Ullah, T. Ahmad, and N. Ahmad, "Comparison of analytical methodologies for analysis of single sided linear permanent magnet flux switching machine: No-load operation," *ACES Journal*, vol. 33, no. 8, pp. 923-930, 2018.

[3] N. Ahmad, F. Khan, N. Ullah, and M. Z. Ahmad "Performance analysis of outer rotor wound field flux switching machine for direct drive application," *ACES Journal*, vol. 33, no. 8, pp. 913-922, 2018.

[4] M. M. Nezamabadi, E. Afjei, and H. Torkama, "Design and electromagnetic analysis of a new rotary-linear switched reluctance motor in static mode," *ACES Journal*, vol. 31, no. 2, pp. 171-179, 2016.

[5] Z. Q. Zhu and J. T. Chen, "Advanced flux-switching permanent magnet brushless machines," *IEEE Trans. Magn.*, vol. 46, no. 6, pp. 1447-1453, June 2010.

[6] X. Zhu, Z. Shu, L. Quan, Z. Xiang, and X. Pan, "Design and multicondition comparison of two outer-rotor flux-switching permanent magnet motors for in-wheel traction applications," *IEEE Trans. Ind. Electron.*, vol. 64, no. 8, pp. 6137-6148, Aug. 2017.

[7] H. Yang, H. Lin, Z. Q. Zhu, D. Wang, S. Fang, and Y. Huang, "A variable-flux hybrid-PM switched-flux memory machine for EV/HEV applications," *IEEE Trans. Ind. Appl.*, vol. 52, no. 3, pp. 2203-2214, May/June 2016.

[8] Z. Xiang, X. Zhu, L. Quan, and D. Fan, "Optimization design and analysis of a hybrid permanent magnet flux-switching motor with compound rotor configuration," *CES Trans. Electrical Machines and Systems*, vol. 2, no. 2, pp. 200-206, 2018.

[9] Z. Z. Wu and Z. Q. Zhu, "Analysis of air-gap field modulation and magnetic gearing effects in switched flux permanent magnet machines," *IEEE Trans. Magnetics*, vol. 51, no. 5, pp. 1-12, 2015.

[10] F. Khan, E. Sulaiman, and M. Z. Ahmad, "Review of switched flux wound-field machines technology," *IETE Technical Review*, vol. 34, no. 4, pp. 343-352, 2017.

[11] E. Sulaiman, T. Kosaka, and N. Matsui, "High power density design of 6-slot–8-pole hybrid excitation flux switching machine for hybrid electric vehicles," *IEEE Trans. Magnetics*, vol. 47, no. 10, pp. 4453-4456, 2011.

[12] E. Sulaiman, M. F. M. Teridi, Z. A. Husin, M. Z. Ahmad, and T. Kosaka, "Performance comparison of 24S-10P and 24S-14P field excitation flux switching machine with single DC-Coil polarity," *7th International Power Engineering and Optimization Conference (PEOCO), IEEE*, pp. 46-51, 2013.

[13] M. F. Omar, E. Sulaiman, M. Jenal, R. Kumar, and R. N. Firdaus, "Magnetic flux analysis of a new field-excitation flux switching motor using segmental rotor," *IEEE Trans. Magnetics*, vol. 53, no. 11, pp. 1-4, 2017.

[14] Y. J. Zhou and Z. Q. Zhu, "Comparison of low-cost single-phase wound-field switched-flux machines," *IEEE Trans. Ind. Appl.*, vol. 50, no. 5, pp. 3335-3345, 2014.

[15] S. Ishaq, F. Khan, N. Ahmad, K. Ayaz, and W. Ullah, "Analytical modeling of low cost single phase wound field flux switching machine," *1st International Conference on Power, Energy and Smart Grid (ICPESG), IEEE*, pp. 1-6, 2018.

[16] J. Yuan, D. Meng, G. Lian, J. Zhang, H. Li, and F. Ban, "The stator slot-type optimization of electrical excitation flux-switching motor and its maximum torque/copper loss control," *IEEE Trans. Appl. Supercond.*, vol. 29, no. 2, pp. 1-5, 2019.

[17] G. Zhao, W. Hua, and J. Qi, "Comparative study of wound-field flux-switching machines and switched reluctance machines," *IEEE Trans. Ind. Appl.*, vol. 55, no. 3, pp. 2581-2591, 2019.

[18] H. J. Park and M. S. Lim, "Design of high power density and high efficiency wound-field synchronous motor for electric vehicle traction," *IEEE Access*, vol. 7, pp. 46677-46685, 2019.

[19] P. Herrmann, P. Stenzel, U. Vogele, and C. Endisch, "Optimization algorithms for maximizing the slot filling factor of technically feasible slot geometries and winding layouts," *6th International Electric Drives Production Conference (EDPC), IEEE*, pp. 149-155, 2016.

[20] T. Komatsu and A. Daikoku, "Elevator traction-machine motors," *Motor Technologies for Industry and Daily Life Edition*, 2003.

[21] A. O. D. Tommaso, F. Genduso, R. Miceli, and C. Nevoloso, "Fast procedure for the calculation of maximum slot filling factors in electrical machines," *12th International Conference on Ecological Vehicles and Renewable Energies (EVER), IEEE*, pp. 1-8, 2017.

[22] F. Khan, E. Sulaiman, and M. Z. Ahmad, "A novel wound field flux switching machine with salient pole rotor and nonoverlapping windings," *Turkish Journal of Electrical Engineering & Computer Sciences*, vol. 25, pp. 950-964, 2017.

Bakhtiar Khan received his B.Sc. and M.Sc. degree in Electrical Engineering from University of Engineering & Technology, Peshawar Pakistan and COMSATS University Islamabad (CUI), Abbottabad Campus, Pakistan in 2007 and 2018 respectively. He is currently enrolled in Ph.D. Electrical Engineering at CUI Abbottabad. His research interest includes design and analysis of electrical machines.

Faisal Khan received his Ph.D. degree in Electrical Engineering from Universiti Tun Hussien Onn Malaysia in 2016. Currently he is working as Assistant Professor at CUI, Abbottabad Campus.

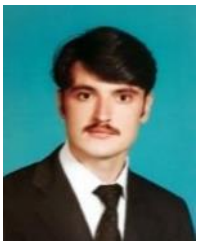

Wasiq Ullah received his B.S. degree in Electrical Engineering from CUI, Abbottabad Campus, Pakisan in 2018 and is currently enrolled in M.S. Electrical Engineering at CUI, Abbottabad Campus, Pakistan. He is research member of Electrical Machine Design Group.

Muhammad Umair received his B.S. degree in Electrical Engineering from CUI, Abbottabad Campus, Pakisan in 2018 and is currently enrolled in M.S. Electrical Engineering at CUI, Abbottabad Campus, Pakistan. He is working as Research Assistant in the Department of Electrical and Computer Engineering CUI, Abbottabad Campus, Pakistan. He is also research member of Electrical Machine Design Group.

Shahid Hussain has completed his B.S. Electrical Engineering degree in July, 2019 from CUI, Abbottabad Campus. He is Research Member of Electrical Machine Design Group.

CPW-Fed Wide Band Micro-machined Fractal Antenna with Band-notched Function

Ashwini Kumar and Amar Partap Singh Pharwaha

Department of Electronics and Communication Engineering
Sant Longowal Institute of Engineering and Technology, Longowal, Sangrur, Punjab, India
ashwiniarya15@gmail.com, aps.aps67@gmail.com

Abstract ─ In this paper, a straightforward yet effective design methodology to design wideband antenna with band notched characteristics has been proposed. Sierpinski carpet fractal geometry has been used to realize the antenna structure. Co-planar waveguide feed is used with a novel structure to achieve larger impedance bandwidth and band notching characteristics. Proposed antenna is designed using High Frequency Structure Simulator (HFSS) on a low cost FR4 substrate (ε_r=4.4) which resonates at three frequencies 1.51 GHz (1.19-2.06GHz), 6.53 GHz and 8.99 GHz (4.44-9.54 GHz) while a band is notched at 10.46 GHz (9.32-11.92 GHz). The proposed antenna has an electrical dimension of 0.36 λ_m× 0.24 λ_m, here λ_m is the wavelength with respect to lowest resonating frequency of the antenna. The resonating and radiation characteristics of the antenna are verified experimentally. Further, investigations are made to achieve easy integration of the antenna to the monolithic microwave integrated circuits. For that the antenna has been designed on micro-machined high index Silicon substrate which improve matching and gain of the antenna. The results of the micro-machined Sierpinski carpet fractal antenna are highly convincing over the conventional FR4 based antenna.

Index Terms ─ Gain, micro-machining, Sierpinski fractal, silicon, wideband.

I. INTRODUCTION

Wideband antennas are potent solution for reducing the number of onboard antennas for such kind of applications which operate in different bands. Design of wideband, compact, light weight antennas with acceptable performance become a more complicated and challenging task for the researcher. Therefore this work is aimed to develop a low profile antenna with wideband performance. Wide bandwidth of antenna is a desirable characteristic to meet the challenges like: high data rate, capacity and multi-functionality etc. There are various techniques to improve the bandwidth like the use of frequency selective surface, multiple resonators, thicker substrate, parasitic patch, folded and self-complementary structures, use of stacked configuration, shorting pins, presenting of U-openings, cavity-backed slot antenna, utilizing of high permittivity substrates, slots, and fractal geometry [1-5], developed by researcher and scientist to meet these challenges. The primary objective of this research is to develop a low profile wideband fractal antenna. Therefore a review of various wideband fractal antennas adopted. Fractal antennas have gained a lot of popularity in comparison of ordinary patch antennas. Many Fractal radiators were used to achieve wideband characteristics like: an effort was made in [6]. Similarly various antennas were proposed using fractal geometries [7-11]. To achieve band-notched function various techniques have been applied in literature like: embedding of slots [12-15] on the patch or ground, and utilizing parasitic elements near the radiator [16]. All these techniques require more space and difficult to implement because of structural complexity, but the proposed technique is very simple to implement and does not consume extra space. Microstrip patch antenna performance predominantly decided by the selection of substrate material and shape of the patch. At high frequency surface wave and substrate losses are more significant in case of substrates which have higher value of dielectric constant like: Silicon and GaAs in comparison to substrates which low dielectric constant [17,18]. In this work, a special method known as micro-machining has been exercised to win over the limitations of the high resistive Silicon substrate. In micro-machining an air cavity is created by etching out a specific portion of the substrate to avoid the surface wave and substrate losses. Micro-machining reduce the dielectric constant of the substrate thus improving the performance [19,20]. Although the antennas reported in literature were wideband in nature, certain limitation exist in terms of design complexity, size and presence of undesired bands/complicated techniques for band notching. Thus from the literature, it is perceptible that there is still a huge possibility of development of micro-machined fractal antenna.

In this paper, a common but proved fractal structure has been used from [21]. The work intends to provide a

Submitted On: January 19, 2020
Accepted On: May 25, 2020
https://doi.org/10.47037/2020.ACES.J.350812

simple yet effective design methodology to design multiband antenna with wide band and band notched characteristics. Proposed fractal antenna covers the frequency bands for fixed satellite services (FSS) in L-Band, C-Band and X-Band. The novelty of the work is twofold as follow: (i) Modified CPW-feed has been utilized to get larger impedance bandwidth (S_{11}<=-10 dB) approximately of 5 GHz and at the same time the undesired frequency band has been notched with only simple structural modification in comparison of the techniques used in literature. (ii) Proposed antenna is designed on high index micro-machined silicon substrate with an additive feature of easy integration of antenna to the Monolithic Microwave Integrated Circuits (MMIC). This specially featured antenna also provides higher order of impedance matching and higher gain than Sierpinski Carpet Fractal Antenna (SCFA) designed on FR4 substrate. The results of the micro- machined SCFA are highly convincing over the conventional FR4 based antenna.

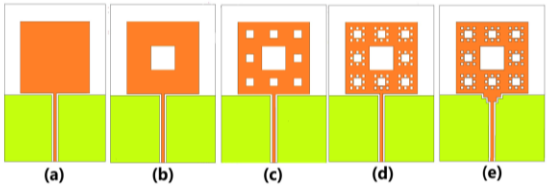

Fig. 1. All iterations of SCFA: (a) 0th Iteration, (b) 1st Iteration, (c) 2nd Iteration, (d) 3rd Iteration, and (e) final design.

The rest of the work is divided in three sections as follow: Section II contains the design procedure and performances of the proposed antenna, Section III discusses the results, Section IV discusses the experimental validation, Section V the micro-machined SCFA is discussed which is followed by Section VI containing conclusion.

II. ANTENNA DESIGN

The antenna design procedure begins by designing a square patch antenna on low index FR4 substrate with a loss tangent of 0.02 and a dielectric constant of 4.4 having a size of The antenna dimensions are simply calculated using the standard equation given in [22]. After designing a square patch antenna of side length 41.08 mm fed by CPW-feed, the Sierpinski carpet fractal geometry has been etched out. Sierpinski Carpet fractal geometry is considered in this work to design the proposed antenna which has been extensively used in literature for designing multiband antenna. For 1st iteration Initial Square is scaled with a factor of 1/3 in both x-axis and y-axis and subtracted from 0th iteration structure as shown in Fig. 1 (b). Same procedure is used to generate further two iterations. In last step CPW-feed is modified to step feed to enhance the bandwidth of the antenna as shown in Fig. 1 (e). Figures 1 (a) to 1 (d) show transformation of the antenna design from basic square patch to 3rd iteration of Sierpinski carper fractal structure, and Fig. 1 (e) shows the final proposed antenna with modified CPW-feed. Figure 2 shows the dimensional details of the proposed antenna which are tabulated in Table 1. The overall size of the proposed antenna is 0.36 λ_m× 0.24 λ_m × 0.0064 λ_m, here λ_m is the wavelength with respect to lowest resonating frequency of the antenna.

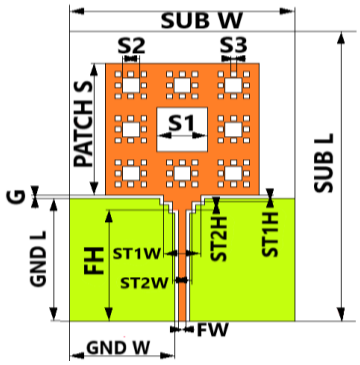

Fig. 2. Dimensional details of SCFA.

Table 1: Dimensional details of SCFA

Parameter	Value (mm)	Parameter	Value (mm)
SUB L	90	GND L	38.05
SUB W	60	GND W	28
PATCH S	41.08	FL	34.55
S1	13.69	FW	1.8
S2	4.56	ST1H	2
S3	1.52	ST1W	10
G	1	ST2H	2.5
		ST2W	5

III. RESULT AND DISCUSSION

High frequency structure simulator (HFSS) is used to design and simulate the proposed antenna. Proposed SCFA is characterized using characteristics like reflection coefficient (S_{11}), radiation pattern, gain and bandwidth. Figure 3 shows the reflection coefficient values for all iterations which have been also tabulated in Table 2 [21]. In iteration 3rd there is a little improvement in performance of antenna in comparison of 2nd iteration therefore the analysis is done up to 3rd iteration only. It is noticed from the Fig. 3 [21] that after changing CPW-feed in CPW-feed with two steps the bandwidth of the antenna is significantly improved and also band notching is achieved for the band 9.32-11.92 GHz which is not useful for desired applications. Without modification the maximum bandwidth of antenna is only 2.6 GHz whereas after feed modification and optimization the

antenna resonates at 1.51 GHz (1.19-2.04 GHz), 6.53 GHz and 8.99 GHz (4.44-9.54 GHz) with a maximum bandwidth of 5.09 GHz in the required frequency band for the desired application. From Fig. 3, it can be seen that the antenna at 3rd iteration is operating at 10.46 GHz whereas for final design with modified CPW-feed the band is notched at 10.46 GHz.

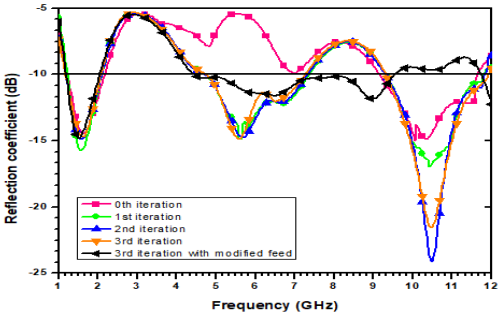

Fig. 3. Simulated reflection coefficient (S_{11}) values of all iterations of SCFA.

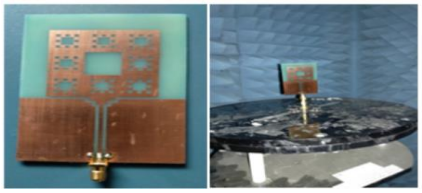

Fig. 4. Fabricated antenna in anechoic chamber.

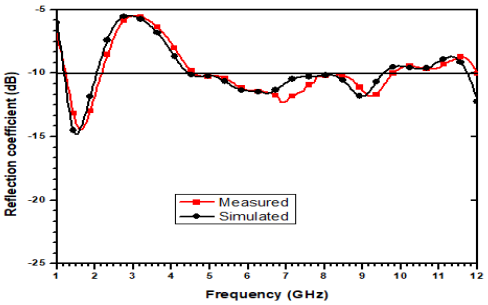

Fig. 5. Simulated and measured reflection coefficient of proposed SCFA.

Table 2: Performance parameters of the proposed antenna

Iterations	Resonating Frequency (GHz)	Reflection Coefficient (dB)	VSWR	Bandwidth (MHz)	Gain (dB)
Zeroth	1.62	-14.4	1.46	900	0.2
	10.35	-14.8	1.21	2450	4.1
First	1.58	-15.7	1.39	870	0.2
	5.62	-14.8	1.40	2650	1.4
	10.42	-16.9	1.14	2490	2.2
Second	1.58	-14.9	1.43	880	-0.4
	5.65	-14.8	1.44	2560	1.4
	10.49	-24.1	1.13	2500	3.2
Third	1.62	-14.7	1.45	820	0.07
	5.58	-14.8	1.43	2470	1.3
	10.46	-21.6	1.16	2600	4.2
Proposed Antenna Design	1.51	-14.8	1.44	850	0.08
	6.53	-11.6	1.71	5100	1.3
	8.99	-11.8	1.68		3.6
Proposed Micro-machined Antenna	1.99	-42	1.02	1320	3.78
	8.07	-31.7	1.05	4690	2.96

IV. EXPERIMENTAL VALIDATION

A. Reflection coefficient

Prototype of the proposed antenna has been fabricated on FR4 substrate as shown in Fig. 4. Measurement of reflection coefficient has been done using Anritsu (Model No. MS46322A) Vector Network Analyzer. Measured and simulated reflection coefficient versus frequency plot is shown in Fig. 5. Measured and simulated results show higher degree of matching for the proposed antenna. The proposed antenna resonates at 1.51 GHz, 6.53 GHz and 8.99 GHz. The frequency bands of interest for FSS are (1.24-1.35 GHz), (1.559-1.626 GHz), (4.5-4.8 GHz), (5-5.65 GHz), (5.725-8.4 GHz) and (8.75-9.5 GHz). The proposed antenna covers desired frequency bands in L-Band, C-Band and X-Band.

B. Radiation pattern

Figure 6 shows the simulated and measured radiation characteristics of the proposed SCFA at 1.51 GHz, 6.53 GHz and 8.99 GHz. Radiation pattern has been measured in receiving mode in anechoic chamber. Experimental measured pattern are shown with simulated radiation pattern to verify the radiation characteristics of the fractal antenna. Measured and simulated results show the

higher degree of matching. It can be observed that, at all frequencies, the antenna has nearly omnidirectional radiation pattern in the H-Plane, while in the E-Plane the radiation pattern at 1.51 GHz is bidirectional, 6.53 GHz and 8.99 GHz patterns are broadside.

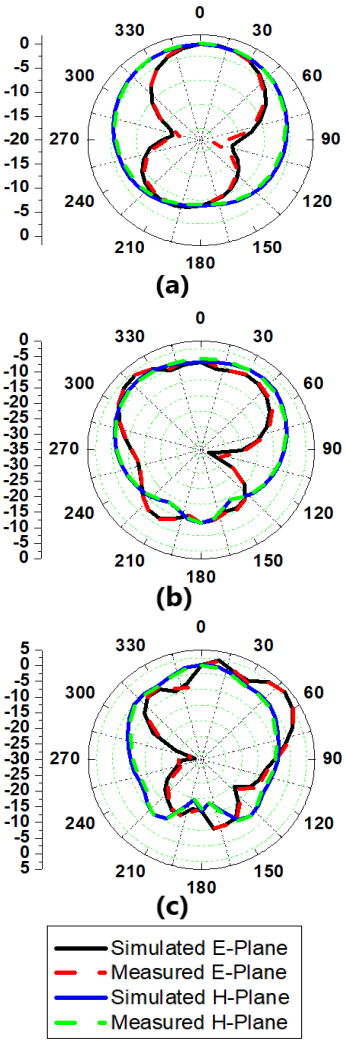

Fig. 6. Radiation pattern proposed SCFA: (a) at 1.51 GHz, (b) at 6.53 GHz, and (c) at 8.99 GHz.

V. MICROMACHINED SCFA

A Monolithic Microwave Integrated Circuit (MMIC) is an integrated circuit that works at microwave frequencies. These circuits are generally fabricated using High Index substrate like: Silicon (ε_r=11.9) or GaAs (ε_r=12.9) to work at high frequencies. To integrate patch antenna over these high index substrate, the limitation of surface wave losses and dielectric losses of these substrate should be avoided. To avoid these losses a process of micromachining is done. In this process selective portion of the high index substrate is removed and an air cavity is created beneath the patch to make a low index conditions. By creating a low index environment in high index substrate performance of the patch antenna can be improved [19,20]. Micro-machining process is of two types: 1) Bulk Micro-machining and 2) Surface micro-machining. When selective bulk material from substrate is removed by etching then it is known as bulk micro-machining. In this work, process of bulk micro-machining is used to design a fractal antenna on low index environment as shown in the Fig. 7. The overall effective dielectric constant has been calculated from the Equations (1-3) [19]:

$$\varepsilon_c = \frac{\varepsilon_a \varepsilon_s}{\varepsilon_a + (\varepsilon_s - \varepsilon_a)k_a}, \quad (1)$$

$$\frac{\varepsilon_f}{\varepsilon_c} = \frac{\varepsilon_a + (\varepsilon_s - \varepsilon_a)k_a}{\varepsilon_a + (\varepsilon_s - \varepsilon_a)k_f}, \quad (2)$$

$$\varepsilon_{reff} = \varepsilon_c \left(\frac{L + 2\Delta L \frac{\varepsilon_f}{\varepsilon_c}}{L + 2\Delta L} \right). \quad (3)$$

Here, ε_s is dielectric constant of substrate. ε_a air dielectric height in the mixed field region. k_f represents ratio of air cavity height to substrate height in the fringing field region. L represents side length of the design.

Proposed SCFA has been designed on high index silicon (ε_r=11.9) substrate having height of 1.6 mm. An air cavity (shown in light blue color underneath the patch) has been created by etching off 43 mm × 49 mm × 1.5 mm substrate volume underneath the patch leaving a 0.1 mm thick membrane under the patch. Figure 8 illustrates comparison of the simulated reflection coefficient of the proposed fractal antenna on FR4 and micro-machined silicon substrate. Micro-machined antenna resonates at1.99 GHz and 8.07 GHz. The best value of reflection coefficient for FR4 antenna is -14.8 dB whereas for micro-machined antenna it is -42 dB. The value of reflection coefficient got improved by nearly -28 dB in case of micro-machined antenna. The performance parameters of micro-machined antenna are tabulated in Table 2. However, the proposed micro-machined antenna has better performance and approximately equal bandwidth to the conventional FR4 antenna but there is a small deviation in the resonating characteristics of the micro- machined antenna which may be due to change in substrate properties. To get deeper physical insight into the behavior of antenna and band rejection, the proposed micro-machined antenna is modeled in terms of lumped components by estimating the value of R, L, and C from the input impedance of the antenna using foster's network synthesis [23-25]. Figure 9 illustrates the impedance versus frequency plot for the micro-machined silicon antenna. It can be observed from the Fig. 9 that the real part of the impedance fluctuate around the 50 ohm value while the imaginary part is nearly zero for both of the resonating bands. The value of real and imaginary part of impedance at 10.46 GHz (Band Notched) is nearly 35 ohm and -28 respectively. It is observed that at the notch frequencies of 10.46 GHz, input impedances are akin to

that of the series RLC circuit, because the imaginary graph is going towards positive (Inductive) value from a negative (Capacitive) value while the real part is falling towards the zero value. The lumped component model with complex input impedance Z_c in Fig. 10 shows the equivalent model of the proposed antenna. Each parallel RLC circuit shown in Fig. 10 signifies the corresponding operating band like: R_1, L_1, and C_1 are corresponding to first operating band, R_2, L_2, C_2 for second operating band and series RLC circuit of R_3, L_3, C_3 signify the rejected band. Figure 11 shows the gain versus frequency plot for the FR4 and micro-machined antenna. It can be seen from the gain plot that the gain of the micro-machined antenna is far better than the FR4 antenna. The gain at 1.51 GHz got improved by nearly more than 4 dB; similarly a significant improvement in gain for second operating band can be seen from the plot. In addition to the above-discussed characteristics, the proposed SCFA on FR4 and Micro-machined silicon substrate has been compared with the existing antennas in Table 3. The proposed fractal antenna on FR4 has multiband performance with wide bandwidth, good gain and better matching as compared to antenna proposed in literature. Moreover, the antenna has been designed successfully on micro-machined silicon substrate for MMIC circuits with enhanced parameters like impedance matching, bandwidth and gain.

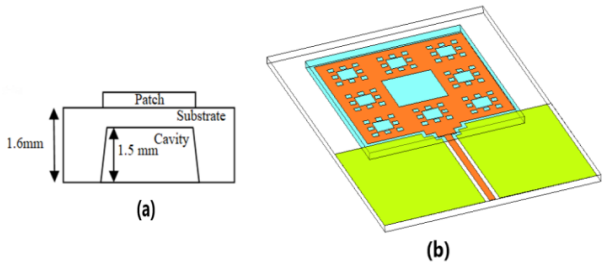

Fig. 7. (a) Micro-machined substrate and (b) 3D view of the proposed antenna.

Table 3: Comparison of the proposed antenna with existing antenna

Reference	Resonating Frequency (GHz)	Reflection Coefficient (dB)	Band Rejected	Bandwidth Improved (MHz)	Max. Gain (dB)	Electrical Dimension	Technique/ Inferences
[1]	2.45	-32	--	10.3	--	0.3 λ_m × 0.34 λ_m	Substrate removal/ difficult and complex process
[2]	2.45	--	--	40	5	0.45 λ_m× 0.51 λ_m	Using via hole/Increase structural complexity
[3]	1.3	-30	--	2600	2	0.65 λ_m× 0.65 λ_m	Folded and self-complementary structures/Increased dimensions by 13%
[4]	1.5, 2.5, 2.8	--	--	11.5	8.9	0.93 λ_m× 0.93 λ_m	Closed resonant slot pair/Small improvement in bandwidth
[5]	UWB	-15	3	--	3	0.31 λ_m× 0.30 λ_m	Quarter-wavelength band-rejected elements/ Complicated design
[15]	UWB	-35	1	--	6	0.41 λ_m× 0.51 λ_m	λ/4 short stub/Increase Structural complexity
Proposed antenna on FR4 substrate	1.51	-14.8	1	2630	4	0.36 λ_m× 0.24 λ_m	Modification in feed completed both requirements of bandwidth enhancement and band rejection
	6.53	-11.6					
	8.99	-11.8					
Proposed Micro-machined Antenna	1.99	-42	1	2220	6	0.36 λ_m× 0.24 λ_m	MMIC compatible antenna with enhanced bandwidth, Impedance matching and band rejection characteristics
	8.07	-31.7					

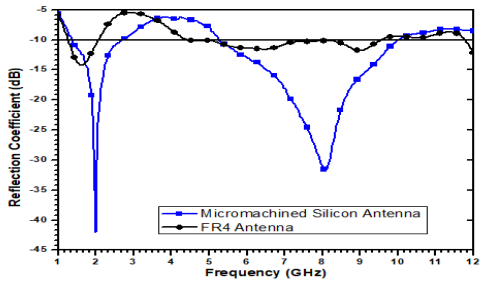

Fig. 8. Comparison of simulated reflection coefficients of the proposed antenna for two different substrates.

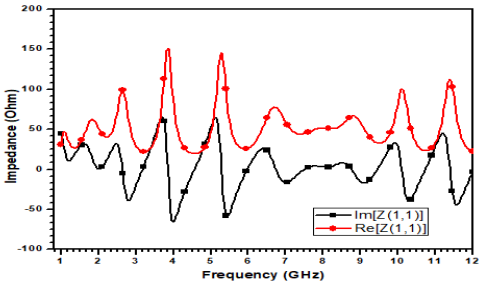

Fig. 9. Simulated impedance versus frequency plot for micro-machined antenna.

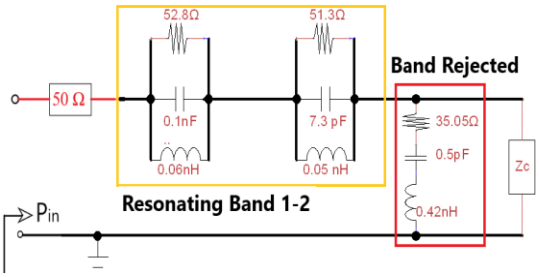

Fig. 10. Equivalent circuit of the proposed antenna.

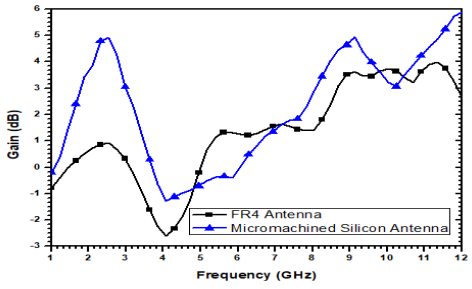

Fig. 11. Comparison of gain of the proposed antenna for two different substrates.

VI. CONCLUSION

A wideband Sierpinski carpet fractal antenna fed with a novel modified CPW feed has been presented here. The modification in CPW feed structure successfully increased the impedance bandwidth of the antenna by 107% and also notched an undesirable frequency band. The antenna has been designed and parametrically optimized to operate at 1.51 GHz (1.19-2.06GHz), 6.53 GHz and 8.99 GHz (4.44-9.54 GHz) covering fixed satellite services in L-Band, C-Band and X-Band. The radiation patterns are stable and approximately omnidirectional in H-plane at all three operating bands and antenna exhibits satisfactory gain at different bands. The measured reflection coefficient and radiation characteristics indicate high degree of matching with the simulated. Further, the proposed antenna has been designed on micro-machined Silicon substrate. Improvement in the crucial parameters like: Gain and Reflection coefficient, of the proposed SCFA has been achieved successfully using micro-machined Silicon substrate. MMIC compatible fractal antenna with very simple structure utilizing a small space has been proposed with effective radiation and resonance characteristics.

ACKNOWLEDGMENT

The authors are immensely thankful to the Department of Electronics and Communication Engineering of Sant Longowal Institute of Engineering & Technology, Punjab, India for providing kindly support and excellent lab facilities.

REFERENCES

[1] S. Yun, D.-Y. Kim, and S. Nam, "Bandwidth and efficiency enhancement of cavity-backed slot antenna using a substrate removal," *IEEE Antennas Wirel. Propag. Lett.*, vol. 11, pp. 1458-1461, 2012.

[2] S. Yun, D.-Y. Kim, and S. Nam, "Bandwidth enhancement of cavity-backed slot antenna using a via-hole above the slot," *IEEE Antennas Wirel. Propag. Lett.*, vol. 11, pp. 1092-1095, 2012.

[3] R. Azadegan and K. Sarabandi, "Bandwidth enhancement of miniaturized slot antennas using folded, complementary, and self-complementary realizations," *IEEE Trans. Antennas Propag.*, vol. 55, no. 9, pp. 2435-2444, Sep. 2007.

[4] S. Fu, Z. Cao, P. Chen, D. Gao, and X. Quan, "A novel bandwidth-enhanced dual-polarized antenna with symmetrical closed-resonant-slot pairs," *IEEE Access*, vol. 7, pp. 87943-87950, 2019.

[5] F. Zhu, S. Gao, A. T. S. Ho, R. A. Abd-Alhameed, C. H. See, T. W. C. Brown, J. Li, G. Wei, and J. Xu, "Multiple band-notched UWB antenna with band-rejected elements integrated in the feed line," *IEEE Trans. Antennas Propag.*, vol. 61, no. 8, pp. 3952-3960, Aug. 2013.

[6] A. Amini, H. Oraizi, and M. A. Chaychi Zadeh, "Miniaturized UWB log-periodic square fractal antenna," *IEEE Antennas Wirel. Propag. Lett.*, vol. 14, pp. 1322-1325, 2015.

[7] A. Kumar and A. P. S. Pharwaha, "Triple band

fractal antenna for radio navigation and fixed satellite services using dragonfly optimization," *Adv. Electromagn.*, vol. 8, no. 3, pp. 43-49, June 2019.

[8] M. A. Dorostkar, R. Azim, M. T. Islam, and Z. H. Firouzeh, "Wideband hexagonal fractal antenna on epoxy reinforced woven glass material," *Appl. Comput. Electromagn. Soc. J.*, vol. 30, no. 6, pp. 645-652, 2015.

[9] G. Singh and A. P. Singh, "On the design of planar antenna using Fibonacci word fractal geometry in support of public safety," *Int. J. RF Microw. Comput. Eng.*, vol. 29, no. 2, p. e21554, Feb. 2019.

[10] X. Bai, J. W. Zhang, L. J. Xu, and B. H. Zhao, "A broadband CPW fractal antenna for RF energy harvesting," *Appl. Comput. Electromagn. Soc. J.*, vol. 33, no. 5, pp. 482-487, 2018.

[11] Y. Zehforoosh and M. Naser-Moghadasi, "CPW-fed fractal monopole antenna for UWB communication applications," *Appl. Comput. Electromagn. Soc. J.*, vol. 29, no. 9, pp. 748-754, 2014.

[12] J.-Y. Sze and J.-Y. Shiu, "Design of band-notched ultrawideband square aperture antenna with a hat-shaped back-patch," *IEEE Trans. Antennas Propag.*, vol. 56, no. 10, pp. 3311-3314, Oct. 2008.

[13] Y.-C. Lin and K.-J. Hung, "Compact ultra-wideband rectangular aperture antenna and band-notched designs," *IEEE Trans. Antennas Propag.*, vol. 54, no. 11, pp. 3075-3081, Nov. 2006.

[14] A. M. Abbosh, M. E. Bialkowski, J. Mazierska, and M. V. Jacob, "A planar UWB antenna with signal rejection capability in the 4-6 GHz band," *IEEE Microw. Wirel. Components Lett.*, vol. 16, no. 5, pp. 278-280, May 2006.

[15] I.-J. Yoon, H. Kim, H. K. Yoon, Y. J. Yoon, and Y.-H. Kim, "Ultra-wideband tapered slot antenna with band cutoff characteristic," *Electron. Lett.*, vol. 41, no. 11, p. 629, 2005.

[16] K.-H. Kim, Y.-J. Cho, S.-H. Hwang, and S.-O. Park, "Band-notched UWB planar monopole antenna with two parasitic patches," *Electron. Lett.*, vol. 41, no. 14, p. 783, 2005.

[17] A. Kumar and A. P. Singh, "Design and optimization of slotted micro-machined patch antenna using composite substrate," *Appl. Comput. Electromagn. Soc. J.*, vol. 34, no. 1, pp. 128-134, 2019.

[18] S. B. Yeap and Z. N. Chen, "Microstrip patch antennas with enhanced gain by partial substrate removal," *IEEE Trans. Antennas Propag.*, vol. 58, no. 9, pp. 2811-2816, Sep. 2010.

[19] A. Kumar and A. P. Singh, "Design of micro-machined modified Sierpinski gasket fractal antenna for satellite communications," *Int. J. RF Microw. Comput. Eng.*, vol. 29, no. 8, Aug. 2019.

[20] I. Papapolymerou, R. Franklin Drayton, and L. P. B. Katehi, "Micromachined patch antennas," *IEEE Trans. Antennas Propag.*, vol. 46, no. 2, pp. 275-283, 1998.

[21] A. Kumar and A. P. Singh Pharwaha, "On the design of wideband Sierpinski carpet fractal antenna for radio navigation and fixed satellite services," in *2019 6th International Conference on Signal Processing and Integrated Networks (SPIN)*, pp. 736-738, 2019.

[22] C. Balanis, *Antenna Theory - Analysis and Design*. 3rd ed., New York, USA: John Wiley & Sons Inc., 2005.

[23] T. Ali, K. D. Prasad, and R. C. Biradar, "A miniaturized slotted multiband antenna for wireless applications," *J. Comput. Electron.*, vol. 17, no. 3, pp. 1056-1070, 2018.

[24] D. Caratelli, R. Cicchetti, G. Bit-Babik, and A. Faraone, "Circuit model and near-field behavior of a novel patch antenna for WWLAN applications," *Microw. Opt. Technol. Lett.*, vol. 49, no. 1, pp. 97-100, Jan. 2007.

[25] G. Sami, M. Mohanna, and M. L. Rabeh, "Tri-band microstrip antenna design for wireless communication applications," *NRIAG J. Astron. Geophys.*, vol. 2, no. 1, pp. 39-44, June 2013.

Ashwini Kumar is pursuing his Ph.D degree in the field of Microstrip Patch Antennas from Sant Longowal Institute of Engineering and Technology (SLIET), Longowal, Sangrur, Punjab, India. His research includes Microstrip patch antennas and Fractal antennas Design.

Amar Partap Singh Pharwaha is a Professor of ECE at SLIET, Longowal. Singh is credited with a professional experience of more than 24 years. He has guided seven Ph.D. thesis and published more than 180 research papers in various national and international journals/ conferences.

Compact Multi-Mode Filtering Power Divider with High Selectivity, Improved Stopband and In-band Isolation

Zhenyao Qian, Yuan Chen, Chunmei Feng, and Wei Wang

School of Electrical and Automation Engineering
Nanjing Normal University, Nanjing, 210046, China
wei_wang_nnu@126.com

Abstract ─ This letter presents a new compact multi-mode filtering power divider (FPD) design based on co-shared FPD topology with sharp frequency selectivity, improved out-of-band harmonic rejection and port-to-port isolation. Power splitting and quasi-elliptic filtering functions are achieved by masterly integrating only one triple-mode resonator. By loading different open-circuited stubs at the input/output ports, multiple additional transmission zeros (TZs) are generated at both lower and upper stopband, resulting in an improved stopband performance. Meanwhile, a better port-to-port isolation is obtained by adopting frequency-dependent resistor-capacitor parallel isolation network. The proposed multi-mode FPD design stands out from those in the literature by both nice operation performance and compact topology with only one resonator. For demonstration purposes, one triple-mode FPD prototype and its improved one are implemented, respectively. Measured results exhibit the superiority of the FPD design.

Index Terms ─ Compact, filtering power divider, harmonic rejection, isolation.

I. INTRODUCTION

Modern mobile communication systems require the RF front-end system to become more compact and multi-functional. In this context, the concept of filtering power divider (FPD) has emerged. By integrating both filtering function and power division function into singly one circuit, such this component can not only decrease insertion loss and avoid cascading mismatch problems to improve the overall performance of the package system, but also significantly reduce the size. In recent years, some achievements have been made in exploring high-performance FPDs [1-10].

In [1], the FPD is designed by using multiple resistors coupled output structures. Although this design achieves well isolation, its return loss (RL) is not satisfactory. In [2], the coupled-resonator circuit theory is utilized to guide narrow band FPD designs. However, its port-to-port isolation performance and its overall size are not ideal. In [7], using two resonators to achieve well two-way power divider filtering performance. However, the adopted topology results in a relatively large size. In order to improve the above operation performance, other discriminating couplings [3], mixed electric and magnetic couplings [4], radial/rectangular-shaped resonators and Ring Resonators [5-6], quarter-wavelength transmission lines [8], and Parallel-Coupled Line Structures [9] are also employed in different power divider configurations, respectively. For good in-band isolation, a coupled line isolation network consisting of a resistor and a capacitor connected in series is put forward in [10]. However, the above series connection results in the design difficulty.

The main intention of the paper is to propose a compact high-performance multi-mode filtering power divider design. By embedding different open-circuited stubs and frequency-dependent resistor-capacitor parallel isolation network into just one triple-mode resonator based design, the proposed FPD exhibits compact size, high selectivity, improved lower/upper stopband and increased in-band isolation performance. To validate the design concept and method, two prototypes including the first presented FPD and its improved one are designed and implemented, respectively. Measured results validate the design concept.

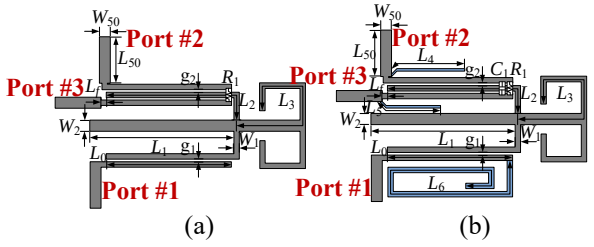

Fig. 1. Configuration of the proposed filtering power dividers. (a) The first presented FPD; (b) the improved FPD. (Substrate Rogers RO4003C: ε_{re}=3.55, tanδ=0.0027, and h=0.508 mm).

Submitted On: August 25, 2019
Accepted On: May 8, 2020
https://doi.org/10.47037/2020.ACES.J.350813

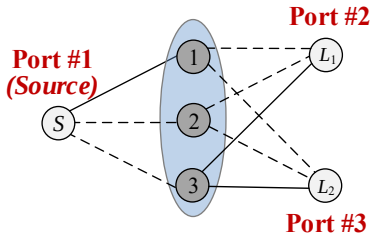

Fig. 2. The design coupling topology of the proposed FPDs.

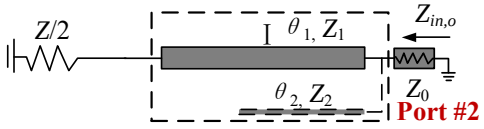

Fig. 3. Equivalent circuit for odd excitation of the improved FPD.

II. PROPOSED FPDS DESIGN

These two prototypes are presented with the structures illustrated in Figs. 1 (a) and (b). The first presented FPD is mainly constructed by only one cross-shaped resonator and one resistor. By elaborately attaching one open-circuited stub at input line and two at output coupled lines, and loading one frequency-dependent capacitor with isolation resistor in parallel, the improved FPD is constructed. With the above loaded stubs, more favorable filtering response is achieved. Simultaneously, the improved isolation network further improves the in-band isolation flexibly and effectively.

For the configurations in Fig. 1, the input signal excited by the source (Port #1) will be coupled to the multi-mode resonator, and then equally divided to the feed-lines of the output ports through another arm of the resonator. The design coupling topology is shown in Fig. 2, where the light gray disks S and L_p (p=1, 2, 3) denote source and loads while dark gray disks 1-3 represent the three modes of the resonator. Since the coupling topology is symmetrical, the isolation network hardly affects the filtering responses [11] and thereby not yet being considered in Fig. 2.

As the proposed structure is symmetric, its resonance characteristic can be analyzed by making use of even-/odd-mode analysis method [11-12]. The standard scattering parameters of the proposed filtering power divider in Fig. 1 can be calculated as [11]:

$$S_{11} = S_{11e}, \tag{1a}$$

$$S_{21} = S_{31} = \frac{S_{21e}}{\sqrt{2}}, \tag{1b}$$

$$S_{23} = \frac{(S_{22e} - S_{22o})}{2}, \tag{1c}$$

$$S_{22} = S_{33} = \frac{(S_{22e} + S_{22o})}{2}, \tag{1d}$$

According to the design principles (1a)-(1d) of the filtering power divider in the manuscript, idea filtering response can be determined at first, then in order to achieve good matching and isolation for output ports, equivalent circuit for odd excitation of the improved FPD can be analyzed. Detailed analysis is given in the followings.

According to the prescribed specifications (f_0=2.5 GHz, ripple bandwidth of 0.33 GHz, the passband return loss of 20 dB), the targeted coupling matrix coefficients is synthesized with the analysis method in [11] as: M_{S1} = M_{L1} = 0.4465, M_{S2} = -M_{L2}= -0.8374, M_{S3} = M_{L3} = 0.4552, M_{11} =1.3933, M_{22} = 0.0165, M_{33} = -1.4006. Based on equation (2), the required even-mode resonant frequencies (f_{e1}, f_{e2}) and odd-mode resonant frequency f_o of the multi-mode resonator (MMR) can be derived as f_{e1} = 2.27 GHz, f_o =2.49 GHz and f_{e2} = 2.73 GHz. With the help of the derived resonant frequencies, the physical dimension of MMR can be determined:

$$f_n = \frac{f_0}{2}\cdot\left[\frac{-BW}{f_0}M_{ii} + \sqrt{\left(\frac{BW}{f_0}M_{ii}\right)^2 + 4}\right], i = 1,2,3; n = e1, o, e2 \tag{2}$$

The I/O couplings to even- and odd-modes can be characterized in terms of external quality factors Q_{e_n} (n =e1, o, e2), which are found from $Q_{e\_n} = f_0/(BW \cdot M_{si}^2)$ as: Q_{e_e1}=37.8, Q_{e_o}=10.5, Q_{e_e2}=36.4. Based on these derived external quality factors, the width (W_1 =0.6 mm) and gap (g_1=0.1 mm and g_2=0.25 mm) can be determined by extracting the I/O couplings from $Q_{e\_n} = \pi f_i \cdot \tau(f_i)$ through the group delays as in [12].

Next, once the filtering response is determined, the port-to-port isolation and matching can be fulfilled by changing the isolation network of the odd mode equivalent circuit as shown in Fig. 3. Z can then be derived with odd mode equivalent circuit. The input impedance is then calculated as:

$$Z_{in,oo} = \frac{AZ + B}{CZ + D} = Z_0, \tag{3}$$

where A, B, C, D are the elements of the transmission matrix [A] for block I, which are derived as follows:

$$[A] = \begin{bmatrix} \cos\theta_1 & j4Z_1\sin\theta_1 \\ j\left(\frac{1}{4Z_1}\right)\sin\theta_1 & \cos\theta_1 \end{bmatrix} \cdot \begin{bmatrix} 1 & 0 \\ \frac{1}{Z_2} & 1 \end{bmatrix}, \tag{4}$$

where Z_1 and θ_1 are the impedance and electrical length for the transmission line as shown in Fig. 3.

Thus, Z can be calculated as 162+j532, in other words, R_1 and C_1 are calculated as 162 and 0.12 pF. Figure 4 plot the theoretical results on the in-band isolation versus the value of the parallel resistor and the capacitor.

Secondly, to clarify the design procedure of the proposal, the detailed design steps are described for explanation.

1) Firstly, according to the given specifications, the targeted coupling matrix coefficients is synthesized.

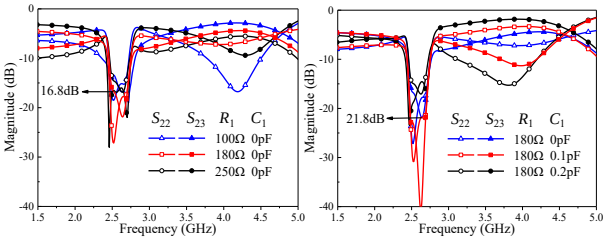

Fig. 4. The corresponding S-paramters S_{22} and S_{23} with varied R_1 and C_1.

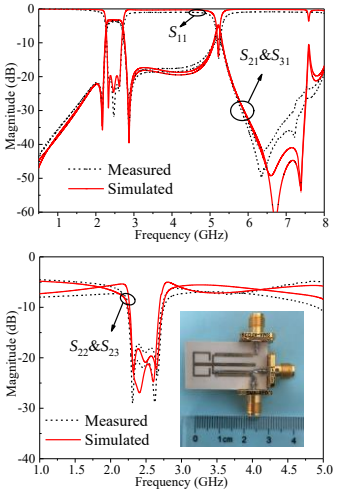

Fig. 5. The operation performance for the first presented FPD.

Based on equation (2), the required resonant frequencies of the multi-mode resonator (MMR) can be derived as f_{e1} = 2.27 GHz, f_o =2.49 GHz and f_{e2} = 2.73 GHz. With the help of the derived resonant frequencies, the physical dimension of MMR can be determined.

2) Subsequently, determine the input/output coupling space (g) and feedline width (w) by extracting the group delays based on the formulas $Q_{e\_n} = f_0 / \left(BW \cdot M_{si}^2 \right)$ and $Q_{e\_n} = \pi f_i \cdot \tau(f_i)$. The first FPD is initially designed and fine-tuned to achieve optimal filtering response.

3) Next, determine initial isolation network to achieve favorable port matching and port-port isolation.

4) Finally, execute the final optimization of the realized entire circuit layout relying on the commercial EM simulator HFSS.

For demonstration, the layouts of the proposed FPDs shown in Figs. 1 (a) and (b) were simulated, fabricated and measured. The images of the fabricated FPDs are exhibited in the insert plot of Fig. 5 and Fig. 6.

The final parameters are determined as follows (Units: mm): L_0=14.45, L_1=15.8, L_2=17.85, L_3=19.8, L_f=0.7, L_{50}=5, W_{50}=1.18, W_1=0.6, W_2=1.2, g_1=0.1, g_2=0.25, R_1=140Ω. The size of the design circuit is about $0.32\lambda_g \times 0.12\lambda_g$, where λ_g is the guided wavelength at the center frequency. Figure 5 shows the simulated and measured results, indicating the first presented FPD operates at the center frequency of 2.48 GHz with a 3-dB fractional bandwidth (FBW) of 17.3%. As expected, two inherent TZs are created due to the virtual grounds existing in the resonators. Within the passband, the measured input return loss (RL) is better than 20.5 dB and the output port RLs are better than 20.5 dB, while the insertion loss (IL) is smaller than 0.8 dB, respectively. The measured port-to-port isolations is higher than 17.3 dB.

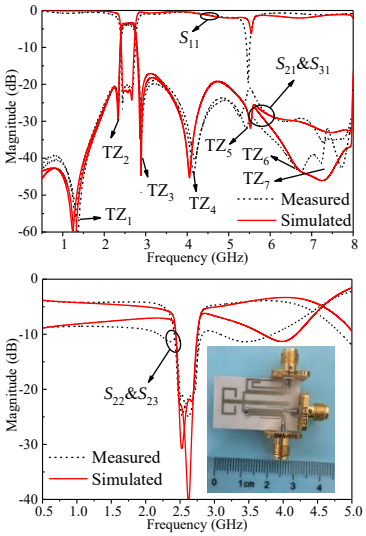

Fig. 6. The operation performance for the second presented FPD.

As for the improved one in Fig. 1 (b), the optimal layout parameters are finally determined as follows (Units: mm): L_0=13.5, L_1=15.7, L_2=16.9, L_3=18, L_4=8, L_5=6.4, L_6=34.7, L_f=0.7, L_{50}=5, W_{50}=1.18, W_1=0.6, W_2=1.2, g_1=0.1, g_2=0.25, R_1=180Ω and C_1=0.1pF. The size of the design circuit is about $0.33\lambda_g \times 0.18\lambda_g$. Figure 6 shows the simulated and measured results. As observed from the figure, the measured center frequency is 2.6 GHz with the 3-dB *FBW* of 13.2%. The corresponding measured in-band IL of the FPD is 0.8 dB, and the input RL is better than 20.0 dB, respectively. Additionally, the RLs at the output ports are better than 21.0 dB while the port-to-port isolations are higher than 21.1 dB. It is worthy noting that seven generated TZs achieve high frequency selectivity and a better than 20 dB harmonic suppression

from DC to 8.0 GHz (3.1f_0). The additional 3λ_{g1}/4 folded open-circuited stub loaded at the input line can introduce two additional TZs (TZ_1 and TZ_4) as showed in Fig. 6. The lengths of loaded open-circuited stubs at output lines mainly determine the position of the fifth TZ as indicated in Fig. 6. The relationship between the position of the TZ_n (n=1, 4, 5) and the electrical length of the loaded stubs (θ_{stub}) can be expressed as:

$$f_{z1/4/5} = \frac{f_0}{\theta_{stub}}(\frac{\pi}{2} + k\pi), k = 0,1,2,\cdots. \quad (5)$$

Table 1: Performance comparisons with other reported works

Ref.	Insertion Loss	Input Return Loss	Output Return Loss	In-band Isolation	TZs	Number-way	Topology	Dimension (λg × λg)	Suppression
[1]	0.74 dB	10.0 dB	12.0 dB	20.0 dB	3	Two-way	Two Double Resonator	0.33×0.25	No
[2]	0.9 dB	17.0 dB	Not given	15.5 dB	4	Two-way	Two Double Resonator	0.89×0.29	Yes
[3]	1.3 dB	15.0 dB	22 dB	16.0 dB	2	Two-way	Four Double Resonator	0.19×0.13	Yes
[7]	1.1 dB	17.0 dB	Not given	21.0 dB	6	Two-way	Two Double Resonator	0.67×0.35	Yes
Work-I	0.8 dB	20.5 dB	20.5 dB	17.3 dB	4	Two-way	Co-shared Single Resonator	0.32×0.12	No
Improved work- II	0.8 dB	20.0 dB	21.0 dB	21.1 dB	7	Two-way	Co-shared Single Resonator	0.33×0.18	Yes

Table 1 illustrates the comparison of the performances of this work with other state-of-the-art FPDs. It indicates that the proposed improved FPD have advantages of nice port matching, sharp frequency selectivity, superior in-band isolation and wide stopband performance. Furthermore, compared with other counterparts, the proposed designs exhibit a very flexible topology and competitive compactness against others.

VI. CONCLUSION

In this letter, a new compact multi-mode filtering power divider (FPD) design has been presented based on co-shared multi-mode coupling topology. It exhibits nice return loss, sharp passband skirt, as well as decent in-band isolation. An improved design is for high port-to-port isolation and wider stopband is realized by loading the additional open-circuited stubs and modifying isolation network. The high port-to-port isolations greater than 21.1 dB and 20-dB harmonic suppression from DC to 8.0 GHz (3.1f_0) are obtained. It is believed that the presented FPD design is promising in many practical modern wireless and mobile communication system applications.

ACKNOWLEDGMENT

This work was supported in part by National Natural Science Foundation of China under Grant 61801226, International Science and Technology Cooperation Program of Jiangsu Province and Universities Natural Science Research General Project under Grant BZ2018027 and Grant 18KJB510021, National Natural Science Foundation of China under Grant 61801226, State Key Laboratory of Millimeter Waves under Grant K201922 and Postgraduate Research & Practice Innovation Program of Jiangsu Province under Grant SJCX18_0369.

REFERENCES

[1] Y. Wang, F. Xiao, Y. Cao, Y. Zhang, and X. Tang, "Novel wideband microstrip filtering power divider using multiple resistors for port isolation," *IEEE Access*, vol. 7, pp. 61868-61873, May 2019.

[2] Y. Deng, Y. He, and J. Wang, "Design of a compact wideband filtering power divider with improved isolation," *The Applied Computational Electromagnetics Society Journal*, vol. 31, no. 9, pp. 1079-1083, Sep. 2016.

[3] X.-L. Zhao, L. Gao, X. Y. Zhang, and J.-X. Xu, "Novel filtering power divider with Wide stopband using discriminating coupling," *IEEE Microwave and Wireless Components Letters*, vol. 26, no. 8, pp. 580-582, Aug. 2016.

[4] G. Zhang, X. Wang, J. Hong, and J. Yang, "A high-performance dual-mode filtering power," *IEEE Microwave and Wireless Components Letters*, vol. 28, no. 2, pp. 120-122, Feb. 2018.

[5] R. Pouryavar, F. Shama, and M. A. Imani, "A miniaturized microstrip Wilkinson power divider with harmonics suppression using radial/ rectangular-shaped resonators," *Electromagnetics*, vol. 38, no. 2, pp. 113-122, 2018.

[6] D. Jiang, Y. Xu, R. Xu, and Z. Shao, "Broad-band power divider based on the novel split ring resonators," *The Applied Computational Electro-*

magnetics Society Journal, vol. 29, no. 2, pp. 157-162, Feb. 2014.

[7] G. Zhang, J. Wang, L. Zhu, and W. Wu, "Dual-band filtering power divider with high selectivity and good isolation," *IEEE Microwave and Wireless Components Letters*, vol. 26, no. 10, pp. 774-776, Oct. 2016.

[8] M. A. Imani, F. Shama, M. Alirezapoori, S. Haghiri, and A. Ghadrdan, "Ultra-miniaturized Wilkinson power divider with harmonics suppression for wireless applications," *Journal of Electromagnetic Waves and Applications*, vol. 33, no. 14, pp. 1920-1932, 2019.

[9] X. Yu, S. Sun, and Y. Liu, "Design of wideband filtering power dividers with harmonic suppression based on the parallel-coupled line structures," *The Applied Computational Electromagnetics Society Journal*, vol. 33, no. 5, pp. 468-475, May 2018.

[10] C.-J. Chen, "A coupled-line isolation network for the design of filtering power dividers with improved isolation," *IEEE Transactions on Components, Packaging and Manufacturing Technology*, vol. 8, no. 10, pp. 1830-1837, Oct. 2018.

[11] D. M. Pozar, *Microwave Engineering*. Third edition, Wiley-New York, 2005.

[12] J. S. Hong and M. J. Lancaster, *Microstrip Filters for RF/Microwave Applications*. Second edition, Wiley-New York, 2001.

Zhenyao Qian received B.S. degree from NJUST, Nanjing, China, in 2017. He is currently working toward the M.Sc. degree in Electromagnetic Field in Nanjing Normal University (NNU), Nanjing, China. His research interest is the design of miniaturized high performance microwave power divider.

Yuan Chen is currently working toward the M.Sc. degree in Electromagnetic Field in Nanjing Normal University (NNU), Nanjing, China. She research interest is the design of miniaturized high performance microwave power divider.

Chunmei Feng is currently working in Electromagnetic Field in Nanjing Normal University (NNU), Nanjing, China. In addition, she serves as the associate dean of the college. Her research interests have mainly been numerical methods of electromagnetic field computation and novel wireless power transfer systems.

Wei Wang was born in Nanjing, China, in 1988. He received the B.S. degree in Electrical Engineering and automation from Jiangnan University, Wuxi, China, in 2011, and the M.S. and Ph.D. degrees in Electrical Engineering from Southeast University, Nanjing, China, in 2013 and 2017, respectively.

He currently works as a Lecturer with the School of Electrical and Automation Engineering, and a Post-doctoral Research Associate with the Post-Doctoral Research Center of Physics, Nanjing Normal University, Nanjing, China. Since 2011, his research interests have mainly been numerical methods of electromagnetic field computation and novel wireless power transfer systems.

Analysis of Crosstalk Problem in Multi-Twisted Bundle of Multi-Twisted Wire Based on BSAS-BP Neural Network Algorithm and Multilayer Transposition Method

Chao Huang [1], Yang Zhao [1*], Wei Yan [1,2], Qiangqiang Liu [1], Jianming Zhou [1], Zhaojuan Meng [1], and Abdul Mueed [1]

[1] School of Electrical & Automation Engineering
Nanjing Normal University, Nanjing 210046, China
1547796467@qq.com, *zhaoyang2@njnu.edu.cn, 61197@njnu.edu.cn, 1376684687@qq.com, 386439740@qq.com, 1409352227@qq.com, engr.mueed@live.com

[2] Zhenjiang Institute for Innovation and Development
Nanjing Normal University, Zhenjiang 212004, China

Abstract ─ Twisted wire used in complex systems has the ability to reduce electromagnetic interference, but crosstalk within the wire is not easy to obtain. This paper proposes a method to predict the crosstalk of multi-twisted bundle of multi-twisted wire (MTB-MTW). A neural network algorithm based on back propagation optimized by the beetle swarm antennae search method (BSAS-BPNN) is introduced to mathematically describe the relationship between the twist angle of the wire harness and the per-unit-length (p.u.l) parameter matrix. Considering the symmetry of the model, the relationship between the unresolved angle of the BSAS-BPNN algorithm and the p.u.l parameter matrix is processed by using the multilayer transposition method. Based on the idea of the cascade method and the finite-difference time-domain (FDTD) algorithm in Implicit-Wendroff format, the crosstalk of the wire is obtained. Numerical experiments and simulation results show that the new method proposed in this paper has better accuracy for the prediction of the model. The new method can be generalized to the MTB-MTW model with any number of wires. All theories provide preliminary theoretical basis for electromagnetic compatibility (EMC) design of high-band circuits.

Index Terms ─ Beetle swarm antennae search (BSAS) method, back propagation neural network (BPNN), crosstalk, multi-twisted bundle of multi-twisted wire (MTB-MTW), multilayer transposition method, multi-conductor transmission lines (MTLs).

I. INTRODUCTION

Multi-conductor transmission lines used in aerospace and automotive machinery are particularly vulnerable to electromagnetic interference, but twisted wires have been shown to improve anti-interference capabilities [1]. With the increase of the current operating frequency, the influence of crosstalk between wires cannot be ignored [2, 3].

This paper discusses an MTB-MTW model. The same wires are twisted into MTW, and multiple sets of MTWs are twisted into MTB-MTW. The MTB-MTW model will have regular twists along with the axis, and there will be corresponding changes in the p.u.l parameter matrix in the MTL equation [4]. Similar models have been proven to have high anti-interference ability, but the problem of crosstalk in its wire is not clear [5].

Recently, a large number of researchers have studied the prediction of twisted wire crosstalk [6]. Most researchers focus their research on the twisted wire pairs (TWP), while the research on twisted wires of multi-core harnesses is relatively few [7-9]. Other researchers have focused on the effects of externally applied excitation fields on MTB-TWP crosstalk [10, 11]. Traditional transmission line models are mostly parallel transmission lines, and crosstalk can be obtained by solving the transmission line equation directly [12]. The research method of non-uniform multi-conductor transmission line can be used as a reference to solve the crosstalk problem [13, 14]. According to the cascaded transmission line theory proposed by Paul and McKnight, cascaded multi-segment transmission lines are used to replace the overall harness [15-17]. The FDTD algorithm is also essentially a special cascaded transmission line method. The FDTD algorithm has been applied to the crosstalk problem of non-uniform transmission lines by some researchers [18, 19]. Therefore, as long as the p.u.l parameter matrix at different positions is obtained, the crosstalk of the wire harness can be obtained by the

Submitted On: January 9, 2020
Accepted On: April 18, 2020
https://doi.org/10.47037/2020.ACES.J.350814

FDTD method.

The different positions of MTB-MTW represent different twist angles, and the p.u.l parameter matrix is affected by the twist angle and the return plane. Considering the symmetry of MTB-MTW, the BPNN algorithm with strong non-linear mapping ability is introduced to mathematically describe the relationship between a part of the angle and the p.u.l parameter matrix [20, 21]. The dimension of the p.u.l parameter matrix will increase with the number of wire harnesses, so the result of the BPNN algorithm will fall into a local minimum. By introducing the BSAS method to optimize the BPNN, the global optimal value of the network is achieved [22, 23]. The relationship between the angles of the remaining parts and the p.u.l parameter matrix can be handled by the multilayer transposition method.

The structure of this paper is as follows. A model of MTB-MTW is established in Section II. In Section III, the extraction method of p.u.l parameter matrix and the prediction process of crosstalk are introduced. In Section IV, the new method is verified by numerical experiments using the MTB-MTW model, and the near-end and far-end crosstalk results are analyzed. The conclusions are given in Section V.

II. MTB-MTW GEOMETRIC MODEL AND ITS MTL MODEL

A. Geometric model of the MTB-MTW

The MTB-MTW cable bundle is a uniform twisted wire bundle, and its inner N group cable bundle contains an n-core uniform twisted wire. The twist direction of the n-core twisted wire and the N group of cable bundles is opposite. The materials of the N sets of cable bundles are all the same, with a total of nN core wires.

The MTB-MTW model is shown in Fig. 1. From the outer cable bundle (MTB-MTW), the transmission line can be divided into S^1 identical small segments, and from the inner n-core stranded wire bundle (MTW) can be further divided into S^2 identical small segments according to its twisted condition:

$$S = \frac{S^2}{S^1}, \tag{1}$$

where S represents the twisting ratio of MTB-MTW. It means that in each S_i^1, the n-core twisted wire in the inner layer will twist S segments.

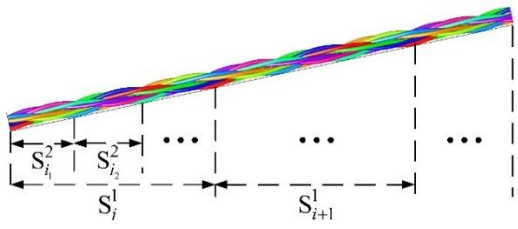

Fig. 1. Segmentation of MTB-MTW.

Since the models of S^1 segments are all the same, only 1 segment needs to be considered. Using the idea of the cascade method, a model of the entire transmission line can be obtained.

For the convenience of description, three groups of cable bundles composed of three core wires are used as examples. The MTB-MTW model and the corresponding cross-section model are shown in Fig. 2. The model takes S=3. After the outer cable bundle (MTB-MTW) is twisted for one turn, the corresponding inner core 3-core twisted wire (MTW) is twisted for 3 turns.

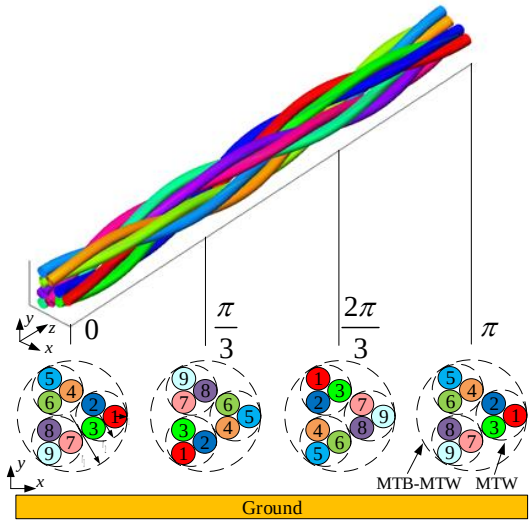

Fig. 2. Cable bundle and section model of MTB-MTW.

The position coordinates of each core are as follows:

$$\begin{cases} x_i = (r_3 - r_2)\cos\{\dfrac{360}{N}N(i) + \theta_1\} \\ \quad + (r_2 - r_1)\cos\{\dfrac{360}{n}n(i) + \theta_2\} \\ y_i = (r_3 - r_2)\sin\{\dfrac{360}{N}N(i) + \theta_1\}, \\ \quad + (r_2 - r_1)\sin\{\dfrac{360}{n}n(i) + \theta_2\} \\ z_i = \rho\theta_1 \end{cases} \tag{2}$$

among them, r_1 represents the radius of the core wire, r_2 represents the radius of MTW, r_3 represents the radius of MTB-MTW, and ρ represents the twist level of the cable bundle. $N(i)$ and $n(i)$ are the twisting degrees of MTB-MTW and MTW, respectively. θ_1 and θ_2 represent the twist angles of the outer and inner wire harnesses relative to the reference ground, respectively. According to formula (1) and the opposite twist direction of the inner and outer layers, it can be seen that it satisfies formula (3):

$$\theta_2 = (S-1)\theta_1. \tag{3}$$

Based on the above analysis, the model of Fig. 2 and the coordinates of formula (2) are generalized to the overall transmission line. MTB-MTW model was established out.

B. MTL model of the MTB-MTW

The established MTB-MTW model is divided uniformly. Each small segment is regarded as a parallel transmission line according to the idea of the cascade method. The multi-conductor transmission line model of its unit length is shown in Fig. 3. r_{ij}, l_{ij}, c_{ij}, and g_{ij} represent the elements in the parameter matrix of resistance **R**, inductance **L**, capacitance **C**, and conductance **G**, respectively, where $i, j = 1, 2, \cdots, nN$.

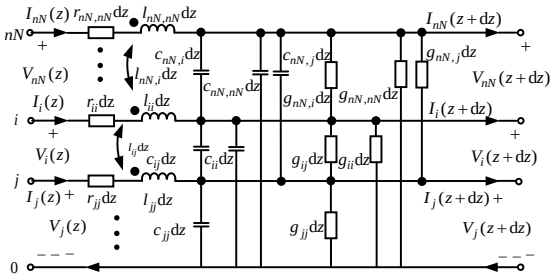

Fig. 3. MTL model of MTB-MTW.

Its satisfied transmission line equation [12]:

$$\begin{aligned} \frac{\partial \mathbf{V}(z,t)}{\partial z} + \mathbf{R}(z)\mathbf{I}(z,t) + \mathbf{L}(z)\frac{\partial \mathbf{I}(z,t)}{\partial t} = 0 \\ \frac{\partial \mathbf{I}(z,t)}{\partial z} + \mathbf{G}(z)\mathbf{V}(z,t) + \mathbf{C}(z)\frac{\partial \mathbf{V}(z,t)}{\partial t} = 0, \end{aligned} \tag{4}$$

where **V**(z,t) and **I**(z,t) are the voltage and current vectors at different positions and different times on the transmission lines, both of which are n-dimensional. The **R**(z), **L**(z), **C**(z) and **G**(z) parameter matrices are variables related to the position z of the transmission lines, and they are all $n \times n$ order matrices.

For simplicity, the four p.u.l parameter matrices can be expressed as:

$$\mathbf{M} = \begin{bmatrix} m_{11} & m_{12} & \cdots & m_{1,nN} \\ m_{21} & m_{22} & \cdots & m_{2,nN} \\ \vdots & \vdots & \ddots & \vdots \\ m_{nN,1} & m_{nN,2} & \cdots & m_{nN,nN} \end{bmatrix}, \tag{5}$$

where **M** represents different **R**, **L**, **C** and **G** parameter matrices. m_{ij} represents the corresponding parameter matrix specific resistance r_{ij}, inductance l_{ij}, capacitance c_{ij} and conductance g_{ij}. The p.u.l parameter matrices at different positions represent different matrices **M**.

III. PREDICTION OF PER-UNIT-LENGTH PARAMETER AND CROSSTALK

A. Predicting p.u.l parameter by BSAS-BPNN algorithm

For MTB-MTW harnesses, different positions represent different twist angles θ_1, and the corresponding p.u.l parameter matrices are also different. Combining (2) and (3), there is a functional relationship between the parameter matrix **M** and the twist angle θ_1, θ_2:

$$\mathbf{M}(\theta_1, \theta_2) = f(\theta_1). \tag{6}$$

Therefore, this paper introduces a BSAS-BP neural network algorithm with strong non-linear mapping capabilities, in which the BSAS algorithm is used to optimize the weight of the BPNN [23]. Its network topology is shown in Fig. 4.

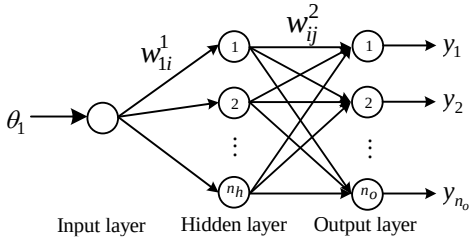

Fig. 4. Network topology of BSAS-BPNN.

The input of the network is the twist angle θ_1 at different positions. Considering the axis symmetry of the MTB-MTW model, $\theta_1 \in [0°, 360°/N)$. The parameter matrices in the other angular ranges can be obtained through part B. The output is a symmetric parameter matrix at this position, which can be represented by the vector Y as:

$$Y = \left[\bar{M}\right] = \left[y_1, y_2, \cdots, y_{n_o}\right], \tag{7}$$

where $\bar{M}$ is a row vector arranged by triangular elements on the parameter matrix.

The number of output layers n_o is determined by the parameter matrix RLCG, and the number of hidden layers n_h is an empirical value determined by the number of input layers and output layers, which is usually as follows:

$$n_h = 0.5(n_o + 1) + a, \quad a = 1, 2, \cdots 10. \tag{8}$$

BSAS algorithm is used to optimize the weights w_{1i}^1 and w_{ij}^2. Specific steps are as follows.

Step 1: Determine the optimized objective function. The output of the network is:

$$y_j = \sum_{i=1}^{n_h} \frac{w_{ij}^2}{1 + e^{-w_{1i}^1 \theta_k}}. \tag{9}$$

For N sets of data, the mean square error between the network output value and the actual value is:

$$f(w) = E(w_{1i}^1, w_{ij}^2) = \frac{1}{2N} \sum_{i=1}^{N} \sum_{j=1}^{n_o} \left(y_j - y_j'\right)^2, \tag{10}$$

where y_j' is the data value of the parameter matrix actually given, and all the weights are listed as a single row vector w. $f(w)$ is the objective function to be

optimized.

Step 2: Initialize the beetle position vector w and the optimal value f_{best} of the objective function:

$$w^{(0)} = rands(k,1), \tag{11}$$

where w represents the initial position of the beetle in the high-dimensional data space. k represents the dimension of the weight vector, and *rands* represents the generation of a uniformly distributed row vector.

Step 3: The direction (dir) and position (w) of M group beetles are randomly generated:

$$\begin{cases} dir_n^{(t)} = \dfrac{rands(k,1)}{\left\| rands(k,1) \right\|_2} \\ w_n^{(t)} = w^{(t)} + dir_n^{(t)} \end{cases}, \tag{12}$$

where $t = 0,1,2,\cdots$. $n = 1,2,\cdots,\mathrm{M}$.

Step 4: Obtaining the optimal objective function value and updating the beetle's position.

When $\min(f(w_n^{(t)})) \le f_{best}^{(t)}$,

$$\begin{cases} f_{best}^{(t+1)} = \min\limits_{1\le n\le m}(f(w_n^{(t)})) \\ w^{(t+1)} = \arg\min\limits_{1\le n\le m}(f(w_n^{(t)})) \end{cases}. \tag{13}$$

When $\min(f(w_n^{(t)})) > f_{best}^{(t)}$, the left and right beard positions of beetle can be calculated by the following formula (14):

$$\begin{cases} w_n^{(t)}(r) = w_n^{(t)} + \dfrac{d}{2}\cdot dir_n^{(t)} \\ w_n^{(t)}(l) = w_n^{(t)} - \dfrac{d}{2}\cdot dir_n^{(t)} \end{cases}, \tag{14}$$

where d is the distance between the left and right beards.

Step 5: The objective function value of the left and right beards can be calculated by the following formula:

$$\begin{cases} f_n^r = f_n(w_n^{(t)}(r)) \\ f_n^l = f_n(w_n^{(t)}(l)) \end{cases}, \tag{15}$$

$$w_n^{(t+1)} = w_n^{(t)} - \delta\cdot dir_n^{(t)}\cdot sign(f_n^r - f_n^l), \tag{16}$$

where δ is the step size of the beetle, which is generally taken as $\sqrt{k}$, and *sign* represents the sign function.

Step 6: In summary, the objective function and the position of the beetle can be obtained:

$$\begin{cases} f_{best}^{(t+1)} = f_{best}^{(t)} \\ w^{(t+1)} = \arg\min\limits_{1\le n\le m}(f(w_n^{(t+1)})) \end{cases}. \tag{17}$$

For the new $w^{(t+1)}$, the position of the beetle in each search direction can be obtained, and the next iteration calculation is performed.

Until iteration to the maximum number of iterations, the global minimum of the average error can be obtained. The process of BSAS optimizing the weight of BPNN is shown in Fig. 5.

The trained BSAS-BPNN algorithm can predict the parameter matrix at the corresponding position of 0~360°/N. However, the BSAS-BPNN algorithm cannot predict the parameter matrix at each position on the transmission line.

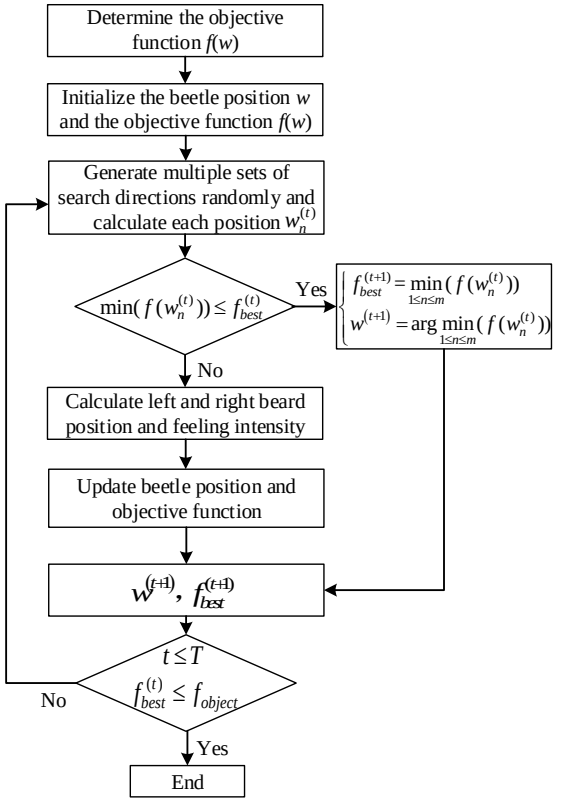

Fig. 5. BSAS algorithm to optimize the weight of BPNN.

B. Multilayer transposition method to obtain p.u.l parameter at arbitrary positions

The parameter matrix at the corresponding position of 0~360°/N has been predicted by the BSAS-BPNN algorithm. Considering the symmetry of the MTB-MTW cable and the periodicity of the twist angle, the parameter matrix at the corresponding position of 360°/N~360° can be obtained by the multilayer transposition method.

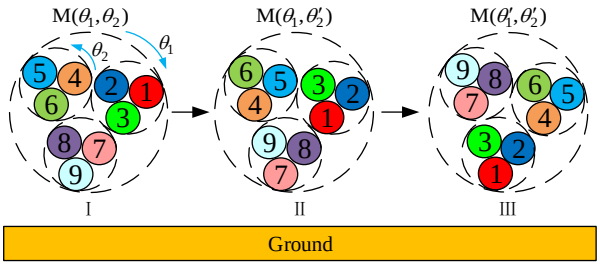

Fig. 6. Parameter matrix transformation between different positions and the same cross-section model.

The transformation process of the parameter matrix

at different positions and the same section is shown in Fig. 6. This means that the cross-section corresponding to any angle in $360^o/N$~360^o ($\theta_1' \in [360°/N, 360°)$), the same cross-section model can always be found in 0~$360^o/N$ ($\theta_1 \in [0°, 360°/N)$). Although the parameter matrices between the two cross-section models are not the same, but the transformation shown in Fig. 6 is also satisfied.

The parameter matrix $\mathbf{M}$ is represented as a block matrix with respect to the MTB-MTW:

$$\mathbf{M} = \begin{bmatrix} \mathbf{M}_{n\times n}^{11} & \mathbf{M}_{n\times n}^{12} & \cdots & \mathbf{M}_{n\times n}^{1N} \\ \mathbf{M}_{n\times n}^{21} & \mathbf{M}_{n\times n}^{22} & \cdots & \mathbf{M}_{n\times n}^{2N} \\ \vdots & \vdots & \ddots & \vdots \\ \mathbf{M}_{n\times n}^{N1} & \mathbf{M}_{n\times n}^{N2} & \cdots & \mathbf{M}_{n\times n}^{NN} \end{bmatrix}, \tag{18}$$

$$\mathbf{M}_{n\times n}^{ij} = \begin{bmatrix} m_{n(i-1)+1,n(j-1)+1} & m_{n(i-1)+1,n(j-1)+2} & \cdots & m_{n(i-1)+1,nj} \\ m_{n(i-1)+2,n(j-1)+1} & m_{n(i-1)+2,n(j-1)+2} & \cdots & m_{n(i-1)+2,nj} \\ \vdots & \vdots & \ddots & \vdots \\ m_{ni,n(j-1)+1} & m_{ni,n(j-1)+2} & \cdots & m_{ni,nj} \end{bmatrix}, \tag{19}$$

where $\mathbf{M}_{n\times n}^{ij}$ represents the parameter matrix between the MTB of the *i*-th and *j*-th bundle. *n* and *N* are the numbers of MTW and MTB, respectively. Because $\mathbf{M}$ is a symmetric matrix, we know $\mathbf{M}_{n\times n}^{ij} = (\mathbf{M}_{n\times n}^{ji})^T$.

The initial cross-section I is transformed to a cross-cection II in Fig. 6. At this time, no twists occurred in MTB. Considering only the twist angle of the MTW, the corresponding transformation is:

$$\mathbf{M}_{n\times n}^{ii}(\theta_1, \theta_2') = \mathbf{T}_n^{\alpha} \mathbf{M}_{n\times n}^{ii}(\theta_1, \theta_2) \mathbf{T}_n^{\alpha}, \tag{20}$$

where $\mathbf{M}_{n\times n}^{ii}(\theta_1, \theta_2)$ represents the parameter matrix of the cross-section I between the wire in the *i*-th bundle, and $\mathbf{M}_{n\times n}^{ii}(\theta_1, \theta_2')$ represents the parameter matrix of the corresponding cross-section II. $\mathbf{T}_n$ represents the transformation matrix of *n*-core MTW under $360^o/n$ twisting. α is the number of twists of MTW:

$$\theta_2' = \alpha \frac{360°}{n} + \theta_2. \tag{21}$$

The mutual parameter matrix $\mathbf{M}_{n\times n}^{ij}(\theta_1, \theta_2')$ between the wires in the *i*-th and *j*-th bundles also satisfies the above transformation:

$$\mathbf{M}_{n\times n}^{ij}(\theta_1, \theta_2') = \mathbf{T}_n^{\alpha} \mathbf{M}_{n\times n}^{ij}(\theta_1, \theta_2') \mathbf{T}_n^{\alpha}. \tag{22}$$

According to equations (20) and (22), the parameter matrix of cross-section II can be obtained as:

$$\mathbf{M}(\theta_1, \theta_2') = [\mathbf{M}_{n\times n}^{ij}(\theta_1, \theta_2')]_{N\times N}. \tag{23}$$

But cross-section II is just a virtual cross-section for the convenience of description. The final cross-section III can be transformed on the basis of cross-section II. The transformation of its parameter matrix is as follows:

$$\mathbf{M}(\theta_1', \theta_2') = \mathbf{P}_N^{\beta} \mathbf{M}(\theta_1, \theta_2') \mathbf{P}_N^{\beta}, \tag{24}$$

where $\mathbf{M}(\theta_1', \theta_2')$ is the parameter matrix of cross-section III, and $\mathbf{P}_N$ is the transformation matrix of MTB-MTW under $360^o/N$ twisting. The MTB-MTW twisting times β satisfy:

$$\theta_1' = \beta \frac{360°}{N} + \theta_1. \tag{25}$$

Combining formulas (3), (21), and (25) shows:

$$\alpha = \frac{n(S-1)}{N} \beta. \tag{26}$$

Different *n* and *N* correspond to different transformation matrices $\mathbf{T}_n$ and $\mathbf{P}_N$. In the MTB-MTW model of *n*=*N*=3 discussed in this paper, $\mathbf{T}_n$ and $\mathbf{P}_N$ are:

$$\mathbf{T}_3 = \begin{bmatrix} 0 & 0 & 1 \\ 1 & 0 & 0 \\ 0 & 1 & 0 \end{bmatrix}, \mathbf{P}_3 = \begin{bmatrix} 0_{3\times3} & 0_{3\times3} & 1_{3\times3} \\ 1_{3\times3} & 0_{3\times3} & 0_{3\times3} \\ 0_{3\times3} & 1_{3\times3} & 0_{3\times3} \end{bmatrix}. \tag{27}$$

C. Solving MTL equations and crosstalk

Combining parts A and B, the p.u.l parameter matrix at any position on the MTL model of MTB-MTW can be obtained. Discrete the MTL equation (4) as [24]:

$$\begin{cases} \mathbf{V}_k^t - \mathbf{V}_{k+1}^t + \mathbf{A}_{vk}(\mathbf{I}_k^t + \mathbf{I}_{k+1}^t) = \mathbf{V}_{k+1}^{t-1} - \mathbf{V}_k^{t-1} + \mathbf{B}_{vk}(\mathbf{I}_k^{t-1} + \mathbf{I}_{k+1}^{t-1}) \\ \mathbf{I}_k^t - \mathbf{I}_{k+1}^t + \mathbf{A}_{ik}(\mathbf{V}_k^t + \mathbf{V}_{k+1}^t) = \mathbf{I}_{k+1}^{t-1} - \mathbf{I}_k^{t-1} + \mathbf{B}_{ik}(\mathbf{V}_k^{t-1} + \mathbf{V}_{k+1}^{t-1}) \end{cases}. \tag{28}$$

The correlation matrix is:

$$\begin{aligned} &\mathbf{V}_k^t = \mathbf{V}(k\Delta z, t\Delta t) \quad , \mathbf{I}_k^t = \mathbf{I}(k\Delta z, t\Delta t) \\ &\mathbf{A}_{vk} = -(\frac{\mathbf{R}(z_k)}{2} + \frac{\mathbf{L}(z_k)}{\Delta t})\Delta z, \mathbf{B}_{vk} = (\frac{\mathbf{R}(z_k)}{2} - \frac{\mathbf{L}(z_k)}{\Delta t})\Delta z \\ &\mathbf{A}_{ik} = -(\frac{\mathbf{G}(z_k)}{2} + \frac{\mathbf{C}(z_k)}{\Delta t})\Delta z, \mathbf{B}_{ik} = (\frac{\mathbf{G}(z_k)}{2} - \frac{\mathbf{C}(z_k)}{\Delta t})\Delta z, \end{aligned} \tag{29}$$

where Δz and Δt represent the length of space division and time division respectively.

According to the p.u.l parameter matrix at different positions, $\mathbf{V}(z,t)$ and $\mathbf{I}(z,t)$ at different positions and times can be iteratively obtained through equations (28) and (29).

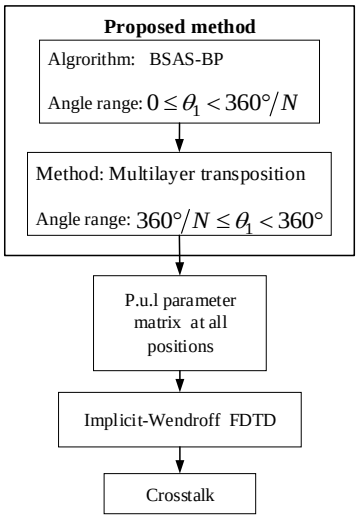

Fig. 7. Crosstalk prediction process of MTB-MTW.

IV. VERIFICATION AND ANALYSIS

A. Verification of BSAS-BPNN algorithm

In order to verify the correctness of the method proposed in this paper, an MTB-MTW cable with n=N=3 is taken as an example to verify the new method. The wires in the model are copper wires with a diameter of 0.8mm. The wire insulation material is polyvinyl chloride (PVC), which has a thickness of 0.6 mm and a relative dielectric constant of 2.7. The length of the wire is 1m along the axial direction, and 50 ohm resistors are connected to both ends of the wire. Some related parameters are shown in Table 1.

Table 1: Related parameters

Name	Value
Wire diameter	0.8mm
Conductivity of the wire	58000000 S/m
Insulation layer thickness	0.6mm
Wire length	1m
Height of center wire from ground	15mm
Twist ratio	3
Number of MTB (N)	3
Number of MTW (n)	3

The initial reference cross-section model is as shown in Fig. 6 (cross-section I), and the p.u.l parameter matrix is extracted using ANSYS simulation software [25]. Figure 8 shows the error E iteration process of the BSAS-BPNN algorithm for four p.u.l parameter matrices. The units of the four p.u.l parameter matrices are Ω/m, nH/m, pF/m, and mS/m. The corresponding iteration errors reach 4×10^{-6}, 5×10^{-3}, 1×10^{-3}, and 2.5×10^{-7}, respectively. Figure 9 shows the average error value of the p.u.l parameter matrix at 10 randomly selected angles, the maximum of which is less than 0.2%.

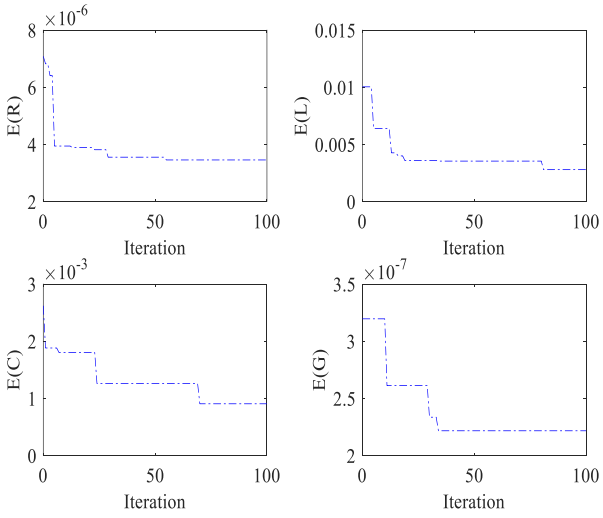

Fig. 8. Error iteration process of BSAS-BPNN algorithm.

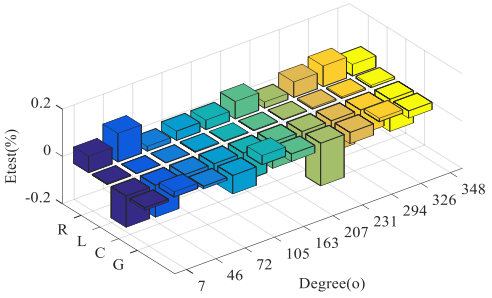

Fig. 9. Mean error of p.u.l parameter matrix.

B. Analysis of crosstalk results

Simulation was performed using CST Cable Studio software based on the transmission line matrix (TLM) method. It is a high-precision numerical calculation method of electromagnetic field, which has high reference value [26]. Its arrangement in CST is shown in Fig. 10.

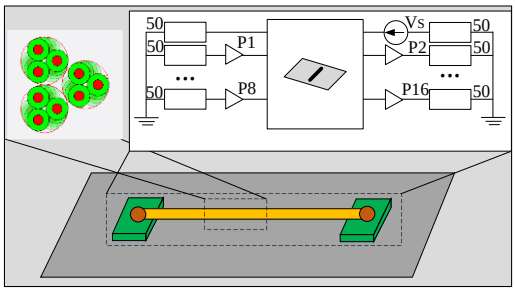

Fig. 10. Full-wave simulation experiment schematic diagram.

Near-end crosstalk (NEXT) and far-end crosstalk (FEXT) of each line are defined as follows:

$$NEXT_i = 20\log_{10}\frac{V_{i,NEXT}}{V_S}, FEXT_i = 20\log_{10}\frac{V_{i,FEXT}}{V_S}, \quad (30)$$

where V_S represents the applied interference voltage on line 1, $V_{i,NEXT}$ represents the disturbed voltage of the i-th line near the interference voltage terminal, and $V_{i,FEXT}$ represents the disturbed voltage of the i-th line away from the interference voltage terminal. $i = 2,3,\cdots,9$.

The crosstalk of the disturbed lines (#2, #3, #5, #6, #8, #9) in MTB-MTW is shown in Fig. 11 and Fig. 12, respectively. The solid line is the result obtained by the method proposed in this paper. The relevant parameters are shown in Table 1. The segmentation point of the FDTD algorithm is divided into 900 segments. The dashed line is the result of the CST simulation, and its arrangement is shown in Fig. 10.

It can be seen from Fig. 11 and 12 that the wires close to the interference wires (#2, #3) are more susceptible to interference than the wires far from the interference wires (#5, #6, #8, #9). Crosstalk between wires (#5, #6, #8, #9) far from the interference wires is very similar.

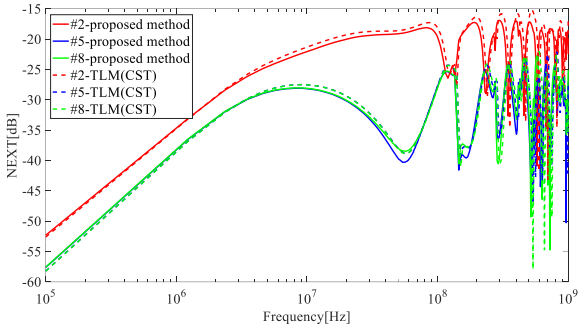

(a)

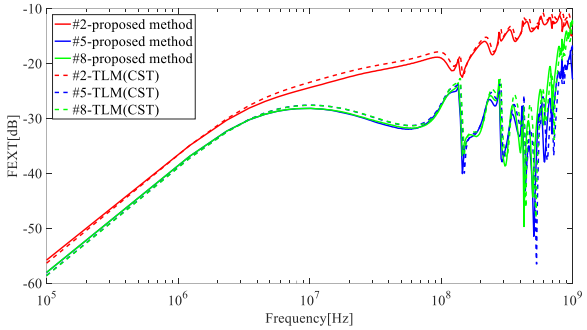

(b)

Fig. 11. Crosstalk prediction and simulation values of different bundle (#2, #5, and #8) in MTB-MTW. (a) NEXT and (b) FEXT.

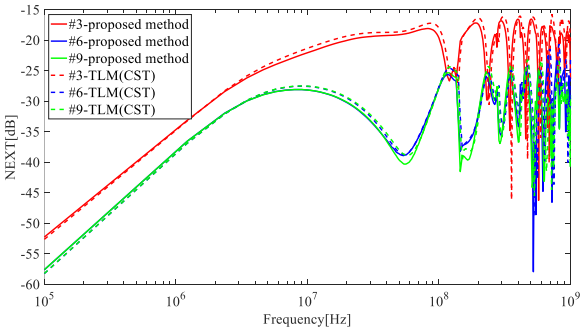

(a)

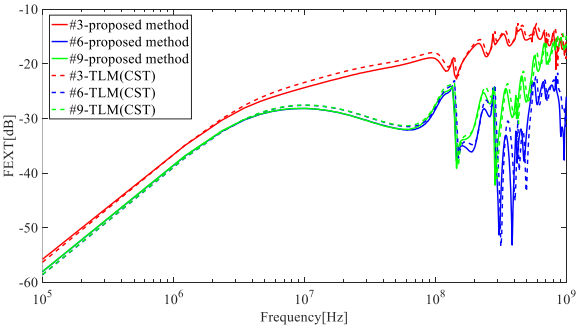

(b)

Fig. 12. Crosstalk prediction and simulation values of different bundle (#3, #6, and #9) in MTB-MTW. (a) NEXT and (b) FEXT.

In the frequency range below 10^7 MHz, the curve obtained by the proposed method and the TLM method agrees very well. In the frequency range higher than 10^7MHz, the approximate contours of the images obtained by the new method and the TLM method are very similar, but the deviations at each frequency point are 0~3dB. This may not take into account that the parameter matrix will change with frequency.

Tables 2 and 3 are the average error percentages between the results of the method proposed in this paper and those obtained by TLM. In the frequency ranges of 0.1~100 MHz, 100~500 MHz, and 500~1000 MHz, the maximum average errors are 4.508%, 13.800%, and 10.536%, respectively. From the perspective of average error, the results of the new method are more accurate in the low frequency and high frequency ranges.

Table 2: Average error (%) of different wires (NEXT)

Frequency (MHz)	0.1~100	100~500	500~1000
#2	3.730	12.436	10.010
#3	3.684	13.800	8.082
#4	1.584	7.960	3.703
#5	2.011	7.638	8.048
#6	1.107	5.944	8.642
#7	1.799	10.771	6.150
#8	1.017	7.727	10.536
#9	2.025	7.551	7.961

Table 3: Average error (%) of different wires (FEXT)

Frequency (MHz)	0.1~100	100~500	500~1000
#2	4.508	4.900	2.721
#3	4.446	4.727	2.912
#4	1.208	4.238	2.143
#5	1.787	7.879	6.988
#6	1.800	10.981	3.487
#7	1.318	4.627	2.764
#8	1.494	10.562	6.174
#9	1.849	7.303	2.831

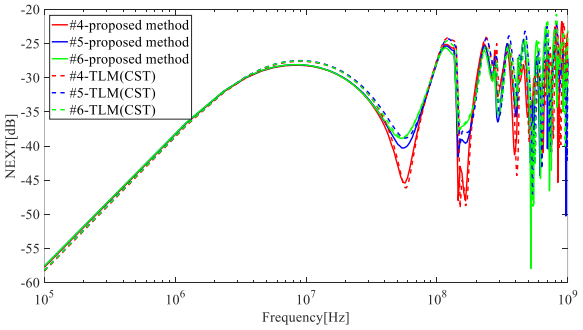

(a)

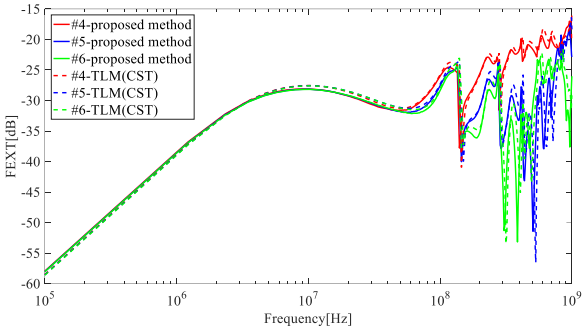

(b)

Fig. 13. Crosstalk prediction and simulation values of the bundle (#4, #5, and #6) in MTB-MTW. (a) NEXT and (b) FEXT.

In addition to the crosstalk curves of #5 and #8 (#6 and #9), it can be seen from Fig. 13 that the crosstalk curves of a bundle (#4, #5, #6) in the MTB-MTW are also very similar. The crosstalk curves of bundle (#7, #8, #9) in another MTB are also similar to Fig. 13. For the MTB-MTW model, the crosstalk between the wires is very close due to its double-layer twist. For the crosstalk suppression measures, only one wire condition needs to be considered, and the other wires are theoretically applicable.

V. CONCLUSION

For the MTB-MTW model, this paper proposes a p.u.l parameter matrix prediction process based on the BSAS-BPNN algorithm and the Multilayer transposition method. And the FDTD method under Implicit-Wendroff difference format is combined to solve the crosstalk. In this paper, the twisted wires under the MTB-MTW model with n=N=3 are studied and compared with the TLM method. The numerical experimental results first show that the iteration error of different p.u.l parameter matrices under the BSAS-BPNN algorithm can reach 4×10^{-6}, 5×10^{-3}, 1×10^{-3}, and 2.5×10^{-7}, respectively. Second, the proposed method is in good agreement with the NEXT and FEXT results of the TLM method at low and high frequencies. Finally, the results show that the crosstalk of the wires far away from the interference lines in MTB-MTW is very similar.

The method in this paper can be generalized to the MTB-MTW model of arbitrary conductors and twists, but the effect of frequency on the p.u.l parameter matrix and the non-uniform twisted wire model have not been considered. Therefore, there is still much research space after this paper.

ACKNOWLEDGMENT

The paper is supported by National Natural Science Foundation of China (51475246), National Natural Science Foundation of Jiangsu Province (BK20161019), and Aviation Science Foundation (20172552017).

REFERENCES

[1] C. R. Paul, "A brief history of work in transmission lines for EMC applications," *IEEE Trans. Electromagn. Compat.*, vol. 49, no. 2, pp. 237-252, May 2007.

[2] S. Chabane, P. Besnier, and M. Klingler, "A modified enhanced transmission line theory applied to multiconductor transmission lines," *IEEE Trans. Electromagn. Compat.*, vol. 59, no. 2, pp. 518-528, Apr. 2017.

[3] Y. Wang, Y. S. Cao, D. Liu, R. W. Kautz, N. Altunyurt, and J. Fan, "A generalized multiple-scattering method for modeling a cable harness with ground connections to a nearby metal surface," *IEEE Trans. Electromagn. Compat.*, vol. 61, no. 1, pp. 261-270, Feb. 2019.

[4] C. P. Yang, W. Yan, Y. Zhao, Y. Chen, C. M. Zhu, and Z. B. Zhu, "Analysis on RLCG parameter matrix extraction for multi-core twisted cable based on back propagation neural network algorithm," *IEEE Access*, vol. 7, pp. 126315-126322, Aug. 2019.

[5] O. Gassab and W. Y. Yin, "Characterization of electromagnetic wave coupling with a twisted bundle of twisted wire pairs (TBTWPs) above a ground plane," *IEEE Trans. Electromagn. Compat.*, vol. 61, no. 2, pp. 251-260, Feb. 2019.

[6] C. D. Taylor and J. P. Castillo, "On the response of a terminated twisted-wire cable excited by a plane-wave electromagnetic field," *IEEE Trans. Electromagn. Compat.*, vol. EMC-22, no. 1, pp. 16-19, Feb. 1980.

[7] Z. Fei, Y. Huang, J. Zhou, and C. Song, "Numerical analysis of a transmission line illuminated by a random plane-wave field using stochastic reduced order models," *IEEE Access*, vol. 5, pp. 8741-8751, May 2017.

[8] Y. Yan, L. Meng, X. Liu, T. Jiang, J. Chen, and G. Zhang, "An FDTD method for the transient terminal response of twisted-wire pairs illuminated by an external electromagnetic field," *IEEE Trans. Electromagn. Compat.*, vol. 60, no. 2, pp. 435-443, Apr. 2018.

[9] G. P. Veropoulos and P. J. Papakanellos, "A probabilistic approach for the susceptibility assessment of twisted-wire pairs excited by random plane-wave fields," *IEEE Trans. Electromagn. Compat.*, vol. 59, no. 3, pp. 926-969, June 2017.

[10] G. Spadacini, F. Grassi, and S. A. Pignari, "Field-to-wire coupling model for the common mode in random bundles of twisted-wire pairs," *IEEE Trans. Electromagn. Compat.*, vol. 57, no. 5, pp. 1246-1254, Oct. 2015.

[11] O. Gassab, L. Zhou, W. Y. Yin, and H. Xie,

"Modelling electromagnetic wave coupling and mode conversion effects in multitwisted bundle of twisted-wire pairs (MTB-TWP) above ground plane," *Int. J. Numer. Model. Electron. Netw. Devices Fields*, 2018, doi: 10.1002/jnm.2539.

[12] C. R. Paul, *Analysis of Multiconductor Transmission Lines*. Hoboken, NJ, USA: Wiley, 1994.

[13] P. Manfredi, D. De Zutter, and D. V. Ginste, "Analysis of nonuniform transmission lines with an iterative and adaptive perturbation technique," *IEEE Trans. Electromagn. Compat.*, vol. 58, no. 3, pp. 859-867, June 2016.

[14] G. Spadacini, ''Numerical assessment of radiated susceptibility of twisted-wire pairs with random nonuniform twisting," *IEEE Trans. Electromagn. Compat.*, vol. 55, no. 5, pp. 956-964, Oct. 2013.

[15] C. Jullien, P. Besnier, M. Dunand, and I. Junqua, "Advanced modeling of crosstalk between an unshielded twisted pair cable and an unshielded wire above a ground plane," *IEEE Trans. Electromagn. Compat.*, vol. 55, no. 1, pp. 183-194, Feb. 2013.

[16] A. Shoory, M. Rubinstein, A. Rubinstein, and F. Rachidi, "Simulated NEXT and FEXT in twisted wire pair bundles," *In Proc. EMC Eur. Symp.*, York, U.K., pp. 266-271, Sep. 2011.

[17] M. Tang and J. Mao, "A precise time-step integration method for transient analysis of lossy nonuniform transmission lines," *IEEE Trans. Electromagn Compat.*, vol. 50, no. 1, pp. 166-174, Feb. 2018.

[18] A. Tatematsu, F. Rachidi, and M. Rubinstein, "A technique for calculating voltages induced on twisted-wire Pairs Using the FDTD method," *IEEE Trans. Electromagn. Compat.*, vol. 59, no. 1, pp. 301-304, Feb. 2017.

[19] V. R. Kumar, B. K. Kaushik, and A. Patnaik, "An accurate FDTD model for crosstalk analysis of CMOS-Gate-Driven coupled RLC interconnects," *IEEE Trans. Electromagn. Compat.*, vol. 56, no. 5, pp. 1185-1193, Oct. 2014.

[20] B. Cannas, A. Fanni, and F. Maradei, "A neural network approach to predict the crosstalk in non-uniform multi-conductor transmission lines," *IEEE In. Symp. on Circuits. and Systems*, Phoenix-Scottsdale, AZ, USA, pp. 573-576, May 2002.

[21] F. Dai, G. H. Bao, and D. L. Su, "Crosstalk prediction in non-uniform cable bundles based on neural network," *Proceedings of the 9th in Symp. on Antennas, Propagation and EM Theory*, Guangzhou, China, pp. 1043-1046, 2010.

[22] J. Wang and H. Chen, "BSAS: Beetle swarm antennae search algorithm for optimization problems," *arXiv preprint*. arXiv:1807.10470, 2018.018, 51(11):60-66.

[23] Q. Wu, Z. Ma, G. Xu, S. Li, and D. Chen, "A novel neural network classifier using beetle antennae search algorithm for pattern classification," *IEEE Access*, vol. 7, pp. 64686-64696, May 2019.

[24] L. Dou and J. Dou, "Time-domain analysis of lossy multiconductor transmission lines based on the Lax–Wendroff technique," *Analog Integrated Circuits and Signal Processing*, vol. 68, no. 1, pp. 85-92, 2011.

[25] C. Che, H. P. Zhao, Y. D. Guo, J. Hu, and H. Kim, "Investigation of segmentation method for enhancing high frequency simulation of Q3D extractor," *IEEE In Conference on Computational Electromagn (ICCEM)*, Shanghai, China, Mar. 2019.

[26] CST Microwave Studio, ver. 2008, Computer Simulation Technology, Framingham, MA, 2008.

Chao Huang was born in Anhui Province, China. He received the B.S degree in School of electrical Engineering and Automation from Anhui University of Technology, Maanshan, China, in 2018. He is currently working toward the Master's degree in Electrical Engineering at Nanjing Normal University, Nanjing, China. His main research interests include multi-conductor transmission lines and EMC.

Yang Zhao received his B.E., M.E., and Ph.D. degree all in Power Electronic Technology from Nanjing University of Aeronautics and Astronautics, Nanjing, China, in 1989 and 1992, and 1995, respectively. He is currently the Professor with Nanjing Normal University. His research interests are in the areas of Electromagnetic Compatibility, Power Electronics and Automotive Electronics.

Wei Yan Doctor & Assoc. Professor from Nanjing Normal University. He obtained the Physics and Electronics Ph.D. and Electrical Engineering M.S. from Nanjing Normal University in 2014 and 2011. He is the Senior Member of China Electrical Technology Association and the evaluation expert of the Electromagnetic Compatibility Calibration Specification of China.

Qiangqiang Liu was born in Anhui Province, China. He received the B.S. degree in School of Electrical Engineering and Automation from Anhui University of Science and Technology, Huainan, China, in 2018. He is currently working toward the Master's degree in Electrical Engineering at Nanjing Normal University, Nanjing, China. His major research interests include new technology of electrical engineering.

Omega-Shaped Tag Antenna with Inductively-Coupled Feeding Using U-Shaped Stepped-Impedance Resonators for RFID Applications

Adam R. H. Alhawari [1], A. H. M. Almawgani [1], Hisham Alghamdi [1], Ayman T. Hindi [1], Tale Saeidi [2], and Alyani Ismail [3]

[1] Electrical Engineering Department, College of Engineering, Najran University, Najran, Saudi Arabia
aralhawari@nu.edu.sa, ahalmawgani@nu.edu.sa, hg@nu.edu.sa, athindi@nu.edu.sa

[2] Department of Electrical and Electronics Engineering, Universiti Teknologi Petronas, Tronoh, Perak, Malaysia
gs32772@gmail.com

[3] Wireless and Photonic Network Research Center, Department of Computer and Communication Systems Engineering, Faculty of Engineering, Universiti Putra Malaysia, Malaysia
alyani@upm.edu.my

Abstract ─ This study proposes a new omega-shaped tag antenna with inductively-coupled feeding (ICF) using U-shaped stepped- impedance resonators (SIRs). It aims at improving the performance of the tag antennas for Radio Frequency Identification (RFID) applications. The radiating body of the antenna is fed using two mirroring symmetrical U-shaped SIRs. This antenna is a simpler alternative for the existing antennas that match the impedance of the antenna to the chip impedance effectively applying varied reinforcement of the equivalent inductance of the radiating structure. In addition to the use of an omega-shaped structure, the proposed feeding technique boosts performance of the antenna impedance, dimensions, and peak gain. The measured size of the antenna was 50×55.55×1.6 mm^3. It attains a peak gain of 1.8 dBi and radiation efficiency higher than 85% at its operating frequency. The experimental results revealed that this tag antenna has the characteristic of good impedance matching within the frequency range of 900-940 MHz, corresponding to a better power reflection coefficient of -3 dB. Comparison between the measured and simulated results verified that the proposed feeding method is capable to improve overall performance of RFID tag antennas.

Index Terms ─ Inductively-coupled feed, omega-shape, Radio Frequency Ddentification (RFID), RFID tag, stepped-impedance resonator.

I. INTRODUCTION

The RFID technology is swiftly progressing to produce simpler and more efficient object identification. Currently, it is inevitable to avoid the rapidly-growing applications of RFID in daily life, particularly passive RFID applications. For example, RFID antennas and sensors are not only embedded into general detection systems, but also involved modern vehicle and transportation devices, access point networks, business transactions, healthcare purposes, and logistics systems [1], [2].

Essentially, the ideal passive RFID tag relies on agreeably matching an antenna into a chip tag, which is combined in a circuit. The perfect matching enhances the chip functionality power, hence, extending the reading range. The most vital section of each passive RFID is considered as the tag antenna. There is growing interest in reducing the cost and size of the RFID for varied applications in numerous fields especially where cost of fabrication and matching networks concerned. The only way is to achieve a direct matching between the antenna and the chip. The suggested approach is to solve the complicated impedance problem, albeit, its variable factors, frequency and the input power magnitude [3].

Recently, among the solutions applied are these tag antennas for RFID purposes mentioned in [4]–[10]. Regrettably, only a few of them offered high omnidirectional gain antennas with miniaturized dimensions. Thus, the urgency is concentrated more on designing methods. For example, an inspiring low-profile antenna design was proposed in [4] that employed a "Vivaldi-like" aperture loaded with meander line and then fed through a slot line which was electromagnetically coupled with the microstrip line. This antenna utilized an ordinary 50-Ω impedance system instead of common chip impedance at a −2.97 dB peak gain. Meanwhile, in [5], a proposed dual-band tag antenna was functioning at both HF and UHF bands. It comprised a spiral shape coil and two meander lines to resonate at HF and UHF bands, respectively. Moreover, it could be easily adjusted and the antenna using various means to handle the coarse and

Submitted On: April 10, 2020
Accepted On: May 30, 2020
https://doi.org/10.47037/2020.ACES.J.350815

fine-tuning. Despite these benefits, it is still considered large at the dimensions of 51.4 × 83.6 mm^2 with a maximum gain of almost −1.5 dB. Another research by Tang et al. [6] developed a rectangular-loop feeding antenna with a bent meandered strip and extra patches to allow it to function in the UHF RFID bands. However, the size of this proposed antenna is 77.5 × 22.2 mm^2 at maximal gain: 1.6 dB.

Several RFID tag antennas were developed with some configurations specifically optimized to be mountable on metallic objects [11]–[14]. Those RFID tag antennas performance offered low gain because of their reduced size. Other different designs of RFID antennas were proposed in [15]–[18] with inductively-coupled feeding (ICF) designed to improve the gain of tag antennas. This proposed feeding method, specifically ICF, yields enhanced performance in relation to gain and impedance. However, the sizes of the antennas presented in [15]–[18] were still considered big. Therefore, the size required further reduction.

A unique broadband UHF RFID tag antenna for bio-monitoring applications was proposed in [19]. This antenna has a bandwidth of 120 MHz, which allows it to operate at all the UHF frequency band. The levels of performance were improved in both free space and on the human body. Yet, at approximately 80 mm× 50 mm× 200 µm, the size of this antenna is still big. Another RFID tag was designed to detect the dielectric materials in [20]. The basic configuration of this antenna included a printed spiral configuration. The testing results confirmed it could produce tags with acceptable readability and showed a reading distance of up to 7 m when incorporated with metallic objects and 10 m in the case of dielectric objects. But it is also big at 115 × 26 × 3.38 mm^3. Next in the list is a high-performance UHF RFID tag antenna consisting of a liquid-filled bottle [21]. It comprised of a folded dipole and a loop-matching unit placed on a water bottle. The testing results determined that the reading range of this antenna can reach up to 4.2 m when placed on a water bottle at the frequency of 915 MHz. Ironically, without the bottle, the reading range of this antenna increased significantly and reached up to 8 m. Yet, it remains a challenge to design a high-performance RFID tag antenna that is suitable to be placed onto a liquid-filled bottle due to the variety of potential liquids and the associated high conductivities and permittivity.

After further review of the literature, this study set forth with the objective to design a cost-effective, high gain, and miniaturized tag antenna with minimal losses to use in RFID applications. The proposed design is based on ICF using U-shaped SIRs that are tuned to operate at a center frequency of 0.915 GHz. Section 2 presents a detailed analysis of the suggested stepped-impedance resonator feeding. Then, the configuration of the proposed tag antenna follows in Section 3. Both the theoretical and evaluated results are presented in Section 4 and then it is concluded in Section 5.

II. ANALYSIS OF THE FEED STRUCTURE OF THE U-SHAPED STEPPED-IMPEDANCE RESONATOR

The stepped-impedance resonators (SIRs) are used extensively in the designs of microstrip and microwave devices for their easier regulator and miniature size. Exclusively, previous studies reported in [22]–[24] reported that the SIRs are tunable over a wide range of frequencies by the effect of the impedance ratio (R_z) of the low-impedance to the high-impedance sections. Once R_z is reduced, the resonator length will also be minimized. The flexibility in reducing the length of the resonator is beneficial in meeting the miniaturization demand of the industry.

Figure 1 shows the U-shaped SIR feeding configuration. It is fed based on two symmetrical U-shaped SIR units to excite the radiating dipole via ICF. Its opposite central points directly connected to the RFID chip at the head of the two U-shaped SIR structures (Fig. 1). The equivalent inductance in the previously stated dipole is achieved by utilizing the proposed feeding configuration. The parameters S_U, L_{Z1}, L_{Z2}, W_{Z1} and W_{Z2} provide flexible control over the inductive coupling strength. Figure 2 depicts the ICF's equivalent circuit. The inductive-coupling unit can be turned into a transformer. The Z_{in} known as the antenna input impedance, is recorded at the terminals of the U-shaped SIR and is estimated as follows [15]:

$$Z_{in} = R_{in} + jX_{in} = \frac{(2\pi fM)^2}{Z_{ant}} + Z_U, \quad (1)$$

where Z_{ant} and Z_U are the dipole antenna impedance and the U-shaped SIR feeds impedance, respectively. Likewise, M has shared inductance between the two impedances. The value of Z_U can be calculated using Equation 2:

$$Z_U = j2\pi f L_U, \quad (2)$$

where L_U is the self-inductance of the SIR feed structure. The equation 3 can assist to calculate the antenna impedance at the resonant frequency ($f = f_0$) of dipole antenna as:

$$Z_{in} = \left(\frac{(2\pi f_0 M)^2}{Z_{ant}}\right) + (j2\pi f_0 L_U). \quad (3)$$

Equation 3 confirms that the inductance of the U-shaped SIR (L_U) specifies the input reactance. Meanwhile, the transformer mutual inductance (M) determines the resistance regardless of whether the radiating dipole antenna is operating at the resonance frequency or at any other frequencies. Theoretically, reactance and resistance can be adjusted independently. Besides, the proposed feeding structure is a simple and ideal alternative to match the antenna impedance to the chip impedance effectively.

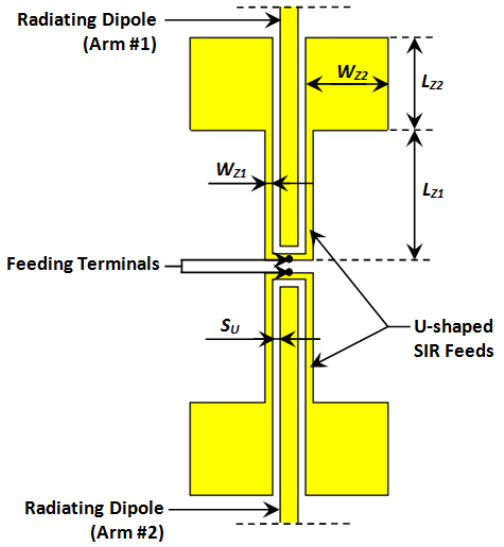

Fig. 1. The proposed layout of ICF using the U-shaped SIRs.

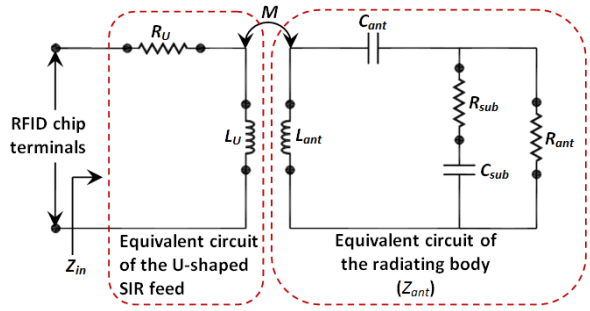

Fig. 2. The equivalent circuit model of ICF.

Figures 3, 4, 5, 6, and 7 shows plots, indicating how the U-shaped SIR designing parameters such as L_{Z1}, L_{Z2}, W_{Z1}, W_{Z2}, and S_U affecting the return loss (dB) results. The return loss plots were simulated using Murata RFID MAGICSTRAP LXMS31ACNA-011 tag chip, with input impedance of (25-j200) Ω at resonance frequency of 915 MHz. The simulation results summary is any increment in the L_{Z1} will reduce the resonant frequency. In contrary, it works for different values of the impedance ratio (R_Z). The results demonstrate that any increment in R_Z value will affect the resonant frequency of the tag antenna and shift it down. It can be concluded that R_Z is a vital electrical parameter for characterizing properties of the U-shaped SIRs feeding structure. Therefore, the selection of R_Z offers a flexible method to tune the resonant frequency of the tag antenna to the desired operating frequency.

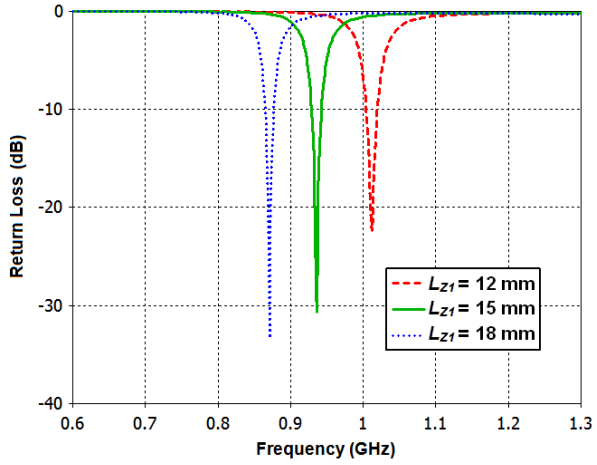

Fig. 3. Simulated return loss at different L_{Z1} values.

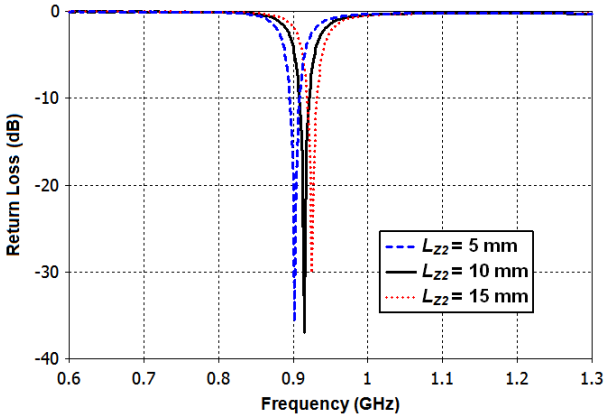

Fig. 4. Simulated return loss at different L_{Z2} values.

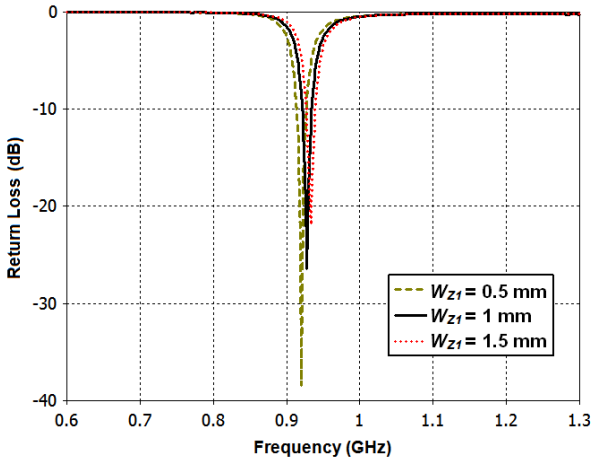

Fig. 5. Simulated return loss at different W_{Z1} values.

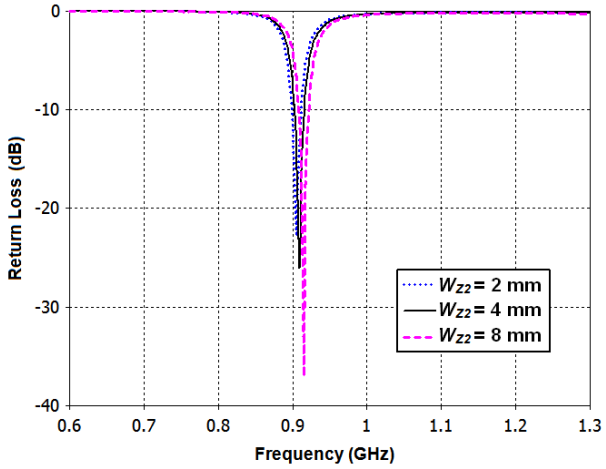

Fig. 6. Simulated return loss at different W_{Z2} values.

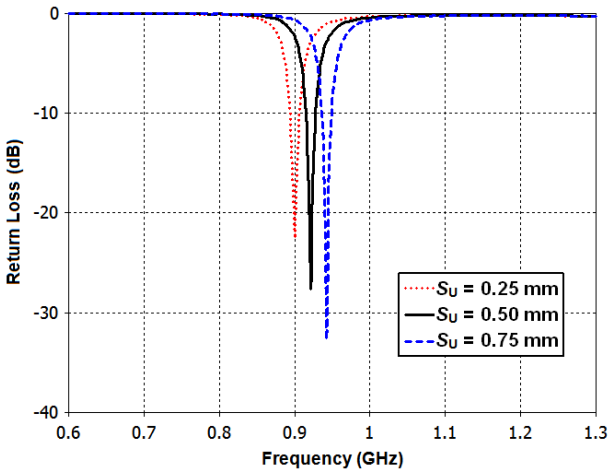

Fig. 7. Simulated return loss at different S_U values.

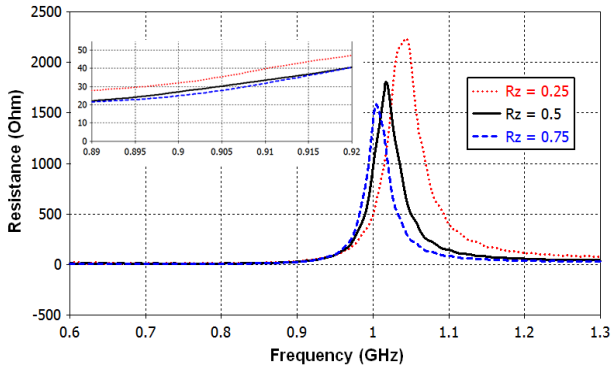

(a)

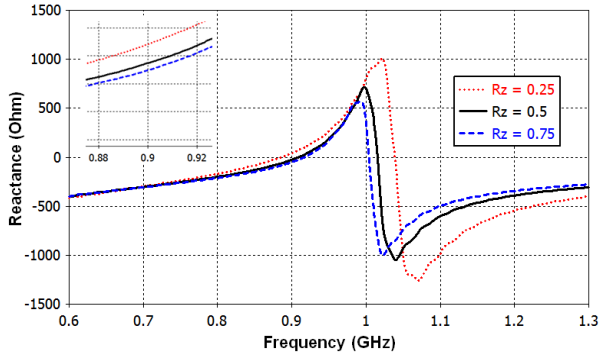

(b)

Fig. 8. Simulated input impedance of the tag antenna for different values of R_Z: (a) resistance and (b) reactance.

III. CONFIGURATION OF THE PROPOSED TAG ANTENNA

A miniaturized microstrip tag antenna is proposed for RFID purposes. It comprises of two U-shaped ICF SIR arms and an omega-shaped resonator as a radiating dipole body. The omega-shaped resonator configurations have competent resonance property and can shrink the length of the resonator, in which such adjustment is frequently adapted by the researchers in many designs applications to meet higher performance enhancement and miniaturization targeted like in the reported works in [25]–[28]. However, based on the authors' knowledge, it has been used solely in the development of RFID tag antennas as proposed in this work.

In this antenna design procedure, both structures (the U-shaped ICF SIR arms and the omega-shaped radiating dipole body) are located on the upper surface of the substrate (Fig. 9). Also, it has no conductor attached to the bottom surface of the substrate. The absence of any direct contact material is purposely done to avoid obstruction during experimental sessions. Its elliptical shapes, and dimensions were carefully specified to improve impedance matching. Its IC chip terminals are placed directly in the middle of the two opposing U-shaped SIR units. Encouragingly, the mutual coupling assists the feeding to communicate with the body of the tag antenna. That is how it offers attractive features in sensing applications. Figures 9 and 10 show the simulated and fabricated prototype of the proposed RFID tag antenna, respectively. Additionally, the geometrical properties of this antenna are tabulated in Table 1. The values of the listed geometrical properties are the optimized values for better functionality to obtain the

antenna in its UHF operation frequency RFID band from 860 to 960 MHz. These optimized values (Table 1) were gained during the simulation process.

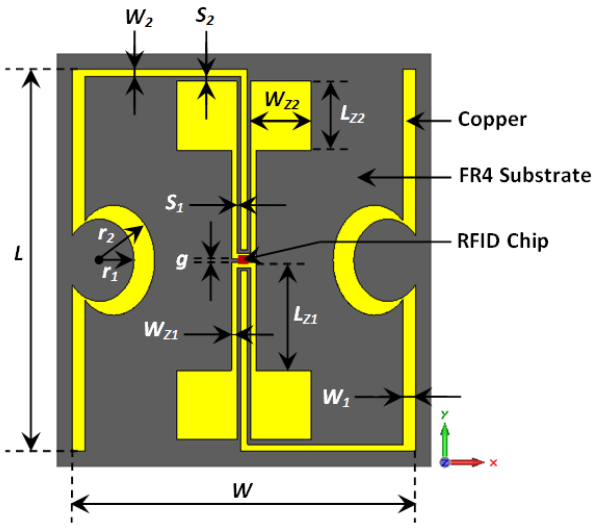

Fig. 9. The simulated prototype of the proposed tag antenna.

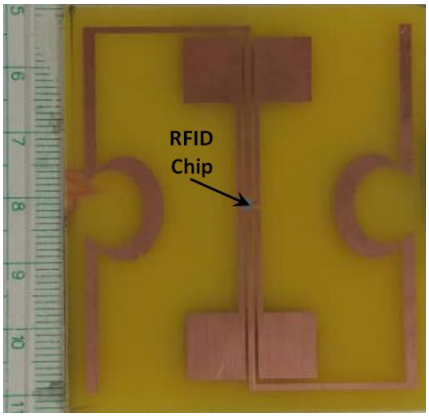

Fig. 10. The fabricated tag antenna prototype.

A Murata RFID MAGICSTRAP LXMS31ACNA-011 tag chip [29] was utilized to fabricate the antenna. At assumed (25-j200) Ω input impedance and operating at 915 MHz resonant frequency, the minimum point of threshold power is -8 dBm. This tag antenna was fabricated on an epoxy FR4 substrate with a loss tangent of 0.02, h= 1.6 mm, and ε_r= 4.4. Its measurement is 50×55.55×1.6 mm^3. These dimensions, as well as the resonance frequency of this antenna are based on optimized simulations that matched the inductance with a conjugate impedance of the selected chip. Furthermore, it has miniaturized dimensions corresponding reductions of nearly 20.64%, 30.5%, 7.1%, 32.18%, and 22.84% in size compared to those antennas proposed in [16], [19], [20], [30], [31], respectively.

The CST Microwave Studio 2019 was used as a full-wave electromagnetic simulator to simulate the proposed tag antennas characteristics using Finite-Difference Time-Domain (FDTD) method [32]. Figures 11 and 12 depict the simulated return losses (R_L) of the proposed antenna in terms of W_1 and W_2, respectively. This step was taken to determine what influences the width of the omega-shaped antenna from its overall performance. The values of parameters presented in Table 1 are considered in the simulation process. It suggests that the increases in W_1 and W_2 will slightly increase the frequency response of the antenna. Therefore, it is concluded that the dimensions of the omega-shaped antenna largely influence its performance.

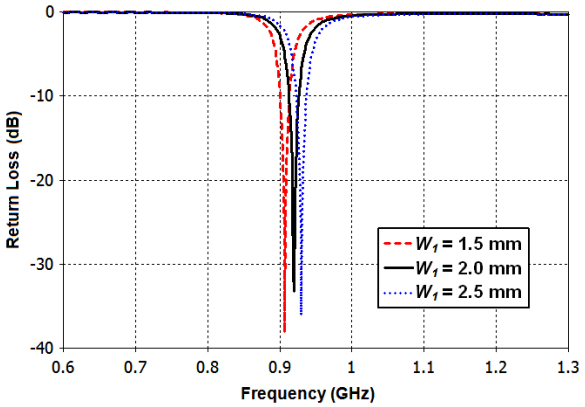

Fig. 11. The simulated return loss of the proposed antenna in terms of W_1.

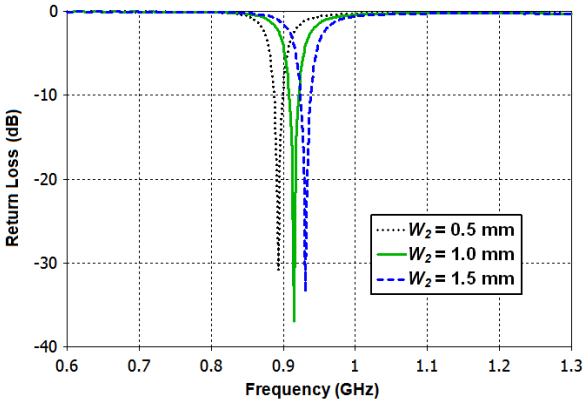

Fig. 12. The simulated return loss of the proposed antenna in terms of W_2.

Figure 13 indicates a plot of the simulated R_L of tag for three antennas of different geometrical shapes according to the geometrical parameters of the antenna listed in Table 1. The simulation results shown in the figure were intended to compare the properties and performance among antenna designs: the proposed design, the ones without omega-shape and without the

U-shaped SIRs. The results (Fig. 13) demonstrate that the proposed tag antenna yields better results in terms of R_L, lower than -35 dB compared to other antennas configurations. Therefore, by combining both techniques of design structures (the U-shaped SIR resonator as feeder structure and the Omega-shaped as a radiating body of the antenna) simultaneously overcomes the mismatching problem between the antenna and its chip impedances. Consequently, also solves the antenna size problems. In fact, using the U-shaped SIR resonator as a feeder structure offers an easier controlling method for resonant frequency by adjusting the impedance ratio (the low-impedance to the high-impedance). However, there are rooms to improve better matching techniques between the antenna impedance and the IC chip impedance. Additionally, the omega-shaped insertion turns the resonator length of the dipole antenna shrinkable. The reducible length of the resonator is advantageous in meeting the miniaturization demand of the industry. Overall, researchers found that the proposed design for the tag antenna meets the current engineering demands on the antenna design for RFID applications.

Next, the lumped-element values of the equivalent circuit model of the proposed ICF tag antenna shown in Fig. 2 were optimized using CST design studio modelling, including its material substrate effects. Then, the results were compared with the ones obtained from the 3D full-wave model as illustrated in Fig. 14. The simulated return loss of the tag antenna shown in Fig. 14 were simulated by considering the lumped-element values of chip impedance operating at the frequency of 915 MHz (based on the geometrical parameters in Table 1). Obviously, both the modeled and the full wave simulated results seemed in good agreement, which validates the equivalent circuital model illustrated in Fig. 2. Also, Fig. 14 indicates that the antenna performs well in terms of the achieved return loss, which is lower than -30 dB.

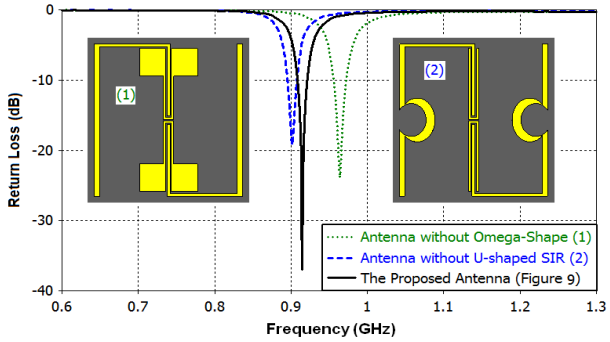

Fig. 13. The simulated return loss results for three various geometrical shapes.

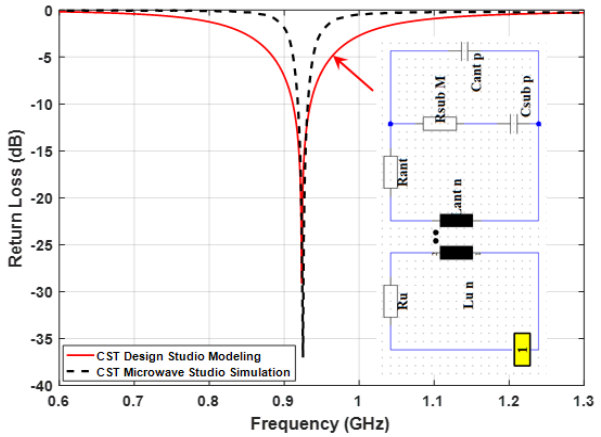

Fig. 14. Comparison between modeled data and full wave simulated results.

Table 1: The antenna designing parameters

Parameter	L	W	W_1	W_2	S_1	S_2	L_{Z1}	L_{Z2}	W_{Z1}	W_{Z2}	r_1	r_2	g
Value (mm)	55.55	50	1.8	1.0	0.5	0.75	15.78	10	0.8	8	5	8	0.5

IV. EXPERIMENTAL RESULTS AND DISCUSSION

In order to conduct standard measurement, a differential probe was utilized in a room environment. The differential probe has a symmetrical structure and it was originally developed by Palmer et al. [33]. Two ports are connected through a fixture with the metal shields of the semi-rigid coaxial cables soldered to build the virtual common ground. After that, the free space measurement was administered connecting the differential probe to a Vector Network Analyzer (Anritsu 37347D model) at one end and then it is soldered to the tag antenna from the other end.

Figure 15 illustrates the comparison between the measured and the simulated impedance results. The former results were achieved after de-embedding the effect of the semi-rigid cables from the reflection and transmission coefficients. And then it was measured at the Sub-Miniature Version A (SMA) connectors applying the technique presented in [33], [34]. Figure 15 shows only a slight difference in the resistance and reactance curves in both measured and simulated results. The main difference observed between these values (Fig. 15) can be attributed to the soldered measurement probe. Another potential explanation is any probable mismatch between the SMA connectors and feeding lines, the potential defects in the fabrication process, and the variations of chip impedance, are usually common in the real implementation. Additionally, Fig. 15 uncovers that the measured and simulated impedances at the center

frequency of 915 MHz are (12.98 + j191.7) Ω and (24.77 + j200.2) Ω, respectively.

In other respects, the present study followed the method for the power reflection coefficient (PRC) analysis described in [35]. The simulated and measured PRC results of the proposed tag antenna with half-power bandwidth (HPBW) are shown in Fig. 16. The HPBW is defined based on the PRC < –3 dB criterion. The simulated and measured HPBW values are 1.97% (906-924 MHz) and 4.35% (900-940 MHz), respectively (their center frequencies are 915 MHz and 919 MHz). The measured results are varied slightly from the simulated results and it might be due to many main reasons such as fabrication process defects, a variation of the chip impedance as well as the soldering imperfection that exists between the differential probe and the tag antenna. In addition, the measurement carried out in a normal room environment, not inside an anechoic chamber. Nonetheless, the results prove that the antenna is working within the standard UHF frequency RFID band between 860 and 960 MHz.

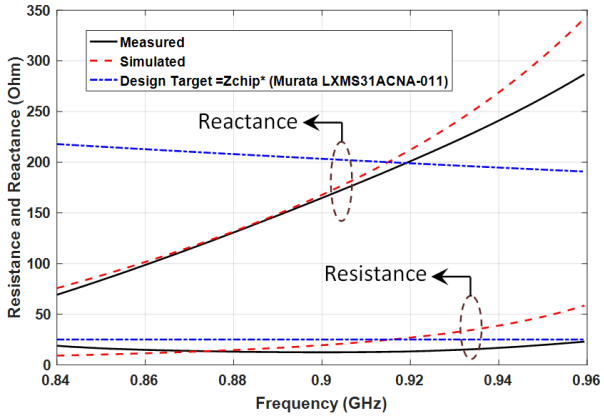

Fig. 15. The measured and simulated impedance.

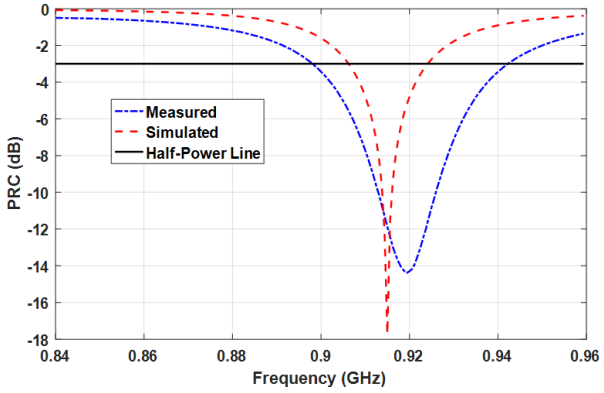

Fig. 16. The power reflection coefficient values in measurement and simulation.

The maximum possible theoretical read range (r_{max}) of the proposed tag antenna can be computed using Friis free-space method [3]:

$$r_{max} = \frac{\lambda}{4\pi}\sqrt{\frac{P_t G_t G_r}{P_{th}}}, \tag{4}$$

where λ is the wavelength, P_t represents the power transmitted by the reader, G_t is the gain of the reader antenna, G_r is the gain of the receiving tag antenna, and P_{th} is the minimum threshold power that required to turn on the chip.

The highest theoretical reading range of the proposed tag antenna calculated using Equation 4 was 5.56 m. To verify the match of the actual reading range with this theoretical value, the measurements were performed at a setting of 30 dBm output power for the reader corresponded to a nearly 4.0 W of equivalent isotropic radiated power (EIRP). With the ATid (AT-870) hand-held reader, the reading range measured 5.1 m, which is approximately 8.2% lower than the maximum theoretical reading range. This difference between the calculated (theoretical) and measured (actual) reading ranges has mainly ascribed the fact that the measurements were taken in the normal room environment.

Figure 17 demonstrates the simulated and measured peak gain of the proposed antenna at the desired UHF RFID frequency band. For further investigation, the simulated radiation efficiency and the far-field radiation pattern of the proposed tag antenna are presented in Figs. 18 and 19, respectively. Besides, the proposed antenna achieves an omnidirectional gain of 1.8 dBi and radiation efficiency of almost 85 % at 0.915 GHz which are higher than those presented in [4]–[6], [11], [13], [14], [18]–[20], [30], [36]. The main improvement of this antenna compared to previous ones is its enhanced performance by ICF using the U-shaped SIRs and the omega shaped design. These parts add inductance to the radiating dipole antenna that does not exist in the conventional feeding techniques such as the coupled open-loop reported in [15].

In order to verify further and highlight the originality of the proposed tag antenna design and feeding configuration, a comparison was made with several recently developed UHF RFID tag antennas in terms of antenna dimensions, gain, and the reading range. The comparisons (Table 2) reveal that the propose one presents size reduction of 20.64%, 30.5%, 7.1%, 32.18%, and 22.84% as compared to the antennas reported in [16], [19], [20], [30], [31], [36], respectively. Furthermore, a higher peak gain is obtained in comparison with tag antennas introduced in [14], [19]–[21], [30], [31], [36] at 915 MHz. Moreover, the proposed antenna shows a longer read range as compared to similar

works in [14], [16], [19], with a better improvement for radiation efficiency. However, the proposed antenna uses the same value of chip impedance (25-j200 Ω) with the antennas reported in [14], [16]. The proposed antenna features a lower read range compared to some existing RFID antennas reported in [20], [21], [30] because of the high minimum threshold power required to turn on the MURATA chip of -8 dBm (160 µW). Using another type of chip may improve the effectiveness in extending the read range further. For instance, some of them may offer lower minimum threshold power (e.g., NXP Ucode8 chip with threshold sensitivity of -20 dBm). Accordingly, the proposed design attracts RFID applications that demand economical choice of compact-sized antennas, an extended reading range, and good performance concerning the gain and radiation efficiency.

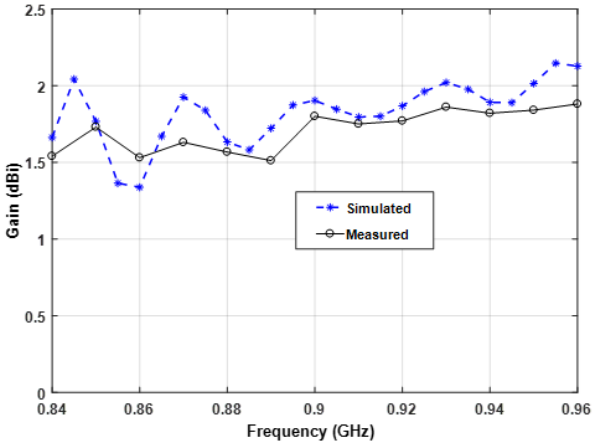

Fig. 17. The measured and simulated realized gain.

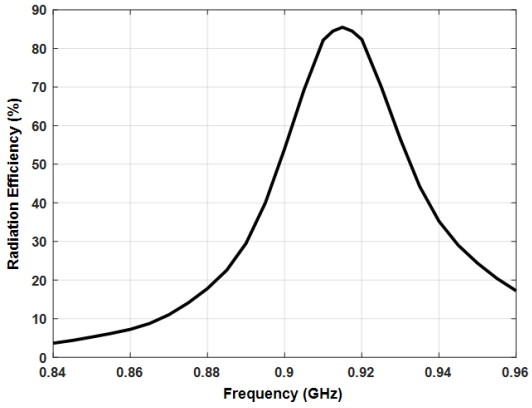

Fig. 18. Simulated antenna radiation efficiency.

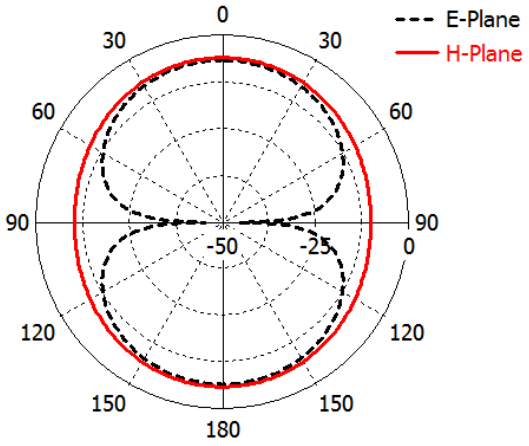

Fig. 19. Simulated far-field radiation pattern at the frequency of 915 MHz.

Table 2: Comparison between the proposed RFID tag antenna and recently developed works

Reference	Chip Impedance (Ω) at 915 MHz	Size (mm^2)	Gain (dBi)	Reading Range (m)
[14]	25-j200	82.75 × 19.5	-0.53	3.72
[16]	25-j200	50 × 70	2.50	4.92
[19]	23-j202	80 × 50	1.75	4.6
[20]	25-j237	115 × 26	2.08	7.5
[21]	24.5-j190	44 × 20	-5.54	5.6
[30]	-	64 × 64	-1.18	10.2
[31]	13.5-j111	60.1 × 60.1	0.25	6.7
[36]	13.5-j111	60 × 60	-9.7	3.36
Proposed Antenna	25-j200	50 × 55.55	1.80	5.1

VI. CONCLUSION

This study develops an omega-shaped tag antenna with ICF using U-shaped SIRs for RFID applications. It consists of two omega-shaped radiating arms that are fed by an innovative method implementing ICF using U-shaped SIRs to reduce the antenna size and improve the gain. It produces an inductance that is equivalent to the radiating dipole antenna. Hence, it offers a transformative method to augment the strength of inductive coupling as well as a simple alternative to perfectly match between antenna and impedance. Furthermore, the simulated and measured results present an omnidirectional peak gain of nearly 1.8 dBi. This peak gain (1.8 dBi) is higher than the peak gains of the traditional antennas recently proposed in [14], [19]–[21], [30], [36]. In addition, the herein proposed tag antenna has a compact size with an

area of just 50×55.55 mm^2. As such, it is 20.64%, 30.5%, 7.1%, 32.18%, and 22.84% smaller in size than the tag antennas proposed recently in [16], [19], [20], [30], [31], respectively. It can be concluded that the tag antenna proposed in this paper has a better overall performance than the other tag antennas due to its higher radiation efficiency, size, gain, and impedance. The overall results of this study suggests turning it into a more desirable design for its potentialities for various applications of the UHF RFID systems.

ACKNOWLEDGMENT

The authors would like to express their gratitude to the Ministry of Education and the Deanship of Scientific Research – Najran University – Kingdom of Saudi Arabia for their financial and technical support under code number (NU/ESCI/16/015).

REFERENCES

[1] H. Li and Y. Ren, "Design and implementation of building structure monitoring system based on radio frequency identification (RFID)," *International Journal of RF Technologies*, vol. 9, pp. 37-49, Aug. 2018.

[2] R.-S. Hsiao, C.-H. Kao, T.-X. Chen, and J.-L. Chen, "A passive RFID-based location system for personnel and asset monitoring," *Technology and Health Care*, vol. 26, pp. 1-6, Oct. 2017.

[3] K. V. S. Rao, P. V. Nikitin, and S. F. Lam, "Antenna design for UHF RFID tags: A review and a practical application," *IEEE Transactions on Antennas and Propagation*, vol. 53, no. 12, pp. 3870-3876, 2005.

[4] E. A. Soliman, M. O. Sallam, W. De Raedt, and G. A. E. Vandenbosch, "Miniaturized RFID tag antenna operating at 915 MHz," *IEEE Antennas and Wireless Propagation Letters*, vol. 11, pp. 1068-1071, 2012.

[5] Z. L. Ma, L. J. Jiang, J. Xi, and T. T. Ye, "A single-layer compact HF-UHF dual-band RFID tag antenna," *IEEE Antennas and Wireless Propagation Letters*, vol. 11, pp. 1257-1260, 2012.

[6] Z.-J. Tang, J. Zhan, Z.-F. Xi, and Y.-G. He, "Broadband UHF RFID tag antenna with a rectangular-loop feed and additional patches," *Microwave And Optical Technology Letters*, vol. 54, no. 5, pp. 1234-1236, 2012.

[7] A. A. Babar, S. Manzari, L. Sydanheimo, A. Z. Elsherbeni, and L. Ukkonen, "Passive UHF RFID tag for heat sensing applications," *IEEE Transactions on Antennas and Propagation*, vol. 60, no. 9, pp. 4056-4064, 2012.

[8] X. Chen, L. Ukkonen, and T. Björninen, "Passive E-textile UHF RFID-based wireless strain sensors with integrated references," *IEEE Sensors Journal*, vol. 16, no. 22, pp. 7835-7836, 2016.

[9] P. Escobedo, M. A. Carvajal, L. F. Capitán-Vallvey, J. Fernández-Salmerón, A. Martínez-Olmos, and A. J. Palma, "Passive UHF RFID tag for multispectral assessment," *Sensors (Switzerland)*, vol. 16, no. 7, 2016.

[10] C. K. Stoumpos, D. E. Anagnostou, and M. T. Chryssomallis, "Experimental characterization of the impedance of balanced UHF RFID tag antennas," *Microwave and Optical Technology Letters*, vol. 59, no. 12, pp. 3127-3134, Dec. 2017.

[11] P. Yang, S. He, Y. Li, and L. Jiang, "Low-profile microstrip antenna with bandwidth enhancement for radio frequency identification applications," *Electromagnetics*, vol. 32, no. 4, pp. 244-253, 2012.

[12] T. Deleruyelle, P. Pannier, M. Egels, and E. Bergeret, "An RFID tag antenna tolerant to mounting on materials," *IEEE Antennas and Propagation Magazine*, vol. 52, no. 4, pp. 14-19, 2010.

[13] A. S. A. Jalal, A. Ismail, A. R. H. Alhawari, M. F. A. Rasid, N. K. Noordin, and M. A. Mahdi, "Miniaturized metal mount Minkowski fractal RFID tag antenna with complementary split ring resonator," *Progress In Electromagnetics Research C*, vol. 39, no. Apr., pp. 25-36, 2013.

[14] F. Erman, E. Hanafi, E.-H. Lim, W. A. W. M. Mahyiddin, S. W. Harun, H. Umair, R. Soboh, and M. Z. H. Makmud, "Miniature compact folded dipole for metal mountable UHF RFID tag antenna," *Electronics*, vol. 8, no. 6, p. 713, 2019.

[15] H.-W. Son and C.-S. Pyo, "Design of RFID tag antennas using an inductively coupled feed," *Electronics Letters*, vol. 41, no. 18, pp. 1-2, 2005.

[16] A. R. H. Alhawari, A. Ismail, A. S. A. Jalal, R. S. A. R. Abudullah, and M. F. A. Rasid, "U-shaped inductively coupled feed radio frequency identification tag antennas for gain enhancement," *Electromagnetics*, vol. 34, no. 6, 2014.

[17] M. S. R. Bashri, M. I. Ibrahimy, and S. M. A. Motakabber, "Design of a wideband inductively coupled loop feed patch antenna for UHF RFID tag," *Radioengineering*, vol. 24, no. 1, pp. 38-44, 2015.

[18] L. Mo and C. Li, "Double loop inductive feed patch antenna design for antimetal UHF RFID tag," *International Journal of Antennas and Propagation*, vol. 2019, 2019.

[19] D. Marques, M. Egels, and P. Pannier, "Broadband UHF RFID tag antenna for bio-monitoring," *Progress In Electromagnetics Research B*, vol. 67, no. 1, pp. 31-44, 2016.

[20] K. Siakavara, S. Goudos, A. Theopoulos, and J. Sahalos, "Passive UHF RFID tags with specific printed antennas for dielectric and metallic objects applications," *Radioengineering*, vol. 26, no. 3, pp.

735-745, 2017.

[21] S. He, Y. Zhang, L. Li, Y. Lu, Y. Zhang, and H. Liu, "High performance UHF RFID tag antennas on liquid-filled bottles," *Progress In Electromagnetics Research*, vol. 165, no. July, pp. 83-92, 2019.

[22] Q.-X. Chu and F.-C. Chen, "A novel dual-band bandpass filter using stepped impedance resonators with transmission zeros," *Microwave and Optical Technology Letters*, vol. 50, no. 6, pp. 1466-1468, Jun. 2008.

[23] Q.-X. Chu and F.-C. Chen, "A compact dual-band bandpass filter using meandering stepped impedance resonators," *Microwave and Wireless Components Letters*, *IEEE*, vol. 18, pp. 320-322, Jun. 2008.

[24] M. Makimoto and S. Yamashita, *Microwave Resonators and Filters For Wireless Communication: Theory, Design and Application*. Berlin: Springer-Verlag, Berlin, Heidelberg, 2001.

[25] O. Altıntaş, M. Aksoy, and E. Ünal, "Design of a metamaterial inspired omega shaped resonator based sensor for industrial implementations," *Physica E: Low-dimensional Systems and Nanostructures*, vol. 116, no. Aug. 2019, p. 113734, 2020.

[26] H. Hatefi Ardakani, S. Fallahzadeh, and J. Rashed-Mohassel, "Phase velocities equalization of coupled microstrip lines using Ω-shaped particles and suppression of the second harmonic," *IEEE Transactions on Microwave Theory and Techniques*, vol. 60, no. 3 PART 1, pp. 464-470, 2012.

[27] M. Labidi, R. Salhi, and F. Choubani, "A design of metamaterial multi-band bowtie antenna based on omega-shaped resonator," *Applied Physics A: Materials Science and Processing*, vol. 123, no. 5, pp. 1-6, 2017.

[28] K. Aydin, Z. Li, M. Hudlička, S. A. Tretyakov, and E. Ozbay, "Transmission characteristics of bianisotropic metamaterials based on omega shaped metallic inclusions," *New Journal of Physics*, vol. 9, 2007.

[29] "Murata." [Online]. Available: https://www.murata.com/products/rfid [Accessed: 08-Oct-2019].

[30] E. Yang and H. Son, "Dual-polarised metal-mountable UHF RFID tag antenna for polarisation diversity," *Electronics Letters*, vol. 52, no. 7, pp. 496-498, 2016.

[31] M. H. Zolghadri and S. Jam, "A wideband circular polarization antenna for UHF tags," *Applied Computational Electromagnetics Society Journal*, vol. 33, no. 3, pp. 319-324, 2018.

[32] "Computer Simulation Technology (CST) Microwave Studio," 2019.

[33] K. D. Palmer and M. W. van Rooyen, "Simple broadband measurements of balanced loads using a network analyzer," *IEEE Transactions on Instrumentation and Measurement*, vol. 55, no. 1, pp. 266-272, 2006.

[34] S. K. Kuo, S. L. Chen, and C. T. Lin, "An accurate method for impedance measurement of RFID tag antenna," *Progress in Electromagnetics Research*, vol. PIER 83, pp. 93-106, 2008.

[35] P. V Nikitin, K. V. S. Rao, S. F. Lam, V. Pillai, R. Martinez, and H. Heinrich, "Power reflection coefficient analysis for complex impedances in RFID tag design," *IEEE Transactions on Microwave Theory and Techniques*, vol. 53, no. 9, pp. 2721-2725, 2005.

[36] U. H. Khan, B. Aslam, J. Khan, M. Nadeem, H. Shahid, M. A. Azam, Y. Amin, and H. Tenhunen, "A novel asterisk-shaped circularly polarized RFID tag for on-metal applications," *Applied Computational Electromagnetics Society Journal*, vol. 31, no. 9, pp. 1035-1042, 2016.

Adam R. H. Alhawari was born in Irbid, Jordan. In 2003, he was awarded a B.Sc. degree in Communication Engineering by Hijjawi Faculty for Engineering Technology at Yarmouk University, Jordan. He obtained both postgraduate degree of M.Sc. and Ph.D. degrees in 2009 and 2012, respectively, in Wireless Communications Engineering from Universiti Putra Malaysia. Previously, he started the entry level with the post of Senior Lecturer in Universiti Putra Malaysia from 2012 to 2015. Currently, he was promoted to the Associate Professorship in the Electrical Engineering Department, College of Engineering, Najran University, Saudi Arabia. His main research interests are microstrip filters, metamaterial antennas, and RFID.

A. H. M. Almawgani was born in Ibb, Yemen, in 1979. He received the B.Sc. degree in Information Engineering from the College of Engineering in Baghdad University in 2003. He received the M.Sc. and Ph.D. degrees in Electronic Systems Design Engineering and Communication Engineering from Universiti Sains Malaysia, in 2008 and 2011, respectively. He was an Assistant Professor in the Electrical Engineering Department, Faculty of Engineering, University of Science and Technology, Sana'a, Yemen, until February 2014. Currently, he is an Associate Professor in the Electrical Engineering Department, College of Engineering, Najran

University, Saudi Arabia. His main research interests are signal-processing algorithms with application to telecommunications and wireless communication networks.

Hisham Alghamdi received his M.Sc. degree in Electrical and Electronics Engineering from the University of Leicester, Leicester, UK, in 2010 and his Ph.D. from University of Southampton 2016, respectively. Currently, he is working as an Assistant Professor in the Electrical Engineering Department at Najran University, Saudi Arabia. His main research areas are in solar energy, building energy technologies and systems, energy efficiency, sustainable and resilient cities, smart grids and energy and environment policies.

Ayman T. Hindi received his B.S. in Electrical Engineering from Vinnitsa Technical University in 1995 and Ph.D. degree in Power Systems Engineering from Vinnitsa Technical University in 2004. Currently he is an Assistant Professor at the Electrical Engineering Department, Najran University, Saudi Arabia. His main research interests include compensation of reactive power energy and consumption in electric installation and systems.

Tale Saeidi was born in Mashhad, Iran in 1985. He received his Bachelor of Science degree in Telecommunication and Electrical Engineering from Khayam University of Mashhad, Iran in 2009 and he completed his Masters in Wireless Communication Engineering from Universiti Putra Malaysia in 2015. Currently, he is working as a Graduate Assistant in Universiti Teknologi Petronas, Malaysia. His research interest includes dielectric measurement of MW absorber materials, microstrip antenna design for MW, mm-wave and THz frequency bands. Furthermore, metamaterial array UWB antennas in MW and UWB imaging.

Alyani Ismail received her Bachelor of Engineering in Electronic and Information Systems Engineering from the University of Huddersfield, UK. She obtained her M.Sc. in Computer, Communication and Human-Centered Systems from the University of Birmingham, UK and Ph.D. in Electronics Engineering also from the University of Birmingham. She is currently a Professor at the Department of Computer and Communication Systems Engineering, Faculty of Engineering, Universiti Putra Malaysia (UPM). Alyani's research interests are in the area of Communication Engineering, Wireless Sensors and antenna systems.

Scattering Characteristic Extraction and Recovery for Multiple Targets Based on Time Frequency Analysis

Xiangwei Liu [1], Jianzhou Li [1], Yi Zhu [1], and Shengjun Zhang [2]

[1] School of Electronics and Information
Northwestern Polytechnical University, Xi'an, 710129, China
lxw1218@mail.nwpu.edu.cn, ljz@nwpu.edu.cn, 958637071@qq.com

[2] National Key Laboratory of Science and Technology on Test Physics & Numerical Mathematical
Beijing, 100076, China
Zhangsj98@sina.com

Abstract ─ The multi-target scattering field consists of the scattering fields of each target, but it is difficult to know the scattering characteristics of the specific target from the total scattering field. However, the scattering characteristics of single target embedded in the total scattered field have important research significance for target recognition and detection. In this paper, a method is proposed to extract and recover each target's scattering characteristics from the total scattering field of multiple targets. The theoretical basis of the method is that the scattering echoes corresponding to different targets reach the receiver at different time. We acquire the total scattering field at first. Then, we perform the signal processing with time-frequency analysis to obtain the arrival time of different scattering echoes. According to the time slot difference, the time domain signal of each target can be extracted to recover its scattering field. Several examples validate the proposed method.

Index Terms ─ Extraction and recovery, radar detection, scattering characteristic, time-frequency analysis.

I. INTRODUCTION

Since the scattering field of multi-target is redundant and aliased, it is very difficult to obtain the individual scattering characteristics of each target from the total scattering field. However, the scattering characteristic of each target is of great significance for target recognition and radar detection [1-4]. In this paper, we extract and recover scattering characteristics from the total scattering field with time-frequency analysis. Time-frequency analysis is used in [5] and [6] to process radar imaging to reduce multiple scattering and clutter in radar images, based on the principle that different scattering echoes have different resolutions. Time-frequency analysis is also used in [7] to process the target's scattering field to suppress the scattering centers caused by the coupling effect in radar imaging. All of them have used time-frequency analysis only to improve the probability of radar recognition. [8] uses the linear frequency-modulated continuous-wave radar system and Gabor-Wigner transform to realize the recognition of multiple targets, which realizes the detection of the number of multiple targets. [9] also uses linear frequency-modulated continuous-wave radar system to achieve the detection of the speed and distance of each target in multiple targets. In the field of multi-target detection, the existing work is mostly to design radar detection systems or methods to improve the detection efficiency and accuracy of multiple targets [10-14], which mainly detects the number, speed, and direction. [15-17] use image processing methods to extract the scattering center in radar imaging, and use the extracted scattering center to rebuild the local scattering characteristics of the target. They depend on the radar images of the target and cannot extract and recovery the scattering characteristics of the target through only one-dimensional data. In this paper, we focus on extracting and recovering the individual scattering characteristics of each target from the multi-target's total scattering field, which has very great significance for multi-target recognition.

The paper is organized as follows. In Section II, we introduce the theoretical basis of the method and its numerical realization. In Section III, some results are presented, and we use specific examples to illustrate how to extract the scattering field. Some conclusions are made in Section IV.

II. EXTRACTION AND RECOVERY FORMULATIONS

In this section, we represent the theory and the process of the extraction and recovery method. In multiple target scattering case, times for scattering echoes of different targets to reach the receiver are

Submitted On: May 13, 2020
Accepted On: June 29, 2020

https://doi.org/10.47037/2020.ACES.J.350816

different. However, when the distance between two targets is very close, it is difficult to distinguish the time difference in testing, so the scattering field received by the radar is usually the total scattering field, i.e., the mixed scattering field of multiple targets. However, this time slot difference can be used to achieve the extraction and recovery of the scattering characteristics of different targets from the total scattered field in simulation. For instance, the distance between the *i*-th target and the radar is D_i, and the time from the electromagnetic wave being transmitted to it being received by the radar is $T_i = 2D_i/c$, where c is the speed of light in free space. There is a time slot difference ΔT_i between the times when the scattering echoes from different targets reach the radar:

$$\Delta T_i = 2\left|\frac{D_i - D_{i+1}}{c}\right|. \tag{1}$$

The total scattered E field E_s of multiple targets is obtained by calculation or experiment.

We perform Short-Time Fourier Transform (STFT) [18] on the scattering field E_s to obtain the time difference, which is defined as (2):

$$STFT_s(t,\omega) = \int_{-\infty}^{+\infty} E_s(\tau)h(\tau - t)\mathrm{e}^{-\mathrm{j}\omega\tau}\mathrm{d}\tau\,. \tag{2}$$

The window function $h(t)$ is a Kaiser window in (2), which is defined as (3):

$$h(n) = \begin{cases} \dfrac{J_0\left[\beta\sqrt{1-(2n/N)}\right]}{J_0(\beta)}, & |n| < \dfrac{N}{2}, n = -\dfrac{N}{2} \\ 0, & |n| > \dfrac{N}{2}, n = \dfrac{N}{2} \end{cases}, \tag{3}$$

where J_0 is 0th-order Bessel function of the first kind, n and N are the width of the window function and the length of the signal, respectively. β is a parameter used to adjust the performance of the window function.

Afterwards, the time domain signal $R(t)$ consisting of multiple peaks at ω_i in $STFT_s(t,\omega)$ is extracted:

$$R(t)\big|_{\omega=\omega_i} = STFT_s(t,\omega)\,. \tag{4}$$

$R(t)$ is a time-domain signal composed of multiple peaks, we can simplify it as (5) and the times corresponding to different peaks are the time when the scattering signal of different targets are received:

$$\begin{aligned} R(t) &= P(\Delta t_1) + P(\Delta t_2) + \cdots \\ &\quad + P(\Delta t_i) + \cdots + P(\Delta t_l)\,, \end{aligned} \tag{5}$$

where $P(\Delta t_i)$ is the peak occupying the time period of Δt_i, l is the number of peaks that $R(t)$ has.

Since the scattering echo of a scatterer may correspond to multiple peaks, the group delay processing, defined as (6), is performed on the scattering field before STFT for better observing the time slot difference [15]:

$$E_s^{'} = E_s \bullet \mathrm{e}^{-\mathrm{j}2\pi f_i d}\,, \tag{6}$$

where d is the group delay time, and $E_s^{'}$ is the scattering data obtained after group delay processing.

We extract the $P(\Delta t)$s, which is the set of peaks belonging to the same scatterer from $R(t)$, and fill them with zero at the default time, so that the length of the reconstructed signal $R^{'}(t)$:

$$R^{'}(t) = P(\Delta t)\mathrm{s} + Z(t - \Delta t)\,, \tag{7}$$

and remain the same with $R(t)$. In (7), $Z(t-\Delta t)$ is the zero signal at the occupied time of other peaks. For the time-domain signal, there is no good way to identify different scatterers correspond to each peak in $R(t)$. However, in principle, we can distinguish each peak in this way. The larger the amplitude of the peak, the earlier the corresponding scattering echo reaches the receiver, since the EM wave is continuously attenuated during the propagation. And, the larger the peak, the larger the volume of the corresponding scatterer.

Finally, the extracted scattering signals are reconstructed with the Inverse Short-Time Fourier Transform (ISTFT) defined as (8) [18]. Thus, the scattered fields of each target in multiple targets can be recovered:

$$S(t) = \frac{1}{2\pi}\int_{-\infty}^{+\infty}\int_{-\infty}^{+\infty} STFT_s(\omega,\tau)\mathrm{e}^{\mathrm{j}\omega t}\mathrm{d}\omega\mathrm{d}\tau\,. \tag{8}$$

The steps of extraction and recovery of scattering characteristics mainly include (see Fig. 1).

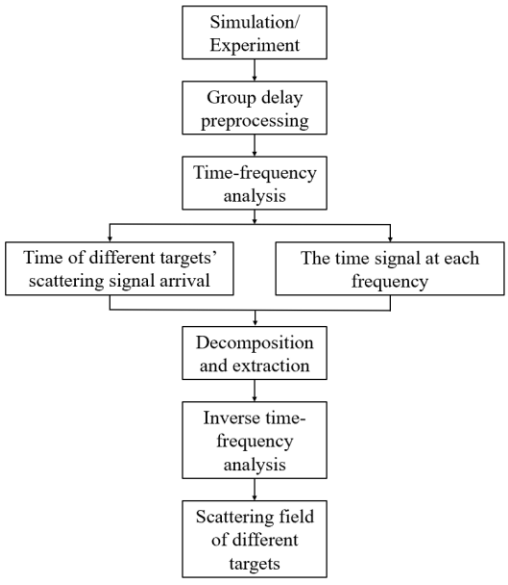

Fig. 1. The steps of extraction and recovery of scattering characteristics.

The range resolution $\Delta r = c/2B$ needs to meet certain conditions. Where B is the frequency bandwidth. Firstly, the resolution needs to be smaller than the size of the target. If the resolution is larger than the size of the target, we cannot observe the scattering echo corresponding to the target in the time-domain signal. Secondly, the resolution also needs to be smaller than the distance between the targets. This is because when the resolution is greater than the separation between objects, the scattering echoes of different objects in the time-domain signal will overlap, which is not conducive to the extraction and recovery of their scattering characteristics.

III. NUMERICAL EXAMPLES

In this section, we explain in detail the method for extraction and recovery of the scattering characteristics through several examples. The incident wave in the paper is horizontally polarized.

A. Double PEC spheres

Firstly, we use double-PEC spheres shown in Fig. 2 to specifically explain the application of this algorithm for scattering characteristic extraction and recovery of different targets. The diameter of the big ball is 1m, and the diameter of the small ball is 0.1m. The Shooting and Bouncing Ray (SBR) algorithm is used to calculate their scattering field [19-20]. The incident direction is $\theta = 20^{\circ}, \varphi = 0^{\circ}$, where θ is the angle between the incident wave and z axis, φ is the angle between the projection of the incident wave on the xoy plane and x axis, and the frequency is from 3GHz to 6 GHz, with 0.05 GHz interval, and the range resolution $\Delta r = 0.05m$ is smaller than the diameter of the small sphere. The radar cross section (RCS) is shown in Fig. 3.

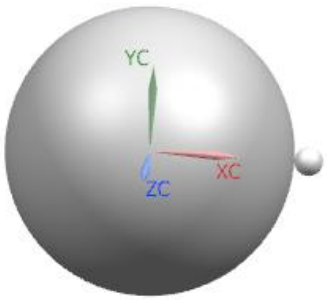

Fig. 2. The double PEC spheres.

Then, group delay is performed on the scattering field to obtain $E_s^{'}$, where $d = 9\times10^{-9}$s. Afterwards, we perform the STFT on the $E_s^{'}$ with $n = 61, \beta = 6$, and these parameters are designed to maximize the resolution of time-frequency analysis.

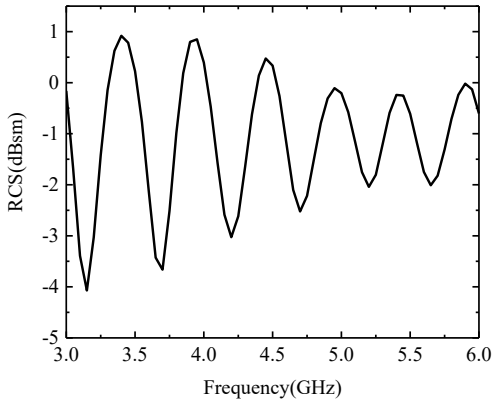

Fig. 3. The RCS of double PEC spheres.

The time-frequency analysis result is shown in Fig. 4 (a). In addition to the two strong scattering echoes, there are obvious smears in Fig. 4 (a). The scattering of the big sphere produces the strongest scattering echo, and the scattering of the small one corresponds to the second strong echoes, while the multiple scattering between the double spheres produces weaker scattering echo and smears [21].

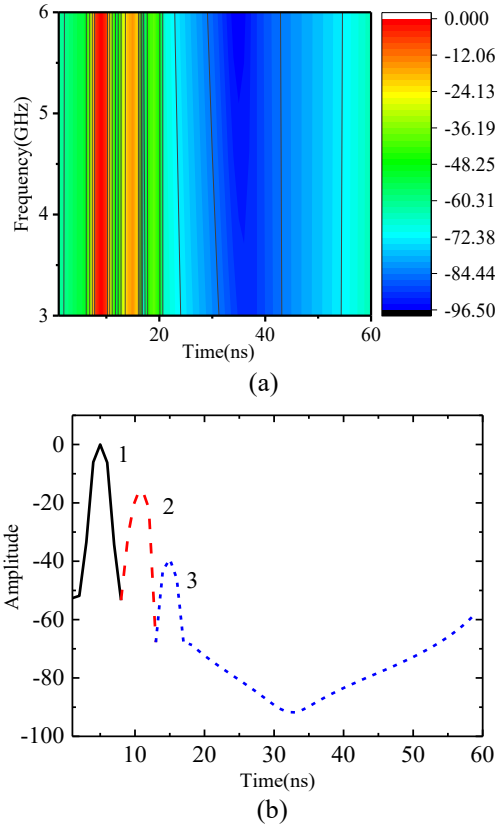

Fig. 4. The time domain signal extracted from the time-frequency result. (a) The time-frequency analysis result, and (b) the extracted time domain signal.

We extract the time domain signal $R(t)$ from the time-frequency analysis result at 6GHz, which is shown in Fig. 4 (b). In $R(t)$, there are three peaks, and they can be decomposed according to the time occupied by themselves. The peak1 indicates the time when the echo by the big sphere reaches the radar, the peak2 is occupied by the small sphere, and the peak3 occupies the time of multiple scattering echoes between the two spheres reaching the radar. When the range resolution cell contains different scatterers, these corresponding scattering echo will be mixed together and appear in the same peak of the time domain signal. Therefore, after we extract the scattering field of such peak in $R(t)$, the extracted scattering field will contain the fore mentioned multiple scatterers' scattering characteristics, and this will cause the extraction and recovery failure in this case.

We do the same for every time domain signals in the time-frequency analysis result. After that, it's necessary to extend the length of extracted signals to N by 'zero padding', and then they are processed with ISTFT to obtain the scattering characteristics corresponding to different targets.

We calculate the scattering field of the big sphere by SBR with the same parameters, and compare the calculated scattering field with the extracted one to verify the validity of the recovered scattered field.

The RCSs of the double spheres and the large sphere are shown in Fig. 5. In Fig. 5, due to the existence of the small sphere, the RCSs of the double-PEC spheres and the large sphere are quite different, with a maximum difference of nearly 3dB. The recovered RCS of the large sphere and its calculated RCS are in good agreement from 3.1GHz to 5.8GHz, which shows that peak1 corresponds to the scattering field of the large sphere. Since the side lobe of the window function $h(t)$ used in STFT is large, so they do not match well at both ends of frequency. This can be improved by using different window functions.

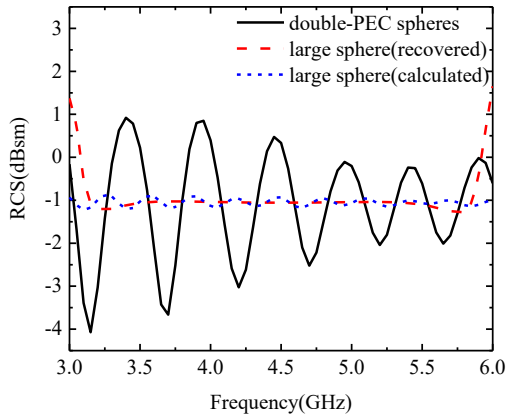

Fig. 5. The comparison of RCSs.

Calculate the scattering E field of the double PEC spheres from $\theta=20^{\circ},\varphi=180^{\circ}$ to $\theta=20^{\circ},\varphi=0^{\circ}$ with 0.67° interval, and the frequency from 3 GHz to 6GHz, with 0.05 GHz interval, and the radar image of the double PEC spheres is shown in Fig. 6 (a), in which there are two scattering centers according to different spheres [22-23]. It is easy to know that the scattering center located at (20,20) corresponds to the large sphere and the scattering field of the small sphere forms the scattering center located at (20,30).

Similarly, we perform the decomposition process on the scattering field at every angle, and image the extracted and recovered scattering fields individually as shown in Figs. 6 (b) and (c). The scattering E fields of the large sphere and the small sphere are recovered well.

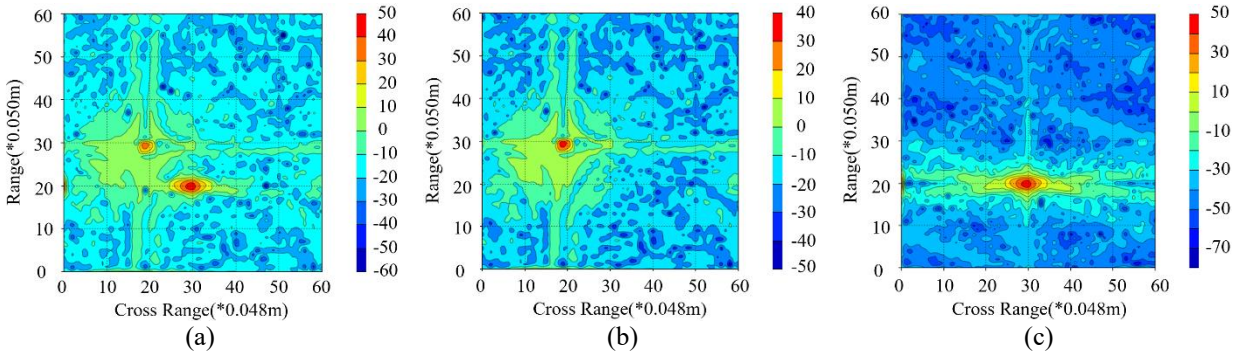

Fig. 6. The radar images of different spheres (calculated and recovered). (a) The double PEC spheres (calculated), (b) the small PEC sphere (recovered), and (c) the big PEC sphere (recovered).

B. Plane with corner reflector

A plane can disguise its own scattering characteristic by emitting a corner reflector as shown in the Fig. 7. Here a plane about 16m long and 10m meters wide, and a 1.5m corner reflector, are shown in Fig. 7. The SBR algorithm is used to calculate the scattering E field at $\theta=0^{\circ},\varphi=0^{\circ}$,

and the frequency is from 1.5GHz to 4.5 GHz, with 0.005 GHz interval. The RCS is shown in Fig. 8.

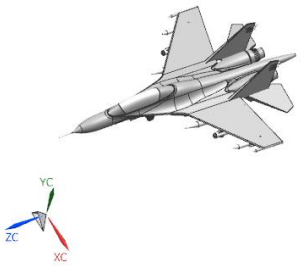

Fig. 7. Plane with corner reflector

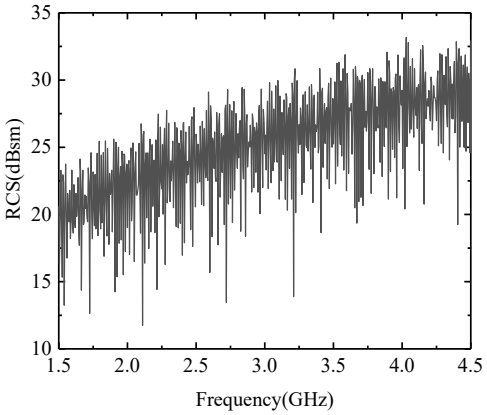

Fig. 8. The RCS of the plane with corner reflector.

The scattering E field is recovered according to the proposed method. In order to verify the accuracy of the recovered field, the RCS of the plane without the corner reflector is calculated with the same calculating parameters. The calculated and recovered RCSs of the plane are shown in Fig. 9.

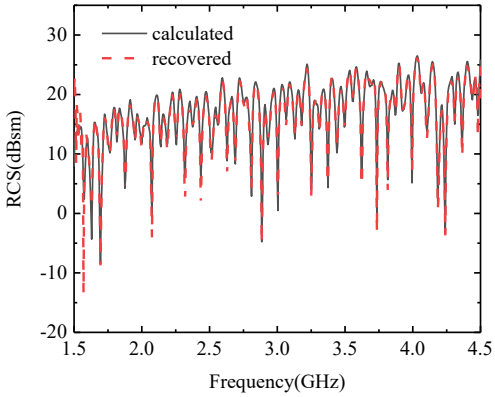

Fig. 9. The calculated and recovered RCSs of the plane.

The two RCS curves in Fig. 9 match very well, which demonstrates that the scattering characteristic of the plane is well recovered and the influence of the corner reflector is eliminated.

Similarly, we calculate the radar image of the plane with the corner reflector, which is shown in Fig. 10 (a). The angle range is form $\theta=-30^{\circ},\varphi=0^{\circ}$ to $\theta=30^{\circ},\varphi=0^{\circ}$, with 0.1° interval, and the frequency is from 1.5GHz to 4.5GHz, with 0.005 GHz interval.

In Fig. 10 (a), the scattering center located at (300,300) is generated by the corner reflector and the scattering centers located at upper area correspond to the plane. Figures 10 (b) and (c) are the radar images of the recovered scattering fields of the plane and the corner reflector respectively, which demonstrate the total scattering filed is decomposed well.

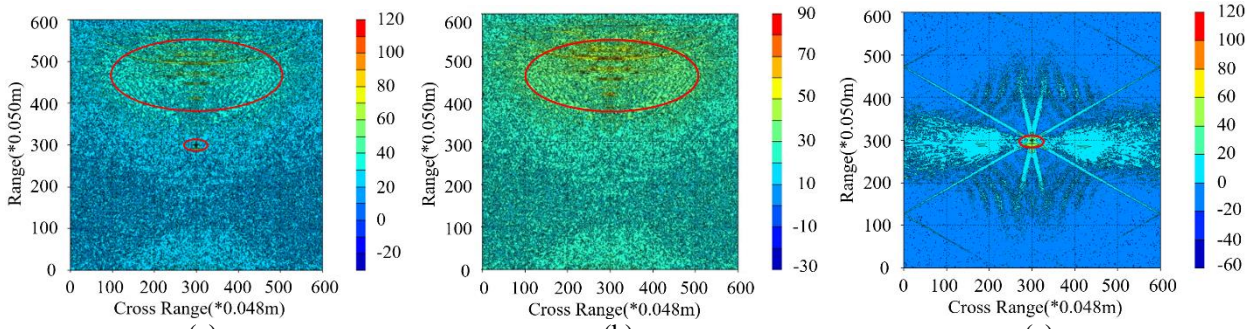

Fig. 10. The radar images of plane and corner reflector (calculated and recovered). (a) Plane with corner reflector (calculated), (b) plane without corner reflector (recovered), and (c) corner reflector (recovered).

C. Target array

As shown in Fig. 11, three types of targets form a target array. The space occupied by the target array is approximately $9\text{m}\times11\text{m}$.

The SBR algorithm is used to calculate the scattering field of the target array at $\theta=-30^{\circ},\varphi=0^{\circ}$, and the frequency is from 1.5GHz to 4.5 GHz, with 0.01 GHz interval. The result is shown in Fig. 12.

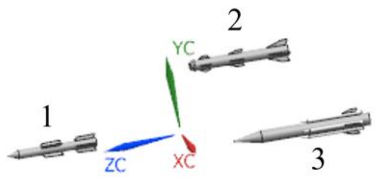

Fig. 11. The target array.

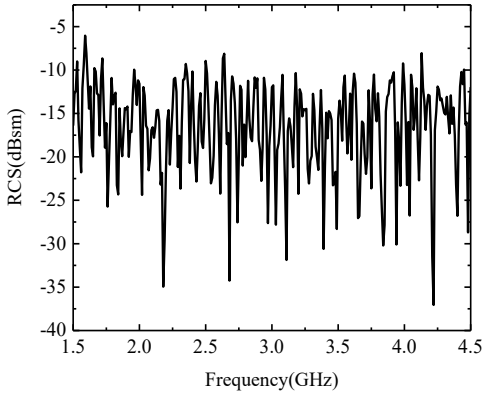

Fig. 12. The RCS of the target array.

We process the total scattering field to recover the scattering fields of each targets. Simultaneously, we calculate the scattering characteristics of each targets separately, and compare the recovered results with the calculated ones as shown in Fig. 13. The respective comparison of target 1 and target 2 are very consistent, indicating that their scattering fields recovered from the total scattering field are very accurate.

However, there is a significant difference between the calculated and the recovered RCS of target 3 in Fig. 13 (c). This is because part of target 3 is blocked by target 1 at $\theta=-30^{\circ},\varphi=0^{\circ}$, which is quite different from the calculated result in which there is no shielding effect from other object.

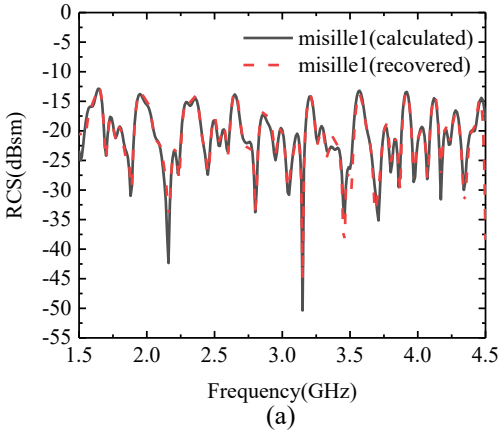

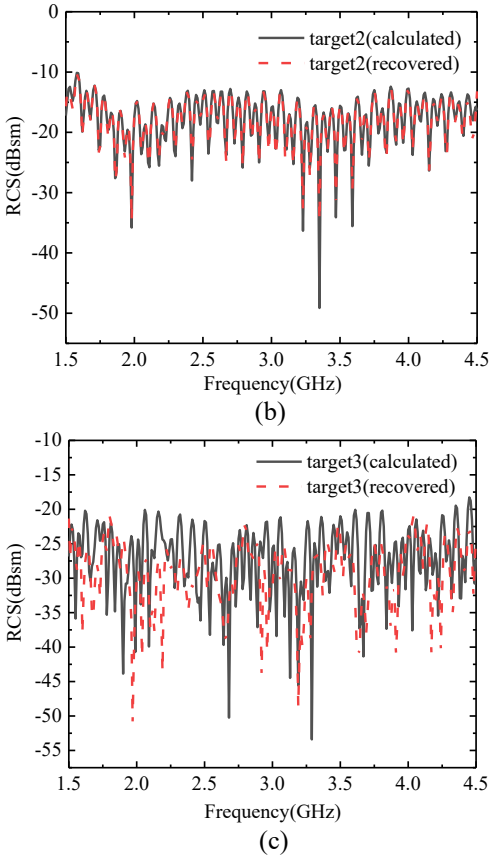

Fig. 13. The calculated and recovered RCSs of each target: (a) target 1, (b) target 2, and (c) target 3.

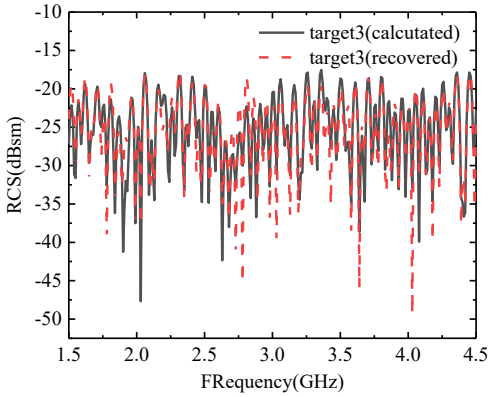

Fig. 14. The calculated and recovered RCSs of target 3 at $\theta=30^{\circ},\varphi=0^{\circ}$.

In order to verify such analysis, we recalculate the scattering fields of the target array and target 3 respectively at $\theta=30^{\circ},\varphi=0^{\circ}$, and the recovered and calculated RCSs of target 3 are shown in the Fig. 14, which shows good agreement. Therefore, to recover the

true scattering characteristics of each target in target array, it is necessary to obtain scattering fields at multiple angles to prevent the target from being shadowed.

D. The test double-PEC spheres

The double-PEC spheres as shown in Fig. 15 are measured in a chamber to obtain the scattering field. The large metal sphere has a diameter of 300mm. The small metal sphere has a diameter of 116mm. The distance between the two spheres is 38mm. The angular is from $\theta = 20^{\circ}, \varphi = 180^{\circ}$ to $\theta = 20^{\circ}, \varphi = 0^{\circ}$, with 1° interval, and the frequency is from 6GHz to 12GHz, with 0.15GHz interval, and the measured radar image of the test double-PEC sphere is shown in Fig. 16.

Fig. 15. The test double-PEC spheres.

In Fig. 16, there are three scattering centers. The scattering center at (13,15) is formed by the scattering of the large sphere, while the scattering field of small sphere forms the scattering center at (22,18). The scattering center at (20,20) is caused by multiple scattering between the double spheres [24]. Despite the interference of multiple scattering, the proposed method can still effectively extract and recovery the scattering characteristics of each sphere.

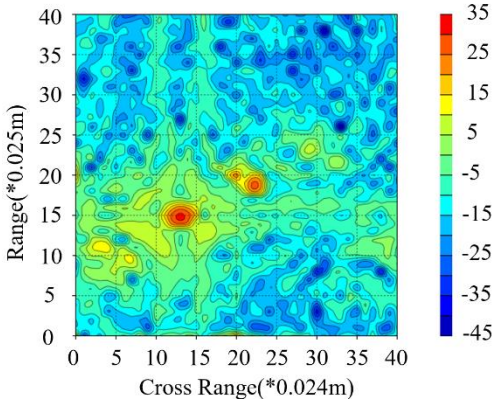

Fig. 16. The radar image of the test double-PEC spheres.

We use the proposed method to deal with the measured scattering field of the double spheres, and extract and recover the scattering fields of the large and small spheres respectively from the total scattering field. Because the scattering mechanism contained in the measured scattering field is more complicated than the calculated one, we directly image the extracted scattering field to observe whether the scattering field has been accurately extracted and recovered.

The recovered scattering fields of the large and small spheres are imaged as shown in Figs. 17 (a) and (b) respectively, which shows that the double spheres' total scattering field is well decomposed, and we have completely extracted the large and small spheres' scattering fields from it, and accurately recovered their scattering characteristics.

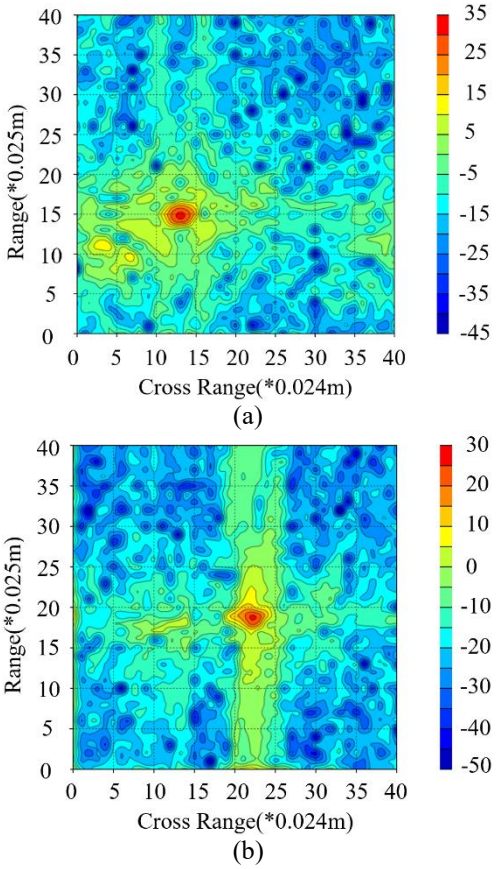

Fig. 17. The rebuild radar images: (a) the large sphere, and (b) the small sphere.

In addition, we extract multiple scattering from the total scattering field, which is imaged in Fig. 18. Extracting different scattering mechanisms from the total scattering field is also of great significance for deep understanding and further controlling of the scattering characteristics, and has a wide range of applications in radar detection such as to improve the accuracy in the target recognition based on radar image.

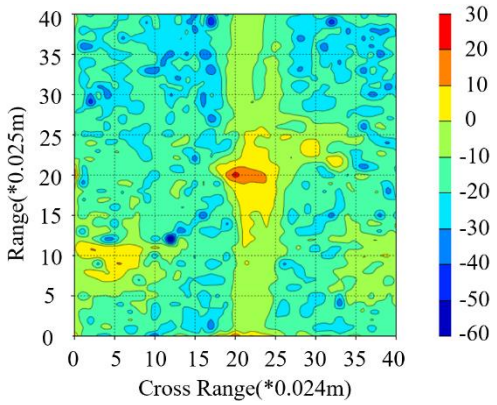

Fig. 18. The radar image of the multiple scattering.

VI. CONCLUSION

In this paper, we extract and recover the scattering characteristics from the total scattered filed of multiple targets based on time-frequency analysis to determine the time of each scattering echoes arrival. For the double PEC spheres, the plane with corner reflector, the target array, and the test double PEC spheres, their scattering characteristics are well recovered, indicating that the proposed method is very useful for scattering field decomposition, and is also of great significance for complex target's electromagnetic scattering cognition and feature recognition.

ACKNOWLEDGMENT

This work is partially supported by the Seed Foundation of Innovation and Creation for Graduate Students in Northwestern Polytechnical University (CX2020160).

REFERENCES

[1] B. Y. Ding, G. J. Wen, X. H. Huang, J. R. Zhong and C. H. Ma, "Target recognition in SAR images via Gaussian mixture modeling of attributed scattering center set," *2016 CIE International Conference on Radar*, Guangzhou, China, Oct. 10-13, 2016.

[2] S. R. Cloude and E. Pottier, "A review of target decomposition theorems in radar polarimetry," *IEEE Transactions on Geoscience and Remote Sensing*, vol. 34, no. 2, pp. 498-518, 1996.

[3] S. P. Xiao, G. R. Guo, Z. W. Zhuang, and M. Y. Luo, "Radar target modeling and recognition based on scattering centers," *Proceedings of National Aerospace and Electronics Conference*, Dayton, OH, USA, May 23-27, 1994.

[4] D. F. Fuller, "Phase History Decomposition for efficient Scatterer Classification in SAR Imagery," *Dissertations & Theses - Gradworks*, vol. 4, no. 8, pp. 921-922, 2011.

[5] E. Giusti, M. Martorella, and A. Capria, "Polarimetrically persistent scatterer based automatic target recognition," *IEEE Transactions on Geoscience and Remote Sensing*, vol. 49, no. 11, pp. 4588-4599, 2011.

[6] T. T. Feng, L. X. Guo, and Y. Zhang, "Inverse synthetic aperture radar imaging of maneuvering targets based on joint time-frequency analysis," *2016 IEEE International Geoscience and Remote Sensing Symposium*, Beijing, China, 2016.

[7] M. Q. Ren and Y. H. Tian, "Radar signal cognition based on time-frequency transform and high order spectra analysis," *2017 IEEE International Conference on Signal Processing, Communications and Computing*, Xiamen, China, 1-4, 2017.

[8] C. Özdemir, *Inverse Synthetic Aperture Radar Imaging with MATLAB Algorithms*. John Wiley & Sons Inc., 2012.

[9] L. Su, H. S. Wu, and C. C. Tzuang, "2-D FFT and time-frequency analysis techniques for multi-target recognition of FMCW radar signal," *Asia-Pacific Microwave Conference 2011*, Melbourne, VIC, USA, Dec. 5-8, 2011.

[10] W. Z. Yan, F. W. Kong, and P. C. Hu, "Algorithm and DSP design of LFMCW radar for multiple," *2018 National Microwave Millimeter Wave Conference*, Chengdu, China, 6, May 2018.

[11] Y. Z. Fan, Z. L. Yang, and X. Y. Bu, "Radar waveform design and multi-target detection in vehicular applications," *2015 International Conference on Estimation, Detection and Information Fusion (ICEDIF)*, Harbin, China, Jan. 10-11, 2015.

[12] L. H. Fan, Y. M. Pi, and S. J. Huang, "Multi-target imaging processing algorithms of ISAR based on time-frequency analysis," *2006 CIE International Conference on Radar*, Shanghai, China, Oct. 16-19, 2006.

[13] P. C. Guo, Z. Liu, and J. J. Wang, "HRRP multi-target recognition in a beam using prior-independent DBSCAN clustering algorithm," *IET Radar, Sonar & Navigation*, vol. 13, no. 8, pp. 1366-1372, 2019.

[14] H. Jiang, X. H. Tang, W. Lv, and Y. Li, "Blind multi-target detection for bistatic MIMO radar based on random matrix theory," *2015 IEEE China Summit and International Conference on Signal and Information Processing*, Chengdu, China, July 12-15, 2015.

[15] J. Z. Li, C. Q. Fan, L. Liu, W. Z. Wang, and X. Y. Wang, "Radar target characteristic extraction and rebuilding of multi-target based on scattering center," *2017 Sixth Asia-Pacific Conference on Antennas and Propagation (APCAP)*, Xi'an, China, 2017.

[16] S. Cui, S. Li, and H. Yan, "A method of 3-D scattering center extraction based on ISAR images," *2016 IEEE International Conference on Electronic Information and Communication Technology (ICEICT)*, Harbin, China, 2016.
[17] Y. S. Lin, L. Zhang, A. K. Xue, D. Peng, and Z. Jin, "SAR imagery scattering center extraction and target recognition based on scattering center model," *2006 6th World Congress on Intelligent Control and Automation*, Dalian, China, 2006.
[18] S. Qian, *Introduction to Time-Frequency and Wavelet Transforms*. China Machine Press, 2005.
[19] T. Q. Fan, L. X. Guo, B. Lv, W. Liu, "An improved backward SBR-PO/PTD hybrid method for the backward scattering prediction of an electrically large target," *IEEE Antennas and Wireless Propagation Letters*, vol. 15, pp. 512-515, 2016.
[20] Y. An, Z. Fan, D. Ding, and R. Chen, "FPO-based shooting and bouncing ray method for wide-band RCS prediction," *The Applied Computational Electromagnetics Society Journal*, vol. 29, no. 4, 2014.
[21] S. M. Yucedag and A. Kizilay, "Time domain analysis of ultra-wide band signals from buried objects under flat and slightly rough surfaces," *The Applied Computational Electromagnetics Society Journal*, vol. 28, no. 8, 2013.
[22] K. T. Kim amd H. T. Kim, "Two-dimensional scattering center extraction based on multiple elastic modules network," *IEEE Transactions on Antennas and Propagation*, vol. 51, no. 4, pp. 848-861, 2003.
[23] B. Y. Ding, G. J. Wen, X. Huang, C. Ma, and X. Yang, "Target recognition in synthetic aperture radar images via matching of attributed scattering centers," *IEEE Journal of Selected Topics in Applied Earth Observations and Remote Sensing*, vol. 10, no. 7, pp. 3334-3347, 2017.
[24] J. Z. Li and X. W Liu, "Decomposition of scattering mechanisms based on time slot difference," *Systems Engineering and Electronics*, vol. 42, no. 3, pp. 513-520, 2020.

Xiang-Wei Liu is currently pursuing Master in Electromagnetic Fields and Microwave at Northwestern Polytechnical University. His current research direction is target electromagnetic scattering decomposition, target scattering characteristics evaluation and complex target modeling.

Jian-Zhou Li is an Associate Professor in Northwestern Polytechnical University. He received the Ph.D. degree in 2005 in Northwestern Polytechnical University. He was a postdoctoral researcher at University of Surrey during 2008-2009. His research interests focus on electromagnetic modeling and simulation.

Yi Zhu is currently pursuing Master in Electromagnetic Fields and Microwave at Northwestern Polytechnical University. His current research direction is electromagnetic calculation of dielectric coating target and complex target modeling.

Sheng-Jun Zhang is a Researcher in National Key Laboratory of Science and Technology on Test Physics & Numerical Mathematical, and his research direction is target feature control technology.

Wideband Microstrip Patch Antennas with Transverse Electric Modes

Tanzeela Mitha and Maria Pour

Department of Electrical and Computer Engineering
The University of Alabama in Huntsville, Huntsville, AL, 35899
tm0078@uah.edu, maria.pour@uah.edu

Abstract ─ A wideband microstrip patch antenna, exciting the fundamental transverse electric (TE) mode, is investigated. The excitation of the TE mode is facilitated through replacing both of the patch and ground plane of a conventional microstrip antenna with artificial magnetic conductors (AMC), consisting of unipolar compact photonic bandgap (UC-PBG) unit cells. The AMC patch and the ground plane of this antenna behave as magnetic conductors within the bandgap region of the unit cells. Similar to conventional patch antennas, it is shown that by cutting a U-shaped slot in the AMC patch, wideband characteristics are realized. The antenna shows a 40% impedance bandwidth and operates at the TE_{10} mode. Moreover, the width of the patch is 1.75 times smaller than its length, reducing the overall size of the antenna by about 60%, compared with the conventional U-slot PEC antenna supporting the transverse magnetic (TM) mode.

Index Terms ─ Microstrip patch antennas, transverse electric modes, wideband antennas.

I. INTRODUCTION

Microstrip patch antennas are narrowband antennas with a maximum bandwidth of 3-6% [1-3]. In emerging wireless communications and radar systems, however, large bandwidths are necessary to transmit massive amounts of data and to enhance the resolution in radar systems. The U-slot technique is used to enhance the bandwidth of a microstrip patch antenna by 30% [4]. If an L-probe is used to excite a U-slot rectangular PEC patch antenna, the bandwidth is increased by 40% [5]. Recently, a novel microstrip patch antenna exciting the TE_{10} mode was reported by the authors in [3], where both the patch and the ground plane consisted of uniformly distributed unipolar photonic bandgap (UC-PBG) [6] unit cells to mimic magnetic conductors' properties in order to satisfy the proper boundary conditions for the TE mode excitation. In [3], it was shown that the TE_{10} patch antenna was 44% smaller in size than its TM_{10} patch antenna counterpart. In this letter, the TE_{10} mode patch antenna is further investigated for wideband applications by implementing a U-slot in its patch layer. The wideband antenna supports the TE_{10} mode, which is excited by an L-probe, and shows a bandwidth of about 40%. Moreover, due to the inherent size reduction property of the TE patch antenna [3] [7], the width of the AMC patch is about 1.75 times smaller than its length, i.e., W=L/1.75. This results in about 60% reduction of the lateral size of the wideband TE antenna. Thus, the lateral dimensions of the proposed U-slot antenna exciting the TE mode would be smaller than those of the conventional U-slot patch antenna exciting the TM mode.

II. ANTENNA GEOMETRY

Herein, wideband characteristics of the TE patch antenna are studied based on the design reported by the authors in [3], which is a narrowband TE_{10} mode microstrip patch antenna. To widen its impedance bandwidth, a U-shaped slot is cut in the patch layer of the AMC antenna, a side view of which is depicted in Fig. 1. The antenna consists of a radiating patch and a ground plane, both made of UC-PBG AMC surfaces that are separated by a layer of air (ε_r=1) with a height of h=6.4 mm. Each AMC surface consists of periodic UC-PBG unit cells backed by a grounded dielectric substrate Rogers RO3010 [8] with relative permittivity of ε_r=10.2 and a height of h_1=0.635mm. The antenna excites the TE_{10} mode by an L-probe connected to a 50Ω SMA connector and oriented perpendicular to the length of the patch. The vertical arm of the L probe has a radius of r_v=0.635mm and a length of L_v=5.535mm, and the horizontal arm has a radius of r_h=1.1mm and a length of L_h=15mm. The L-probe is placed at an offset of L_f=7mm from the center of the patch. This antenna is numerically finalized to obtain a bandwidth of ~40%, which makes it suitable for wideband wireless communications. The numerical computations are carried out by ANSYS HFSS, V. 18 [9], which is a finite-element full-wave electromagnetic solver. The patch and the ground plane layers are detailed in the following sections.

A. Antenna patch layer

In order to excite the TE_{10} mode, the top and bottom walls of the antenna cavity should be made of magnetic

Submitted On: October 23, 2019
Accepted On: June 19, 2020
https://doi.org/10.47037/2020.ACES.J.350817

conductors. To this end, the patch layer itself is constructed by an AMC, consisting of 7×4 UC-PBG unit cells placed on one side of the 82.6mm×82.6mm dielectric material Rogers RO3010 with relative permittivity ε_r =10.2 and a height h_1=0.635mm. The other side of the substrate contains a PEC metal plate of dimensions L×W=46.2mm×26.4mm. The top and bottom views of the patch layer are shown in Fig. 2. The combination of the unit cells and the metal plate, separated by the dielectric material, acts as an AMC within the frequency bandgap of the UC-PBG material. The vertical and horizontal arms of the U-slot, denoted by L_s and W_s in Fig. 2, are equal to 46 mm and 6 mm, respectively. The entire U-slot has a uniform thickness of 1 mm. The vertical and horizontal arms of the slot, i.e., L_s and W_s, are placed 4 mm and 0.1 mm away from the length and the width of the patch, respectively.

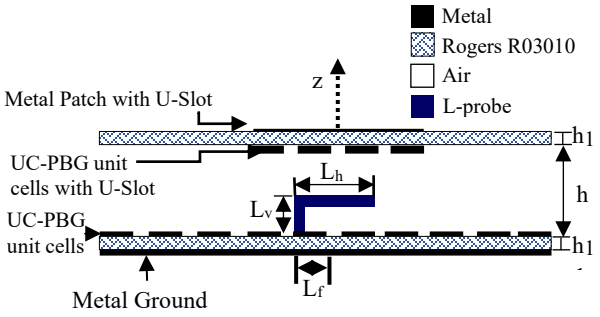

Fig. 1. Side-view of the wideband TE_{10} patch antenna with UC-PBG unit cells in both the patch and the ground plane excited by an L-probe with L_v=5.535 mm, L_h=15 mm, L_f=7mm, h=6.4mm, and h_1=0.635mm.

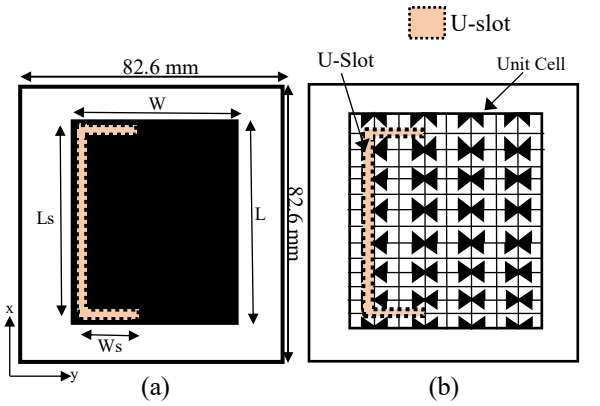

Fig. 2. (a) Top-view of the patch with PEC metal plate with a U-slot. (b) Bottom-view of the patch with unit cells and U-slot placed exactly below the PEC metal plate with dimensions of L×W=46.2mm×26.4mm; L_s=46mm, W_s=6mm.

B. Antenna ground layer

To satisfy the proper boundary conditions for the TE patch antenna under study, the ground plane should also be made of an AMC layer, which consists of 12×12 UC-PBG unit cells etched on the thin grounded Rogers RO3010 of ε_r=10.2 and height h_1=0.635mm. It has 144 UC-PBG unit cells placed above the dielectric material with a size of 82.6 mm×82.6 mm. The UC-PBG unit cells along with the dielectric material and the metal plate together form the AMC ground plane. This ground plane behaves as a high impedance surface within the frequency band of the UC-PBG unit cells. The top and bottom views of the designed AMC ground plane are depicted in Fig. 3.

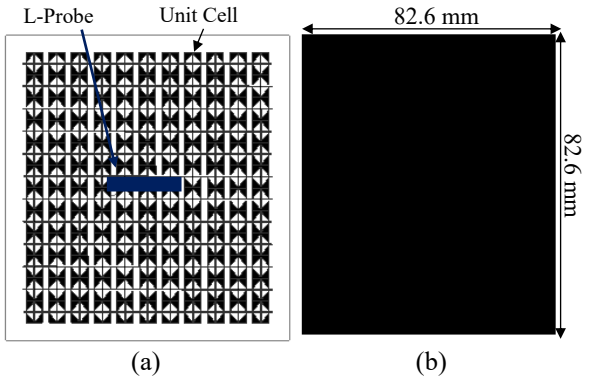

Fig. 3. (a) Top-view of the ground plane consisting of a 12×12 unit cells. (b) Bottom-view of the ground plane consisting of a solid PEC metal plate.

III. NUMERICAL RESULTS

The proposed U-slot AMC antenna shows a wide bandwidth of ~40%, ranging from 3.1 GHz to 4.8 GHz. The reflection coefficient of the antenna with the U-slot is plotted in Fig. 4. It is worth mentioning that the AMC antenna without the U-slot shows a bandwidth of 10% due to the L-probe, whose result is also overlaid in Fig. 4 for comparison. The impedance bandwidth increases to ~40%, when the U-slot is cut from the patch layer. The frequncy range of the UC-PBG material in [3] will shift down due to the miniaturization attribution of the U-slot in the patch layer. More specifically, it is observed that the AMC antenna with the U-slot has three distinct resonat frequencies of 3.2 GHz , 3.9 GHz and 4.6 GHz below the -10 dB line, which are closely coupled together to widen the impedance bandwidth. It is found that the bandwidth is quite sensitive to the length of the longer arm (L_s) of the U-slot, which is manily due to the strong interaction of the U-slot with the unit cells of the engineered magnetic material in the patch layer.

The antenna peak gain versus frequency is plotted in Fig. 5, reaching to a maximum value of 8.4 dBi near the frequency of 3.3 GHz, with less than a 2-dB gain variation over the entire frequency range of 3.1 to 4.8 GHz. Such a small variation in the antenna gain is in part attributed to the potential impact of the U-slot on the effective bandwidth of the reflection phase response of

the UC-PBG unit cell.

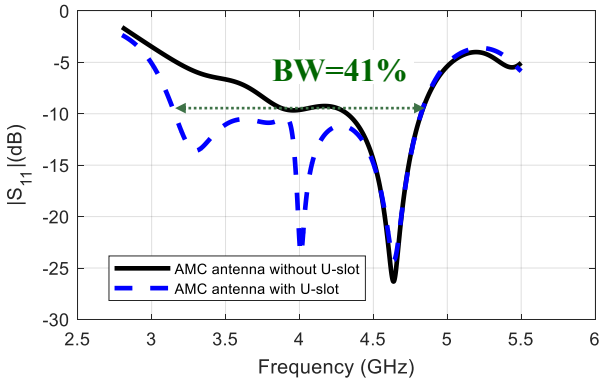

Fig. 4. Reflection coefficients of the AMC antenna exciting the TE_{10} mode with and without the U-slot.

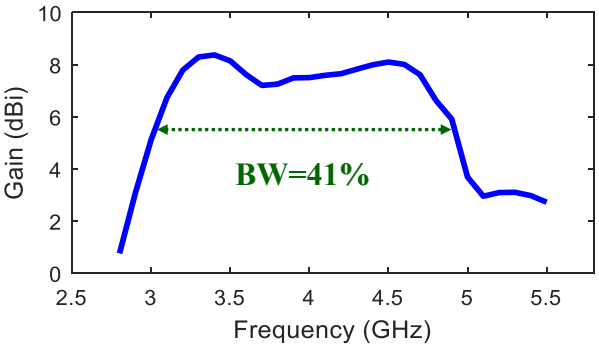

Fig. 5. Peak gain of the wideband U-slot AMC antenna against frequency.

The radiation patterns of the antenna at the three distinct frequencies of 3.2 GHz, 3.9 GHz and 4.6 GHz are plotted in Fig. 6. It is found that the antenna generates broadside radiation patterns up to 4.3 GHz. As the frequency increases beyond 4.3 GHz, higher order modes are excited to some extent, which create a saddle-shaped pattern. The same trend is also observed for the conventional U-slot antennas [4]. Thus, the bandwidth within which the radiation pattern of this PMC antenna remains broadside is ~30%.

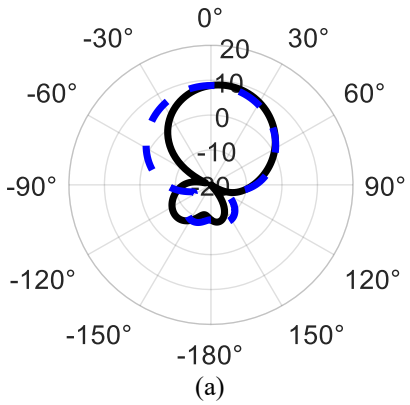

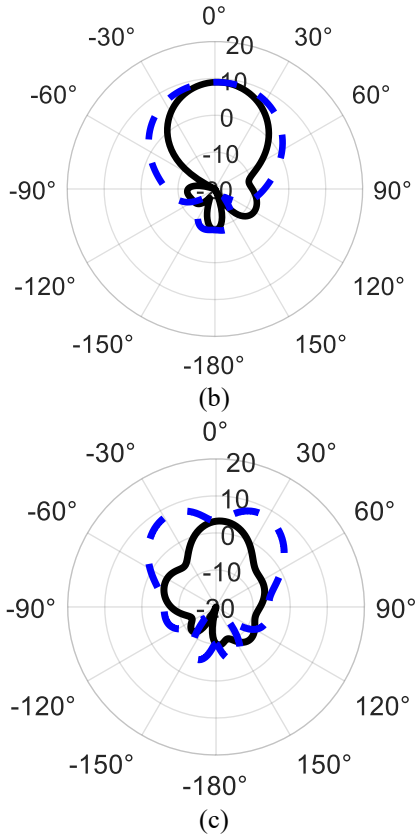

Fig. 6. Radiation patterns of the wideband AMC U-slot patch antenna at: (a) 3.2 GHz, (b) 3.9 GHz, and (c) 4.6 GHz; E-plane: solid black line, H-plane: dashed blue line.

IV. CONCLUSION

The concept of the U-slot patch antenna was investigated in the AMC microstrip patch antenna, exciting the TE_{10} mode using an L-probe. It was shown that the U-slot AMC antenna proposed in this letter provided a bandwidth of ~40%, ranging from 3.1 GHz to 4.8 GHz. The antenna parameters such as impedance bandwidth, gain, and radiation patterns were studied. The radiation patterns remained broadside for about 30% of the bandwidth. More importantly, it was demonstrated that the width of the U-slot TE_{10} patch is 1.75 times smaller than its length, i.e., W=L/1.75, resulting in ~60% reduction in the overall size, compared with the conventional U-slot patch antennas.

ACKNOWLEDGMENT

This work was supported in part by the National Science Foundation (NSF) CAREER under Award ECCS-1653915.

REFERENCES

[1] C. A. Balanis, *Antenna Theory: Analysis and Design*. 4th ed., Hoboken, NJ: John Wiley, 2016.

[2] S.-L. S. Yang, A. A. Kishk, and K.-F. Lee, "Rectangular patch antenna supported by artificial magnetic conducting surface," in *2008 URSI General Assembly Chicago*, Aug. 2008.
[3] T. Mitha and M. Pour, "Investigation of dominant transverse electric mode in microstrip patch antenna," *IEEE Trans. Antennas Propag*., vol. 67, no. 1, pp. 643-648, Jan. 2019.
[4] T. Huynh and K.-F. Lee, "Single-layer single-patch wideband microstrip antenna," *Electron. Lett*., vol. 31, no. 16, pp. 1310-1312, Aug. 1995.
[5] A. Shackelford, K.-F. Lee, and D. Chatterjee, "On reducing the patch size of U-slot and L-probe wideband patch antennas," *2000 IEEE-APS Conf. Antennas Propag. Wireless Commun.*, Waltham, MA, pp. 35-38, 2000.
[6] S.-L. S. Yang, A. A. Kishk, and K.-F. Lee, "The forbidden bandgap characteristic of EBG structures," *Microw. Opt. Tech. Lett*., vol. 50, pp. 2965-2967, 2008.
[7] T. H. Mitha and M. Pour, "Effect of ground plane size on a rectangular microstrip patch antenna based on TE modes supported by perfect magnetic conducting surface," in *2017 IEEE Int. Symp. Antennas Propag. & USNC/URSI National Radio Science Meeting*, San Diego, CA, pp. 2237-2238, 2017.
[8] Rogers Corporation, "RO3000® Series Circuit Materials RO3003™ RO3006™ RO3010™ and RO3035™ High Frequency Laminates," 2018.
[9] ANSYS High Frequency Electromagnetic Field simulator HFSS (version 18.1), Canonsburg, PA, 2018.
[10] S. Weigand, G. H. Huff, K. H. Pan, and J. T. Bernhard, "Analysis and design of broad-band single-layer rectangular U-slot microstrip patch antennas," *IEEE Trans. Antennas Propag*., vol. 51, no. 3, pp. 457-468, Mar. 2003.

Tanzeela H. Mitha was born in Pune, India in 1993. She received her B.E. in Electronics and Telecommunication from University of Pune, Maharashtra, India in 2016. She received her Masters of Science degree in Electrical Engineering from The University of Alabama in Huntsville, Alabama, USA in 2018. She is presently a Ph.D. student at The University of Alabama in Huntsville, working with Dr. Maria Pour. Her research interests include microstrip patch antennas, wideband antennas, dual-mode antennas and phased array antennas.

Maria Pour (S'06–M'11–SM'16) received the Ph.D. degree in Electrical Engineering from the University of Manitoba, Winnipeg, MB, Canada, in 2012. She joined the Department of Electrical and Computer Engineering, The University of Alabama in Huntsville, AL, as an Assistant Professor in August 2015. Prior to her current appointment, she was a Research Associate and Assistant Director with the Antenna Laboratory, University of Manitoba. She has coauthored six book chapters and has published over 80 journal articles and conference proceedings. Her research interests are in the areas of applied electromagnetics and antennas. Since 2016, she has been serving as an Associate Editor for the IEEE Transactions on Antennas and Propagation.

Design of a New Wideband Single-Layer Reflective Metasurface Unit Cell for 5G-Communication

Muhammad A. Qureshi [1], Abdul Aziz [1], Asjad Amin [1], Hafiz Faiz Rasool [2*], and Faisal Hayat [3]

[1] Department of Telecommunication Engineering, The Islamia University of Bahawalpur, 63100, Pakistan
ali.qureshi@iub.edu.pk, abdul.aziz@iub.edu.pk, asjad.amin@iub.edu.pk

[2] School of Information and Electronics, Beijing Institute of Technology, Beijing, China
hafiz@bit.edu.cn*

[3] Department of Computer Engineering, University of Engineering and Technology, Lahore, Pakistan
faisal.hayat@kics.edu.pk

Abstract ─ In this paper, a new single layer subwavelength unit cell is designed for reflective metasurface at 28 GHz suitable for 5G communication with linear phase response and wide bandwidth characteristics. The proposed unit cell is analyzed through Floquet mode analysis for two different sizes. The unit cell with conventional half-wavelength size (HWS) has achieved 590° phase range while the unit cell with a subwavelength size (SWS) of $\lambda/3$ has achieved exactly 360°phase range. It is observed that the unit cell with SWS provides linear phase response as compared to the unit cell with HWS. Since non-linear phase response may produce more phase errors on wide range of frequencies, so SWS unit cell with 360° phase range and linear phase response is more suitable option for wideband operation as compared to conventional HWS unit cell with more than 360° phase range.

Index Terms ─ 5G communication, metasurface, reflectarray, reflective, subwavelength, wideband.

I. INTRODUCTION

Antenna array beamforming has a key role to achieve higher data rates in 5G communication system [1,2]. Reflective metasurface (RM) or reflectarray antennas are widely used to generate high directional pencil beams and considered as the most promising solution for point to point and 5G communication systems [3-6]. RM is a low-cost and low-profile solution as compared to the conventional parabolic reflectors. Despite its various advantages, RM has narrow bandwidth due to inherent narrow-band nature of microstrip elements and phase dispersion due to non-linear phase response of such elements.

An RM unit cell needs to achieve at least 360° phase shift range for compensation of phase delays [7]. This phase shift range is usually achieved by varying the size of the patch element within the fixed size of the unit cell. A conventional unit cell size is usually half-wavelength at designed frequency to avoid grating lobes [7]. However, the phase curve achieved by such unit cell size is usually non-linear that results in significant phase errors particularly when frequency is different from the designed frequency [8]. Due to such significant phase errors the metasurface cannot be used for wideband operation. However, if phase response is linear then such phase errors will be reduced significantly due to less sensitivity of phase curve.

During the past few years, various wideband approaches have been proposed to improve bandwidth performance for RM. Multi-resonant element [9-11] and subwavelength element [12-17] are famous techniques, which are usually designed with multilayer configurations with air-gap to enhance bandwidth. However, RM with multi-layer elements leads to more fabrication complexity with higher cost. In the proposed technique a single layer simple element is designed without any air-gap by combining multi-resonant element and subwavelength element techniques to achieve linear phase response and hence wideband operation for 5G communication.

To achieve the goal, first a single layer unit cell with conventional half-wavelength size (HWS) is designed that achieves 590° phase range with non-linear phase response at 28 GHz. The size of the unit cell is then restricted to sub-wavelength size (SWS) that achieves sufficient 360° phase range with linear phase response at 28 GHz for 5G communication system.

As, SWS unit cell achieved 360° phase range that is sufficient for phase compensation, so redundant phase range can be avoided to achieve linear phase response and hence wideband performance. SWS unit cell is also compared with HWS unit cell through sensitivity response at designed frequency and phase response over a wide range of frequencies to verify its wideband

Submitted On: November 15, 2019
Accepted On: June 16, 2020
https://doi.org/10.47037/2020.ACES.J.350818

performance.

The rest of the paper is as follows. In Section II, the structure of the proposed unit cell for RM is briefly discussed. Section III discusses the performance analysis of the unit cell and finally the paper is concluded in Section IV.

II. PROPOSED UNIT CELL FOR RM

RM antenna design is mainly depending on the unit cell. The first step in the design of RM is to choose a unit cell that can span a 360° reflection phase range. By achieving this condition, we can compensate for the total phase delay from the feed to all RM elements on aperture plane in order to transform a spherical wavefront to a plane wave.

A. Unit cell structure

The unit cell for RM operates around 28 GHz for 5G communication system. The unit cell is a part of a square lattice in which proposed multi-resonant microstrip element printed on a substrate layer without air gap is shown in Fig. 1.

The proposed microstrip element of the unit cell is simple and cost effective without any fabrication complexity. The substrate used is Rogers RT/duroid 5880 with dielectric permittivity εr = 2.55, thickness h_s = 1.575 mm, loss tangent δ = 0.0009. Diameter D_o is the main parameter of the microstrip element, which is varied to control phase response. Other geometrical parameters, which are optimized through parametric analysis for the proposed microstrip element are following: W_o = 0.3 mm, g_1 = 0.3mm, W_g = 0.3 mm, L_c = 0.5 mm.

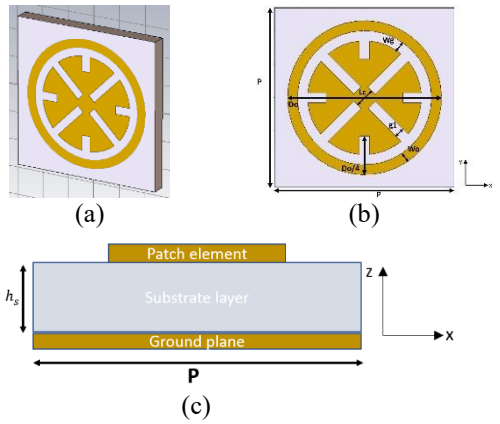

Fig. 1. Configuration of the unit cell element in the proposed RM: (a) unit cell, (b) front view, and (c) side view.

B. Simulation setup and phase response

Floquet mode of CST Microwave studio suite is used to analyze the scattering characteristics of the unit cell. We use periodic boundary conditions along *x* and *y* axes whereas boundary condition for z-axis is kept open. Surface roughness of the unit cell is ignored during simulation due to availability of smooth lithographic printing facility for microstrip elements. The phase response of unit cell is analyzed for two sizes, i.e., conventional HWS with $P = 5.35$ mm (λ/2 at 28 GHz), and SWS for which $P = 3.5$ mm (λ/3 at 28 GHz). The phase responses for the SWS and HWS unit cells at 28 GHz are shown in Figs. 2 (a) and 2 (b) respectively. The diameter D_o is varied from 2 to 5.3 mm and 2 to 3.5 mm with a step size of 0.01 mm for HWS and SWS unit cells at 28 GHz, respectively. The conventional HWS unit cell achieves 590° phase range, however the phase response is non-linear, due to which more phase errors will be generated when frequency deviates from 28 GHz. On the other side, the phase response of SWS unit cell is almost linear and it achieves sufficient 360° range required to compensate phase delays. For RM design, the value of D_o may not be fixed to a single value instead several different values of D_o may be used for compensation of phase delays from 0 to 360 degree. Due to linear phase response of the SWS unit cell wideband performance is expected.

C. Parametric analysis

To achieve more than 360°phase range and linear phase response, optimum parameters are selected through parametric analysis. The phase response of a unit cell depends on element size, shape, substrate thickness and dielectric permittivity. The parametric analysis for the two critical geometrical parameters of the unit cell (L_c, and W_g) are shown here in Figs. 3 and 4 for both HWS and SWS unit cells. Other geometrical parameters are not much sensitive to phase response, so the effect of their variation is not shown here for brevity.

First, L_c is varied from 0.1 mm to 0.5 mm as shown in Fig. 3, and it can be seen that non-linear phase response of HWS unit cell is more obvious and phase response of SWS unit cell remains almost linear at all values, L_c = 0.3 mm is selected as an optimum value because at other values the phase range is less than 360°for SWS unit cell. Thereafter, W_g is varied from 0.2 mm to 0.4 mm while other parameters are fixed. Figure 4 shows that the phase response of HWS unit cell is still non-linear with more than 360° phase range for all values of W_g. While, the phase response for SWS unit cell becomes more linear as W_g increases, however W_g = 0.3 mm is selected as optimum value because it achieves exactly 360° phase range.

III. PERFORMANCE ANALYSIS

The performance of the proposed unit cell is evaluated using sensitivity, bandwidth and cross-polarization analysis.

A. Sensitivity analysis

The sensitivity of the unit cell is determined by

computing the partial derivative of the reflection phase response with respect to microstrip patch size (D_o). The sensitivity analysis helps in determining the tolerance against the fabrication errors and related to the slope of the reflection phase curve, i.e., the smooth reflection phase curves exhibit more stable bandwidth performance as well as lower fabrication sensitivity or high tolerance over a wide range of frequencies with less fabrication and phase errors. Figure 5 shows the sensitive responses of the SWS and HWS unit cells. From the plots, it is observed that the SWS unit cell is less sensitive to fabrication and phase errors as compared to the HWS unit cell.

B. Bandwidth analysis

The bandwidth of the RM antenna is also determined from the reflection phase curves of the unit cell. The phase responses of both HWS and SWS unit cells are analyzed for different frequencies to observe the bandwidth of the unit cell. Figure 6 shows reflection phase response of the unit cell from 26 GHz to 30 GHz, it is observed that the reflection phase curves are linear and parallel to each other for the SWS unit cell as shown in Fig. 6 (a). On the other hand, the phase curves for HWS unit cell in Fig. 6 (b) are not as much parallel and linear particularly at the lower ends as compared to SWS unit cell and hence more significant phase errors are expected from HWS unit cell for wideband operation. It verifies significant superiority of SWS unit cell over HWS unit cell for wideband performance.

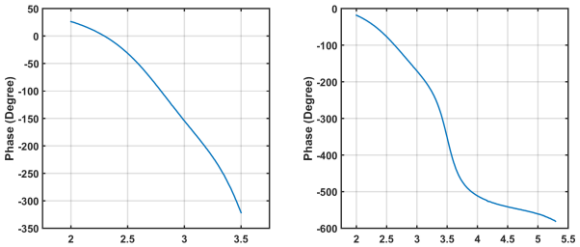

Fig. 2. Phase response for the proposed: (a) SWS unit cell and (b) HWS unit cell.

C. Cross polarization analysis

The cross polarization shows isolation of a co-polarized radiation wave with an orthogonal polarized radiation wave. Since the unit cell structure is symmetric so cross polarization can be suppressed, so it is necessary to analyze cross polarization of the unit cell. The unit cell is analyzed through Floquet ports in CST Microwave Studio. For cross polarization analysis the two ports of the unit cell are used in cross polarized modes, if one port is in TE mode then the other port is converted to TM mode to see cross polarization response of the unit cell. The cross polarization of both types of unit cells is shown in Fig. 8. It is clear that the cross-polarization level is less than −40 dB in both cases. It confirms that the proposed unit cell is also suitable to achieve cross polarization isolation.

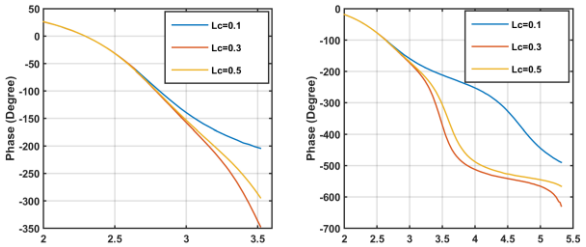

Fig. 3. Phase response for the proposed unit cell for different L_c values: (a) SWS unit cell and (b) HWS unit cell.

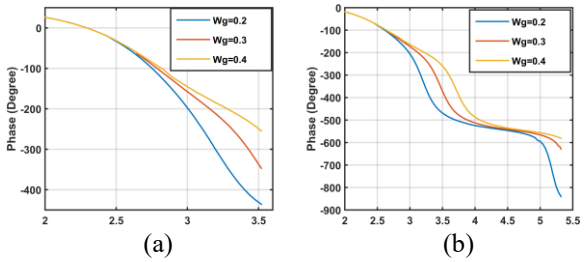

Fig. 4. Phase response for the proposed unit cell for different W_g values: (a) SWS unit cell and (b) HWS unit cell.

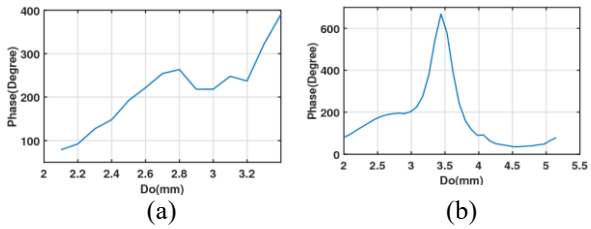

Fig. 5. Sensitivity response of proposed unit cell: (a) SWS unit cell and (b) HWS unit cell.

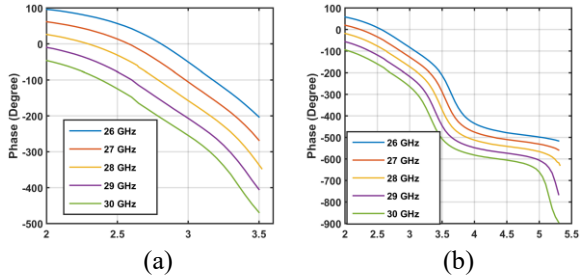

Fig. 6 Bandwidth response of unit cell at 28 GHz: (a) SWS unit cell and (b) HWS unit cell.

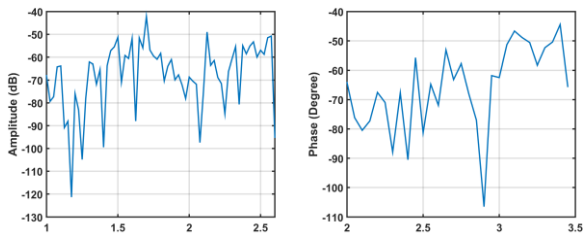

Fig. 7 Cross polarization response for the proposed unit cell: (a) SWS unit cell and (b) HWS unit cell.

IV. CONCLUSION

A simple single layer RM unit cell was proposed to achieve wideband performance. The unit cell was analyzed for both HWS and SWS for a wide range of frequencies. HWS unit cell achieves 590° phase range (Fig. 2b) with non-linear phase response which is not suitable for wideband operation. The phase response for HWS unit cell remains almost linear for D_o = 2 to 3.3mm and becomes non-linear for D_o = 3.3 to 5.35mm. Thus, more phase errors will be generated due to non-linearity of phase curve that may reduce performance of the RM for a wide range of frequencies. While, the SWS unit cell provided exactly 360° phase range with almost linear phase response for D_o = 2 to 3.5 mm (Fig. 2 (a)). Moreover, the phase response curves remain almost linear and parallel for a wide range of frequencies (Fig. 6 (a)), which complements the wide bandwidth requirement of RM for 5G communication systems. Sensitivity (Fig. 5) and cross polarization analysis (Fig. 7) of the unit cell also demonstrated that SWS unit cell is simple and cost effective without any fabrication complexity and it also achieves good cross polarization isolation.

REFERENCES

[1] E. Ali, M. Ismail, R. Nordin, and N. F. Abdulah, "Beamforming techniques for massive MIMO systems in 5G: Overview, classification, and trends for future research," *Frontiers Inf. Technol. Electronic Eng.*, vol. 18, no. 6, pp. 753-772, 2017.

[2] A. Aziz, M. A. Qureshi, M. J. Iqbal, S. Z. A. Zaidi, U. Farooq, and U. Ahmad, "Performance and quality analysis of adaptive beamforming algorithms (LMS, CMA, RLS & CGM) for smart antennas," *Int. Conference on Computer and Electrical Engineering*, vol. 6, pp. 302-306, 2010.

[3] M. H. Dahri, M. H. Jamaluddin, M. I. Abbasi, and M. R. Kamarudin, "A review of wideband reflect-array antennas for 5G communication systems," *IEEE Access*, vol. 5, pp. 17803-17815, 2017.

[4] R. R. Elsharkawy, M. Hindy, A. A. Saleeb, and E. S. M. El-Rabaie, "A reflectarray with octagonal unit cells for 5-G applications," *Wireless Pers. Commun.*, vol. 97, no. 2, pp. 2999-3016, 2017.

[5] W. Hong, Z. H. Jiang, C. Yu, J. Zhou, P. Chen, Z. Yu, H. Zhang, B. Yang, X. Pang, M. Jiang, Y. Cheng, M. Al-Nuaimi, Y. Zhang, J. Chen, and S. He, "Multibeam antenna technologies for 5G wireless communications", *IEEE Trans. Antennas Propag.*, vol. 65, no. 12, pp. 6231-6249, 2017.

[6] J. Huang and J. A. Encinar, *Reflectarray Antennas*. vol. 30, John Wiley & Sons, 2007.

[7] J. Shaker, M. R. Chaharmir, and J. Ethier, *Reflectarray Antennas: Analysis, Design, Fabrication, and Measurement.* Artech House, 2013.

[8] P. Nayeri, F. Yang, and A. Z. Elsherbeni, *Reflectarray Antennas: Theory, Designs and Applications.* John Wiley & Sons, 2018.

[9] M. Chaharmir and J. Shaker, "Broadband reflectarray with combination of cross and rectangle loop elements," *Electron. Lett.*, vol. 44, no. 11, pp. 658-659, 2008.

[10] J. A. Encinar and J. A. Zornoza, "Broadband design of three-layer printed reflectarrays," *IEEE Trans. Antennas Propag.*, vol. 51, no. 7, pp. 1662-1664, 2003.

[11] E. C. Choi and S. Nam, "W-band low phase sensitivity reflectarray antennas with wideband characteristics considering the effect of angle of incidence," *IEEE Access*, 2020.

[12] J. Wang, Y. Zhou, S Gao, and Q. Luo, "An efficiency-improved tightly coupled dipole reflect-array antenna using variant-coupling-capacitance method," *IEEE Access*, vol. 8, pp. 37314-37320, 2020.

[13] P. Nayeri, F. Yang, and A. Z. Elsherbeni, "Broadband reflectarray antennas using double-layer subwavelength patch elements," *IEEE Antennas Wirel. Propag. Lett.*, vol. 9, pp. 1139-1142, 2010.

[14] P. Nayeri, F. Yang, and A. Z. Elsherbeni, "Bandwidth improvement of reflectarray antennas using closely spaced elements," *Prog. Electromagn. Res. C*, vol. 18, pp. 19-29, 2011.

[15] J. Wu, X. Da, B. Lin, J. Zhao, and K. Wu, "Circularly polarized low-cost wide band reflect-array antenna constructed with subwavelength elements," *Int. J. RF Microwave Comput. Aided Eng.*, vol. 28, no. 6, pp. e21277, 2018.

[16] J. Wang, Y. Zhou, and X. Feng, "A dual-polarized wideband tightly coupled reflectarray antenna proposed for 5G communication," *Proc. Computing, Communications & IoT Applications (ComComAp)*, IEEE, pp. 200-203, 2019.

[17] Z. Akram, X. Li, Z. Qi, A. Aziz, L. Yu, H. Zhu, X. Jiang, and X. Li, "Wideband vortex beam reflectarray design using quarter-wavelength element," *IEEE Antennas Wirel. Propag. Lett.*, vol. 18, no. 7, pp. 1458-1462, 2019.